The Growth & Transformation of Galaxies Across Cosmic Time

by

Katherine A. Suess

A dissertation submitted in partial satisfaction of the

requirements for the degree of

Doctor of Philosophy

in

Astrophysics

in the

Graduate Division

of the

University of California, Berkeley

Committee in charge:

Professor Mariska Kriek, Chair
Professor Eliot Quataert
Professor Martin White

Summer 2021

The Growth & Transformation of Galaxies Across Cosmic Time

Abstract

The Growth & Transformation of Galaxies Across Cosmic Time

by

Katherine A. Suess

Doctor of Philosophy in Astrophysics

University of California, Berkeley

Professor Mariska Kriek, Chair

Deep surveys have allowed us to precisely chart the evolution of galaxies from billions of years ago through to the present day. We've found that galaxies in the distant past are dramatically different than those in the local universe: the stellar masses, sizes, structures, star formation rates, gas contents, and kinematics of galaxies all evolve with redshift. One of the few constants is the bimodality between star-forming and quiescent galaxies, which persists across a wide redshift range. Despite these observational advances, the exact nature of the physical processes governing the growth and transformation of galaxies remain unknown.

The first section of this thesis concentrates on the *growth* of galaxies. Previous studies have used half-light radii to trace the evolution of galaxy sizes. However, radial color gradients cause the light and mass profiles of galaxies to differ, biasing these measurements. I develop and test multiple techniques for measuring the mass profiles of galaxies from high-resolution multi-band *Hubble Space Telescope* imaging, then use these techniques to create the largest-ever catalog of galaxy half-mass radii at $0 \lesssim z \leq 2.5$. This unique catalog enables me to correct for biases in previous studies of size evolution and discover that galaxies grow much more slowly than previously thought. I then examine how the structures of galaxies change as they age along the quiescent sequence, providing support for a merger-driven "inside-out" growth mechanism. Finally, I investigate how the structures of galaxies change as they gradually move up the star-forming sequence towards quiescence. These results pave the way for a new interpretation of the star-forming size-mass relation, and provide evidence for multiple distinct pathways for galaxies to shut down their star formation.

The second section of this thesis addresses the *transformation* of galaxies from star-forming to quiescent. Because stars form out of cold molecular gas, most theoretical mechanisms for this "quenching" process rely on heating, depleting, or removing molecular gas reservoirs. Post-starburst galaxies, whose spectra indicate that they have recently and rapidly shut down a major burst of star formation, are the ideal laboratory to test these theoretical quenching mechanisms. I introduce the SQuIGG$\vec{L}$E multi-wavelength survey of intermediate-redshift

post-starburst galaxies. After selecting $\sim 1,300$ of these rare recently-quenched galaxies by their Sloan Digital Sky Survey spectroscopy, I perform detailed Bayesian spectral modeling to constrain their star formation histories. I also present Atacama Large Millimeter/submillimeter Array measurements of the CO(2–1) line in two SQuIGG$\vec{L}$E galaxies. I show that, in contrast to theoretical predictions, these recently-quenched galaxies can retain large molecular gas reservoirs. These puzzling observations challenge our understanding of how galaxies shut down their star formation.

Contents

Acknowledgments

So many people have helped shape this dissertation and its author over the past six years. I am grateful to all of you for sharing your encouragement, wisdom, and friendship.

This work would not have been possible without the guidance of Mariska Kriek. Thank you for teaching me how to ask interesting questions and weave stories out of the answers; your advice and unflagging support has helped shape me into the scientist I am today. While I'm grateful that you supported me looking for a job outside academia, I'm even more grateful that you sent me to a bunch of ski conferences that convinced me to stay (for now).

I lucked into the most fantastic set of collaborators I could have ever asked for. I am especially grateful to the whole SQuIGG$\vec{L}$E team, including Rachel Bezanson, Justin Spilker, Jenny Greene, and David Setton. Working with and learning from all of you has been a joy, and I hope we continue writing last-minute telescope proposals together for many years to come. I would also like to thank Sedona Price for immeasurable help during my early grad career, Joel Leja & Ben Johnson for answering my many `Prospector` questions, and the Keck Observatory support astronomers and telescope operators.

I am grateful to all of the Respect is Part of Research facilitators and coordinators who dedicated their time to making our scientific community a more welcoming place, including Simca Bouma, Sam Kohn, Gwen Hanley, and many more— but especially my co-conspirator Micah Brush. I am so proud of the work that we did to grow and expand RPR.

Thank you to my wonderful family. To my parents, Barb & Terry Suess, who together provided the perfect balance between "work hard" and "take more days off," and who always so clearly believed I would succeed at whatever I decided to do. To my west coast parents Diana & Rich Martins, who were so welcoming from the very first moment I arrived in Berkeley; I know we'll have many more dinners and board game nights to come. And to my big sister Alison Suess, Matt Rigsby, Rustle the corgi, & Lane Suess Rigsby: I can't imagine a better place to have quarantined for job application season. Thanks for keeping me sane, cooking me dinner, and commiserating about grad school.

I will always cherish the years I spent in grad school as some of the best in my life, in no small part due to my incredible network of friends. I am grateful to so many BADGrads— including Tom Zick, Abi Polin, Fatima Abdurrahman, Lea Hirsch, Ellie Abrahams, Michael Medford, Chris Moeckel, Kareem El-Badry, and Hannah Klion— for getting through this PhD thing with me and making the intervening years vastly more fun. I am also so thankful for the incredible community at the Palace. I could not possibly say enough wonderful things about my Mineral Queens, Rebecca Barter & Shreya Thatai. Thank you to Mika Endo, JB & Mike Chapman, Bryant Garcia, Oakley Jennings-Fast, Ned Molter, and so many others for helping me explore the wilds of California. I can't get over how lucky I am to have so many climbing and backpacking buddies who are always up for a quick trek to Yosemite. Thank you to the Meditations book club for bringing some much-needed stability as I endeavored to finish a thesis during a global pandemic. I would also like to thank Eric Junkins for convincing me to move back to Colorado to climb and write my thesis, Annie Didier for all the ski days, and Peter Johnsen for backpacking, road trips, and conversation.

Chapter 1

Introduction

Images and spectra of distant galaxies have revealed that galaxy properties have evolved significantly across cosmic time. Local galaxies tend to be large and massive, with relatively small reservoirs of cold molecular gas; structurally, we see a high fraction of elliptical galaxies as well as well-settled star-forming disks (e.g., Blanton et al., 2003; Giovanelli et al., 2005; Noeske et al., 2007). The distant universe, however, is a much more chaotic place. Galaxies at $z \gtrsim 1$, when the universe was less than half of its current age, tend to be smaller and clumpier; gas fractions are higher, galaxies appear to have "burst-y" episodes of star formation, and most galaxies are still actively forming stars (e.g., Muzzin et al., 2013; Tacconi et al., 2013; van der Wel et al., 2014). One of the few constants across redshift is the apparent bimodality in the galaxy population: galaxies tend to either be blue star-forming disk galaxies supported by rotational motion, or "quiescent" red elliptical galaxies that are no longer forming stars.

The fundamental question of galaxy evolution is: how do we get from there to here? How and why do the sizes, morphologies, and gas contents of galaxies evolve over time? Furthermore, why do galaxies cease forming stars and transform from star-forming to quiescent?

There are two different approaches to answer these unsolved questions. The first is a *statistical approach*, where we look at changes in galaxy populations over time. For example, we could measure the sizes of thousands of galaxies then investigate how the average size of quiescent galaxies changes with redshift. This approach is able to effectively leverage the power of large, deep public surveys— with such large numbers of galaxies to study, we can lower the error bars on inferred quantities. However, this statistical approach has downsides: it may average over phenomena that occur on short timescales, or gloss over rare but interesting sub-populations. Furthermore, when using this statistical approach we must take great care in correctly connecting the dots across different redshift ranges: selection effects and biases can mimic apparent changes in galaxy populations. The alternative is a *resolved approach*, where we perform detailed multi-wavelength studies of individual galaxies. This approach has the advantage of allowing us to take a deep dive into the current conditions of the galaxy: with truly multi-wavelength data, we can synthesize a complete view of the stars, dust, and gas of the galaxy as well as the properties of its central supermassive black hole. While this approach can yield enormous insights about the physics that is responsible

for the evolution of individual galaxies, it is too resource-intensive for samples larger than ∼tens of galaxies.

In this thesis, I will blend the statistical and resolved approaches. First, I'll investigate galaxy growth and transformation from a statistical angle by using public *HST* data to study the sizes and structures of $> 10,000$ galaxies across a wide redshift range. Through these studies, I'll argue that "post-starburst" galaxies are an interesting sub-population to study in further detail. In the second part of this thesis, I'll do a detailed multi-wavelength dive into the properties of these post-starburst galaxies. I will study the connection between their star formation histories, their current star formation rates, and their molecular gas reservoirs in order to inform our understanding of the processes responsible for shutting down star formation in galaxies.

1.1 Galaxy growth: the size-mass relation and its evolution with redshift

The galaxy size-mass relation

When studying the statistics of galaxy populations, both stellar masses and sizes are key physical observables. The half-light radii of both quiescent and star-forming galaxies are related to their stellar masses, such that massive galaxies are larger than low-mass galaxies. This galaxy mass-size relation has now been studied over a large range of redshifts and stellar masses (e.g., Shen et al., 2003; van der Wel et al., 2014; Mowla et al., 2019b). Examining how star-forming and quiescent galaxies grow in size over cosmic time can provide clues about galaxy evolution. In combination with other measured properties, sizes inform studies of the mass assembly history of galaxies (e.g., Bezanson et al., 2009; Naab et al., 2009), the connections between galaxies and their host dark matter halos (e.g., Mo et al., 1998; Kravtsov, 2013; Somerville et al., 2018; Jiang et al., 2019), how galaxy populations change (e.g., Carollo et al., 2013; Poggianti et al., 2013) and how disks build up over time (e.g., van Dokkum et al., 2013). Figure 1.1 shows the best-fit size-mass relations for both quiescent and star-forming galaxies across a range of redshifts (figure adapted from van der Wel et al. 2014; Mowla et al. 2019b).

The size-mass relation for star-forming galaxies has a relatively shallow slope that remains approximately constant across redshift. Figure 1.1 shows that the sizes of star-forming galaxies have increased between $z \sim 2.75$ and $z \sim 0.25$. Interestingly, this growth appears slower than zeroth-order expectations for dark matter halo growth (Mo et al., 1998), perhaps due to evolving halo spin parameters (e.g., Somerville et al., 2008) or feedback processes (e.g., Dutton & van den Bosch, 2009). Recent abundance matching studies including this additional physics have found that the observed sizes of disky star-forming galaxies are indeed proportional to the virial radii of their host halos (e.g., Kravtsov, 2013; Huang et al., 2017; Somerville et al., 2018). Cosmological simulations have also found good agreement between

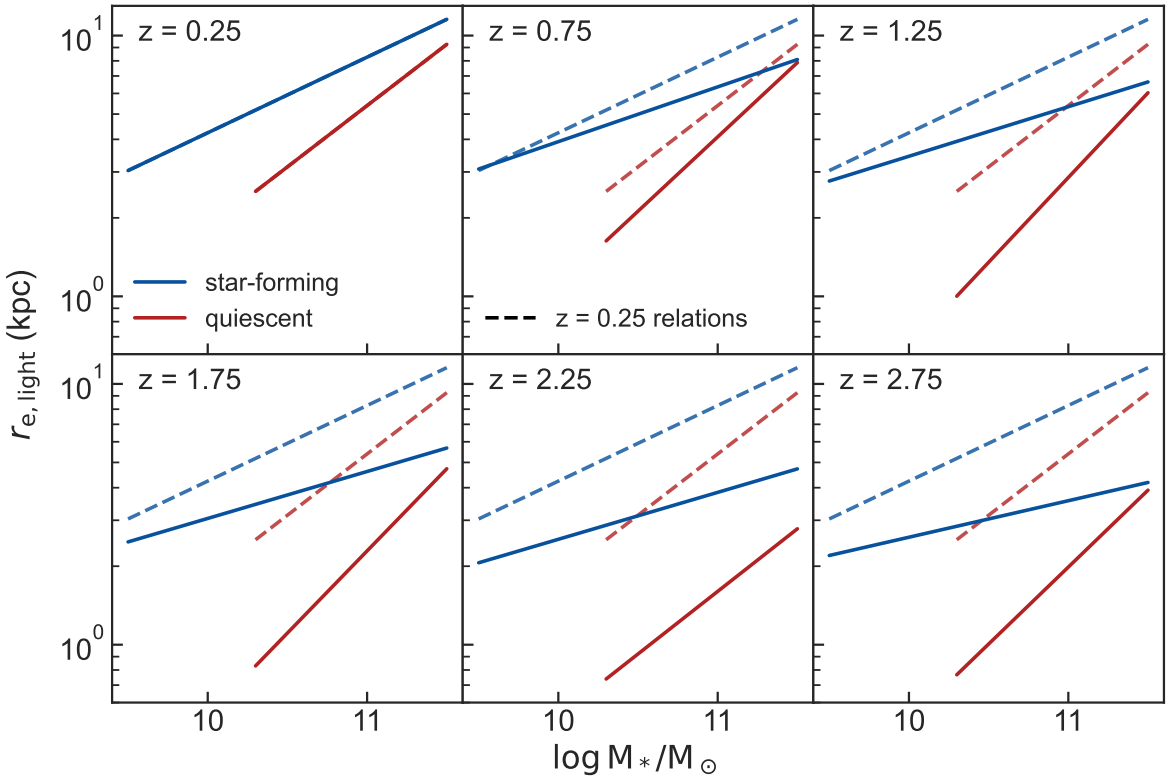

Figure 1.1: The best-fit relation between the size and stellar mass of star-forming and quiescent galaxies. Each panel shows a different redshift regime; the dashed lines show the $z = 0.25$ fits to guide the eye. Figure adapted from van der Wel et al. 2014; Mowla et al. 2019b.

observed and modeled star-forming galaxy size evolution (Furlong et al., 2017; Genel et al., 2018).

Quiescent galaxies exhibit a much steeper slope in the $r_{\rm e,light} - M_*$ relation and are more compact than similar-mass star-forming galaxies at all epochs (e.g., van der Wel et al., 2014). Furthermore, it now seems well-established that quiescent galaxies have experienced remarkable size growth over cosmic time, more than doubling their half-light radii between $z \sim 2$ and $z \sim 0$ (e.g., Daddi et al., 2005; van Dokkum et al., 2008; Damjanov et al., 2009; Szomoru et al., 2010; Damjanov et al., 2011; van der Wel et al., 2014). This extreme size growth is difficult to explain: after all, these galaxies are no longer forming stars, so it is difficult to alter the shapes of their light profiles. In the decade since this size growth was first discovered, multiple competing interpretations have arisen. In the 'inside-out growth' scenario, quiescent galaxies grow at late times via minor mergers that increase their radii without significantly increasing their stellar mass (e.g., Bezanson et al., 2009; Naab et al.,

2009; van de Sande et al., 2013; Hopkins et al., 2009). In the 'progenitor bias' scenario, galaxies that quench later are larger, introducing bias into average size evolution (e.g., van Dokkum & Franx, 2001; Carollo et al., 2013; Poggianti et al., 2013). Recent work has suggested that neither one of these two scenarios alone is sufficient to explain the rapid size growth of quiescent galaxies; instead, each growth mechanism seems to be responsible for roughly half of the total size evolution of quiescent galaxies (Belli et al., 2015).

A wrinkle: half-light and half-mass radii can differ

Previous studies of the galaxy size-mass relation rely on galaxy half-light radii. Because light is a biased tracer of mass, half-light radii are *not a direct probe* of the underlying stellar mass profiles of galaxies. Differences in half-mass and half-light radii arise from radial gradients in mass-to-light ratios. These radial mass-to-light ratio gradients can be physically caused by radial gradients in stellar populations: older, more metal-poor, or dustier stellar populations have higher mass-to-light ratios than younger or more metal-rich ones. Stellar mass-to-light ratio gradients can be observed as *color* gradients– stellar populations with high mass-to-light ratios are redder than those with low mass-to-light ratios. These color gradients bias studies of galaxy evolution that use half-light radii instead of half-mass radii. A robust catalog of galaxy half-mass radii is required to understand the effects that this bias has on studies of galaxy size evolution.

Studying galaxy color gradients also allows us to directly probe the assembly histories of galaxies, because different assembly histories naturally lead to different mass-to-light ratio profiles. For example, inside-out growth via minor mergers results in negative color gradients, as the accreted younger and/or lower-metallicity stellar populations primarily reside in the outskirts of the galaxy (e.g., Naab et al., 2009). Similarly, inside-out growth via star formation— where star formation occurs in the outer disk of a galaxy, but not its central bulge (e.g., Nelson et al., 2016b)— would result in negative color gradients. A central starburst (without extreme dust obscuration) will result in positive color gradients, where younger stars are found preferentially in the center of the galaxy. Uniform growth at all radii would result in no radial color gradient. Studying galaxy mass-to-light ratio profiles thus serves two important purposes: first, it gives us a less biased tracer of galaxy mass profiles; second, it probes the assembly histories of galaxies.

Some work has been done to understand galaxy mass-to-light ratio gradients, both in the $z \sim 0$ and $z > 1$ universe. In the local universe, radial color gradients attributed to metallicity gradients have been observed in quiescent galaxies (e.g., Saglia et al., 2000; La Barbera et al., 2005; Tortora et al., 2010). At higher redshifts, where galaxy half-light radii are smaller and observations are more difficult, it is challenging to break the age-metallicity degeneracy; still, negative color gradients implying radial variations in age, metallicity, or dust have been observed in many quiescent galaxies (e.g., Wuyts et al., 2010; Guo et al., 2011; Szomoru et al., 2012; Chan et al., 2016; Liu et al., 2017; Mosleh et al., 2017).

Previous studies at $z \gtrsim 1$ have typically used one of two methods to study M/L variations within galaxies. The first technique exploits the empirical correlation between rest-frame

color and mass-to-light ratio (e.g., Bell & de Jong, 2001). A intrinsic rest-frame color profile is constructed for the galaxy using `GALFIT` (Peng et al., 2002), converted to a mass-to-light ratio profile, and used to calculate a mass profile and a half-mass radius (e.g., Zibetti et al., 2009; Szomoru et al., 2010, 2012, 2013; Chan et al., 2016). The second technique uses multi-band imaging to measure the spatially-resolved spectral energy distribution (SED) of the galaxy; stellar population synthesis modeling of each spatially-resolved SED can recover the mass, age, and metallicity of the region (e.g., Wuyts et al., 2012; Lang et al., 2014). After accounting for the effects of the point spread function (PSF), half-mass radii can then be extracted from the mass maps of the galaxy.

These techniques have different strengths and potential pitfalls, but there has not yet been a direct comparison between these two major methods for calculating half-mass radii. Furthermore, while studies at $z \sim 0$ have large sample sizes (typically via the SDSS, e.g. Tortora et al., 2010), most studies of color gradients in more distant galaxies have focused on relatively small samples (< 200) of high-mass quiescent galaxies. Only a single study, Mosleh et al. (2017), has included a larger sample over a wider stellar mass range. In this thesis, we wish to perform a large, systematic study of the color gradients and half-mass radii of both quiescent and star-forming galaxies over a large range of stellar masses and redshifts. This type of study requires a large, deep, multi-band imaging survey— like CANDELS (Grogin et al., 2011)— that has excellent PSF-matching (now available from the 3D-HST collaboration, Skelton et al., 2014). Chapters 2 & 3 will use this remarkable public dataset, in combination with the multi-wavelength medium- and broad-band photometric catalog from ZFOURGE, to calculate the half-mass radii of $> 10,000$ galaxies at $0 \lesssim z \leq 2.5$ in a stellar mass range of $9.0 \leq \log(M_*/M_\odot) \lesssim 11.5$. We will then present the evolution of the galaxy size-mass relation, *corrected* for evolving color gradients.

1.2 Galaxy transformation: quenching and the buildup of the red sequence

For nearly a century, astronomers have divided galaxies into two distinct categories based on their morphologies: spirals and ellipticals (Hubble, 1926). This "galaxy bimodality" has since been shown to extend to a myriad of other properties, including color, size, environment, molecular gas content, and star formation rate (e.g., Blanton et al., 2003; Kauffmann et al., 2003; Shen et al., 2003; Noeske et al., 2007; Wuyts et al., 2011). Star-forming galaxies tend to be large, blue, rotationally-supported, and gas-rich; in contrast, quiescent galaxies are red, smaller at fixed mass, supported by random motions, and gas-poor. However, the fundamental question of *why* this galaxy bimodality exists remains unanswered to the present day. What physical processes are responsible for "quenching" star formation in galaxies? And why does a cessation of star formation appear to go hand-in-hand with structural and kinematic changes?

Structural clues towards quiescence: size & Σ_1

The largest structural changes that take place as galaxies evolve appear to be closely linked to the quenching process. In addition to characteristic differences in their star formation rates, colors, and stellar masses (e.g., Blanton et al., 2003; Kauffmann et al., 2003; Shen et al., 2003; Noeske et al., 2007; Wuyts et al., 2011), average star-forming and quiescent galaxies have significantly different structures. Star-forming galaxies tend to have disk-like light profiles, whereas quiescent galaxies have more significant bulge components and higher Sérsic indices (e.g., Bell, 2008; Wuyts et al., 2011; van Dokkum et al., 2011; Lang et al., 2014; Bluck et al., 2014). As shown in Figure 1.1, star-forming and quiescent galaxies also have distinct sizes: quiescent galaxies are smaller at fixed mass than their star-forming counterparts, and follow a steeper relation in size-mass space (e.g., Shen et al., 2003; van der Wel et al., 2014; Mowla et al., 2019b; Suess et al., 2019a). Understanding why and how these structural changes take place could be key to understanding the physical mechanism(s) responsible for shutting down star formation and creating the galaxy bimodality.

Despite characteristic differences in the sizes and masses of star-forming and quiescent galaxies, neither size nor mass alone is a clear and unique predictor of quiescence (e.g., Omand et al., 2014; Whitaker et al., 2017b). Combining these quantities to estimate the effective surface mass density, Σ_e, can effectively separate star-forming and quiescent galaxies both in the local universe (e.g., Kauffmann et al., 2003; Brinchmann et al., 2004) and beyond (e.g., Franx et al., 2008; Maier et al., 2009). Recent work has suggested that the central mass density in a *fixed* aperture of one kiloparsec, Σ_1, provides an even clearer predictor of quiescence (e.g., Cheung et al., 2012; Fang et al., 2013; van Dokkum et al., 2014; Barro et al., 2017b; Whitaker et al., 2017b; Lee et al., 2018; Woo & Ellison, 2019). Σ_1 is also easier to interpret than Σ_e: Σ_e can increase or decrease as a galaxy evolves, depending on the evolution of both the galaxy's mass density and its effective radius. In contrast, Σ_1 does not directly depend on the evolution of the effective radius, and can only decrease with significant mass loss or adiabatic expansion (e.g., Damjanov et al., 2009; Poggianti et al., 2013; Barro et al., 2017b).

Figure 1.2 shows the relationship between Σ_1 and stellar mass for star-forming and quiescent galaxies across redshift (adapted from Barro et al., 2017b). In the Σ_1-mass plane, both star-forming and quiescent galaxies lie on tight and well-defined relations with similar slopes of $\sim 0.8-1$, with quiescent galaxies offset to higher Σ_1 than star-forming galaxies (e.g., Fang et al., 2013; Barro et al., 2017b). These measurements seem to indicate that building a dense core and reaching high Σ_1 is a necessary prerequisite for quenching (e.g., Fang et al., 2013; Barro et al., 2017b; van Dokkum et al., 2015; Tacchella et al., 2015b; Mosleh et al., 2017; Whitaker et al., 2017b; Suess et al., 2020). The Σ_1-mass relations do *not* evolve rapidly with redshift, unlike the size-mass relations.

Understanding the details of how this structural transformation takes place requires investigating the sizes and Σ_1 values of possible quiescent progenitors. Several types of these transitional galaxies have been identified in the literature. Post-starburst galaxies, which recently and rapidly stopped a major star-forming epoch, have small sizes and high Σ_1 (e.g.,

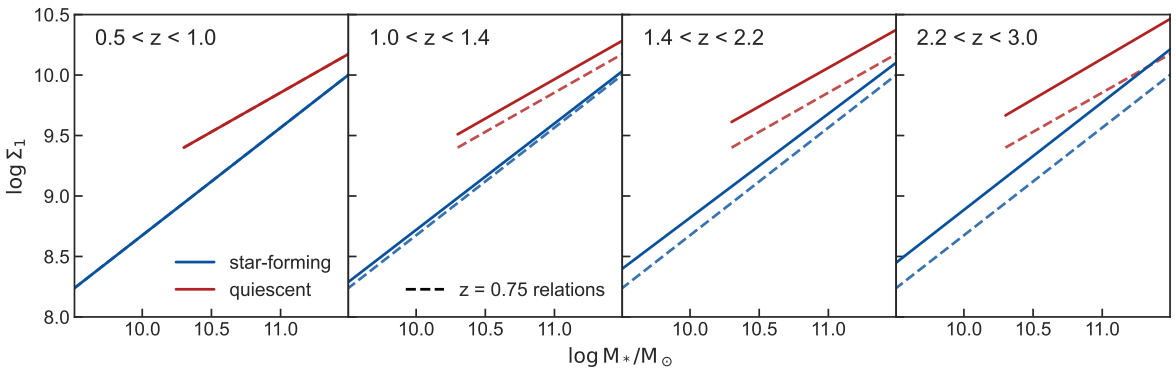

Figure 1.2: The best-fit relation between the central stellar mass surface density (Σ_1) and stellar mass of star-forming and quiescent galaxies. Each panel shows a different redshift regime; the dashed lines show the $z = 0.75$ fits to guide the eye. Figure adapted from Barro et al. (2017b).

Whitaker et al., 2012a; Yano et al., 2016; Almaini et al., 2017; Belli et al., 2019; Suess et al., 2020). These galaxies are much more compact than average star-forming galaxies, indicating that the process that shuts down star formation in post-starburst galaxies also alters their structures. Green valley galaxies, which have intermediate colors and specific star formation rates, seem to have relatively large sizes indicating that their star formation may cease without a need for sudden structural transformation (e.g., Martin et al., 2007; Mendez et al., 2011; Wu et al., 2018). Finally, massive compact star-forming galaxies have similar structures and number density evolution as compact quiescent galaxies at $z \sim 2$, suggesting an evolutionary link between the two populations (e.g., Barro et al., 2013, 2014; van Dokkum et al., 2015). The varying structures of these different classes of possible quiescent progenitors have led to an emerging picture of at least two distinct pathways to quiescence, a "fast" quenching process which produces compact post-starburst galaxies, and a "slow" quenching process that produces more extended green valley galaxies (e.g., Barro et al. 2013; Woo et al. 2015; Belli et al. 2019; Woo & Ellison 2019; though see also Lilly & Carollo 2016; Abramson et al. 2016).

The majority of these structural studies divide the galaxy population into just a few groups: typically a bimodal star-forming/quiescent separation, or potentially adding 1-2 classes of transitional galaxies. Further advances in understanding how the structures of galaxies change as they grow and quench requires understanding how galaxies move *through* the size-mass and Σ_1-mass planes. In Chapters 4 & 5, we will move beyond the galaxy bimodality to study the sizes and Σ_1 values of many different evolutionary stages of galaxies.

Post-starburst galaxies as laboratories to study quenching

A variety of theoretical mechanisms have been proposed to form massive compact quiescent galaxies. These proposed mechanisms range from intense centrally-concentrated starbursts triggered by gas-rich major mergers (e.g., Hopkins et al. 2008, Wellons et al. 2015), very early assembly in a much denser universe (e.g., Naab et al. 2009, Wellons et al. 2015), or "morphological" quenching, where the transition from disk to spheroid stabilizes gas reservoirs (e.g., Martig et al., 2009). While all of these mechanisms could shut down star formation by depleting, removing, heating, or stabilizing molecular gas reservoirs, the resulting quenched galaxies differ in key observables including age gradients, rotational support, and morphology. Detailed multi-wavelength follow up of quenched galaxies holds the key to distinguishing between these theoretical quenching mechanisms. This multi-wavelength follow-up is most effective when performed in galaxies that have *just* concluded their major star-forming phase: the signatures of the quenching mechanism should still be apparent, and not diluted by later mergers or secular evolution. The question then becomes how to identify these recently-quenched galaxies.

Growing observational evidence suggests that there are at least two distinct pathways to quenching: galaxies can quench rapidly through the post-starburst phase, or quench slowly through the green valley phase (e.g., Barro et al., 2013, 2014; Schawinski et al., 2014; Wild et al., 2016; Carnall et al., 2018; Forrest et al., 2018; Wu et al., 2018; Rowlands et al., 2018; Belli et al., 2019; Suess et al., 2021). In Chapters 6 & 7 of this thesis, we focus on the rapid quenching mode. These fast-quenching post-starburst galaxies, sometimes also called "K+A" or "E+A" galaxies, experienced a recent burst of intense star formation that concluded within the past ∼gigayear (e.g., Dressler & Gunn, 1983; Couch & Sharples, 1987). Observationally, these galaxies are characterized by spectra that are dominated by A-type stars: the burst finished long enough ago that the most massive stars have died, but recently enough that the slightly longer-lived and less massive stars are still alive to dominate the optical spectrum. These spectra typically show strong Balmer breaks, deep Balmer absorption lines, weak or absent nebular emission lines, and blue slopes redward of the Balmer break.

A variety of observational techniques have been used to select post-starburst galaxies over a wide redshift range. "E+A" or "K+A" post-starburst galaxies in the local Universe are often selected by their high Hδ equivalent widths and low [OII] luminosities; in combination, these spectral features indicate significant recent star formation but little ongoing star formation (e.g., Zabludoff et al., 1996; Dressler et al., 1999; Goto, 2005; Brown et al., 2009; French et al., 2015). Some works use spectral template fitting approaches, which can identify galaxies whose light is dominated by young stars (e.g., Quintero et al., 2004; Pattarakijwanich et al., 2016). An alternate technique pioneered by Wild et al. (2014) uses principal component analysis (PCA), which effectively selects for the unique spectral shape of post-starburst galaxies (see also, e.g., Almaini et al., 2017; Maltby et al., 2018). A similar spectral shape indentification approach was also used by Kriek et al. (2010), using synthetic rest-frame colors instead of PCA-based "supercolors". Finally, some studies have selected post-starburst galaxies based on their location in the UVJ plane (e.g., Whitaker et al. 2012a;

Belli et al. 2019; Suess et al. 2020; see also Akins et al. 2021). These different methods of selecting post-starburst galaxies produce samples that are relatively similar, but do not fully overlap.

While massive post-starburst galaxies are relatively rare across cosmic time (making up $\lesssim 5\%$ of the total $M_* > 10^{10} M_\odot$ population at $z \leq 2$, Wild et al., 2016), their number density evolves rapidly with redshift. At $z \sim 2$, post-starburst galaxies are common enough to explain half of the total growth in the red sequence; by $z \sim 1.4$, they represent just $\sim 20\%$ of all transitioning galaxies (Belli et al., 2019). By $z \sim 0$, massive post-starburst galaxies are so rare that they contribute negligibly to the growth of the quiescent population (Rowlands et al., 2018). These results imply that, while post-starburst galaxies play an important role in quenching at cosmic noon, their importance to the overall landscape of galaxy transformation diminishes towards lower redshifts.

The nature of post-starburst galaxies may also differ between $z \sim 0$ and $z \sim 1$. Higher-redshift post-starburst galaxies generally appear to be more burst-dominated than their low-redshift counterparts: simple modeling of Hδ and D_n4000 values indicates that $z \sim 0$ post-starburst galaxies formed just $5-10\%$ of their mass in the recent burst, whereas $z > 0.5$ post-starburst galaxies appear to have formed the majority of their mass in the recent burst (Suess et al., 2017). Full spectral modeling of post-starburst star formation histories (SFHs) confirms these findings: the median burst mass fraction of $z \sim 0$ post-starburst galaxies is $\sim 10\%$ (French et al., 2018), in contrast to the $\sim 70\%$ median burst mass fractions of $z \sim 1$ post-starburst galaxies (Wild et al., 2020). Low-redshift post-starburst galaxies also tend to be less massive than their higher-redshift counterparts (e.g., Wild et al. 2016; Rowlands et al. 2018), although they are not so low-mass that environmental effects play significant roles in their quenching, (e.g. Zabludoff et al. 1996; Feldmann et al. 2011). Taken together, these results indicate that high-redshift post-starburst galaxies are in the process of rapidly quenching their *primary* epoch of star formation, whereas low-redshift post-starburst galaxies are rapidly shutting down a smaller burst of late-time star formation that does not contribute as significantly to their stellar mass.

This redshift dependence complicates observational studies of quenching: pinpointing the physics responsible for shutting down the bulk of star formation requires looking beyond the local universe, but detailed follow-up observations require significant (and potentially prohibitive) telescope investments at $z \gtrsim 1$. Even spectroscopic confirmation of post-starburst galaxies is difficult at $z > 1$, with samples consisting of a few tens of galaxies (e.g., Bezanson et al., 2013; Maltby et al., 2016; Wild et al., 2020) as opposed to the hundreds or thousands of $z \lesssim 0.1$ post-starburst galaxies that can be identified from large all-sky surveys (e.g., Dressler et al., 1999; Quintero et al., 2004; Goto, 2005; Brown et al., 2009; French et al., 2015; Alatalo et al., 2016). Intermediate redshifts, where bright post-starburst galaxies in the process of shutting down their primary burst of star formation can be identified, are the ideal bridge between these low- and high-redshift samples. In Chapters 6 & 7, we will identify and study the properties of intermediate-redshift post-starburst galaxies.

1.3 This thesis

This thesis aims to address three open questions about galaxy growth and transformation:

- How do radial color gradients affect the evolution of galaxy sizes?
- How do galaxies move through the size-mass and Σ_1-mass planes?
- What can post-starburst galaxies tell us about the quenching process?

Chapter 2 will introduce the methods used to calculate radial color gradient strengths and half-mass radii from multi-band, high-resolution *Hubble Space Telescope* imaging. We will evaluate the efficacy of these methods by directly comparing half-mass radii measured using three different techniques. We will explore correlations between the strength of color gradients and other physical properties, then show how the evolution of color gradient strength with redshift affects the star-forming and quiescent size-mass relations. In Chapter 3, we extend this work to $z \sim 0$ to present the largest catalog of galaxy half-mass radii beyond the local universe. We chart the evolution of color gradient strength and half-mass radii from $z \sim 0$ up to $z = 2.5$. Finally, we discuss what the evolution of half-mass radii implies about galaxy assembly histories and the growth of quiescent galaxies.

In Chapters 4 & 5, we push these structural studies beyond the galaxy bimodality. By moving beyond simple groupings of galaxies as either star-forming or quiescent, we hope to build an understanding of how galaxies assemble their stellar mass and move *through* the size-mass and Σ_1-mass diagrams. Chapter 4 concentrates on the evolution of galaxy structures along the quiescent sequence. We use an innovative color-based technique from Belli et al. (2019) to estimate the ages of quiescent galaxies in our sample, then study how color gradient strength, half-mass radii, and central mass densities change as quiescent galaxies age. The results of this study support the idea that quiescent galaxies grow inside-out via minor mergers. In Chapter 5, we move even further beyond the galaxy bimodality and use a clustering algorithm to divide our galaxy sample into sixteen different groups with similar rest-frame spectral energy distributions. Each of these sixteen groups represents a different stage of galaxy evolution. This technique allows us to study how the sizes and Σ_1 values of star-forming galaxies change as they grow and present a new way to view the star-forming size-mass relation. We are also able to study the structures of multiple different types of transitioning galaxies, and argue for two distinct pathways to quenching: slow quenching through the green valley, and rapid quenching through the post-starburst phase.

Chapters 6 & 7 will concentrate on the products of this rapid quenching process, post-starburst galaxies. We will select bright, intermediate-redshift post-starburst galaxies that serve as the ideal testbeds to understand the physics of rapid quenching. By targeting intermediate redshifts, we are able to identify a large sample of galaxies that have high burst mass fractions and are therefore in the process of shutting down their major epoch of star formation. At the same time, these intermediate-redshift galaxies are bright enough to conduct full multi-wavelength follow-up studies with modest telescope investments. Chapter 6

will perform a pilot study of two $z \sim 0.7$ post-starburst galaxies. We use the Atacama Large Millimeter/submillimeter Array (ALMA) to measure their molecular gas content. In contrast to theoretical predictions, we find that these galaxies retain large reservoirs of gas despite low ongoing star formation rates. In Chapter 7, we introduce the SQuIGG$\vec{L}$E survey: Studying Quenching in Intermediate-z Galaxies– Gas, angu$\vec{L}$ar momentum, and Evolution. SQuIGG$\vec{L}$E leverages the large sky coverage of the Sloan Digital Sky Survey (SDSS) to select ~ 1300 bright post-starburst galaxies at $z \geq 0.5$. We use Bayesian non-parametric star formation history modeling to constrain the burst mass fractions and quenching timescales of all galaxies in the sample. We then describe the future goals of the SQuIGG$\vec{L}$E survey, which include expanding the sample of intermediate-redshift post-starburst galaxies with molecular gas measurements.

Finally, Chapter 8 will summarize the main findings of this thesis and discuss several avenues for future research.

Chapter 2

Half-mass radii for $\sim 7,000$ galaxies at $1.0 \leq z \leq 2.5$: most of the evolution in the mass-size relation is due to color gradients

The content of this chapter is drawn from Suess et al. (2019a), with permission from the co-authors.

In this chapter, we develop and test three different methods for measuring mass profiles, color gradient strengths, and half-mass radii. We leverage the large public dataset of high-resolution multi-band *Hubble Space Telescope (HST)* imaging through the CANDELS program to create a catalog of half-mass radii. In Section 2.1, we describe our data and sample selection. Section 2.2 describes each of the three methods that we use to measure half-mass radii. Section 2.3 presents our color gradients and half-mass radii, explores the correlations between color gradient strength and other physical properties of galaxies, and presents the galaxy mass - half-mass radius relation. Section 2.4 discusses potential sources of uncertainties, how our results compare with previous studies, and the implications for the size growth of galaxies.

2.1 Data and sample selection

Sample Selection

For our sample selection, we use the multi-wavelength photometric catalogs from ZFOURGE (Straatman et al., 2016), which overlap with the CANDELS survey in the COSMOS, GOODS-S, and UDS fields. These catalogs contain medium- and broad-band photometry spanning from the optical to IRAC, for a total of 26-40 photometric bands. Our sample consists of

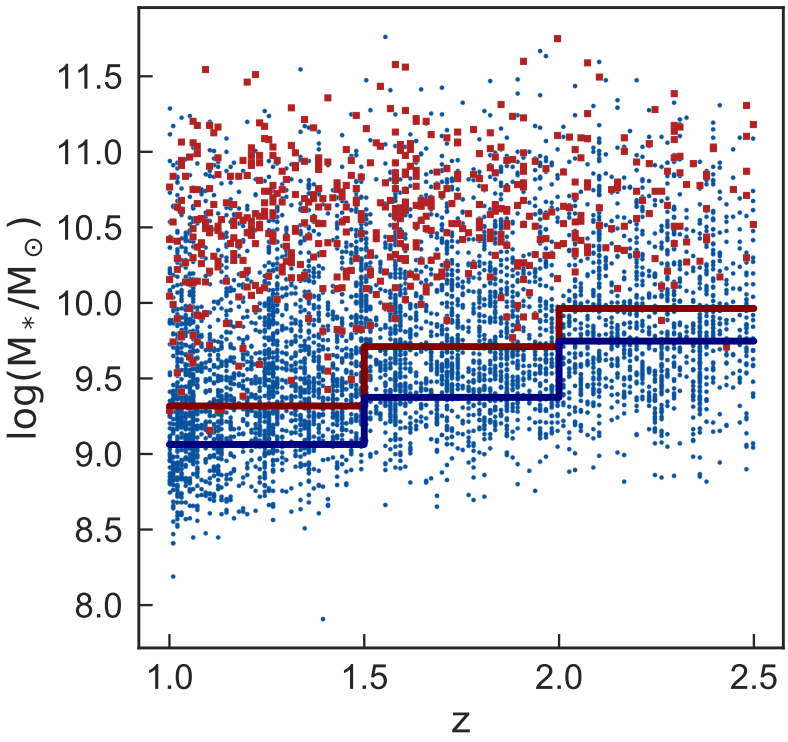

Figure 2.1: The 7,006 galaxies included in this analysis. Galaxies are classified as star-forming or quiescent by their UVJ colors; quiescent galaxies are shown as red squares, and star-forming galaxies are shown with blue points. The mass completeness in each redshift bin is shown as a red (blue) solid line for quiescent (star-forming) galaxies.

all galaxies in the ZFOURGE catalog with a use flag[1] equal to one, a reliable photometric or spectroscopic redshift (z_q < 3), $1.0 \leq z \leq 2.5$, high signal-to-noise ratio in the detection band ($S/N_K \geq 10$), $\log M_*/M_\odot > 9.0$, and a match in the 3D-HST catalog (Brammer et al., 2012; Momcheva et al., 2016; Skelton et al., 2014, catalog cross-matching provided as part of the ZFOURGE catalogs). We select from ZFOURGE because the medium bands included as part of the survey provide extra SED coverage, which allows for better stellar population fitting. Because the footprints of the 3D-HST and CANDELS catalogs are slightly different, we also ensure that each galaxy has CANDELS multi-band imaging (Grogin et al., 2011; Koekemoer et al., 2011).

We classify each of these 7,006 galaxies as either star-forming or quiescent by their rest-

[1]See Table 5 of Straatman et al. (2016) for a full definition of this flag. The `use` flag is intended to provide a "standard selection of galaxies" and ensures that the object is not a star or too close to a star for reliable observations; the object was observed in all optical bands; the object has reasonable EAZY and FAST fits; and that ground- and space-based observations in similar filters have similar fluxes.

frame $U - V$ vs $V - J$ colors (Wuyts et al., 2007) using the classification from Whitaker et al. (2012b). A total of 582 galaxies ($\sim 8\%$ of the sample) are quiescent. Throughout this work, we use the stellar masses and redshifts as presented in the ZFOURGE catalog. We correct the stellar masses to be consistent with the van der Wel et al. (2012) morphological measurements by multiplying the ZFOURGE stellar masses by the ratio of the F160W flux in the van der Wel et al. (2012) `GALFIT` catalog and the F160W flux in the ZFOURGE catalog. On average, this small correction increases the stellar mass by 5%.

We calculate the mass completeness of both the quiescent and star-forming galaxies using a method similar to those of Quadri et al. (2012) and Tomczak et al. (2014): we select galaxies with a S/N_K close to our cutoff ($10 \leq S/N_K \leq 50$), scale their fluxes and masses down to a $S/N = 10$, and take the 90th percentile of the resulting masses as the mass completeness. We calculate the mass completeness in three redshift bins, $1.0 \leq z < 1.5$, $1.5 \leq z < 2.0$, and $2.0 \leq z \leq 2.5$. The 90% completeness level is, in effect, calculated at the center of each redshift bin; the lower-redshift portions of each bin are $> 90\%$ complete, and the higher-redshift portions of each bin are $< 90\%$ complete.

Figure 2.1 shows our full sample of galaxies in stellar mass-redshift space. Star-forming and quiescent galaxies are indicated with blue points and red squares, and the mass completeness in each redshift bin is shown with a solid line. For both quiescent and star-forming galaxies at all redshifts, the sample is complete above $\sim 10^{10} M_{\odot}$.

HST Imaging & Morphologies

We make extensive use of the high-resolution multi-band imaging and integrated photometry in the COSMOS, UDS, and GOODS-S fields obtained by the CANDELS program (Grogin et al., 2011; Koekemoer et al., 2011). For this analysis, we use the PSF-matched images created by the 3D-HST team (Skelton et al., 2014; Momcheva et al., 2016).

We adopt the half-light radii and Sérsic indices for each galaxy from the morphological catalogs presented in van der Wel et al. (2012). These half-light radii, like the half-mass radii presented later in this work, are measurements of the galaxy's major axis. We correct all half-light radii to rest-frame 5,000Å using the procedure described in van der Wel et al. (2014). This technique applies a mass- and redshift-dependent correction to the measured half-light radii of star-forming galaxies. A redshift-dependent correction is applied in a similar fashion to quiescent galaxies.

2.2 Methods

We explore three different methods to calculate half-mass radii. We introduce a new technique that builds on the methods used by Wuyts et al. (2012): we divide the galaxy into annuli, measure multi-band aperture photometry in each annulus, then use stellar population synthesis (SPS) modeling to fit the resulting SEDs and obtain a mass map of the galaxy. We then use two separate techniques to account for the *HST* PSF and derive the

intrinsic mass profiles. The first approach uses a forward modeling technique that assumes the mass-to-light ratio gradient is a power-law function of radius; the second approach uses `GALFIT` (Peng et al., 2002) to fit the mass map of the galaxy (similar to the technique used by Lang et al., 2014; Chan et al., 2016). Our third and final method replicates the analysis of Szomoru et al. (2010, 2012, 2013), and uses the rest-frame intrinsic $u - g$ color profile to create a mass profile and measure a half-mass radius. The following sections describe each of these methods in greater detail. Figure 2.2 shows a graphical representation of the major steps for each method, and Figure 2.3 shows example images and mass profiles for three galaxies in our sample. Similar to van der Wel et al. (2014) and Mowla et al. (2019b), all half-mass and half-light radii presented in this chapter are measurements of the major axis of the galaxy.

Methods 1 & 2: extracting the M/L gradient in convolved space

We begin by dividing each galaxy into distinct spatial regions. Because we aim to measure the radial mass profiles of galaxies, we define these spatial regions as concentric elliptical annuli; this geometry allows us to extract radial profiles much more simply than if we define regions using the Voronoi binning technique used by Wuyts et al. (2012). The annuli are centered at the right ascension and declination of the galaxy as listed in the van der Wel et al. (2012) F160W catalog, with the same position angle as the best-fit `GALFIT` model in van der Wel et al. (2012). We do not calculate half-mass radii for galaxies that do not have Sérsic models listed in the van der Wel et al. (2012) catalog. We fix the axis ratio of the annuli to a convolved version of the `GALFIT` axis ratio, $q_{\rm conv} = \sqrt{(r_e^2 + r_{PSF}^2)/([qr_e]^2 + r_{PSF}^2)}$, where r_{PSF} is the half width at half maximum (HWHM) of the PSF and r_e is effective radius measured by GALFIT in the F160W band. Using this convolved axis ratio allows us to extract photometry that more closely follows the geometry of the observed galaxy. The semimajor axis of each annulus is set to an integer value of $r_{\rm PSF}$; this ensures that we are not measuring photometry on scales that are entirely "blurred out" by PSF effects. Because all images are convolved to the F160W PSF with a FWHM of 0.19 arcseconds, $r_{\rm PSF}$ is equal to $0\farcs095$ (~ 0.5 kpc over our full redshift range).

We use the *photutils* python package to measure aperture photometry in each annulus, repeating the measurement for each galaxy in all available 3D-HST PSF-matched images. For galaxies in the COSMOS and UDS fields, this typically yields five bands in our resolved SED: F160W, F125W, F140W, F606W, and F814W. For galaxies in the GOODS-S field, there are typically eight bands in our resolved SED: F160W, F125W, F140W, F435W, F606W, F775W, F850LP, and F814W. Errors on the measured aperture photometry are calculated using the empty aperture scaling law described in Skelton et al. (2014), which parameterizes the error on a photometric measurement in terms of the area of the measurement aperture and the value of the weight map in the aperture. We define the outermost annulus to be the last annulus where the signal-to-noise ratio of the photometry in the F160W band is greater than 10.0. Beyond this radius, the low S/N of the photometry in each annulus does not allow for a robust mass determination. Each galaxy has measured aperture photometry for 2-43 annuli;

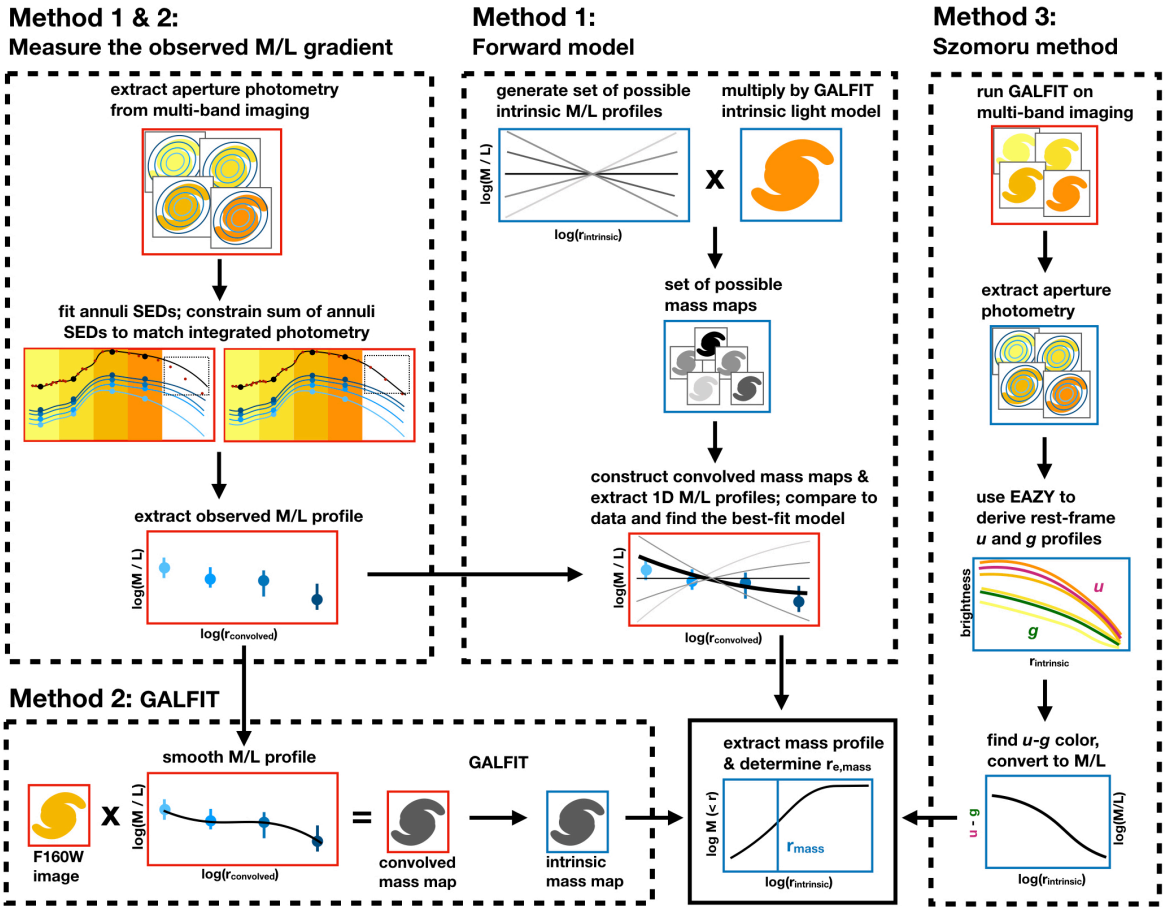

Figure 2.2: Graphic representation of the three methods used to calculate half-mass radii. Individual steps enclosed with a red box indicate that the measurements are in *convolved* space, and steps enclosed with a blue box indicate that the measurements are in deconvolved space.

most galaxies have photometry in 7-10 annuli. When calculating aperture photometry, we do not include flux from pixels that are identified as part of another adjacent galaxy in the segmentation maps.

Next, we use the SPS fitting code FAST (Kriek et al., 2009) to independently fit the SED of each annulus. In these fits, we assume the Bruzual & Charlot (2003) stellar population library, a Chabrier (2003) initial mass function, a delayed exponential star formation history, and the Kriek & Conroy (2013) dust attenuation law. Fitting each annulus separately allows the mass, age, star-formation timescale, and dust extinction of each annulus to vary independent of the best-fit values for other annuli and the best-fit values for the galaxy as

a whole. The free parameters in the fit are the age, star formation timescale τ, and dust extinction A_v of the annulus. The mass is not a free parameter: it is set by the overall scaling of the measured photometry. We fix the redshift of each annulus to the ZFOURGE photometric (or spectroscopic, when available) redshift of the galaxy so that different regions of the galaxy are not modeled at different best-fit redshifts. We allow $\log(\tau/\mathrm{yr})$ to vary between 7.0 and 10.0 in steps of 0.2, $\log(\mathrm{age/yr})$ to vary between 8.0 and 10.0 in steps of 0.1, and A_v to vary between 0.0 and 3.0 mag in steps of 0.1 mag; the metallicity is fixed to 0.02 $Z_\odot$. We use the FAST version 0.2 template error function.

By considering only the $5-8$ filters where we can measure spatially resolved photometry, we are ignoring the wealth of ancillary data available in these well-studied extragalactic fields. In addition to the resolved photometry, each galaxy has integrated photometry in ~ 20 additional filters ranging from the UV to near-IR. Following Wuyts et al. (2012), we use this integrated photometry to adjust the best-fit model for each annulus so that the sum of the modeled SEDs for each annulus matches the observed photometry of the galaxy as a whole. Mathematically, this amounts to minimizing a χ^2 equation with two terms. The first term describes how well the SPS model for each annulus fits the resolved photometry in that annulus. This first term is what SPS fitting codes like FAST minimize:

$$\chi^2_{\mathrm{res}} = \sum_{i=1}^{N_{\mathrm{annuli}}} \sum_{j=1}^{N_{\mathrm{res}}} \frac{(F_{i,j} - M_{i,j})^2}{(E_{i,j})^2},$$

where N_{annuli} is the total number of elliptical annuli, N_{res} is the number of filters with spatially resolved photometry, $F_{i,j}$ represents the measured flux in annulus i and filter j, $M_{i,j}$ represents the modeled flux in annulus i and filter j, and $E_{i,j}$ is the error on the measured flux for annulus i and filter j.

The second term in our χ^2 function describes how well the sum of the modeled SEDs of all annuli matches the observed integrated photometry for the entire galaxy:

$$\chi^2_{\mathrm{int}} = \sum_{j=1}^{N_{\mathrm{int}}} \frac{(F_j - \sum_{i=1}^{N_{\mathrm{annuli}}} M_{i,j})^2}{(E_j)^2}.$$

Here, N_{int} is the number of bands with integrated photometry, $M_{i,j}$ again represents the modeled flux in annulus i and filter j, and F_j represents the observed integrated photometry in filter j. To account for aperture differences between the catalog and our largest annulus, we scale the integrated photometry down by the error-weighted average of the difference between the catalog flux and sum of the annuli fluxes in all bands with resolved photometry. This correction factor is typically between ~ 0.75 and 1.

Unlike Wuyts et al. (2012), who minimize $\chi^2_{\mathrm{res}} + \chi^2_{\mathrm{int}}$, we minimize

$$\chi^2_{\mathrm{tot}} = \frac{1}{\nu_{\mathrm{res}}}\chi^2_{\mathrm{res}} + \frac{1}{\nu_{\mathrm{int}}}\chi^2_{\mathrm{int}},$$

where ν is the number of bands fitted minus the number of free parameters in the fit (three: age, τ, and A_v). We account for the number of bands we fit in our total χ^2 because there are

many more bands with integrated photometry than resolved photometry; without this term, the minimization essentially ignores how well the model for each annulus fits the resolved photometry in that annulus in favor of ensuring that the sum of the annuli models exactly matches the integrated photometry. This could result in the individual annuli fits, which we ultimately use to measure the mass profiles, to be quite poor.

Following Wuyts et al. (2012), we use an iterative approach to minimize $\chi^2_{\rm tot}$. We use the best-fit values from the resolved photometry SED modeling for the age, τ, and A_v of each annulus as an initial condition, and evaluate $\chi^2_{\rm tot}$. Then, we allow the age, τ, and A_v of the innermost annulus to simultaneously move to an adjacent position on the FAST grid and re-calculate $\chi^2_{\rm tot}$ for each of the possible new (age, τ, A_v) combinations. The age, τ, and A_v for the innermost annulus that yield the smallest $\chi^2_{\rm tot}$ are taken to be the new best-fit parameters for that annulus. We repeat this process of finding the new best-fit values for each of the remaining annuli in turn. We continue to repeat this process of finding new best-fit values for all annuli until $\chi^2_{\rm tot}$ remains constant or we reach 500 iterations; in practice, most galaxies converge in $20 - 100$ iterations. At the end of this constraint process, we have determined the best-fit age, τ, and A_v for each annulus— including information from the integrated bands— and can read off the best-fit mass that corresponds to these best-fit parameters for each annulus.

We use a Monte Carlo technique to determine error bars on the mass of each annulus. We use the FAST 1σ error contour to randomly select a new best-fit starting age, τ, and A_v for each annulus. We repeat the constraint process beginning from these perturbed initial conditions. Additionally, we vary the total flux values for the integrated filters according to the error bars listed in the catalog. We perform 200 of these simulations, and take the 68% confidence interval on the resulting annuli masses as our 1σ error bars. To ensure that these error bars are realistic, we enforce a minimum 10% error on the annuli masses.

To obtain a mass-to-light ratio measurement, we use EAZY to interpolate the observed aperture photometry to a rest-frame g band profile, assuming the SDSS g-band filter curve. We then report mass-to-light ratios as M/L_g. We also report M/L_{F160W}, the mass-to-light ratio in the *observed* F160W filter; these measurements are used in conjunction with morphologies measured from F160W images. We stress that, at this point in our analysis, the mass and M/L profiles are based on the observed (convolved-space) data, mitigating the large uncertainties that can arise when using deconvolved data.

Despite the advantages of measuring the mass profile in convolved space— namely, that the measured profile does not strongly depend on the deconvolution algorithm— measurements in convolved space can only tell us whether the half-mass radii of these galaxies are larger, smaller, or the same as their half-light radii. Here, we also wish to quantify *how much* larger or smaller the half-mass radii are than the half-light radii. This requires correcting for the PSF and moving to deconvolved space. In this chapter, we use two different techniques to recover intrinsic M/L profiles and half-mass radii from the observed M/L gradients we find from spatially-resolved SED fitting.

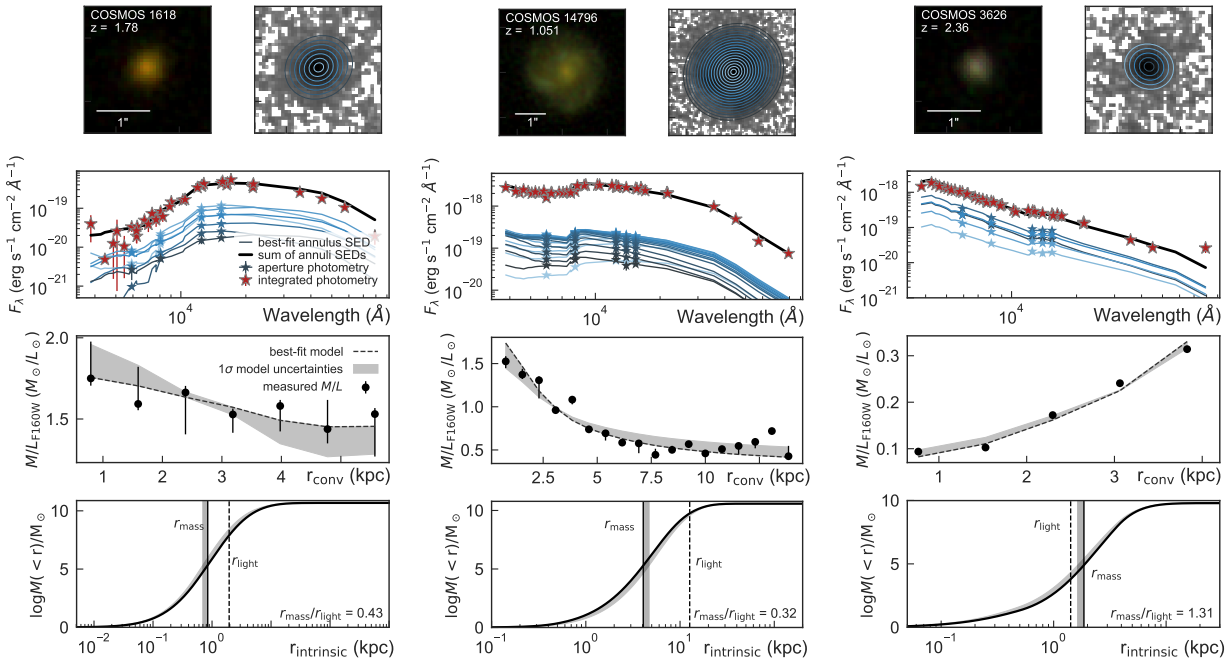

Figure 2.3: Examples of Method 1 for three galaxies in our sample. The top row shows a color image of the galaxy, as well as a log-scaled F160W image with the locations of the annuli used to extract aperture photometry. The second row shows the measured aperture photometry in each band (blue stars), the best-fit SED for each aperture (blue lines), the sum of all best-fit annuli SEDs (black line), and the integrated catalog photometry for the whole galaxy (red stars). The shade of blue used for the aperture photometry and the best-fit annulus SED matches the shade used in the top panel image (dark blue are inner annuli, light blue are outer annuli). The third row shows the measured M/L profile as a function of radius (in convolved space). Points represent the measured values for each annulus; the black dashed line shows the best-fit power-law model, and the grey shaded region shows the 1σ error bars on the best-fit model. The bottom row shows the mass profile corresponding to this best-fit model, as a function of *intrinsic* radius. The vertical line and shaded region represent the half-mass radius and its 1 σ error bar; the dashed line shows the half-light radius.

Method 1: interpreting observed M/L gradients with a simple forward modeling technique

We first test a simple forward modeling technique to fit the observed M/L_{F160W} profile: we make a series of models assuming different intrinsic M/L profiles, convolve each model with the PSF, then use χ^2 minimization to find the best intrinsic M/L profile and half-mass radius. Details of this method are described below.

We assume that the intrinsic 2D light profile of the galaxy follows the `GALFIT`-derived best-fit Sérsic model measured in van der Wel et al. (2012) using the F160W CANDELS images. We evaluate this Sérsic model on a 2D grid with the same pixel scale as the data. Then, we apply a range of possible intrinsic M/L profiles to obtain a series of possible intrinsic mass profiles for the galaxy. We parameterize the intrinsic M/L profile as a power-law function of radius r— i.e., $\log M/L \propto \alpha \times \log r$ — as suggested by, e.g., Chan et al. (2016). The slope of the relation is allowed to vary between $-2.3 \leq \log([M/L|_{2r_{\rm e,light}}]/[M/L|_{r_{\rm e,light}}]) \leq 2.3$; these bounds were chosen to fit the range of observed convolved M/L profiles in this sample. It is clearly possible for galaxies to have more complex radial M/L profiles than a simple power law; however, many of our galaxies are not significantly larger than the PSF and we do not typically have a large number of data points in our M/L profiles. Including a large number of parameters in our intrinsic M/L model would quickly result in overfitting.

We set the M/L profile at radii smaller than one pixel ($0\farcs06$) to the value at one pixel, and set the M/L profile at very large radii to the last value where we have measured aperture photometry. This prevents artificially small (large) half-mass radii from strongly decreasing (increasing) M/L profiles.

We then convolve both the 2D light profile and all possible 2D mass profiles with the F160W PSF (using the F160W PSF for each field as provided by the 3D-HST team). We extract the 1D convolved mass and light profiles in annuli, again using the *photutils* python package to measure aperture photometry. The resulting model M/L_{F160W} profiles are arbitrarily normalized to $M/L = 1$ at $r = r_{\rm e,light}$. We scale the model M/L_{F160W} profiles to the observed M/L_{F160W} profile by multiplying the model by $\Sigma(\text{model} \times \text{data})/\Sigma(\text{model}^2)$. Then, we calculate the χ^2 value between the modeled and observed M/L profiles and take the model with the smallest χ^2 as the best fit. If there is no model with $\chi^2 < 15$, we do not report a half-mass radius for that galaxy.

We calculate the half-mass radius for the best-fit intrinsic mass model using the analytic 1D Sérsic profile (based on the F160W `GALFIT` model) instead of the 'pixelated' 2D profile to ensure accuracy. We multiply this analytic 1D Sérsic profile by the best-fit intrinsic M/L profile, and evaluate the profile out to 500 pixels (30") to ensure that we have captured the total mass of the galaxy. We then find the half-mass radius by calculating the radius where the mass profile reaches half its total value.

We use a Monte Carlo method to estimate the uncertainties of the best-fit intrinsic M/L model. We choose a new half-light radius and Sérsic index according to the error bars listed in van der Wel et al. (2012), and create a new grid of models. We perturb the observed M/L profile according to its error bars, then use χ^2 minimization to find the best-fit model.

We record the 68% confidence intervals of 200 such simulations as the 1σ error bars on the half-mass radius and M/L slope of the models.

Figure 2.3 shows example images, SEDs, M/L profiles, and mass profiles derived using this method for three galaxies in our sample. Section 2.5 shows that the half-mass radii recovered using this method do not have significant biases with stellar mass, half-light radius, redshift, or the number of annuli in the fit.

Method 2: interpreting observed M/L gradients with GALFIT

We also test a second way to derive half-mass radii and intrinsic M/L gradients from the M/L profiles measured in Section 2.2. This recovery technique is similar to that used by Lang et al. (2014) and Chan et al. (2016): we create an as-observed 2D mass map for each galaxy, then fit it with GALFIT to find the intrinsic half-mass radius. We describe this method in more detail below.

To create a mass map, we first smooth the 1D observed $\log M/L - \log r_{\rm obs}$ profile using a cubic spline interpolation; this decreases the edge effects at the boundaries between annuli and results in better residuals on the GALFIT fits. As with the forward-modeling method described above, we fix M/L at radii larger than $r_{\rm max}$ to the value at $r_{\rm max}$. Then, we map this profile from 1D to 2D using the ellipticity and position angle of the elliptical annuli. Multiplying this 2D M/L_{F160W} map by the original F160W image of the galaxy yields a mass map that we then fit with GALFIT.

Unlike Chan et al. (2016), we keep the same range of allowed Sérsic indices in both the mass and light profile fits. Because the best-fit Sérsic indices for the light profiles of many compact quiescent galaxies reaches the maximum value of $n = 8.0$, allowing a different range of n values between the light and mass GALFIT fits may result in measurements of the half-light radii being biased with respect to measurements of the half-mass radii. Following van der Wel et al. (2012), then, in our GALFIT fits to the mass maps we allow n to vary between 0.2 and 8.0 and r_e to vary between 0.3 and 400.0 pixels. We do not fix the total mass, position, position angle, or axis ratio of the best-fit model. Because the F160W images are already sky-background subtracted, we fix the sky background to zero in the fits.

We again turn to a Monte Carlo method to determine error bars on the measured half-mass radii. We perturb each M/L measurement within its error bars, re-create a mass map, and re-fit it with GALFIT. We take the 68% confidence interval of 200 such realizations as our 1σ error bars. The error bars are dominated by uncertainties in our M/L profile, and are significantly larger than the errors estimated by GALFIT.

Method 3: The Szomoru et al. method

For each galaxy, we also derive mass profiles and half-mass radii following the method used by Szomoru et al. (2010, 2012, 2013). This method relies on intrinsic surface brightness profiles, which are used to measure a rest-frame $u - g$ color; an empirical relation between

this color and the mass-to-light ratio is then used to derive a mass profile. We describe this method in detail below.

We fit each galaxy in all available filters using `GALFIT` (Peng et al., 2002). The input image used is a ~ 3" cutout of the 3D-HST image in a given filter, centered at the galaxy's position as listed in the van der Wel et al. (2012) catalog. As for the two methods described above, we use the images convolved to the F160W PSF; this ensures that we perform a fair comparison between the the three methods by beginning with identical data products. The 'sigma' image is constructed as the inverse square root of the 3D-HST weight image. We use the 'mask' image to exclude all pixels identified in the 3D-HST segmentation map as belonging to adjacent sources. Because all images are convolved to the F160W PSF, we use the F160W PSF as provided by 3D-HST as the input PSF for `GALFIT`. Following van der Wel et al. (2012), we constrain the Sérsic index n of the best fit to lie between 0.2 and 8.0, the effective radius r_e to lie between 0.3 and 400.0 pixels, and the total magnitude of the best-fit model to be within three magnitudes of the galaxy's catalog magnitude in the filter being fit.

If `GALFIT` ran successfully — i.e., it did not reach the maximum number of iterations and there were no 'suspected numerical convergence errors' — we construct the galaxy's surface brightness profile. We measure the flux in the `GALFIT` residual image in concentric annuli with the same geometry as the best-fit model, then add these residuals to the best-fit Sérsic model. Following Szomoru et al. (2012), we correct the best-fit Sérsic model with residuals only out to 10kpc; the profile from 10-100kpc is not residual-corrected because of difficulties in constraining the sky background at these scales. We derive errors on the intrinsic profiles using the empty aperture scaling laws described in Skelton et al. (2014). After ensuring that we have measured surface-brightness profiles both redward and blueward of the SDSS u and g filters, we use `EAZY` (Brammer et al., 2008) to interpolate the observed surface brightness profiles into rest-frame u and g profiles. Because of this interpolation, half-mass radii at $z > 2.23$– where the central wavelength of the redshifted g band is redder than the central wavelength of the F160W filter– cannot be measured using this technique.

A galaxy's rest-frame $u-g$ color is well correlated with its mass-to-light ratio, $\log M/L_g$, primarily because changes in stellar age, metallicity, and dust attenuation are degenerate in the $u-g$ - $\log M/L_g$ space (Bell & de Jong 2001). We use the masses and rest-frame colors for the full 3D-HST survey to determine the best-fit linear relation between $u-g$ and $\log M/L_g$. Because the slope of the relation varies as a function of redshift (Szomoru 2013), we derive the best-fit relation for each target galaxy in a redshift slice of width $\Delta z = 0.4$ centered at the target's redshift. We use this best-fit relation to calculate the $\mathrm{M/L}_g$ profile of each galaxy in our sample. We then multiply the $\log M/L_g$ profile by the `EAZY`-derived L_g profile to obtain the mass profile of the galaxy. Finally, the half-mass radius is calculated as the radius where the mass profile reaches half of its maximum value.

Errors on the half-mass radius are estimated using a Monte Carlo technique: we vary the $u-g$ profile within its 1σ error bars, re-derive an $\mathrm{M/L}_g$ profile, and re-calculate the half-mass radius. In contrast to Szomoru et al. (2010, 2012, 2013), we also include uncertainties caused by scatter in the $u-g$ - $\log \mathrm{M/L}_g$ relation by perturbing each simulated $\log \mathrm{M/L}_g$ profile

according to the observed scatter in the $u-g$ - $\log \mathrm{M/L}_g$ relation.

2.3 Results: half-mass radii for $\sim 7,000$ galaxies

Table 2.1 lists the half-mass radii for all galaxies in the sample calculated using each of the three methods described above. Other basic galaxy properties, such as stellar mass and redshift, are also listed. The full table is available online. The total number of galaxies successfully fit with each method differs. Method 1 succeeded for 5,649 galaxies– the rest were not well-fit with our power-law model for M/L. Method 2 succeeded for 6,552 galaxies; the rest did not have successful `GALFIT` mass profile fits. Method 3 succeeded for 6,072 galaxies; the rest did not have measured surface brightness profiles both redward and blueward of the rest-frame u and g filters.

Figure 2.4 compares the half-mass radii of all galaxies in our sample calculated using each of the three methods discussed in Section 2.2. UVJ-classified star-forming galaxies are shown in blue, and quiescent galaxies are shown in red. The black dashed line shows the one-to-one relation, and the grey dashed ellipse shows the middle 68% of the points. On average, we see that galaxy half-mass radii are remarkably consistent for all three measurement techniques.

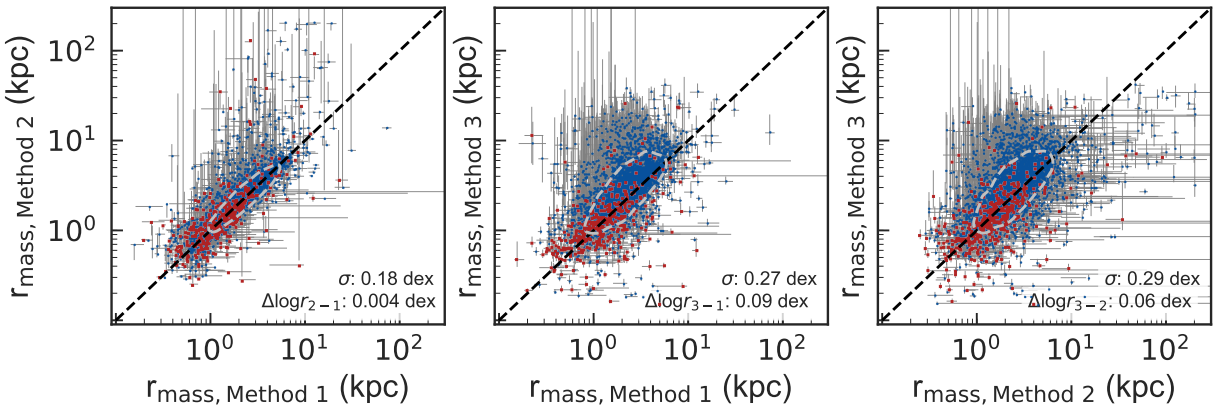

Figure 2.4: Comparison of half-mass radii calculated with three different methods (described in Section 2.2). Red squares represent galaxies classified as quiescent using a UVJ selection; blue points represent star-forming galaxies in a UVJ selection. The grey dashed ellipse represents the 1σ error contour, and the black dashed line shows the one-to-one relation.

As expected, Methods 1 & 2 (which fit the same observed M/L gradient, but use different techniques to account for the PSF), produce very consistent results. There is a typical scatter of 0.22 dex between the two measurements; the median offset between the two sets of half-mass radii is very small, with $\Delta r_{\mathrm{mass}} < 0.01$ dex.

Table 2.1: Half-mass radii for 7,006 galaxies.

ID[a]	Field	RA[b]	Dec[b]	z[c]	$\log \frac{M_*}{M_\odot}$ [d]	$r_{\rm e,light}$ (kpc)[e]	n[f]	$r_{\rm e,mass}$ (kpc) Method 1	$r_{\rm e,mass}$ (kpc) Method 2	$r_{\rm e,mass}$ (kpc) Method 3
10571	GOODS-S	53.101357	-27.860300	2.04	9.45	0.603 ± 0.056	3.11 ± 0.67	$0.660^{+1.071}_{-0.631}$	-	$0.827^{+0.998}_{-0.706}$
10784	GOODS-S	53.130981	-27.860407	1.37	9.99	3.143 ± 0.073	3.75 ± 0.11	$2.064^{+2.104}_{-1.967}$	$2.413^{+2.392}_{-2.280}$	$2.829^{+3.219}_{-2.586}$
13870	GOODS-S	53.083248	-27.847992	1.27	10.06	5.560 ± 0.052	0.68 ± 0.02	$4.400^{+4.448}_{-4.354}$	$4.103^{+4.110}_{-4.100}$	$5.006^{+5.318}_{-4.727}$
14567	GOODS-S	53.089684	-27.844601	1.49	9.99	5.045 ± 0.066	0.88 ± 0.04	$3.474^{+3.553}_{-3.414}$	$3.377^{+3.459}_{-3.366}$	$4.030^{+4.428}_{-3.704}$
17184	GOODS-S	53.123787	-27.832561	1.04	9.09	2.399 ± 0.119	1.32 ± 0.18	$1.856^{+2.003}_{-1.744}$	$1.898^{+1.948}_{-1.893}$	$2.572^{+3.216}_{-2.229}$
17469	GOODS-S	53.190910	-27.831028	1.16	9.47	2.006 ± 0.020	0.52 ± 0.02	-	$1.757^{+1.758}_{-1.757}$	$2.117^{+2.287}_{-1.979}$
18116	GOODS-S	53.186100	-27.827543	1.98	9.95	3.846 ± 0.158	2.48 ± 0.14	$3.437^{+3.617}_{-3.268}$	$2.900^{+2.977}_{-2.684}$	$1.941^{+2.287}_{-1.683}$
19865	GOODS-S	53.081169	-27.818588	1.24	9.55	2.525 ± 0.038	1.02 ± 0.04	$2.190^{+2.204}_{-2.086}$	$2.064^{+2.143}_{-2.061}$	$2.695^{+3.031}_{-2.489}$
21868	GOODS-S	53.226711	-27.808552	1.91	9.82	1.642 ± 0.041	0.78 ± 0.09	$1.621^{+1.711}_{-1.358}$	$1.920^{+1.899}_{-1.581}$	$1.557^{+1.805}_{-1.367}$
...	...	...	...	...	...	...	...	...	...	...

[a] From the v4.0 3D-HST catalog.

[b] Taken from van der Wel et al. (2012) catalog to match the morphological measurements.

[c] z_p taken from the ZFOURGE catalog (Straatman et al., 2016). By comparing photometric and spectroscopic redshifts, Straatman et al. (2016) estimate photometric redshift errors of $\Delta z/(1+z) \sim 0.01$.

[d] Taken from the ZFOURGE catalog (Straatman et al., 2016). Corrected to be consistent with morphological measurements by multiplying the catalog mass by the ratio of the total F160W flux measured by `GALFIT` to the total F160W flux measured in the Straatman et al. (2016) catalog. Uncertainties on stellar masses are dominated by systematics, and are estimated to be $\sim 0.2 - 0.3$ dex.

[e] From the van der Wel et al. (2012) catalogs. Corrected to rest-frame 5,000Å using the procedure in van der Wel et al. (2014).

[f] From the van der Wel et al. (2012) catalogs.

All listed radii represent measurements of the *major axis* of the galaxy.

(This table is available in its entirety in a machine-readable form in the online journal. A portion is shown here for guidance regarding its form and content.)

There is slightly more scatter, $\sim$0.3 dex, when comparing half-mass radii calculated using Method 3 to those calculated using Method 1 or 2. The Method 3 half-mass radii are also offset slightly larger than the Method 1 & 2 half-mass radii, by 0.09 dex and 0.06 dex respectively. This systematic bias is especially apparent for large star-forming galaxies. Intriguingly, this is similar to the offset that Price et al. (2017) found between the intrinsic half-mass radii of simulated massive galaxies and the half-mass radii recovered using their implementation of the Szomoru et al. (2010, 2012, 2013) method (our Method 3).

The simplest explanation for the offset between the Method 3 radii when compared to the Method 1 & 2 radii is that imperfect sky modeling at large radii led to errors in the deconvolved Method 3 profiles. If the sky subtraction is not perfect at large radii, then the shape of each `GALFIT` profile at large radii is incorrect. Both the u and g profiles will converge to approximately the same value, the noise level. Because the outskirts of most galaxies tend to be bluer than the centers (explored further in Section 2.3), this would lead to the observed color gradient being *flatter* than the true, blue, gradient. Consequently, M/L would be overestimated, $r_{\rm mass}/r_{\rm light}$ would be overestimated, and the half-mass radius for Method 3 would be overestimated. This effect would be more apparent for large galaxies, as more of their outskirts would be subsumed by residual sky noise. Since blue galaxies are typically larger than red galaxies at fixed stellar mass, this effect is also generally more apparent for blue galaxies. Again, we note that the magnitude of the difference in half-mass radii calculated with Method 3 as opposed to Method 1 or 2 is only $\sim$0.3 dex.

In Appendix 2.5, we further investigate how well the half-mass radii measured using Methods 1 and 3 agree. We show that the differences between the two sets of half-mass radii do not depend on galaxy stellar mass, redshift, Sérsic index, or $U - V$ color.

Overall, the consistency between half-mass radii calculated with Methods 1, 2, & 3 indicates that, despite difficulties in measuring half-mass radii and in accounting for the PSF, these methods are converging towards a physically-meaningful half-mass radius. While our conclusions for the remainder of the chapter do not depend on the method we use to calculate half-mass radii, we wish to pick one method as the 'primary' method to show in our plots.

Each of the three methods has its own strengths and weaknesses. Using both Methods 1 & 2, we can examine the observed-space M/L profile before performing modeling to account for the PSF. This allows us to verify whether half-mass radii are smaller, larger, or equal to half-light radii with minimal dependence on modeling. Furthermore, because these methods model the full SED of each annulus, they make use of all of the available multi-band data. Method 1 uses a fairly simple and easy-to-interpret approach to account for PSF effects; however, complex M/L profile shapes are likely not well-described by our power law function. Method 2– which uses GALFIT to fit a mass map– suffers from issues common to this type of modeling: it can be difficult to perfect sky subtraction at large radii, and galaxies with non-Sérsic mass distributions are not modeled well. Method 3 is quite straightforward and easy-to-implement. It is also ideal for cases where only a few bands of imaging are available, because it is based off of a single color; by the same token, this method does not fully utilize the multi-band data available for the galaxies in our sample. Furthermore, by accounting for PSF effects in each band separately and then subtracting deconvolved profiles, any possible

errors in the deconvolution process can have a large effect on the final half-mass radius. Considering these strengths and weaknesses, we choose to present our results below using the Method 1 half-mass radii. Again, we stress that our conclusions are unchanged if we instead use the half-mass radii from Method 2 or 3.

Quantifying the strength of galaxy color gradients

The ratio of half-mass to half-light size, $r_{\rm mass}/r_{\rm light}$, describes the strength of the color gradient in a galaxy. If there is no color gradient present, the half-mass and half-light sizes will be equal. If there is a weak negative color gradient, meaning that the galaxy is slightly bluer at larger radii, the half-mass size will be slightly smaller than the half-light size and $r_{\rm mass}/r_{\rm light} < 1$; a strong negative color gradient will result in a much smaller half-mass size than half-light size, and $r_{\rm mass}/r_{\rm light} \ll 1$. Similarly, a weakly positive color gradient means that $r_{\rm mass}/r_{\rm light} > 1$ and a strong positive color gradient means that $r_{\rm mass}/r_{\rm light} \gg 1$. By examining $r_{\rm mass}/r_{\rm light}$, we can examine the strength of color gradients in galaxies and how they correlate with other galaxy properties.

In Figure 2.5, we show correlations between $r_{\rm mass}/r_{\rm light}$ and galaxy stellar mass, half-light radius, the Sérsic index n measured from the galaxy's F160W light profile, $U-V$ color, and stellar mass surface density within the *circularized* effective radius $\Sigma_{\rm eff} = 0.5M_*/(\pi[r_{\rm e,mass} \times \sqrt{b/a}]^2)$. We use a circularized half-mass radius to compute $\Sigma_{\rm eff}$ for consistency with other works. To minimize the effects of any redshift evolution on the observed correlations, we show three different redshift intervals. We only plot galaxies with masses above the mass completeness level for each redshift interval (dashed vertical lines in left column of Figure 2.5). Small blue points and red squares show individual star-forming and quiescent galaxies, and large blue points and red squares show a running error-weighted average.

We use a least squares technique to fit a line of the form $\log r_{\rm mass}/r_{\rm light} = s(\log M/M_\odot - 10)+b$ to the trend as a function of mass, a line of the form $\log r_{\rm mass}/r_{\rm light} = s(\log r_{\rm e,light}/{\rm kpc} - 1) + b$ to the trend as a function of half-light radius, a line of the form $\log r_{\rm mass}/r_{\rm light} = s(\log n - 1) + b$ to the trend as a function of Sérsic index, a line of the form $\log r_{\rm mass}/r_{\rm light} = s([U-V] - 1) + b$ to the trend as a function of $U-V$ color, and a line of the form $(\log r_{\rm mass}/r_{\rm light} = s(\log \Sigma_{\rm eff} - 9) + b)$ to the trend as a function of stellar mass surface density. We fit the individual data points, not the mean points also shown in Figure 2.5. We estimate error bars on the fits by performing 500 bootstrap simulations. The best-fit slopes and intercepts for these fits, as well as their error bars, are listed in Table 2.2. The best-fit relations for all parameters are also plotted in Figure 2.5. The fits are outlined in grey if their slopes are consistent with zero within the 1σ error bars, and outlined in black if the slopes are not consistent with zero. We see significant trends in $r_{\rm mass}/r_{\rm light}$ with both stellar mass, stellar mass surface density, half-light radius, $U-V$ color, and $\Sigma_{\rm eff}$ for blue and red galaxies. In the highest-redshift bin, the trends are generally less significant. This is likely due to flatter color gradients in this redshift interval (explored further in Figure 2.6). The strongest trend we see is in $r_{\rm mass}/r_{\rm light}$ as a function of $\Sigma_{\rm eff}$. Interestingly, this trend remains

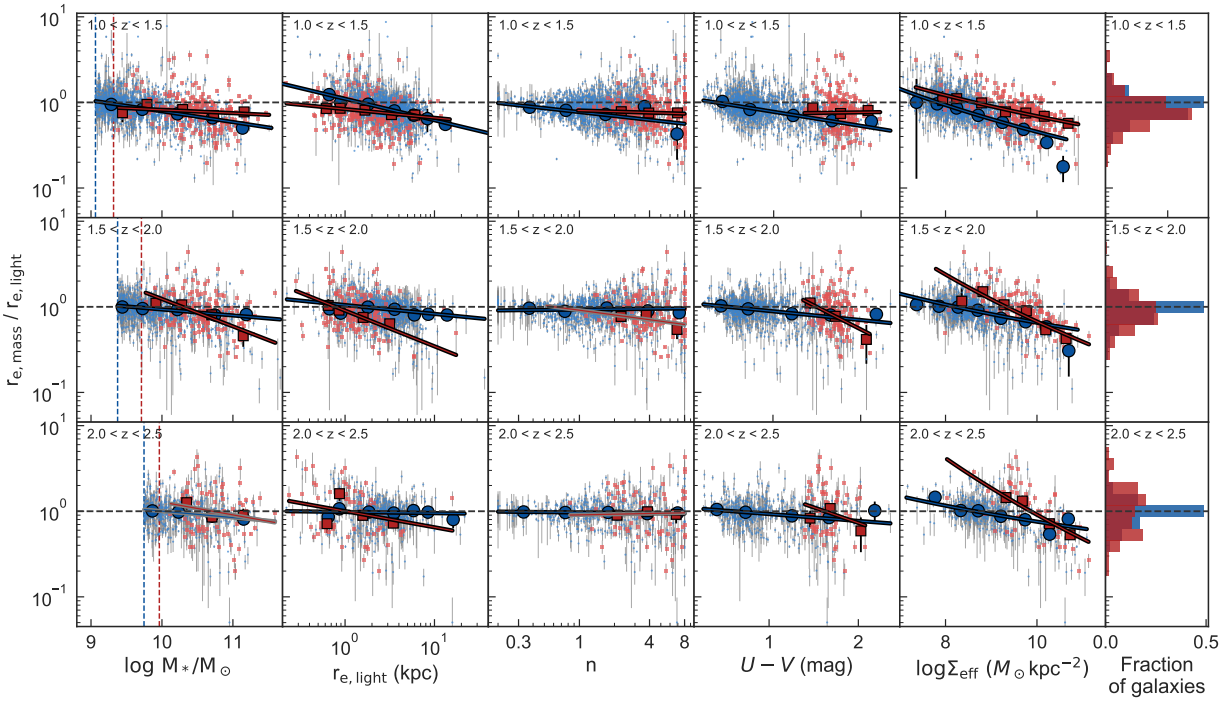

Figure 2.5: Half-mass to half-light ratio as a function of other galaxy properties. Each row shows one redshift slice. From left to right, each column shows the correlation with: stellar mass, half-light radius, Sérsic index, $U - V$ color, and mass surface density $\Sigma_{\rm eff} = 0.5M_*/(\pi r^2_{\rm e,mass})$. The rightmost column shows a histogram of $r_{\rm e,mass}/r_{\rm e,light}$ for all star-forming (blue) and quiescent (red) galaxies in the redshift range. Individual star-forming and quiescent galaxies are plotted as small light blue circles and small light red squares. The running error-weighted mean of star-forming and quiescent galaxies is plotted as large blue circles and large red squares; error bars on these mean points are the standard error on the mean ($\sigma/\sqrt{N}$). The data set is binned such that each mean point represents the same number of individual data points. Best fits to the trends for star-forming and quiescent galaxies are shown as solid blue and red lines. Best-fit lines are outlined in black if the slopes are inconsistent with zero, and outlined in grey if the slopes are consistent with zero. The horizontal grey dashed line in each panel indicates where $r_{\rm mass} = r_{\rm light}$. Mass completeness limits for star-forming and quiescent galaxies are shown as blue and red dashed vertical lines in the leftmost column; galaxies below the mass completeness limits are neither included in the fits nor plotted in this figure.

significant in the highest-redshift bin, even though trends in other galaxy properties are often consistent with being flat.

To ensure that the trends we see are not driven by differences in mass completeness cuts for star-forming and quiescent galaxies at different redshifts, we also calculated the trends shown in Figure 2.5 while considering only galaxies with $M_* > 10^{10.08} M_\odot$. This mass corresponds to the most stringent mass completeness cut in our sample. We saw no significant differences in the best-fit relations, indicating that these trends are not driven by the exact value of our mass completeness limits.

While $r_{\rm mass}/r_{\rm light}$ does not appear to depend strongly on Sérsic index, we do find that the color gradient strength correlates with stellar mass, half-light radius, $U-V$ color, and $\Sigma_{\rm eff}$ such that larger, more massive, and redder galaxies have more steeply negative color gradients. These trends are apparent both in the binned data and the values of the best-fit lines. We discuss the possible interpretations of these trends, as well as how they compare to previous studies, in Section 2.4.

In Figure 2.6, we show the median of $r_{\rm mass}/r_{\rm light}$ as a function of redshift for all galaxies with $M_* > 10^{10.08} M_\odot$. We see that both star-forming and quiescent galaxies in all redshift ranges typically have negative color gradients, where the outskirts of the galaxies are bluer— and thus likely younger, more metal-poor, or less dusty— than the centers of the galaxies. This is consistent with the histograms shown in the rightmost column of Figure 2.5, which show that from $1.0 < z < 2.0$, $r_{\rm mass}/r_{\rm light}$ is clearly not centered at one. This also agrees with many previous studies (Tortora et al., 2010; Wuyts et al., 2010; Guo et al., 2011; Szomoru et al., 2013; Chan et al., 2016; Mosleh et al., 2017). Furthermore, we see evidence that color gradients are, on average, nearly flat at $z \gtrsim 2$, then decrease steadily towards lower redshifts. Interestingly, quiescent and star-forming galaxies show no significant differences in their color gradient strength evolution. We explore the physical interpretation of this redshift evolution in Section 2.4.

We note that the trend shown in Figure 2.6 does not appear to be driven by differences in the average stellar masses of galaxies in each redshift bin; we see the same trend if we break the sample up into two mass bins of $10.0 \leq \log M/M_\odot \leq 10.5$ and $10.5 \leq \log M/M_\odot \leq 11.0$. This trend also does not appear to be driven by small galaxies, whose half-mass radii may be more difficult to recover: the redshift evolution for galaxies with $r_{\rm light} > 2$ kpc shows the same trend as Figure 2.6. Finally, we note that we see very similar trends between $r_{\rm mass}/r_{\rm light}$ and redshift when using any of the three methods of calculating half-mass radii described in Section 2.2.

The galaxy mass - half mass radius relation

Because $r_{\rm mass}/r_{\rm light}$ varies with both stellar mass (Figure 2.5 and redshift (Figure 2.6), the galaxy $M_* - r_{\rm mass}$ relation differs from the galaxy $M_* - r_{\rm light}$ relation. Here, we show the galaxy $M_* - r_{\rm mass}$ relation for star-forming and quiescent galaxies at $1.0 \leq z \leq 2.5$.

Instead of directly fitting $r_{\rm mass}$ as a function of stellar mass, we 'correct' the Mowla et al. (2019b) mass-size relations from half-light radii to half-mass radii using our fits to

Table 2.2: Best-fit values to the trends shown in Figure 2.5.

z	Galaxies fit	s	b
$\log M$	$(\log r_{\rm mass}/r_{\rm light} = s(\log M/M_\odot - 10) + b)$		
$1.0 \leq z < 1.5$	blue	$-0.143^{+0.017}_{-0.018}$	$-0.097^{+0.008}_{-0.007}$
$1.0 \leq z < 1.5$	red	$-0.042^{+0.021}_{-0.037}$	$-0.084^{+0.026}_{-0.018}$
$1.5 \leq z < 2.0$	blue	$-0.073^{+0.014}_{-0.015}$	$-0.030^{+0.006}_{-0.006}$
$1.5 \leq z < 2.0$	red	$-0.316^{+0.092}_{-0.069}$	$0.088^{+0.035}_{-0.047}$
$2.0 \leq z < 2.5$	blue	$-0.083^{+0.021}_{-0.022}$	$0.004^{+0.006}_{-0.005}$
$2.0 \leq z < 2.5$	red	$-0.145^{+0.163}_{-0.105}$	$0.101^{+0.096}_{-0.149}$
$\log r_{\rm e,light}$	$(\log r_{\rm mass}/r_{\rm light} = s(\log r_{\rm e,light}/{\rm kpc} - 1) + b)$		
$1.0 \leq z < 1.5$	blue	$-0.325^{+0.073}_{-0.059}$	$-0.233^{+0.026}_{-0.021}$
$1.0 \leq z < 1.5$	red	$-0.103^{+0.027}_{-0.038}$	$-0.180^{+0.024}_{-0.039}$
$1.5 \leq z < 2.0$	blue	$-0.100^{+0.027}_{-0.029}$	$-0.081^{+0.016}_{-0.020}$
$1.5 \leq z < 2.0$	red	$-0.417^{+0.164}_{-0.117}$	$-0.461^{+0.146}_{-0.096}$
$2.0 \leq z < 2.5$	blue	$-0.034^{+0.029}_{-0.030}$	$-0.029^{+0.016}_{-0.016}$
$2.0 \leq z < 2.5$	red	$-0.187^{+0.124}_{-0.130}$	$-0.186^{+0.125}_{-0.121}$
n	$(\log r_{\rm mass}/r_{\rm light} = s(\log n - 1) + b)$		
$1.0 \leq z < 1.5$	blue	$-0.198^{+0.054}_{-0.046}$	$-0.110^{+0.009}_{-0.008}$
$1.0 \leq z < 1.5$	red	$-0.045^{+0.051}_{-0.093}$	$-0.092^{+0.052}_{-0.030}$
$1.5 \leq z < 2.0$	blue	$0.014^{+0.023}_{-0.025}$	$-0.032^{+0.006}_{-0.007}$
$1.5 \leq z < 2.0$	red	$-0.185^{+0.187}_{-0.163}$	$-0.039^{+0.080}_{-0.076}$
$2.0 \leq z < 2.5$	blue	$-0.001^{+0.030}_{-0.033}$	$-0.009^{+0.006}_{-0.007}$
$2.0 \leq z < 2.5$	red	$0.016^{+0.151}_{-0.185}$	$-0.038^{+0.107}_{-0.083}$
$U - V$	$(\log r_{\rm mass}/r_{\rm light} = s([U - V] - 1) + b)$		
$1.0 \leq z < 1.5$	blue	$-0.170^{+0.016}_{-0.016}$	$-0.106^{+0.011}_{-0.008}$
$1.0 \leq z < 1.5$	red	$0.006^{+0.045}_{-0.113}$	$-0.123^{+0.094}_{-0.038}$
$1.5 \leq z < 2.0$	blue	$-0.103^{+0.014}_{-0.013}$	$-0.052^{+0.007}_{-0.007}$
$1.5 \leq z < 2.0$	red	$-0.520^{+0.233}_{-0.162}$	$0.258^{+0.112}_{-0.151}$
$2.0 \leq z < 2.5$	blue	$-0.091^{+0.021}_{-0.028}$	$-0.031^{+0.010}_{-0.011}$
$2.0 \leq z < 2.5$	red	$-0.376^{+0.348}_{-0.174}$	$0.236^{+0.125}_{-0.223}$
$\log \Sigma_{\rm eff}$	$(\log r_{\rm mass}/r_{\rm light} = s(\log \Sigma_{\rm eff} - 9) + b)$		
$1.0 \leq z < 1.5$	blue	$-3.452^{+0.279}_{-0.233}$	$-27.968^{+2.253}_{-1.881}$
$1.0 \leq z < 1.5$	red	$-2.504^{+0.579}_{-0.484}$	$-20.192^{+4.632}_{-3.883}$
$1.5 \leq z < 2.0$	blue	$-2.264^{+0.194}_{-0.196}$	$-18.305^{+1.576}_{-1.587}$
$1.5 \leq z < 2.0$	red	$-5.647^{+0.894}_{-0.737}$	$-45.349^{+7.172}_{-5.925}$
$2.0 \leq z < 2.5$	blue	$-2.022^{+0.455}_{-0.620}$	$-16.303^{+3.668}_{-5.004}$
$2.0 \leq z < 2.5$	red	$-6.623^{+0.942}_{-0.721}$	$-53.028^{+7.505}_{-5.765}$

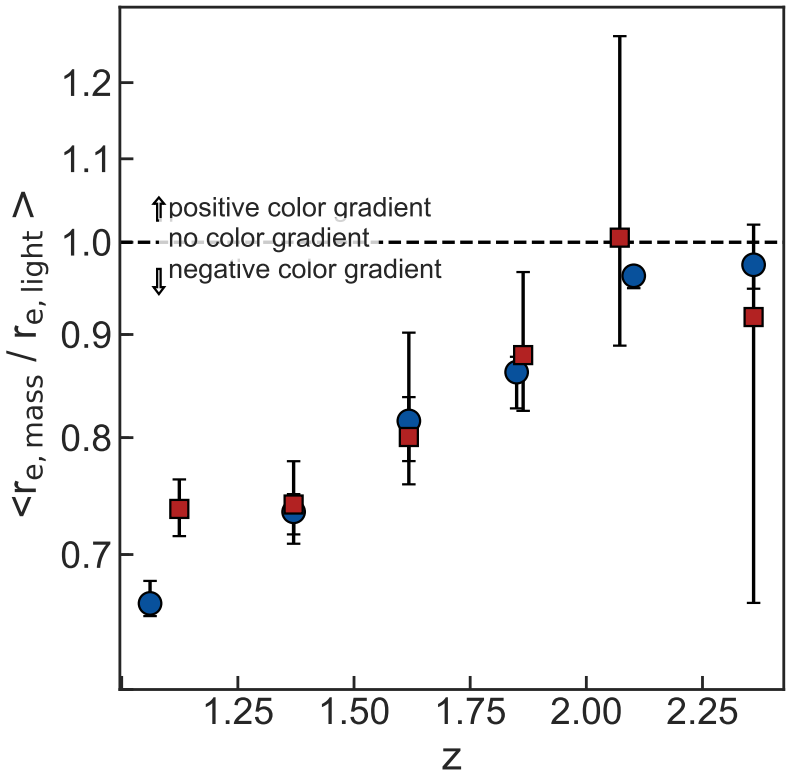

Figure 2.6: Median half mass-to-half light ratio for bins of star-forming (blue circles) and quiescent (red squares) galaxies as a function of median redshift. Only galaxies with masses greater than the most stringent mass completeness cut ($\sim 10^{10} M_{\odot}$) are included. Error bars represent the middle 68% of 500 bootstrap samples.

$r_{\rm mass}/r_{\rm light}$ as a function of mass. We take this approach because here we are interested in how the relation *changes* when half-mass radii are considered instead of half-light radii. By using the Mowla et al. (2019b) fits as the assumed true galaxy mass-light size relation, we minimize the effects that using a smaller sample size and a slightly different fitting technique would have on our conclusions. We note that we use the Mowla et al. (2019b) mass-size relations over the van der Wel et al. (2014) relations because the Mowla et al. (2019b) fits use the same methods as van der Wel et al. (2014), but add a significant number of additional high-mass galaxies.[2]

To obtain the $M_* - r_{\rm mass}$ relation, we simply multiply the Mowla et al. (2019b) $r_{\rm light} - M_*$ relations by the $r_{\rm mass}/r_{\rm light}$ fits shown in Figure 2.5 and Table 2.2. The resulting $r_{\rm mass} - M_*$ relations are shown in Figure 2.7. Each panel shows a different redshift range. Solid lines

[2]Both the half-mass radii presented here and the half-light radii used by Mowla et al. (2019b) and van der Wel et al. (2014) are semi-major axis measurements, not circularized radii.

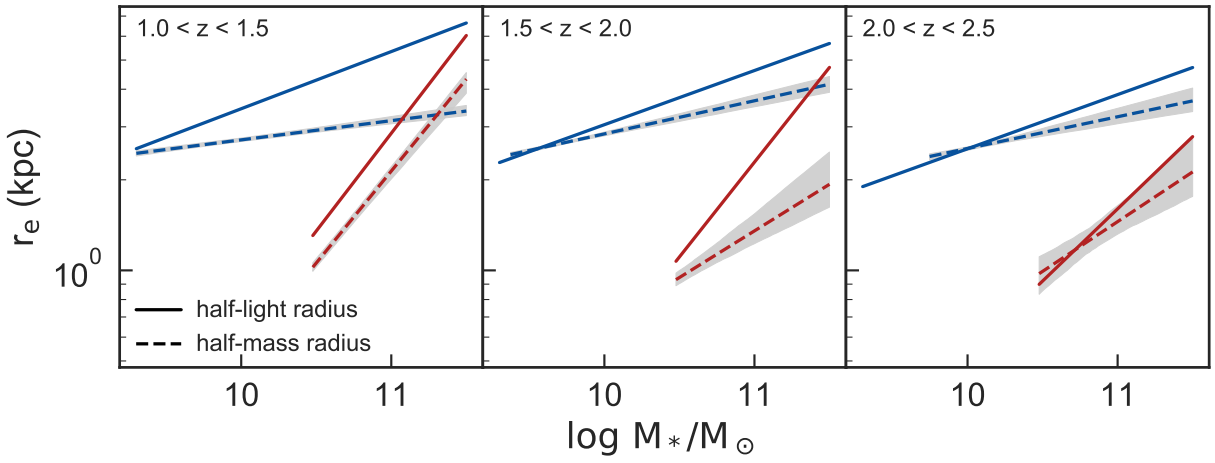

Figure 2.7: Mass-size relations for three redshift slices. The solid blue and red lines show the $M_* - r_{\rm light}$ relations from Mowla et al. (2019b), and the dashed lines show the $M_* - r_{\rm mass}$ relations from this analysis. Light grey regions show the 1σ error region from 500 bootstrap simulations of the $M_* - r_{\rm mass}$ relation.

represent the Mowla et al. (2019b) $r_{\rm light} - M_*$ relations, while the dashed lines represent our $r_{\rm mass} - M_*$ relations. We only calculate the $r_{\rm mass} - M_*$ relations for masses where both our sample and the Mowla et al. (2019b) sample are complete. The light grey region in Figure 2.7 shows the middle 68% of 500 bootstrap realizations of the $r_{\rm mass} - M_*$ relation. Because galaxies tend to have smaller half-mass radii than half-light radii, the normalization of the $r_{\rm mass} - M_*$ relation is smaller than the normalization of the $r_{\rm light} - M_*$ relation for both star-forming and quiescent galaxies at all redshifts. The slope of both the star-forming and quiescent relations also clearly flattens at $1.0 \leq z < 2.0$. In the $2.0 \leq z \leq 2.5$ bin, the slope of the star-forming relation also flattens; however, large uncertainties in the $r_{\rm mass}/r_{\rm light}$ fit for quiescent galaxies makes it difficult to draw conclusions for this population without a larger sample of galaxies. The slope of the $M_* - r_{\rm mass}$ relations are still approximately constant with redshift.

In Figure 2.8, we view the mass-size relation in a slightly different way: we use the best-fit mass-size relations to plot the radius at a fixed mass, $M_* = 10^{10.5} M_\odot$, as a function of redshift. The open circles show the values for the Mowla et al. (2019b) fits to the $r_{\rm light} - M_*$ relation at $0.1 \leq z \leq 3.0$. The filled circles show the corresponding values of the $r_{\rm mass} - M_*$ relation fits (calculated from Table 2.2, also shown in Figure 2.7). Over the $1.0 \leq z \leq 2.5$ range studied in this chapter, galaxy half-mass radii clearly evolve less than their half-light radii. While the half-light radii of star-forming galaxies at $M_* = 10^{10.5} M_\odot$ increase by $1.17^{+0.41}_{-0.41}$ kpc (37^{+19}_{-15}%) between $z = 1.25$ and $z = 2.25$, their half-mass radii only grow by $0.04^{+0.41}_{-0.42}$ kpc (1^{+16}_{-13}%). Similarly, while the half-light radii of $M_* = 10^{10.5} M_\odot$ quiescent

galaxies increase by $0.43^{+0.15}_{-0.13}$ kpc ($47^{+26}_{-19}\%$) over this redshift interval, their half-mass radii only grow by $0.08^{+0.21}_{-0.21}$ kpc ($8^{+29}_{-20}\%$). Over this redshift range, then, half-mass radii grow much less than half-light radii do. We note that the percentage growth in the half-mass and half-light radii of quiescent galaxies is consistent within the 1σ error bars; a larger sample of high-redshift quiescent galaxies is required to tighten these error bars and further investigate galaxy size growth at high redshift.

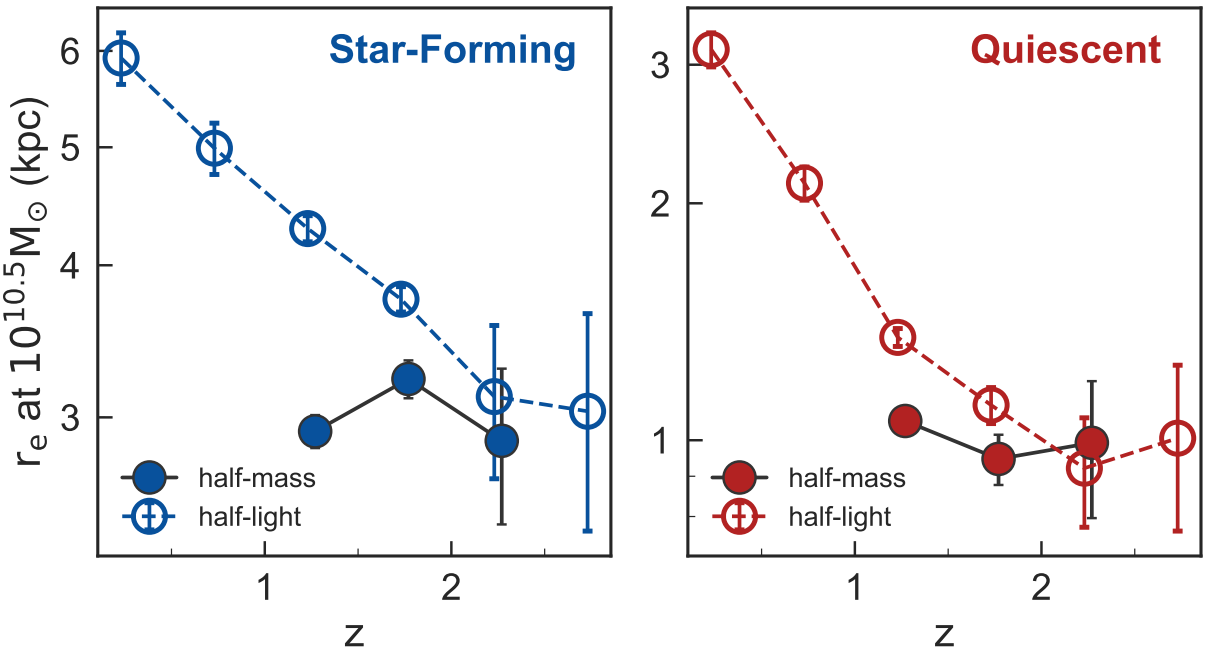

Figure 2.8: Half-light radii (open circles) and half-mass radii (filled circles) at $M_* = 10^{10.5} M_\odot$ for star-forming and quiescent galaxies as a function of redshift. Half-light radii are taken from the Mowla et al. (2019b) fits, and half-mass radii are calculated using the fits in Table 2.2. Over the $1.0 \leq z \leq 2.5$ range, the half-mass radii of both star-forming and quiescent galaxies evolve significantly less than their half-light radii.

2.4 Discussion

Sources of uncertainty

Before providing a physical interpretation of the trends we see between color gradient strength and galaxy stellar mass, half-light radius, $U - V$ color, $\Sigma_{\rm eff}$, and redshift, we want to ensure that they do not arise from systematic uncertainties or biases in how well we are able to recover half-mass radii.

The trends we see in color gradient strength (Figure 2.5) are present regardless of which method we use to calculate half-mass radii. For both Method 1, Method 2, and Method 3, we find that $r_{\rm mass}/r_{\rm light}$ is nearly flat at $z \gtrsim 2$ and decreases with decreasing redshift (Figure 2.6); similarly, we see correlations between $r_{\rm mass}/r_{\rm light}$ and stellar mass, half-light radius, $U-V$ color, and $\Sigma_{\rm eff}$ for all three methods. The values of the best-fit trends for Methods 2 & 3 are slightly different than those presented in Table 2.2 for Method 1, but generally agree within the error bars. While this agreement is expected because the three sets of half-mass radii are quite consistent (Figure 2.4, Section 2.5), it helps ensure that the trends we see are not simply a function of which method we chose to use.

All three of these methods, however, are based on the same multi-band imaging. One can imagine that it is simply easier to recover accurate mass profiles for galaxies which are physically larger on the sky— because there are more pixels— or more massive galaxies, which likely have higher signal-to-noise ratios. If this were the case, then color gradients in small or low-mass galaxies would be washed out and approach unity. These are the same trends that we see in the data. However, our methods do *not* appear to be significantly biased against recovering the half-mass radii of small or low-mass galaxies. In Section 2.5, we test how well our primary method can recover the half-mass radii of modeled galaxies as a function of the properties of the modeled galaxy. We do not see any significant trends with half-light radius, stellar mass, or redshift. We do see that there is some dependence on color gradient, such that the half-mass radii of galaxies with negative color gradients tend to be overestimated more often than underestimated, and the half-mass radii of galaxies with positive color gradients tend to be underestimated more often than overestimated. In other words, the intrinsic color gradients are very slightly 'washed out' for all galaxies. We note that this is a $\lesssim 0.05$ dex effect; furthermore, correcting for this would only strengthen the trends that we see in $r_{\rm mass}/r_{\rm light}$.

Another potential bias in the imaging data is the PSF matching. The PSF of the F606W and F814W images is significantly smaller than the F125W, F140W, and F160W images. Therefore, if these images are not PSF-matched, galaxies will appear smaller in bluer bands, where the effect of the PSF is smaller. This will result in an artificial color gradient, such that the outskirts of a galaxy will seem redder than the center. We use PSF-matched images from the 3D-HST team (Skelton et al., 2014) to mitigate this issue; however, errors in the PSF matching could similarly induce artificial color gradients. Figure 11 of Skelton et al. (2014) shows tests of the PSF matching, and they conclude that the PSF matching is accurate to 1% for all bands and all fields. We have performed similar tests on the PSF-matched images using the same method we use to extract aperture photometry of galaxies, and find similar results. Therefore, it is unlikely that the color gradients we see in this chapter are due to errors in the PSF matching.

When we fit the SEDs of each annulus in a galaxy, we fix the metallicity and leave only dust, age, and star formation timescale free. However, color gradients can also be caused by metallicity gradients— by not allowing for metallicity gradients in our fits, we could be biasing the strength of the M/L gradient. We chose to fix metallicity because allowing for a variable metallicity with only $5-8$ bands of resolved photometry results in

poorly-constrained fits. The only parameter we use from the annuli SED fits is the stellar mass, which is generally considered the most well-constrained property from SED fits (and is largely agnostic to the age-metallicity degeneracy, e.g. Bell & de Jong, 2001). We are careful not to interpret the color gradients we see as gradients in any specific physical property, and focus on only the recovered half-mass radii. Significant additional work would be required to disentangle whether the gradients we see are due to age or metallicity.

Another potential concern is the effect of dust. It is possible that we are systematically underestimating the masses of optically thick regions. Until we have spatially-resolved rest-frame mid- to far-IR data for a large number of galaxies, the best we can do is the integral constraint we use in this chapter, where we ensure that the sum of the annuli SEDs matches the IRAC data points. We expect that the galaxies most likely to be affected by high dust obscuration are massive star-forming galaxies, whose centers are likely highly dust-obscured (e.g., Barro et al., 2016). By 'missing' mass in the centers of these galaxies, we could be overestimating their half-mass radii and thus overestimating their $r_{\rm mass}/r_{\rm light}$. We note that this would result in an even steeper trend in $r_{\rm mass}/r_{\rm light}$ as a function of mass than the one that we observe. We test the importance of this effect— which, again, is likely strongest for dusty star-forming galaxies— by removing all star-forming galaxies with $V - J > 1.2$ from our sample, re-fitting the trends shown in Figure 2.5, and re-calculating the effects on the mass-size relation shown in Figures 2.7 & 2.8. While the exact values change slightly (such that the implied growth in the half-mass radii of star-forming galaxies is $4^{+17}_{-13}\%$, instead of $\sim 1\%$), the overall trends we see are not significantly altered by excluding dusty star-forming galaxies from our sample. Nonetheless, dust remains a significant uncertainty in this work, and our catalog of half-mass radii should be used with this consideration in mind.

Trends in $r_{\rm mass}/r_{\rm light}$ are also affected by uncertainties in $r_{\rm light}$ measurements. For this work, the most significant correction we make to $r_{\rm light}$ is to follow the van der Wel et al. (2014) procedure to correct the measured F160W and F125W sizes to rest-frame 5,000Å. This correction allows us to consistently compare half-light radii for galaxies at different redshifts. While it is important to apply this correction for consistency— most other works in the literature apply this correction, including the van der Wel et al. (2014) and Mowla et al. (2019b) mass-size relation papers— we note that it may affect trends in $r_{\rm mass}/r_{\rm light}$. For completeness, we have also studied the trends in $r_{\rm mass}/r_{\rm light}$ as a function of other galaxy properties if we take $r_{\rm light}$ to be the measured F160W size for all galaxies. All trends, at all redshifts, are still present.

We do not measure color gradients on scales smaller than the HWHM of the PSF. For small galaxies, then, we are only able to measure color gradients in the outer portions of the galaxy. Section 2.5 shows that we are still able to accurately recover the half-mass radii of small galaxies *if* their intrinsic M/L profiles are power-law functions of radius. If the central regions of small galaxies deviate from this power-law M/L profile, then the half-mass radii we recover for small galaxies may be biased. While we see evidence in this work (and in previous works, e.g. Chan et al., 2016) that a power law is a good model for the M/L profiles of galaxies, higher-resolution imaging would be required to fully test this assumption for small galaxies.

Finally, our results— and the results of all observational studies— rely on the accuracy with which we can recover the intrinsic properties of galaxies from observations. Price et al. (2017) uses cosmological simulations of massive galaxies ($10^{10} - 10^{11.5} M_{\odot}$) at $1.7 \leq z \leq 2.0$ to assess how well observational techniques are able to recover stellar masses and half-mass radii. On average, they found that intrinsic half-mass radii were 0.1 dex smaller than observed half-mass radii as calculated with the Szomoru et al. (2010, 2012, 2013) method. However, they found substantial scatter between the recovered and intrinsic properties; in particular, the viewing angle had strong effects on the scatter in the mass-size relation. The results presented here are likely subject to these effects.

In summary, we stress that the methods for calculating half-mass radii are complex, and in some respects lie towards the edge of what is possible with current data. Half-mass radii of individual galaxies should be treated with their error bars in mind. On the whole, however, we believe that the half-mass radii presented in this chapter are not affected by strong systematic biases, and that the trends we see in $r_{\rm mass}/r_{\rm light}$ are a reflection of true trends in the data.

Comparison with previous studies

The most basic trend we see is that color gradients in galaxies tend to be negative, such that the outskirts of galaxies are bluer than the central regions. We observe these generally negative color gradients for both star-forming and quiescent galaxies over the full $1.0 \leq z \leq 2.5$ redshift range we study. This is in agreement with the consensus in the literature. Previous works explicitly measuring color gradients also find that they tend to be negative (e.g., Tortora et al., 2010; Wuyts et al., 2010; Guo et al., 2011; Szomoru et al., 2013; Chan et al., 2016; Mosleh et al., 2017). This effect is also seen by studies such as van der Wel et al. (2014) that calculate galaxy sizes in multiple imaging bands: galaxies appear smaller if they are measured in longer-wavelength bands, implying negative color gradients.

The dependence of galaxy color gradients on other galaxy properties is more difficult to quantify; still, previous works have studied these correlations at both $z \sim 0$ and $z \sim 1-2$. At $z \sim 0$, Tortora et al. (2010) measured the color gradients of $\sim 50,000$ galaxies in the SDSS. They find that color gradients are stronger for both higher-mass and larger galaxies, consistent with the trends we find at $1 \leq z \leq 2$. They additionally find that the strength of color gradients in quiescent galaxies seems to plateau at $\log M/M_{\odot} \geq 11$. Our data does not replicate this trend, perhaps due to the relatively low number of very high-mass quiescent galaxies in our sample or to genuine evolution of the high-mass quiescent population between $z \sim 1$ and $z \sim 0$. Tortora et al. (2010) attribute the trends they see mainly to metallicity gradients, while age gradients play a smaller but still significant role (see also Greene et al., 2012, 2015). In this study, we are unable to separate the effects of age and metallicity.

At $z > 0$, previous studies have typically been hampered by small sample sizes, and have generally *not* found significant relationships between the strength of color gradients and other galaxy properties. For example, Chan et al. (2016) did not find significant correlations between $r_{\rm mass}/r_{\rm light}$ and stellar mass, size, or Sérsic index in a sample of massive cluster

galaxies at $z \sim 1.4$. Szomoru et al. (2013) found that $r_{\rm mass}/r_{\rm light}$ had no correlation with galaxy mass or surface density; they found very weak trends such that $r_{\rm mass}/r_{\rm light}$ was smaller for galaxies with higher Sérsic indices, smaller sizes, and lower sSFRs. The discrepancy between the Szomoru et al. (2013) and Chan et al. (2016) results and the results presented in this chapter are almost certainly due to large differences in sample size and mass range: the Szomoru et al. (2013) study only included 177 galaxies with $\log M_*/M_\odot > 10.7$, and the Chan et al. (2016) only studied 36 quiescent galaxies with $\log M_*/M_\odot > 10.2$; our analysis includes more than an order of magnitude more galaxies and spans two additional orders of magnitude in stellar mass. We note that if we consider only the quiescent galaxies in our sample with $\log M_*/M_\odot > 10.7$, we would see similarly weak or non-existant trends between color gradient strength and other galaxy properties. Our large sample size and long lever arm on stellar mass are thus crucial to see the clear dependence of $r_{\rm mass}/r_{\rm light}$ on both stellar mass, half-light radius, $U-V$ color, $\Sigma_{\rm eff}$, and redshift.

Mosleh et al. (2017) used CANDELS data to calculate the half-mass radii of $\sim 2,000$ galaxies at $0.5 < z < 2.0$. Similar to our results, they find that the half-mass radii of star-forming galaxies evolve much more slowly than their half-light radii, and that color gradient strength depends on stellar mass. However, they find that the growth of quiescent galaxies is *not* significantly affected by color gradients. This discrepancy is likely due to differences in the methods used to calculate half-mass radii. Mosleh et al. (2017) find the best-fit single Sérsic model for each band of imaging, then— without correcting for residuals— divide these fits into 1D spatial bins. They use SED fitting to find the mass in each bin, and fit the resulting mass profile with another Sérsic model to extrapolate the mass profile to large radii. Using this method, the final half-mass radii depend strongly on the initial Sérsic fits to each band of imaging data; errors on these fits do not appear to be included in the uncertainties on the final half-mass radii. Because this method is quite comparable to our Method 3 without the residual correction step, we do not implement it in this chapter.

Physical interpretation of the trends in color gradient strength

In Section 2.3, we see that $r_{\rm mass}/r_{\rm light}$ decreases with increasing stellar mass, increasing half-light radius, increasing $U-V$ color, and increasing stellar mass surface density. Each of these trends is self-consistent in the framework of known galaxy correlations: more massive galaxies tend to be larger (the mass-size relation, e.g. Shen et al., 2003; van der Wel et al., 2014; Mowla et al., 2019b) and have redder colors (e.g. Williams et al., 2009). $U-V$ color is also a proxy for sSFR— galaxies redder in $U-V$ have lower sSFRs (e.g. Williams et al., 2009). The main degeneracy when using $U-V$ as a sSFR proxy is between dusty star-forming galaxies and quiescent galaxies at the same $U-V$; our UVJ selection has effectively separated these populations. So, the trend in $r_{\rm mass}/r_{\rm light}$ as a function of $U-V$ tells us that, to first order, star-forming galaxies with lower sSFRs tend to have lower $r_{\rm mass}/r_{\rm light}$. Again, this fits into the framework of galaxy correlations: due to the shallow slope of the star-forming main sequence (e.g., Whitaker et al., 2012b) more massive galaxies tend to have lower sSFRs.

While we do see that star-forming and quiescent galaxies occupy different regions of stellar mass, half-light radius, Sérsic index, $U - V$, and Σ_e space, the trends in $r_{\rm mass}/r_{\rm light}$ extend smoothly across the two populations. While the values for the best-fit trend lines (Table 2.2) are somewhat different, the fits generally overlap within the error bars. This lack of bimodality in color gradient strength seems to suggest that color gradients may *gradually* become stronger as galaxies evolve from star-forming to quiescent.

Our findings are broadly consistent with the inside-out growth scenario. Before they quench, star-forming galaxies form new stars preferentially at large radii (Nelson et al., 2016b; Hill et al., 2017), causing negative color gradients. Once they become quiescent, galaxies grow their sizes via minor mergers, which 'puff up' the outskirts of the galaxy with bluer younger and/or lower-metallicity stars accreted in the mergers (e.g. Bezanson et al., 2009; Naab et al., 2009). This would further steepen negative color gradients. This scenario could also explain why color gradients in quiescent galaxies are stronger at lower redshift: they have had more time to build up their bluer outer envelopes via mergers. Our basic findings are also consistent with other proposed quenching mechanisms that operate "inside-out," such as quenching via wet compaction (e.g., Zolotov et al., 2015).

In Chapter 5, we will split our sample of galaxies by rest-frame SED shape (Kriek et al., 2011) and study the strength of color gradients in different types of galaxies. By going beyond a simple 'star-forming or quiescent' selection, we hope to test whether trends in color gradients change smoothly as galaxies evolve. We will also test whether recently-quenched galaxies have different half-mass radii or color gradients than older quiescent galaxies; this may provide clues to the physical mechanisms behind the processes that quench galaxies.

Implications for the mass-size relation and its evolution with redshift

The $r_{\rm mass} - M_*$ and $r_{\rm light} - M_*$ relations have several notable differences. Because galaxy color gradients tend to be negative, the intercept of the mass-size relation is smaller for half-mass radii than it is for half-light radii. This is true for both star-forming and quiescent galaxies at $1.0 \leq z \leq 2.5$. However, half-mass radii are not smaller than half-light radii by a consistent amount across all redshifts: high-redshift galaxies tend to have $r_{\rm mass}/r_{\rm light} \sim 1.0$, whereas lower-redshift galaxies tend to have $r_{\rm mass}/r_{\rm light} \sim 0.7$. This implies that there is *less evolution* in the $r_{\rm mass} - M_*$ relation than there is in the $r_{\rm light} - M_*$ relation. This trend can clearly be seen in Figure 2.8, where we show that at $M_* = 10^{10.5} M_\odot$ and over the $1.0 \leq z \leq 2.5$ redshift range, half-mass radii only increase by about ∼one-third the amount that half-light radii increase (however, this measurement has large error bars).

This slower size evolution sheds light on a longstanding question about the cause of the rapid size growth of quiescent galaxies at $z \gtrsim 1$. Both the growth of individual galaxies and growth of the population as a whole (i.e., progenitor bias) can contribute to observed size growth. However, several studies have shown that neither the growth of individual galaxies via minor mergers (e.g., Nipoti et al., 2009; Newman et al., 2012; Bédorf & Portegies Zwart,

2013) nor progenitor bias (Belli et al., 2015) alone is enough to account for the observed evolution in the half-light radii of galaxies between $z \sim 2.5$ and $z \sim 1$. It appears that each method for size growth can only account for up to $\sim 50\%$ of the observed increase in half-light radii (Newman et al., 2012; Belli et al., 2015). Here we show that the explanation for this remarkable size growth may simply be that the growth is not as rapid as was previously thought: the half-mass radii of quiescent galaxies at $M_* = 10^{10.5} M_\odot$ only increase by $8^{+29}_{-19}\%$ between $z = 1.25$ and $z = 2.25$, less than the $47^{+25}_{-21}\%$ increase in their half-light radii (Figure 2.8). It it therefore possible that minor mergers (or progenitor bias) *alone* is enough to account for the growth in the half-mass radii of quiescent galaxies.

Because our current study focuses on the $1.0 < z < 2.5$ redshift range, we cannot address in detail how color gradients affect the size growth of quiescent galaxies below $z = 1$ (Figure 2.8). We can, however, use low-redshift color gradient studies to estimate the median half-mass radii of $z = 0$ quiescent galaxies. We assume that $z = 0$ quiescent galaxies have power-law M/L profiles which decrease from $M/L_g \sim 0.8$ to $M/L_g \sim 0.3 - 0.4$ from 0–2.5r_e, as suggested by the M/L_g profiles for E and S0 galaxies in Fig. 2 of García-Benito et al. (2019). We also assume that the light profiles of these galaxies are well-described by a $n \sim 4.5$ Sérsic profile (e.g., Mowla et al. 2018). Then, we calculate the mass profiles and half-mass radii in a similar fashion to our Method 1. We estimate that $r_{\rm mass}/r_{\rm light} \sim 0.55$ for $z = 0$ quiescent galaxies. This implies that color gradients may continue to evolve slightly below $z = 1$. By applying this color gradient correction to the effective radii of low-redshift galaxies (Figure 2.8), we can calculate the effect on galaxy size evolution: between $z \sim 2.5$ and $z \sim 0$, the half-mass radii of galaxies may grow by only $\lesssim$ half of the amount that galaxy half-light radii grow. However, we caution that this estimate is subject to large uncertainties— the data sets, sample selection, and methods used to calculate color gradients at $z \sim 0$ and $z > 1$ are substantially different. Careful future analysis is required to fully understand the growth of half-mass radii over cosmic time. In Chapter 3, we will calculate the half-mass radii of $0.25 < z < 1.0$ galaxies in the CANDELS fields using the same methods presented in this chapter. By using a uniform data set and methodology, we hope to understand in detail how quiescent galaxies grow over cosmic time.

The dependence of color gradient strength on redshift also has implications for star-forming galaxies: their half-mass radii at $M_* = 10^{10.5} M_\odot$ increase by only $1^{+16}_{-13}\%$ between $z = 1.25$ and $z = 2.25$, significantly less than the $37^{+20}_{-15}\%$ increase in their half-light radii. This may affect the nearly-linear scaling seen between the effective radii of galaxies and the virial radii of their host dark matter halos, and the resulting predictions for the redshift evolution of average disk effective radii (Kravtsov, 2013; Huang et al., 2017; Somerville et al., 2018). However, re-creating these abundance matching analyses using our catalog of half-mass radii is beyond the scope of this study.

We note that— like the $r_{\rm light} - M_*$ relations— the star-forming and quiescent $r_{\rm mass} - M_*$ relations converge at the highest masses. Even when using half-mass radii, it is impossible to tell massive quiescent galaxies apart from massive star-forming galaxies by size alone. It is tempting to interpret the high-mass convergence of the two relations as part of an evolutionary sequence: perhaps one path to quiescence involves galaxies growing along the

star-forming mass-size sequence until they reach a critical mass, after which they quench. This evokes the 'parallel track' galaxy evolution model proposed in van Dokkum et al. (2015). In Chapter 5, we will examine this in more depth by studying where galaxies with different rest-frame SED shapes lie in mass-size space, and how galaxies evolve through mass-size space to build up the star-forming and quiescent mass-size relations we see in Figure 2.7.

2.5 Additional tests of half-mass radius measurement techniques

How well does Method 1 recover half-mass sizes?

Here, we assess whether Method 1 has significant systematic biases in recovering the half-mass radii of small, low-mass, or high-redshift galaxies. We begin by taking the half-light radius, Sérsic index, annuli boundaries, and M/L gradient error bars for an observed galaxy in our sample. We use these quantities to model a hypothetical galaxy with a known half-mass radius: we assume that this galaxy has a 'true' M/L gradient parameterized as a power-law function of radius, and use the galaxy's light profile to calculate the resulting mass profile. We convolve this mass profile with the PSF and extract a convolved M/L gradient. To ensure that we have realistic error bars, we assume that the error bars on this convolved M/L gradient are the same as the error bars we measured for the real galaxy, with an unknown intrinsic M/L profile. We randomly perturb the convolved M/L gradient within these error bars to produce an 'as-observed' M/L gradient for this galaxy.

Then, we check how well Method 1 is able to recover the 'true' M/L gradient from the 'as-observed' M/L gradient. As described in Section 2.2, we perturb the galaxy's n and $r_{\rm e}$, generate a set of possible convolved-space M/L gradients, then use the χ^2 statistic to find the best-fit model. We then compare the recovered half-mass radius with the 'true' half-mass radius that we chose for this galaxy.

We repeat this test using the n, r_e, annuli boundaries, and M/L gradient error bars of every galaxy in our sample that lies in the COSMOS field. Additionally, for each galaxy we assume 27 different 'true' M/L gradient slopes covering the full range of M/L slopes we include in Method 1. Figure 2.9 shows the ratio of the recovered half-mass radius to the 'real' half-mass radius as a function of half-light radius, stellar mass, M/L gradient slope, redshift, and number of annuli. The scatter between the recovered and true half-mass radii is 0.1 dex, and the two measurements have an offset of < 0.001 dex. There does not appear to be any significant trend in how well we are able to recover the half-mass radii with either half-light radius, stellar mass, redshift, or number of annuli. There is a slight trend with M/L gradient such that the half-mass radii of galaxies with strongly decreasing M/L gradients are slightly more difficult to recover than those with strongly increasing M/L gradients; this ~ 0.05 dex effect does not significantly affect our measurements.

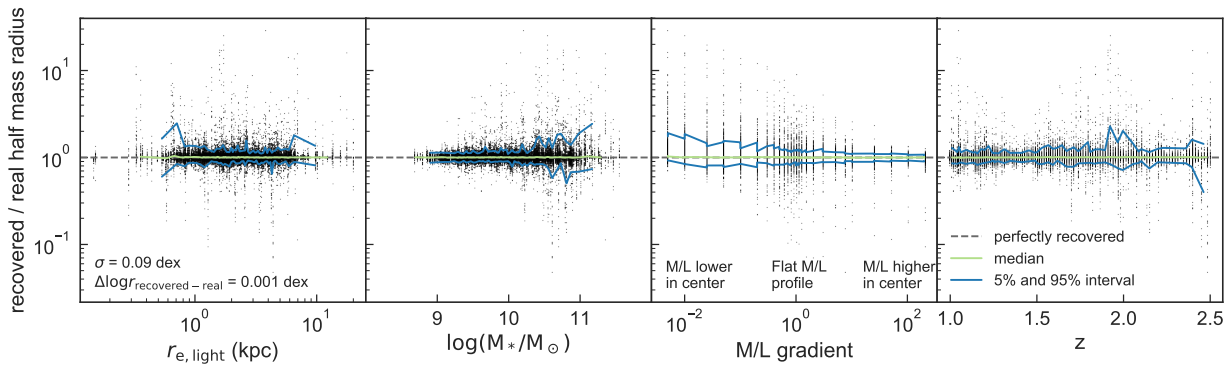

Figure 2.9: Ratio of recovered to real half-mass radius as a function of half-light radius, stellar mass, M/L gradient, redshift, and number of annuli. The grey dashed line indicates where the recovered and real half-mass radii are equal. The green line shows the running median, and the blue lines show the 5% and 95% confidence intervals. In general, the scatter in the recovered half-mass radii are quite low, and there do not appear to be significant biases in how well Method 1 is able to recover the half-mass radii of small, low-mass, low-S/N, or high-redshift galaxies. Thus, the trends shown in Figures 2.5 & 2.6 are not explained by biases in how well our methods are able to recover half-mass radii. It does appear that the half-mass radii of galaxies with strongly decreasing M/L gradients are slightly more difficult to recover than those with strongly increasing M/L gradients.

Do differences between Method 1 and Method 3 half-mass radii depend on galaxy properties?

In Figure 2.4, we show that the half-mass radii derived using three different methods generally agree. Here, we show in more detail that the differences between Method 1 and Method 3 half-mass radii do not depend on other galaxy properties.

Figure 2.10 shows the ratio of Method 1 to Method 3 half-mass radii as a function of other galaxy properties. While there is ~ 0.3 dex of scatter between the two methods of measuring half-mass radii, there are no significant trends with stellar mass, redshift, half-light radius, Sérsic index, or $U-V$ color. There is a slight trend with Σ_{eff}, such that Method 3 predicts higher half-mass radii than Method 1 for galaxies with higher Σ_{eff}. If Method 3 half-mass radii were used in Figure 2.5 instead of Method 1 half-mass radii, the trend with Σ_{eff} would be slightly less steep (but is still significant). All other trends would be essentially unchanged.

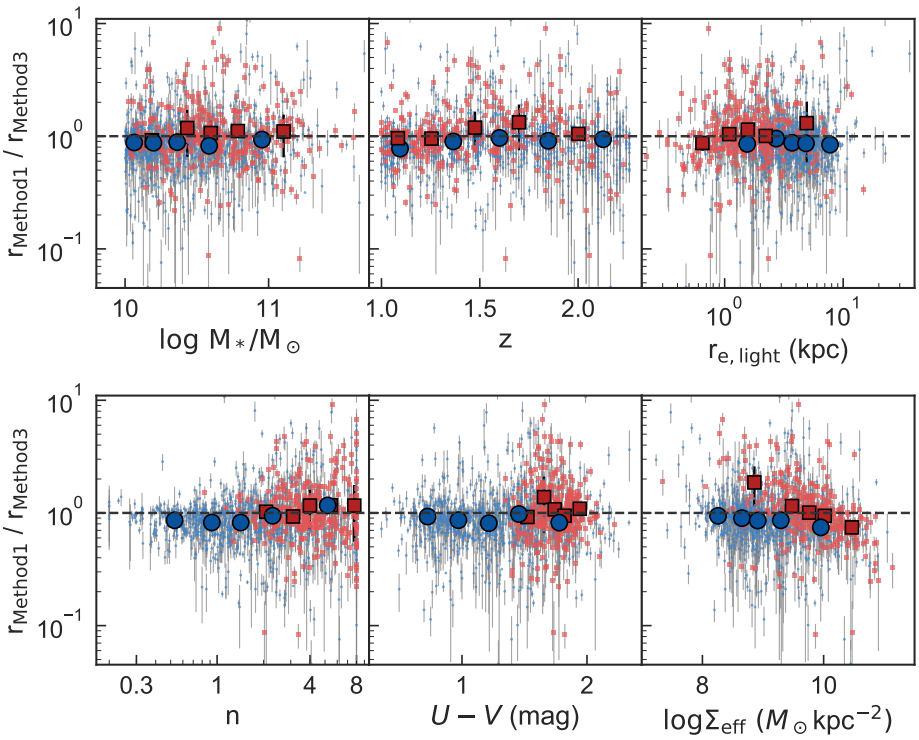

Figure 2.10: Ratio of Method 1 to Method 3 half-mass radii as a function of galaxy stellar mass, redshift, half-light radius, Sérsic index, $U-V$ color, and $\Sigma_{\rm eff}$. We include all galaxies with stellar masses above $10^{10} M_\odot$ to ensure the sample is complete at all redshifts. Light blue points and light red squares represent individual galaxies. Large blue circles and red squares represent error-weighted means. The points are binned such that each mean point represents an equal number of individual data points.

2.6 Summary

In this chapter, we present the largest study to date of galaxy color gradients and half-mass radii at $z > 1$. We have tested three different methods for recovering galaxy half-mass radii from multi-band imaging. Two methods use a spatially-resolved SED modeling technique inspired by Wuyts et al. (2012) to measure observed M/L gradients. We then account for the effects of the PSF in two separate different ways: the first method uses a simple forward modeling technique that assumes the instrinsic M/L gradient is a power-law function of radius, and the second technique uses `GALFIT` to fit a mass map of the galaxy. Our third and final method replicates the analysis of Szomoru et al. (2010, 2012, 2013) by using an intrinsic rest-frame color profile to infer a mass profile and half-mass radius. We find that all three methods produce remarkably consistent half-mass radii, with a scatter of 0.22 dex between the first two methods, and a scatter of ~ 0.3 dex between those two methods and

the Szomoru et al. (2010, 2012, 2013) method.

With galaxy half-mass radii in hand, we study the strength of galaxy color gradients—quantified by the ratio of half-mass to half-light radius $r_{\rm mass}/r_{\rm light}$— as a function of various galaxy properties. We find that in general, both star-forming and quiescent galaxies have negative color gradients, such that they are redder in the centers and bluer on the outskirts. This result agrees with previous studies at both $z \sim 0$ and $z > 1$. The strength of these color gradients is, however, found to be a function of other galaxy properties. These trends have not been seen before in studies of color gradients at $z > 1$; we are able to detect them due to our large sample size (more than an order of magnitude more galaxies than most previous studies) and large range of galaxy stellar masses. We find that color gradients become more strongly negative as galaxies become more massive, larger, and redder. Interestingly, these trends stretch across the star-forming and quiescent population smoothly without a clear bimodality. Furthermore, we measure significant evolution in the color gradient strength of both quiescent and star-forming galaxies as a function of redshift: color gradients are nearly flat at $z \gtrsim 2$, then decrease steadily as redshift decreases. In total, $r_{\rm mass}/r_{\rm light}$ decreases by ~ 0.3 dex between $z \sim 2$ and $z \sim 1$.

The observed trends appear consistent with the 'inside-out growth' scenario (Bezanson et al., 2009; Naab et al., 2009; Nelson et al., 2016b). Star-forming galaxies at these redshifts preferentially form stars in their outskirts; perhaps coupled with bulge growth, this would cause flat color gradients to become negative. Once galaxies quench and become quiescent, they grow their sizes via minor mergers, which introduce young and/or metal-poor stars to the galaxy outskirts; this also causes color gradients to decrease with time.

Finally, we used the dependence of $r_{\rm mass}/r_{\rm light}$ as a function of stellar mass and redshift to determine the effect of color gradients on the galaxy mass-size relation. Both the intercepts and the slopes of the quiescent and star-forming $r_{\rm mass} - M_*$ relations are smaller than those of the $r_{\rm light} - M_*$ relations. Moreover, we find that galaxy half-mass sizes grow *less rapidly* with redshift than half-light sizes: at $M_* = 10^{10.5} M_\odot$, the half-mass radii of star-forming and quiescent galaxies only grow by $0.04^{+0.42}_{-0.42}$ and $0.08^{+0.21}_{-0.20}$ kpc ($1^{+16}_{-13}\%$ and $8^{+29}_{-19}\%$) between $z = 2.25$ and $z = 1.25$, whereas their half-light radii grow by $1.17^{+0.42}_{-0.42}$ and $0.43^{+0.15}_{-0.15}$ kpc ($37^{+20}_{-15}\%$ and $47^{+25}_{-21}\%$).

Further work remains to be done to understand galaxy half-mass radii and color gradients at $z > 0$. In particular, in this study we are unable to determine the physical origin of galaxy color gradients, as we are not able to differentiate between the effects of age and metallicity. Dust is also a concern in this work: regions with very high attenuation may not be accounted for in any of the three methods we use, and our half-mass radii for very dusty galaxies should be treated with some caution. It is an open question whether the trends we see in color gradient strength as a function of redshift hold at lower or higher redshifts; examining color gradients over a wider redshift range could have further implications for the size growth of galaxies over cosmic time. Finally, the results presented here raise interesting questions as to how galaxies evolve and quench over the $1.0 < z < 2.5$ redshift range. In a future study, we will examine the color gradients and half-mass radii of galaxies as they transition from star-forming to quiescent.

Chapter 3

Half-mass radii of quiescent and star-forming galaxies evolve slowly from $0 \lesssim z \lesssim 2.5$: implications for galaxy assembly histories

The content of this chapter is drawn from Suess et al. (2019b), with permission from the co-authors.

In this chapter, we extend on our work in Chapter 2 by calculating the half-mass radii of both star-forming and quiescent galaxies down to $z \sim 0$. We use these measurements to probe the size evolution of galaxies— corrected for color gradients— across cosmic time.

3.1 Sample, methods, & galaxy half-mass radii

In this chapter, we present the evolution of galaxy half-mass radii from $z = 2.5$ to $z \sim 0$. From $1.0 \leq z \leq 2.5$, we use the sample of galaxy half-mass radii presented in Suess et al. (2019a). This high-redshift sample consists of 7,006 galaxies selected from the ZFOURGE photometric catalog (Straatman et al., 2016) to have $\log M_*/M_\odot > 9.0$, $\mathrm{S/N_K} \geq 10$, a use flag equal to one, a match in the 3D-HST catalog (Brammer et al., 2012; Momcheva et al., 2016; Skelton et al., 2014), and a convergent `GALFIT` fit (Peng et al., 2002; van der Wel et al., 2014).

Here, we expand our previous work by presenting the half-mass radii of an additional 9,543 galaxies at $z \leq 1.0$. This low-redshift sample consists of all galaxies in the 3D-HST photometric catalog with $z \leq 1.0$, $\log M_*/M_\odot > 9.0$, $\mathrm{S/N_{F160W}} \geq 10$, a use flag equal to one, and a convergent `GALFIT` fit. These selection criteria are equivalent to those of the higher-redshift sample presented in Suess et al. (2019a), but using the 3D-HST catalogs as opposed to the ZFOURGE catalogs. This allows us to include galaxies from the AEGIS

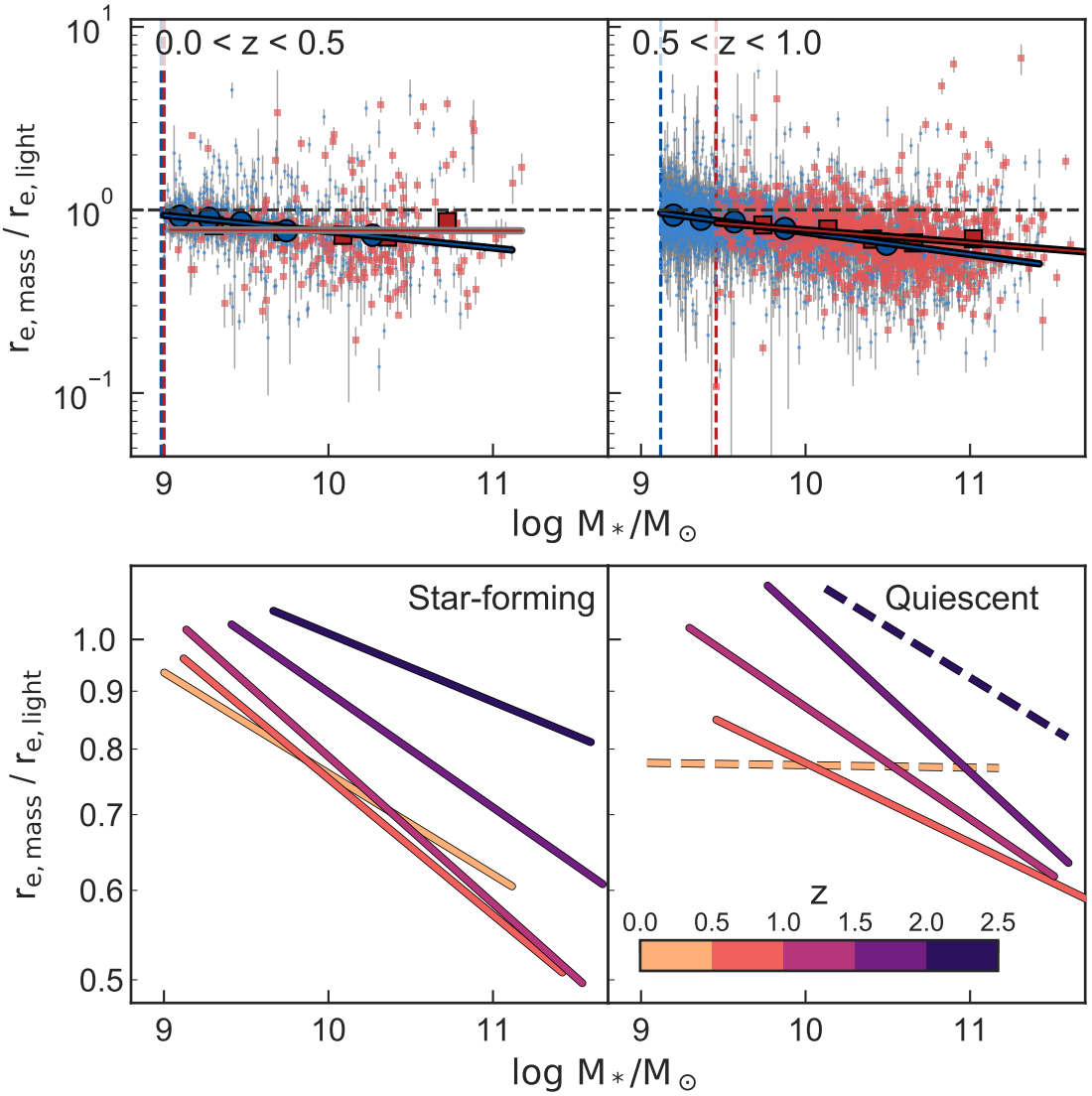

Figure 3.1: Top: color gradient strength as a function of stellar mass for two redshift intervals. Small light blue points and light red squares show individual star-forming and quiescent galaxies; large blue points and red squares show a running median. The blue and red lines show best-fit linear relations to each trend; lines are outlined in black if the slope of the relation is inconsistent with zero, and outlined in grey if the slope is consistent with zero. Dashed vertical blue and red lines show the mass completeness of the star-forming and quiescent samples. Bottom: best-fit relation between color gradient strength and stellar mass for star-forming (left) and quiescent (right) galaxies as a function of redshift. Dashed lines represent fits whose slopes are consistent with zero. We see clear redshift evolution in the best-fit color gradient-mass relations for both quiescent and star-forming galaxies.

and GOODS-N fields (not included in ZFOURGE) and better sample the $z \lesssim 0.5$ universe. Furthermore, we note that recovered galaxy properties at $z < 1$ do not change significantly with the inclusion of the ZFOURGE data: at these low redshifts, the medium-band filters in ZFOURGE no longer sample the Balmer break.

We calculate the half-mass radii of galaxies in the low-redshift sample following the methods of Suess et al. (2019a). In brief: we calculate aperture photometry in elliptical annuli for each galaxy in each band of PSF-convolved *HST* imaging (Skelton et al., 2014), then use FAST (Kriek et al., 2009) to model the resulting spatially-resolved spectral energy distributions (SEDs). This method produces an as-observed M/L profile for each galaxy. We correct for the effects of the point spread function with a simple forward modelling technique which assumes that that the intrinsic M/L profile is a power-law function of radius. We then use the best-fit intrinsic M/L profile in conjunction with the galaxy's light profile and the point spread function to find the half-mass radius. Full details of this method and comparisons with other techniques for measuring half-mass radii are presented in Suess et al. (2019a). Suess et al. (2019a) also shows that the half-mass radii recovered using our technique are not significantly biased by the galaxy's half-light radius, stellar mass, or redshift.

In Figure 3.1, we show the strength of galaxy color gradients (i.e., $r_{\rm e,mass}/r_{\rm e,light}$) as a function of stellar mass for two redshift slices in our new low-redshift sample. We divide the sample into star-forming and quiescent populations using the UVJ diagram and the quiescent definition from Whitaker et al. (2012a). In Suess et al. (2019a), we found that there was a significant trend between color gradient strength and stellar mass for galaxies at $1.0 \leq z \leq 2.5$. Here, we find that this trend continues to lower redshifts. The only exception is in the lowest-redshift quiescent bin, where our sample is quite small. In the lower panels of Figure 3.1, we also show how the best-fit relation between $r_{\rm e,mass}/r_{\rm e,light}$ and stellar mass varies as a function of redshift for our full $0 \lesssim z \leq 2.5$ sample.

In Figure 3.2, we show the median strength of color gradients for all galaxies with $\log M_*/M_\odot > 10.1$, the completeness limit of our full sample. In Suess et al. (2019a), we showed that the strength of galaxy color gradients decreases sharply between $z \sim 2.5$ and $z \sim 1$. Here we find that this evolution may flatten below $z \sim 1$; $r_{\rm e,mass}/r_{\rm e,light}$ for both quiescent and star-forming galaxies remains roughly constant at a value of ~ 0.7.

3.2 The growth of quiescent galaxies is consistent with minor merger predictions

Over the past decade, numerous studies have assessed how merger-driven inside-out growth and progenitor bias can contribute to the size evolution of quiescent galaxies (e.g., Bezanson et al., 2009; van de Sande et al., 2013; Hopkins et al., 2009; Carollo et al., 2013; Poggianti et al., 2013; Williams et al., 2017; Damjanov et al., 2019). Several studies— notably Newman et al. (2012) and Belli et al. (2015)— attempt to tease out the relative contributions of these

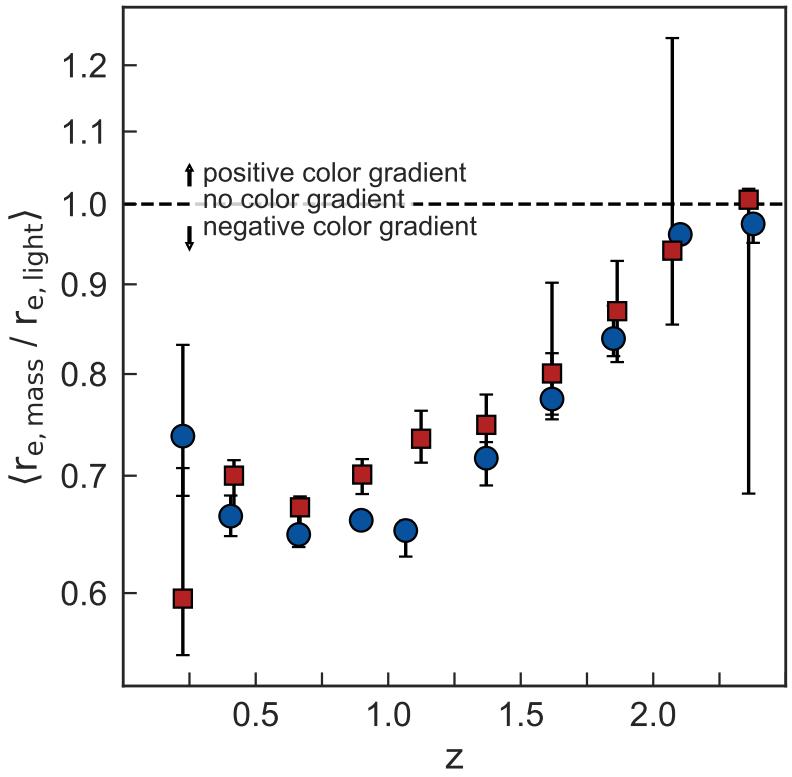

Figure 3.2: Median half-mass to half-light radius ratio for star-forming and quiescent galaxies (blue circles and red squares) as a function of redshift. $r_{\rm mass}/r_{\rm light}$ traces the strength of radial color gradients; values less than one indicate negative color gradients, where the center of the galaxy is redder than the outskirts. Only galaxies with $\log M_*/M_\odot > 10.1$, where our sample is complete, are included. Error bars show the central 68% of 500 bootstrap samples. The strong color gradient evolution previously observed at $z \gtrsim 1$ appears to flatten at $z \lesssim 1$.

two growth mechanisms. Newman et al. (2012) studied the merger rates of galaxies in the CANDELS survey and calculated the resulting effect on galaxy sizes. They found that while minor mergers could explain the relatively slow growth in half-light radii at $z \sim 1$, minor mergers were *insufficient* to explain the much more rapid growth at $z \sim 2$. In a similar vein, Belli et al. (2015) infer the star formation histories of quiescent galaxies and reconstruct the size evolution of the quiescent population. They find that both individual growth and progenitor bias must contribute (in roughly equal proportions) to the observed increase in the half-light radii of quiescent galaxies. Both individual and population growth seem to be necessary to explain the increase in quiescent galaxy sizes, especially at early times when half-light radii grow very rapidly. However, both of these studies used half-light radii to study quiescent size growth; here, we use half-*mass* radii to account for the bias due to

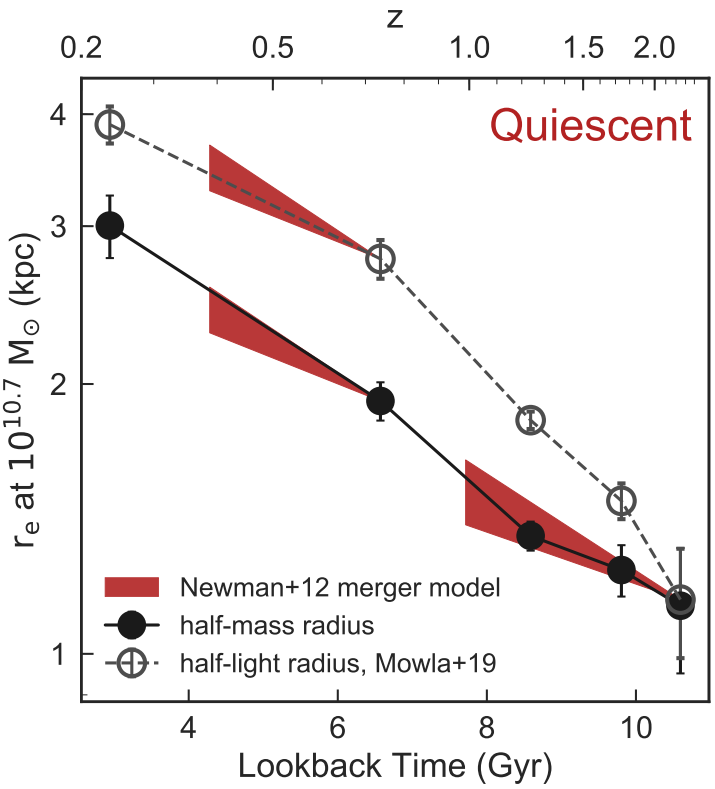

Figure 3.3: Half-light radius (open grey points) and half-mass radius (filled black points) of quiescent galaxies at $10^{10.7} M_\odot$ as a function of lookback time. Red shaded regions show the expected growth via minor mergers using the Newman et al. (2012) models, assuming a merger timescale of $\tau_e = 1.0$ Gyr. Minor mergers alone are sufficient to explain the growth of half-mass radii.

evolving color gradients.

In Figure 3.3, we show the evolution of the half-light and half-mass radii of quiescent galaxies at $M_* = 10^{10.7} M_\odot$. The grey curve shows the half-light radius evolution, with data taken from Mowla et al. (2019b). The black curve shows the evolution of quiescent half-*mass* radii at the same stellar mass. The half-mass radius data points are calculated by multiplying our best-fit relation for $r_{\rm e,mass}/r_{\rm e,light} - M_*$ (Figure 3.1) by the Mowla et al. (2019b) $r_{\rm e,light} - M_*$ relations, as described in more detail in Suess et al. (2019a). While the half-mass and half-light radii of massive quiescent galaxies are nearly equal at $z = 2.25$, half-mass radii grow much less rapidly than half-light radii do.

We compare this size evolution to the Newman et al. (2012) predictions for quiescent galaxy growth via minor mergers. Like Newman et al. (2012), we assume a merger timescale $\tau_e = 1.0$ Gyr. The shaded red region in Figure 3.3 shows this model; the width represents

the measured uncertainty in the merger fraction. Between $z = 2.25$ and $z = 1$, this data-based model predicts that minor mergers cause galaxy sizes to grow by (0.12 ± 0.04) dex. As identified by previous works, minor mergers alone cannot explain the 0.28 dex increase in galaxy half-light radii found over the same redshift range. However, the growth in half-mass radii (which we measure to be 0.14 dex) is fully consistent with a model that includes minor mergers *alone*. No additional mechanism for size growth at high redshift is necessary to explain the observed half-mass radius evolution. Between $z = 0.75$ and $z = 0.4$, the Newman et al. (2012) model predicts a size increase of (0.10 ± 0.04) dex due to minor mergers. Observed half-light radii grow by 0.10 dex, and observed half-mass radii grow by 0.14 dex; both are consistent with the data-based merger growth model. As discussed in Suess et al. (2019a), our observed color gradient evolution at high redshift also supports an inside-out growth or two-phase formation scenario (Naab et al., 2009; Oser et al., 2010): minor mergers deposit bluer stars at the outskirts of the galaxy, creating negative color gradients. As redshift decreases and galaxies experience more minor mergers, these color gradients become stronger.

We note that in Figure 3.3 we invoke a fast merger timescale of $\tau_e = 1.0$ Gyr. A slower merger timescale would decrease the amount of size growth that minor mergers can account for. In this case, there would still be additional growth in quiescent half-mass radii that must be accounted for by progenitor growth. A careful study of the half-mass radii of the smallest quiescent galaxies over time (e.g., Carollo et al., 2013), potentially in combination with stellar abundance studies (e.g., Kriek et al., 2016, 2019), is required to fully understand how much progenitor bias contributes to quiescent half-mass radius growth.

3.3 The slow growth of star-forming galaxies is inconsistent with simulations

We now examine the growth of star-forming galaxies when including the effects of color gradients. Figure 3.4 shows how the half-light and half-mass radii of star-forming galaxies evolve. The overall picture is similar to quiescent galaxies: star-forming galaxies have roughly equal half-mass and half-light radii at early times; however, half-mass radii evolve much more slowly than half-light radii. This shallow size evolution is supported by spatially-resolved spectral studies: low- and intermediate-mass star-forming galaxies at $z \sim 2$ have nearly flat sSFR profiles, implying self-similar growth and thus slow size evolution (Tacchella et al., 2015a,b; Nelson et al., 2016b).

Many cosmological simulations and semi-analytic models predict the size evolution of star-forming galaxies based on their mass distributions. Interestingly, the evolution of these simulated half-mass radii generally matches the observed half-*light* radius evolution, not the slower half-mass radius evolution we show in Figure 3.4. Hence, the simulations predict a much stronger evolution in star-forming half-mass radii than our observations. For example, Furlong et al. (2017) show that the predicted half-mass radii of disk galaxies in the EAGLE

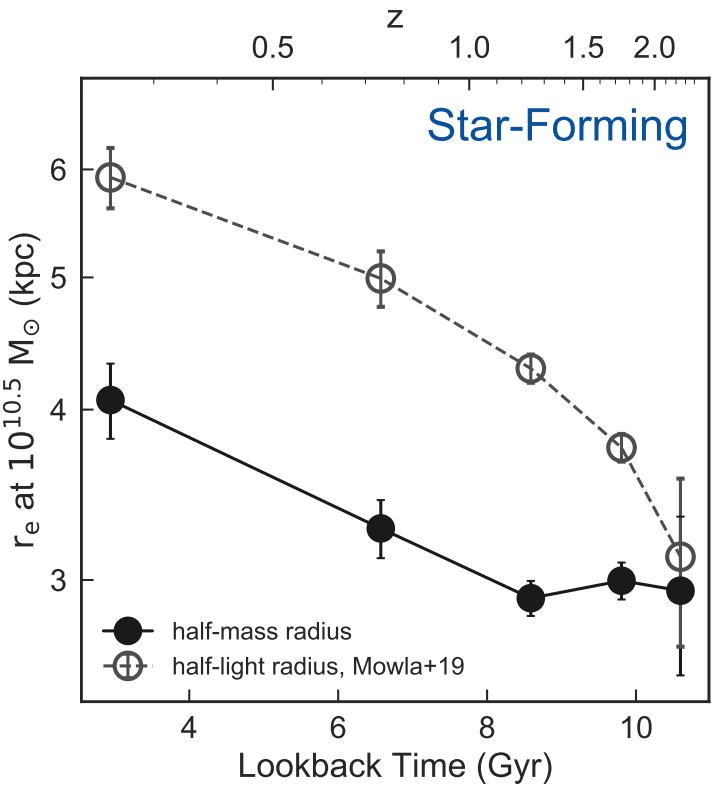

Figure 3.4: Half-light radius (open grey points) and half-mass radius (filled black points) of star-forming galaxies at $10^{10.5} M_\odot$ as a function of lookback time. Half-mass radii evolve much less rapily than half-light radii.

simulations are consistent with observed half-light radii within $\lesssim 0.1$ dex; their modeled half-mass radii show a similar redshift evolution as the van der Wel et al. (2014) half-light radius observations. The half-mass radii of galaxies in Illustris-TNG also evolve at a similar rate as observed half-light radii (Genel et al., 2018). The semi-analytic model of Dutton et al. (2011) predicts the evolution of disk sizes as well as the strength of color gradients in disk galaxies; their half-mass radius evolution is generally consistent with observations of half-light radii, not with our observed half-mass radii.

Several physical processes could account for this discrepancy between simulated and observed half-mass radii. Dutton & van den Bosch (2009) found that including feedback in semi-analytic models slows down the expected size evolution of disk galaxies. If the effects of feedback were slightly stronger— or the physics of feedback was slightly different— it may be possible to further slow the modeled evolution of star-forming half-mass radii and bring them in line with our observations. Higher merger rates at high redshift could also weaken the evolution of simulated disk sizes. Additional explanations for this discrepancy—

which could apply to measurements of half-mass radii for both star-forming and quiescent galaxies— are discussed in more detail below.

3.4 Discussion

In general, most modern simulations predict both the mass distributions *and* the light distributions of model galaxies, then report half-light radii which can be directly compared to observations. The measured half-light radius evolution of both star-forming and quiescent galaxies from these simulations is in good agreement with observations: the half-light radii typically agree to within $0.1 - 0.25$ dex (Somerville et al., 2008; Dutton et al., 2011; Price et al., 2017; Genel et al., 2018). This is particularly interesting in light of our results: first, if the modeled half-light radii agree with observations while the modeled half-mass radii do not (Section 3.3), then both the half-mass radii *and* the color gradients in the simulations may differ from what we observe; second, because these simulations *already* include color gradients, these simulated color gradients can now be directly compared with our new color gradient measurements.

To date, very few studies have discussed color gradients in simulated galaxies. Dutton et al. (2011) used a semi-analytic model of disks evolving within dark matter halos to compare observed and simulated galaxy scaling relations. They report both half-mass radii and half-light radii in several different filters. Color gradients in their simulated galaxies seem to evolve less rapidly than our observations, decreasing by only ~ 0.1 dex between $z = 2.5$ and $z = 0.25$; over the same redshift range, our measured color gradients decrease by ~ 0.3 dex. The Dutton et al. (2011) model did not, however, account for the effects of dust or mergers. Both dust and mergers can affect the strength of color gradients in galaxies, and their inclusion in the Dutton et al. (2011) models would likely change how their simulated color gradients evolve. There are no studies which examine color gradient strength or evolution in modern high-resolution cosmological simulations. Such studies would provide an invaluable comparison to our recent observations, and allow us to more fully contextualize our findings.

Such a comparison of simulated and observed half-mass radii and color gradients— while necessary— will also be difficult. There are a host of choices to make when analyzing simulations that complicate a direct comparison with observations. Aperture effects can bias galaxy sizes by ~ 0.1 dex, and varying the viewing angle can change the inferred half-light size by $\sim 0.1 - 0.2$ dex (Price et al., 2017). Even the total stellar mass of the galaxy— and thus its location in the mass-size diagram— can change based on how far out the mass profile is integrated (causing variations of $0.1 - 0.2$ dex; Genel et al., 2018) and/or differences in the stellar mass loss prescription used by the simulation and by the stellar population synthesis modeling of the observations (e.g., Price et al., 2017). Selection effects may also play a role: our observations compare the sizes of star-forming and quiescent galaxies at fixed mass, but if these populations evolve differently in the simulations (e.g., if galaxies quench at a different rate), then the galaxy populations will differ between the observations and simulations. To perform a fair comparison between observations and simulations, it is

thus necessary to analyze mock observations of the simulations using the *same techniques* that are used for the real observations Price et al. (see 2017).

Finally, we note that measuring color gradients and half-mass radii from observed data is difficult; we refer the reader to Suess et al. (2019a) for a full discussion of the sources of possible biases in our measurements. In particular, it is difficult to account for the most highly dust-obscured star formation with our methods. Measurements at longer wavelengths (with ALMA, e.g. Barro et al., 2017a), are crucial to understand the mass profiles of such obscured systems.

3.5 Summary

In this chapter, we extended the Suess et al. (2019a) analysis of color gradients and half-mass radii of both star-forming and quiescent galaxies to $z \sim 0$. This data set, together with our previous results, represents the largest collection of galaxy half-mass radii at $z > 0$ in the literature. This large sample of half-mass radii, calculated in a uniform way across a wide range of redshifts and stellar masses, allows us to conduct a detailed examination of how the half-mass sizes of galaxies grow over cosmic time.

We find that color gradients in both star-forming and quiescent galaxies evolve between $z = 2.5$ and $z \sim 0$. When taking these color gradients into account, the sizes of both star-forming and quiescent galaxies grow much less rapidly than previously found. For quiescent galaxies, the evolution of half-mass radii is fully consistent with the expected growth due to minor mergers *alone* (Figure 3.3) based on the observed merger rates of Newman et al. (2012) and assuming a relatively fast merger timescale of 1 Gyr. A slower merger timescale would allow additional room for progenitor bias to contribute to the growth of quiescent galaxies. For star-forming galaxies, the evolution of half-mass radii is much slower than predicted by cosmological simulations and semi-analytic models, and raises questions as to the physical mechanisms responsible for this slow size growth.

Further work is required to reconcile these new observational results with the apparent consensus in the literature. For quiescent galaxies, the magnitude of growth due to progenitor bias is still not fully understood; this may be addressed by detailed examinations of the half-mass radii of the smallest galaxies over cosmic time (as in Carollo et al., 2013; Poggianti et al., 2013). The slow size evolution of star-forming galaxies is more challenging to address, as it is in tension with available theoretical predictions. Additional work to understand the effects of feedback and mergers on half-mass radii and color gradients is required to address this discrepancy. Finally, studies that directly compare half-mass and half-light radii in cosmological simulations in a consistent manner as the observations (e.g. Price et al., 2017) are essential to understand the origins and impacts of our observed evolving color gradients.

Chapter 4

Color gradients along the quiescent sequence: clues to quenching & structural growth

The content of this chapter is drawn from Suess et al. (2020), with permission from the co-authors.

In Chapters 2 & 3, we divided the galaxy population into just two groups, star-forming and quiescent. While this allowed us to study the size evolution of these two populations, it does not allow us to investigate *why* galaxies shut down their star formation and join the quiescent population. In this chapter, we study the sizes and color gradients of quiescent galaxies as a function of their age. This allows us to investigate whether younger quiescent galaxies are truly smaller than their older quiescent counterparts, and provides clues as to the mechanisms responsible for quenching galaxies.

4.1 Sample & methods

In this study, we use the Suess et al. (2019a) catalog of color gradients and half-mass radii of galaxies at $1.0 \leq z \leq 2.5$ in three CANDELS fields (Grogin et al., 2011; Koekemoer et al., 2011). These measurements were made by fitting spatially-resolved spectral energy distributions (SEDs) to find an observed-frame mass-to-light ratio (M/L) gradient. Then, a forward modeling technique was used to account for the point-spread function and recover intrinsic M/L gradients and half-mass radii.

We select 385 quiescent galaxies from the Suess et al. (2019a) catalog using the Whitaker et al. (2012a) definition for quiescence based on rest-frame UVJ colors. We only include galaxies with $\mathrm{M}_* > 10^{10.1} M_\odot$, where our sample is mass-complete (Suess et al., 2019a). Our sample lies in the overlap of the CANDELS and ZFOURGE (Straatman et al., 2016) fields, allowing for accurate measurements of both mass profiles and rest-frame SEDs.

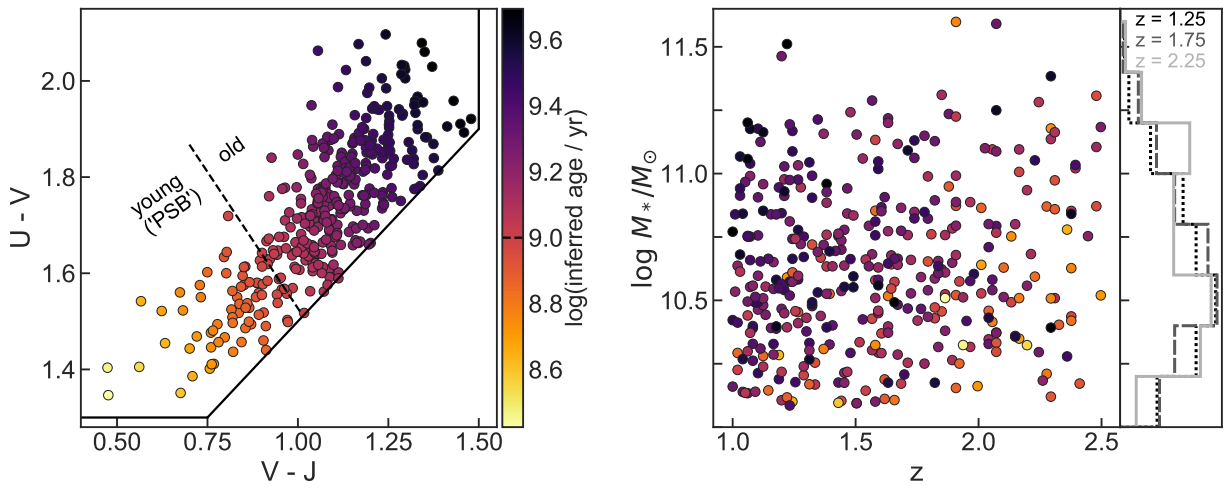

Figure 4.1: UVJ diagram (left) and stellar mass as a function of redshift (right) for our quiescent galaxy sample. Each galaxy is colored by its inferred stellar age using the Belli et al. (2019) mapping from UVJ colors to ages. Histograms show the normalized distribution of stellar masses in the three redshift bins used in this work. We only include quiescent galaxies with $M_* > 10^{10.1} M_\odot$, where our sample is complete.

Our study also requires estimates of the age of each galaxy. We use the Belli et al. (2019) prescription, who use deep continuum spectroscopy of quiescent galaxies to calibrate a mapping between UVJ colors and average stellar ages. Systematic uncertainties on ages calculated using this method are $\sim$ 0.13 dex. We refer to the youngest quiescent galaxies as "post-starburst" galaxies; however, see e.g. Wild et al. (2020) for a discussion of spectroscopically- versus photometrically-selected post-starburst galaxies.

Figure 4.1 shows our sample in UVJ and mass-redshift space. Each galaxy is colored by its inferred stellar age using the Belli et al. (2019) technique.

4.2 Sizes & color gradients of quiescent galaxies as a function of age

We begin by examining the size-mass relation for galaxies along the quiescent sequence. The left panel of Figure 4.2 shows the size-mass relation using half- light radii at rest-frame 5,000Å (van der Wel et al., 2014). Large points show the median sizes of both old (inferred age >1 Gyr) and young or 'post-starburst' (inferred age <1 Gyr) quiescent galaxies in bins of stellar mass. We recover the result that post-starburst galaxies have smaller half-light radii than older quiescent galaxies (Whitaker et al., 2012a; Belli et al., 2015; Yano et al., 2016; Almaini et al., 2017; Maltby et al., 2018; Wu et al., 2018; Belli et al., 2019). As noted

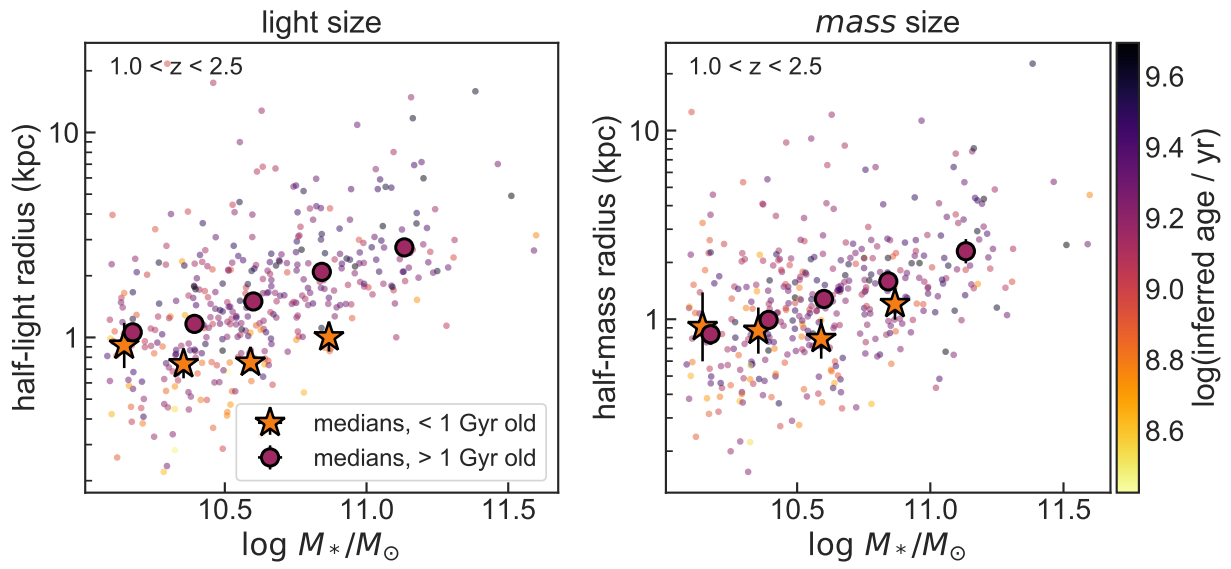

Figure 4.2: Half-light (left) and half-mass (right) radius as a function of stellar mass for quiescent galaxies at $1.0 \leq z \leq 2.5$. Points represent individual galaxies, colored by inferred age. Large purple circles and yellow stars show medians for old (age $>$ 1 Gyr) and young (age $\leq$ 1 Gyr) quiescent galaxies; medians are only shown for bins with ≥ 5 galaxies. While there is a 0.3 dex difference in the median half-light radii of young and old quiescent galaxies, this difference is reduced to only $\sim$0.1 dex when considering half-mass radii.

by Almaini et al. (2017), this size difference is especially apparent at $M_* > 10^{10.5} M_\odot$.

The right panel of Figure 4.2 shows the size-mass relation for the same sample, this time using half-*mass* radii. The stark difference between the sizes of young and old quiescent galaxies disappears. While young quiescent galaxies have median half-light radii 0.3 dex smaller than their older counterparts, the difference in their median half-mass radii is only $\lesssim$0.1 dex.

We note that the large difference in the half-light radii of young and old quiescent galaxies is partially a redshift effect: the post-starburst galaxies in our sample have a slightly higher median redshift, and thus smaller half-light radii. However, our general result holds in narrow redshift slices: post-starburst galaxies have smaller half-light radii than older quiescent galaxies, but their half-mass radii are essentially consistent.

The fact that the difference between young and old quiescent galaxy sizes significantly shrinks when using half-mass radii is an indication that the two populations have systematically different color gradients. In Figure 4.3, we show color gradient strength versus galaxy age. Following Suess et al. (2019a,b), we quantify color gradient strength by the log ratio of the half-mass and half-light radii of the galaxy: negative (positive) values indicate that the center of the galaxy is redder (bluer) than the outskirts. We show three redshift slices,

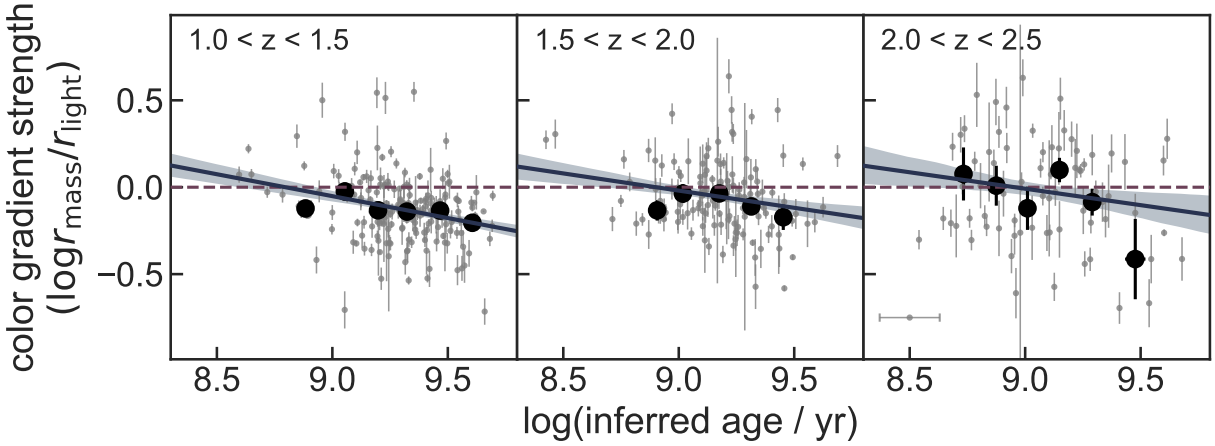

Figure 4.3: Color gradient strength as a function of inferred age for quiescent galaxies ($M_* \geq 10^{10.1} M_\odot$) in three redshift bins. Small grey points represent individual galaxies, black circles are median age bins, and the blue line and shaded region show a best-fit linear relation (and 1σ confidence interval, determined by bootstrap resampling) to the individual points. Typical uncertainties in inferred ages are shown by the error bar in the lower left of the right panel. The dashed purple line denotes no color gradient; values above (below) this line indicate bluer (redder) centers. There is a clear trend between color gradient strength and age, such that older galaxies have stronger color gradients. The slope of the relation is consistent across redshift. Spearman's ρ (p-values) for each redshift interval are -0.26 (< 0.001), -0.20 (0.02), and -0.14 (0.25).

because color gradient strength varies with redshift (Suess et al., 2019a,b).

At all redshifts, there is a clear relation between color gradient strength and inferred age. A Spearman correlation test indicates that this trend is statistically significant in the two lower-redshift intervals; flatter color gradients and larger error bars on individual galaxies likely contribute to the larger p-value in the highest redshift bin. We fit this color gradient-age relation with LEO-Py, including systematic errors on inferred ages and intrinsic scatter around the relation (Feldmann, 2019). We find that young quiescent galaxies have nearly flat color gradients. This result agrees with Maltby et al. (2018), who found that the optical and near-infrared sizes of post-starburst galaxies are similar. Galaxies with older stellar ages have increasingly more negative color gradients, with redder centers and/or bluer outskirts. The slope of the best-fit relation is consistent across redshift, while the normalization decreases towards lower redshift (consistent with Suess et al., 2019a).

Because color gradients tend to be stronger in more massive galaxies (e.g. Tortora et al., 2010; Suess et al., 2019a) and the older galaxies in our sample have higher median stellar masses, we test whether the trend between color gradient strength and galaxy age is a reflection of the color gradient - mass relation. The trend we see in Figure 4.3 persists in

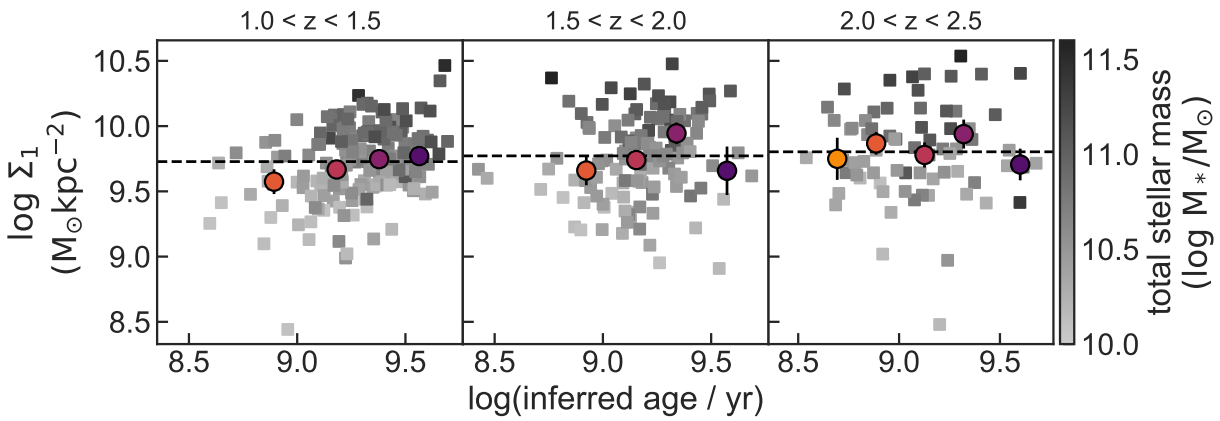

Figure 4.4: Mass density in the central kiloparsec of the galaxy, Σ_1, as a function of inferred age in three redshift bins. Squares show individual galaxies, shaded by total stellar mass; colored circles represent median bins in age. The dashed black line shows the median Σ_1 of all galaxies in a given redshift bin. While Σ_1 depends on total stellar mass (especially evident in the lowest-redshift bin), it varies only slightly with redshift, and does not depend on stellar age. This supports the idea that galaxies quench with consistently high Σ_1.

mass-matched subsamples, with a consistent slope; this indicates there is a relation between color gradient and age even at fixed mass. We also test whether there is a correlation between residuals in the color gradient-mass relation and residuals in the age-mass relation (e.g. Salim et al., 2015; Sanders et al., 2018). We find that there is a statistically significant trend between the two sets of residuals at all redshifts, further emphasizing that the trend between color gradient strength and age we see in Figure 4.3 is not purely a mass effect.

Together, Figures 4.2 and 4.3 indicate that the observed difference between the half-light radii of young and old quiescent galaxies is *not* a true difference in their sizes: instead, it is a systematic difference in their color gradients. Older quiescent galaxies have negative color gradients, making them appear larger than they truly are; meanwhile, young quiescent galaxies have flat color gradients, and appear their 'true' size. This systematic difference in color gradient strength results in older quiescent galaxies *appearing* larger than post-starburst galaxies, even though their half-mass radii differ by at most ~ 0.1 dex.

4.3 Central densities of quiescent galaxies as a function of age

We now turn to the mass profiles of galaxies along the quiescent sequence. Previous studies have found that quiescent galaxies have consistently high central mass densities, implying that the build-up of a dense central core is a prerequisite for quenching (e.g. Cheung et al.,

2012; Fang et al., 2013; van Dokkum et al., 2014; Tacchella et al., 2015a; Barro et al., 2017b; Whitaker et al., 2017b; Mosleh et al., 2017). We calculate the central mass surface density, $\Sigma_1 \equiv \mathrm{M}_{*,r<1kpc}/\pi$, from the Suess et al. (2019a) mass profiles. In Figure 4.4 we show Σ_1 as a function of inferred age.

While the central mass densities of quiescent galaxies clearly depend on total stellar mass, at fixed mass Σ_1 is remarkably consistent across age and redshift. We find a best-fit relation[1] of

$$\begin{aligned}\log \Sigma_1 =&(9.40 \pm 0.06) + (0.69 \pm 0.03)(\log M_*/M_\odot - 10.5) \\ &+ (0.78 \pm 0.17) \log (1+z) \\ &+ (-0.03 \pm 0.04)(\log \mathrm{age/yr} - 9.5)\end{aligned} \tag{4.1}$$

Previous studies have found a dependence of $\Sigma_1 \propto (M_*/M_\odot)^{0.64}$ (Fang et al., 2013; Barro et al., 2017b; Saracco et al., 2017; Tacchella et al., 2017), consistent with our fit within 1σ error bars. Both Barro et al. (2017b) and Mosleh et al. (2017) calculated slightly shallower redshift evolution, $\Sigma_1 \propto (1+z)^{0.55-0.68}$, but again the values are consistent within 1σ errors. We note that the redshift evolution we find is still relatively slow, and indicates that Σ_1 decreases by only ~ 0.13 dex between our highest and lowest redshift bin.

We find that the dependence of Σ_1 on galaxy age is consistent with zero (Equation 4.1, Figure 4.4). This implies that more compact galaxies do *not* quench earlier: in that case, older galaxies at fixed mass would have higher Σ_1. We note that the most massive galaxies quench first (e.g., Cowie et al., 1996), and more massive galaxies tend to have higher Σ_1. This effect fully accounts for the slight trend of increasing Σ_1 in older and more massive galaxies in our $1.0 \leq z \leq 1.5$ bin, and suggests that the results of Saracco et al. (2017)— who find that older and more massive galaxies have higher Σ_1— are driven by mass, not age, effects.

While we find that Σ_1 depends on stellar mass and redshift but not age, Estrada-Carpenter et al. (2020) find that Σ_1 depends on stellar mass and formation redshift. These two interpretations are not inconsistent: Σ_1 is highest in massive galaxies that form early in the universe, but does not appear to evolve as galaxies age after quenching.

Tacchella et al. (2017) find that older galaxies at fixed mass have higher Σ_1, inconsistent with our results. However, their study was performed at $z = 0.05$: this discrepancy may reflect differences in quenching mechanisms or the properties of recently-quenched galaxies at $z > 1$ and $z \sim 0$ (e.g. Maltby et al., 2018).

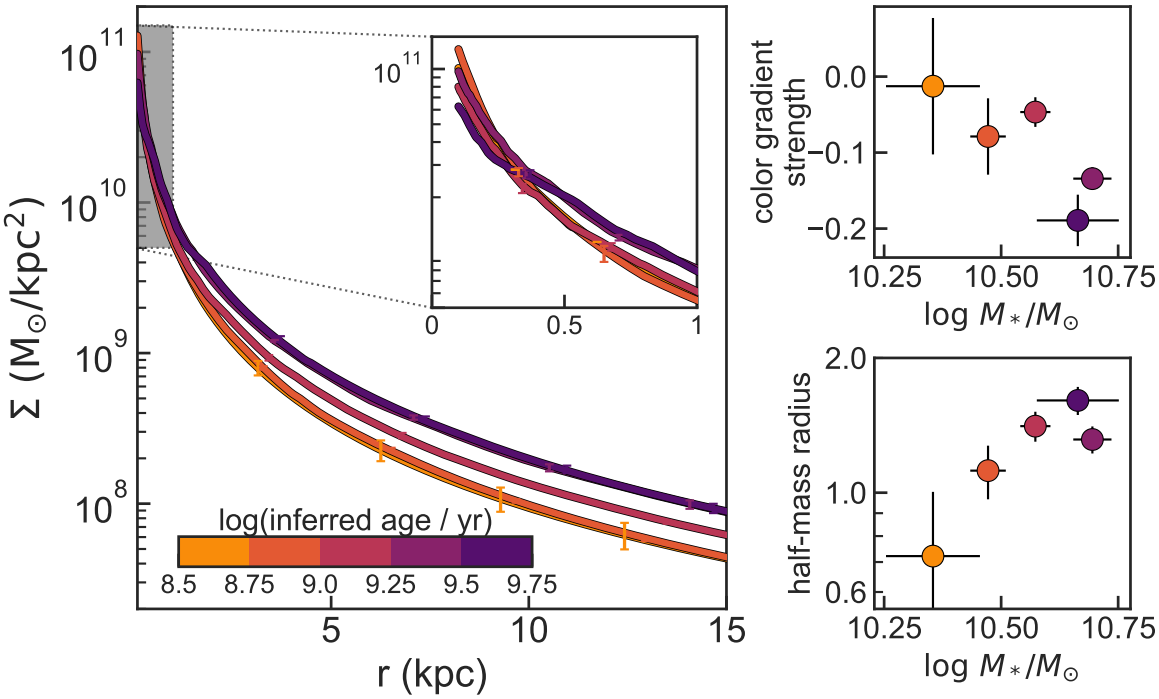

Figure 4.5: Left: mass profiles of quiescent galaxies ($1.0 \leq z \leq 2.5$) split into age bins. The central mass profiles are similar across age; extra mass in older galaxies is deposited mostly in the wings. Right: median color gradient strength ($\log r_{\rm mass}/r_{\rm light}$, top) and half-mass radius (bottom) as a function of median stellar mass for the same age bins. color gradients are flatter in younger galaxies; the older galaxies in our sample are also generally more massive (and thus larger).

4.4 Discussion

In this Chapter, we investigate the half-mass radii, color gradients, and central mass densities of $1.0 \leq z \leq 2.5$ quiescent galaxies as a function of age. We find that post-starburst galaxies are *not* significantly smaller than older quiescent galaxies of the same stellar mass; they only appear smaller because they have systematically flatter color gradients (Figures 4.2 & 4.3). At the same time, we see that post-starburst galaxies are compact, with central mass densities consistent with those of older quiescent galaxies of the same mass (Figure 4.4).

These observations can help address two separate questions: what mechanism caused

[1]This least-squares fit was performed using the python `lmfit` package for consistency with Fang et al. (2013) and Barro et al. (2017b) in order to facilitate a direct comparison of the results. A LEO-Py fit including systematic error bars on the independent variables as well as intrinsic scatter around the relation finds a slightly steeper mass dependence and slightly shallower redshift dependence, consistent with the `lmfit` results within 1.5σ.

post-starburst galaxies to stop forming stars? And how do quiescent galaxies evolve after they quench? To place our observations in context, Figure 4.5 shows the median mass profiles, color gradients, and half-mass radii of all quiescent galaxies in our sample, binned by age. Each binned point includes galaxies across our full mass and redshift range. We bin across redshift because neither half-mass radii nor Σ_1 evolve significantly over our $1.0 \leq z \leq 2.5$ range (Eqn 4.1; Suess et al., 2019b). However, we note that the older quiescent galaxies in our sample are also more massive; therefore, each age bin probes a different stellar mass. This is not simply selection bias: our sample is complete to the same mass limit in each redshift bin (Figure 4.1).

First, we consider how post-starburst galaxies halt their star formation. If slow or gradual processes such as gas exhaustion are responsible, we would expect the sizes, structures, and color gradients of post-starburst galaxies to resemble those of their progenitors. However, we see in Figures 4.3 and 4.5 that post-starburst galaxies have flat color gradients, while Suess et al. (2019a) found that star-forming galaxies at similar masses and redshifts typically have negative color gradients. Because color gradients indicate radial variations in the underlying stellar populations, in order to alter the color gradients in a galaxy some physical process must either create new stellar populations or re-arrange existing ones. Candidate processes include mergers— which could flatten or destroy radial color gradients— or a central starburst, which could create an excess of young stars at the center of the galaxy and flatten a pre-existing negative color gradient. Both of these processes are popular candidates for the fast quenching process, whereby galaxies rapidly build a massive core before shutting off their star formation (e.g., Zolotov et al., 2015; Tacchella et al., 2015a; Barro et al., 2017b; Woo & Ellison, 2019).

Second, we turn to the question of how galaxies evolve after they quench. In Figures 4.3 and 4.5 we see that older and more massive galaxies also have stronger negative color gradients; this indicates that some process must re-establish negative color gradients after quenching. At the same time, we see that the shapes of their mass profiles change (left, Figure 4.5) and their half-mass radii grow (bottom right, Figure 4.5). Older quiescent galaxies have slightly less centrally-peaked mass profiles, potentially due to post-quenching adiabatic expansion (e.g., Choi et al., 2018) or dynamical friction from mergers (e.g., Naab et al., 2009). Older quiescent galaxies also have more mass at large radii, resulting in larger average sizes. These observations are consistent with a picture where quiescent galaxies grow "inside-out" at late times: minor mergers deposit younger and/or lower-metallicity stars at the outskirts of galaxies, causing negative radial color gradients (e.g., Bezanson et al., 2009; Naab et al., 2009; Suess et al., 2019a). In this scenario, we would expect older quiescent galaxies— which have had time for more inside-out growth— to have more negative color gradients, higher total stellar masses, more mass in their outskirts, and thus larger sizes. This is a good match for what we see in Figure 4.5.

This picture relies on interpreting the ages of quiescent galaxies as an evolutionary sequence. It is important to verify this assumption and ensure that our results are not driven by selection effects. One possibility is that the trends we see are caused by evolution in the properties of recently-quenched galaxies ("progenitor bias", e.g. Carollo et al., 2013; Pog-

gianti et al., 2013). In the Lilly & Carollo (2016) model, star-forming galaxies have negative color gradients, which strengthen as galaxies grow; these color gradients cease to evolve after quenching. In a pure progenitor bias scenario, older quiescent galaxies formed earlier and should thus have flatter color gradients, because star-forming galaxies at higher redshift have flatter color gradients (Suess et al., 2019a,b). However, we see that older quiescent galaxies actually have *steeper* color gradients (Figure 4.3). This model is thus inconsistent with our observations. Furthermore, while quiescent galaxies at high redshift have flat or even positive color gradients, old quiescent galaxies at low redshift have negative color gradients (Figure 4.3). This also implies that color gradients evolve after quenching, inconsistent with the Lilly & Carollo (2016) model. Finally, the observed evolution of half-mass radii at $1.0 \leq z \leq 2.5$ can be almost entirely explained by minor mergers alone, without the need for progenitor bias (Suess et al., 2019b).

A second possibility is that not all quiescent galaxies go through a post-starburst phase, so not all of the progenitors of old quiescent galaxies are included in our sample. Indeed, the number densities of post-starburst galaxies are not sufficiently high to explain the full growth of the quiescent sequence at these redshifts (e.g., Wild et al., 2016; Belli et al., 2019). Recent work has suggested that green valley galaxies— which lie just outside of our UVJ selection— may represent a second, slower, path to join the quiescent sequence (e.g., Bremer et al., 2018; Wu et al., 2018; Belli et al., 2019; Woo & Ellison, 2019). If green valley galaxies quench without significantly altering their structural properties (Wu et al., 2018), we would expect them to have negative color gradients inherited from their star-forming progenitors. The trend we see between color gradient strength and age could thus be explained without appealing to post-quenching evolution *if* all old quiescent galaxies with negative color gradients quenched via the green valley, and all old quiescent galaxies with flat color gradients quenched via the post-starburst route. However, the presence of old quiescent galaxies with negative color gradients in our highest-redshift bin— where quenching through the green valley is less prevalent (e.g., Belli et al., 2019)— indicates that this selection effect does not fully account for the trends we see in this Letter. We will investigate the color gradients and half-mass radii of green valley galaxies in detail in a forthcoming paper.

Altogether, our observations appear consistent with a picture where post-starburst galaxies quench after experiencing a rapid core-building process; after quenching, we observe changes in the quiescent population that appear consistent with inside-out growth via minor mergers. This work was enabled by studying radial color gradients and their evolution directly: not only are color gradients a valuable observable in their own right, they are essential for obtaining an unbiased view of galaxy size evolution. In the future, when upcoming missions such as *JWST* provide spatially-resolved information through the infrared, we hope that this work will spur future investigations into color gradients as a powerful probe of galaxy evolution.

Chapter 5

Dissecting the size-mass & Σ_1-mass relations at $1.0 < z < 2.5$: galaxy mass profiles and color gradients as a function of spectral shape

The content of this chapter is drawn from Suess et al. (2021), with permission from the co-authors.

Chapter 4 demonstrated the insights that can be gained from moving beyond a simple bimodal picture of galaxies as either star-forming or quiescent. In this chapter, we work to further move beyond this simple bimodal picture of galaxies by classifying the $\sim 7,000$ galaxies from Chapter 2 (Suess et al., 2019a) into sixteen groups with similar spectral shapes. Each of these groups represents a different evolutionary stage. Using this approach, we investigate how half-mass radii, central surface mass densities (Σ_1), and color gradients change as galaxies evolve.

This chapter is organized as follows. In Section 5.1, we describe our sample of galaxies and summarize the methods used to calculate mass profiles and half-mass radii. In Section 5.2, we describe the methods used to separate our sample into groups with similar rest-frame SEDs. In Section 5.3, we show where different groups of galaxies lie in size-mass and Σ_1-mass space. Section 5.4 discusses implications for the star-forming sequence, and Section 5.5 discusses implications for transitioning and quiescent galaxies. Finally, Section 5.6 places our results into a unified picture of how galaxies grow and quench.

5.1 Sample, mass profiles, & half-mass radii

For this work, we use the galaxy sample presented in Suess et al. (2019a). This sample consists of all galaxies in the ZFOURGE survey (Straatman et al., 2016) with high signal-to-noise ratio in the ZFOURGE detection band ($S/N_K > 10$), a ZFOURGE use flag equal

to one, a match in both the 3D-HST photometric catalog and the van der Wel et al. (2012) structural catalog, overlapping CANDELS imaging, $1.0 \leq z \leq 2.5$, and $\log M_*/M_\odot > 9.0$. The catalog of half-mass radii for this sample of galaxies is publicly available, and was released with Suess et al. (2019a). The half-light radii and Sérsic indices used in this work are taken from the van der Wel et al. (2012) catalogs. To facilitate comparisons with other studies, we correct these half-light radii to rest-frame 5,000Å using the procedure described by van der Wel et al. (2014). Both the half-light and half-mass radii used in this chapter are measurements of the galaxy's major axis, not circularized radii.

We use the photometric redshifts and stellar masses from the ZFOURGE catalog; the stellar masses are corrected to agree with the van der Wel et al. (2012) structural measurements by multiplying the masses by the ratio of the F160W flux reported in the van der Wel et al. (2012) catalog and the ZFOURGE catalog (Straatman et al., 2016). We note that stellar mass estimates from SED fitting are affected by the choice of star formation history (e.g., Wuyts et al., 2009). Models which use "non-parametric" star formation histories may more accurately recover stellar masses than models which use delayed exponential star formation histories (e.g., Iyer & Gawiser, 2017; Iyer et al., 2019; Leja et al., 2019a,b; Lower et al., 2020). We use ZFOURGE stellar masses, calculated using delayed exponential star formation histories, for consistency with previous studies of the size-mass and Σ_1-mass relations as well as our half-mass radius measurement techniques (Suess et al., 2019a). The difference between these stellar masses and those estimated using non-parametric star formation histories on the order of 0.1 - 0.2 dex, and does not significantly depend on sSFR; these stellar mass uncertainties do not change the major conclusions of this study.

The color gradients and half-mass radii used in this chapter are calculated using the primary method described in detail in Suess et al. (2019a). In summary, this method uses spatially-resolved SED fitting to calculate mass profiles. We use the high-resolution multi-band imaging and integrated photometry in the COSMOS, GOODS-S, and UDS fields obtained by the CANDELS program (Grogin et al., 2011; Koekemoer et al., 2011) and PSF-matched by the 3D-HST team (Skelton et al., 2014; Momcheva et al., 2016). For each available filter, we measure the galaxy's flux in concentric elliptical annuli that follow the geometry of the best-fit structural parameters from the van der Wel et al. (2012) catalog. Then, we use FAST (Kriek et al., 2009) to fit these spatially-resolved SEDs with stellar population synthesis models to obtain the mass in each annulus. These spatially-resolved FAST fits assume a Chabrier (2003) IMF, the Bruzual & Charlot (2003) stellar population models, the (fixed-slope) Kriek & Conroy (2013) dust law, a delayed exponential star formation history, and solar metallicity. This procedure yields the observed-space M/L gradient profile. We then correct for the effects of the telescope point spread function (PSF) by using a forward modeling approach to convert this observed M/L to an intrinsic M/L. We assume that the intrinsic M/L is a power-law function of radius, then find the intrinsic M/L profile that, when convolved with the PSF, best reproduces our observed M/L profile. We multiply this best-fit intrinsic M/L model by the galaxy's intrinsic light model to obtain the mass profile, then integrate to find the half-mass radius.

Suess et al. (2019a) demonstrates that the half-mass radii measured in this way are

robust, and are not significantly biased by the galaxy's stellar mass, redshift, or half-light radius. Furthermore, the half-mass radii determined using this method agree well with those obtained using other common methods for measuring half-mass radii (Lang et al., 2014; Chan et al., 2016; Szomoru et al., 2010, 2012, 2013; Mosleh et al., 2020). In addition to calculating half-mass radii, we use the mass profiles described above to calculate Σ_1, the surface mass density in each galaxy's central kiloparsec (e.g., Fang et al., 2013). Finally, we probe the strength of color gradients in each galaxy as the ratio of half-mass to half-light radii.

5.2 Methods: creating composite SED groups

Here, we go beyond separating galaxies into just two groups— star-forming or quiescent— and "dissect" the traditional size-mass and Σ_1-mass relations for many different types of galaxies. We use the Kriek et al. (2011) technique to separate the ∼7,000 galaxies in our sample into groups with similar rest-frame SED shapes. The medium-band filters included as part of the ZFOURGE survey provide high-resolution SEDs, which are essential to create clean groups with this technique (Kriek et al., 2011). While this rest-frame SED grouping technique may appear similar to grouping by specific star formation rate (sSFR), it has several advantages. First, SED shape encodes multiple properties: in addition to sSFR, the SED shape is also influenced by dust, age, and star-formation timescale. Therefore, grouping by SED shape allows us to separate galaxies with the same sSFR but differences in other properties. Second, SED shape is a direct observable— it is simply the galaxy's observed photometry— while sSFR must be estimated by fitting models to the observed photometry. The method described below relies on models only to estimate photometric redshifts and to interpolate rest-frame colors from observed photometry. Grouping galaxies directly by their SED shapes is therefore nearly model-independent when compared to grouping galaxies by their estimated sSFR; thus, this technique produces cleaner groups.

Following Kriek et al. (2011), we construct 22 synthetic rest-frame filters equally spaced in $\log\lambda$ between 1,250Å and 40,000Å. We use EAZY (Brammer et al., 2008) to measure the rest-frame flux of each galaxy in each rest-frame filter that falls within the observed wavelength coverage of the galaxy. For each pair of galaxies in our sample, we calculate a similarity score:

$$b_{12} = \frac{\Sigma(f_1 - a_{12}f_2)^2}{\Sigma(f_2)^2}, \tag{5.1}$$

where f_1 is f_λ for galaxy 1, f_2 is f_λ for galaxy 2, a_{12} is a scaling factor given by

$$a_{12} = \frac{\Sigma f_1 f_2}{\Sigma f_2^2}, \tag{5.2}$$

and the sums are performed over all rest-frame filters that the two galaxies have in common. Two galaxies are considered analogs if their similarity score $b_{12} \leq 0.07$.

We find the galaxy in our sample with the largest number of high-S/N analogs. We quantify this as the galaxy where $N_{\rm analogs} \times ({\rm S/N}_{\rm analogs})^2$ is maximized. We include this S/N

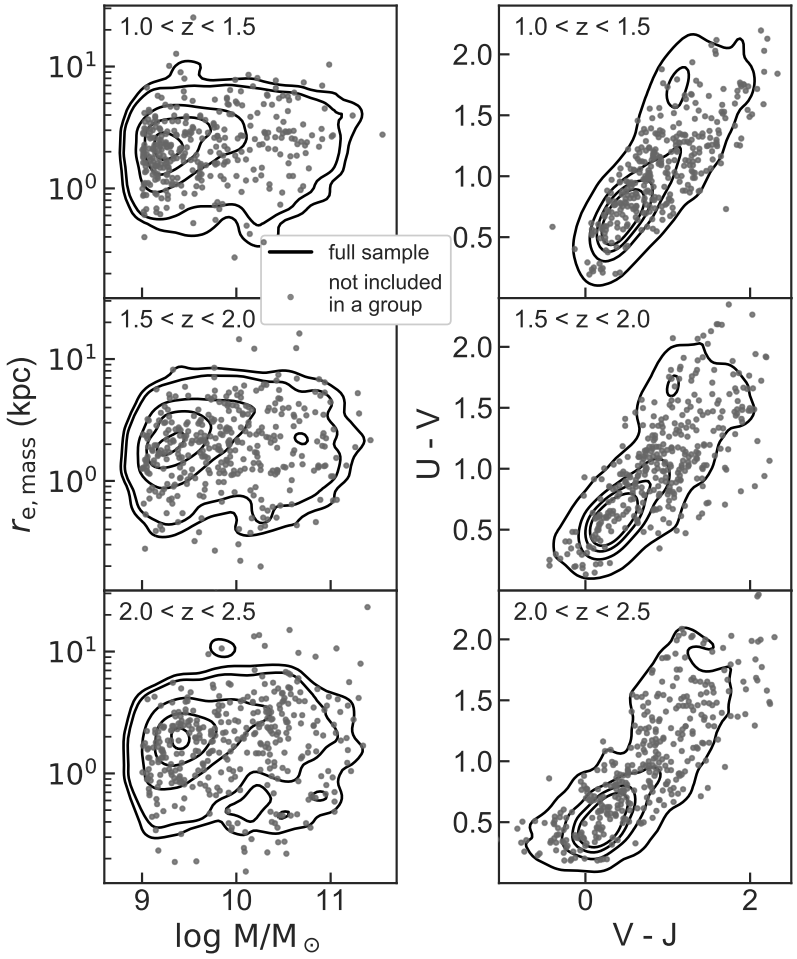

Figure 5.1: Size-mass and UVJ distribution of our full sample (black contours) and galaxies that are not classified in a group (grey points). Each row shows a different redshift interval. The galaxies not included in a group are spread uniformly across size-mass and UVJ space.

factor to prevent forming very large groups composed of noisy, low-S/N star-forming galaxies. After finding this first primary galaxy, we remove it and its analogs from our sample.

We repeat this process until there are no galaxies remaining that have more than 19 analogs. Because some galaxies removed in early groups may be more similar to primary galaxies found later in the algorithm, after identifying the groups we re-assign analog galaxies to the group whose primary they are the most similar to. After this process, a total of 5,840 galaxies (83% of the parent sample) are classified into 26 groups. To perform the rest of our analysis, we wish to have a relatively small number of groups, each of which has a large number of galaxies. To achieve this goal, we aggregate any groups of galaxies whose primaries have a similarity score of $b_{12} < 0.1$. After this process, we have 16 groups of galaxies.

Table 5.1: Best-fit stellar population synthesis fitting results for the composite SED of each group of galaxies. Uncertainties in these derived properties are dominated not by formal uncertainties (calculated to be < 0.05 dex from the stellar population fits), but by systematic uncertainties. These systematic uncertainties are expected to be ~ 0.2 dex (e.g., Marchesini et al., 2009; Muzzin et al., 2013).

Group	$N_{\rm galaxies}$	$\log \tau$	log(age)	$A_{\rm v}$	log(sSFR)
1	1060	8.3	8.7	0.15	-8.69
2	1363	8.3	8.75	0.3	-8.8
3	1170	8.5	8.9	0.45	-8.87
4	535	8.3	8.8	0.6	-8.92
5	295	8.5	8.95	0.75	-8.98
6	233	8.7	9.1	0.85	-9.06
7	88	9.1	9.3	1.05	-9.06
8	100	8.4	9.0	1.0	-9.29
9	168	8.9	9.2	1.35	-9.05
10	104	8.6	9.1	1.55	-9.19
11	97	8.3	8.9	1.95	-9.2
12	42	8.1	8.8	2.35	-9.37
13	110	8.3	9.05	0.95	-9.77
14	123	8.0	8.95	0.55	-10.7
15	285	8.2	9.15	0.5	-10.88
16	67	8.2	9.2	0.7	-11.29

The contours in Figure 5.1 show the distribution of the full Suess et al. (2019a) parent sample in both size-mass space and $U-V$ vs $V-J$ ('UVJ') color-color space. Points indicate galaxies that were *not* classified into a group. The 17% of galaxies that are not included in a group are spread fairly uniformly across both size-mass and UVJ space. The fraction of galaxies not classified into a group is highest in the highest-redshift bin ($2.0 \leq z \leq 2.5$), likely because these galaxies tend to be fainter and thus have lower signal-to-noise ratios and less reliable photometry.

Figure 5.2 shows the composite SED of each group (black points) as well as the observed data for each individual galaxy in the group (small grey points). We create these composite SEDs following the Kriek et al. (2011) technique: the observed SEDs of all galaxies in each group are de-redshifted, scaled to the same arbitrary flux normalization using the a_{12} scaling factor, then median binned. Scaled data points are binned such that there are at least 50 individual points in each composite SED point and no more than 100 total points in the composite SED. Error bars on the composite SED points are computed by bootstrap resampling the individual galaxy SEDs. We also construct an effective filter response curve for each composite SED point by de-redshifting the true filter response curves for each data point in the median point, then normalizing and adding them.

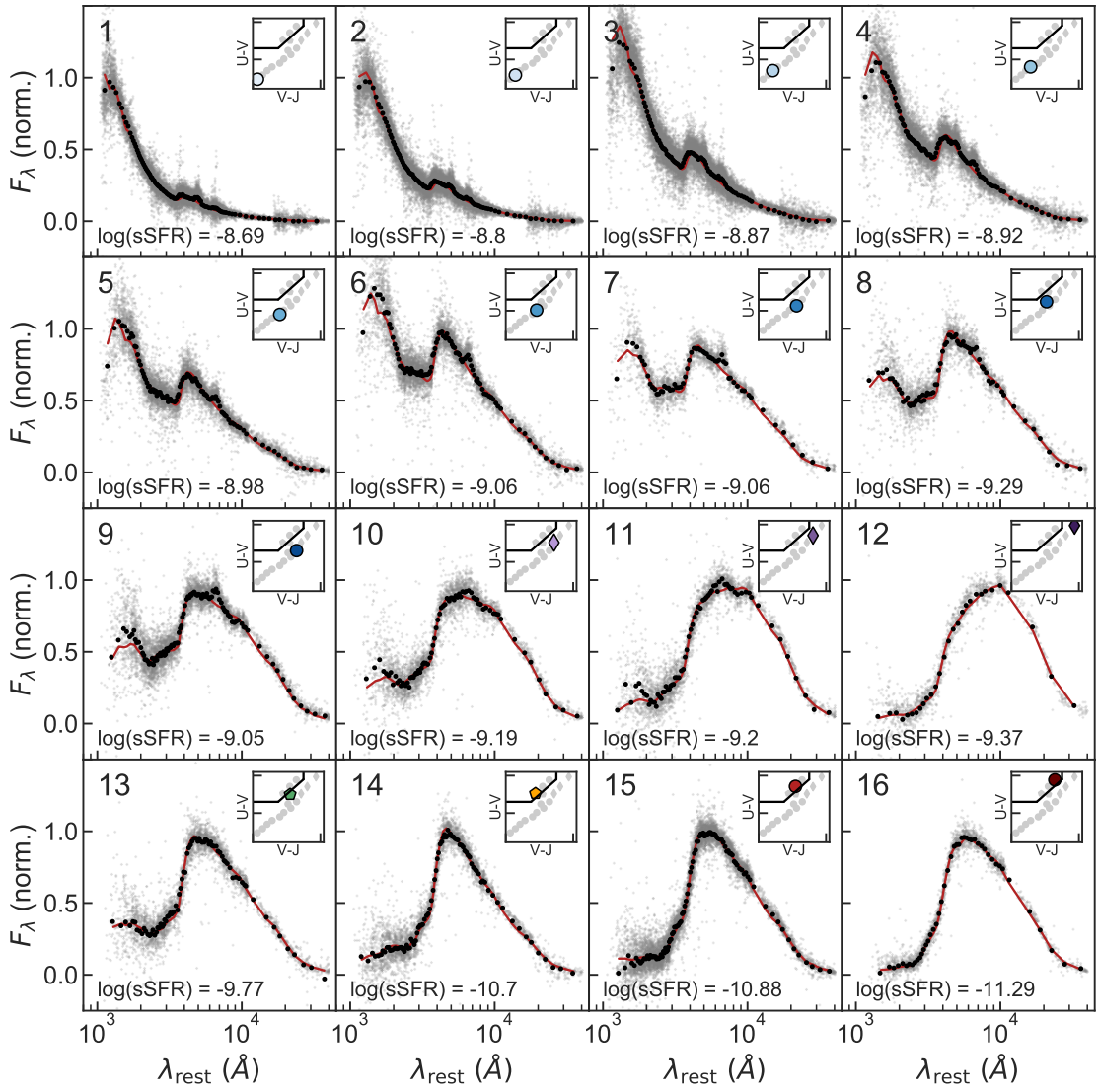

Figure 5.2: Composite SEDs for each group, ordered by their location in UVJ space. Individual galaxy data points are shown in grey, the binned composite SED is shown in black, and the best-fit stellar population synthesis model (binned to the same resolution as the composite SED) is shown in red. The specific star formation rate of the best-fit model is listed in the lower left of each panel; other best-fit values are shown in Table 5.1. The inset at the top right of each panel shows the location of the composite SED in UVJ space (see Figure 5.5 for a larger UVJ diagram with axis labels). The colors and symbols used to represent each group in the UVJ inset remain the same throughout the remainder of this chapter.

We use these effective filter response curves to fit each composite SED with the FAST stellar population synthesis fitting code (Kriek et al., 2009). In these fits, we fix the redshift of the composite SED to $z = 0$ and assume the Bruzual & Charlot (2003) stellar population library, a Chabrier (2003) initial mass function, the Kriek & Conroy (2013) dust attenuation law, and a delayed exponential star formation history. We mask points in the composite SED within 400Å of the Hα, Hβ, and [OIII]λ5007 lines, as well as points within 75Å of the [OII]λ3727 line; these points are often visibly contaminated by line emission, which is not included in the FAST templates. The red lines in Figure 5.2 show the best-fit model to each composite SED, binned to the same resolution as the composite SED. The best-fit age, star-formation timescale, dust attenuation, and sSFR for each composite SED is listed in Table 5.1; the sSFR is also shown in the bottom left of each panel in Figure 5.2. Figure 5.3 shows the sSFR and A_v of all groups in UVJ space. These quantities are mass-independent, and therefore are not affected by the arbitrary normalization of the composite SEDs. We note that the masses of galaxies in each group do systematically differ, and generally increase as we move through Figure 5.2 and sSFR decreases; these differences are explored in detail in later sections of this chapter. The inset in the upper right of each panel in Figure 5.2 shows the location of each group's composite SED in UVJ space; the line in this inset demarcates the quiescent region (again, using the definition from Whitaker et al., 2012b).

Figures 5.2 & 5.3 show the incredible diversity of rest-frame SED shapes present in our sample. Because groups 1-13 all lie in the star-forming section of the UVJ diagram, they are traditionally all grouped together to study the structural relations for star-forming galaxies. However, Figures 5.2 & 5.3 show that these galaxies have vastly different properties: the star-formation timescale, age, dust content, *and* sSFR vary dramatically from group to group. Figure 5.2 also allows us to see a more gradual shift from star-forming galaxies to quiescent ones: there are a number of 'intermediate' SED shapes that have shapes between highly star-forming and fully quenched.

To guide the eye, we plot each galaxy's SED type using a different color and marker for the remainder of this chapter. We plot star-forming galaxies as blue points; the shade describes how far up the UVJ star-forming sequence the group lies. We identify three groups (10, 11, and 12) of very dusty star-forming galaxies which have $A_v > 1.5$. These galaxies are shown using purple diamonds. Fully quiescent galaxies, with sSFR < -10.8, are shown as red points. Finally, groups 13 and 14 are located very close to the boundary of the star-forming and quiescent sections of the UVJ diagram. These 'transitioning' galaxies are shown with pentagons. Group 13 consists of galaxies just on the star-forming side of the UVJ diagram that have some UV flux, relatively high dust obscuration, and fairly low specific star formation rates. We refer to these galaxies as 'green valley' galaxies and plot them with a green pentagon (see, e.g., Patel et al., 2011; Fang et al., 2018; Gu et al., 2018). Group 14 consists of galaxies at the lower-left corner of the UVJ quiescent region with low UV fluxes, low specific star formation rates, short star-formation timescales, and a sharp Balmer break. These galaxies are often referred to as 'post-starburst' (e.g., Whitaker et al., 2012a; Belli et al., 2019); we plot them with a yellow pentagon.

We calculate the mass completeness of each group using a technique similar to Quadri

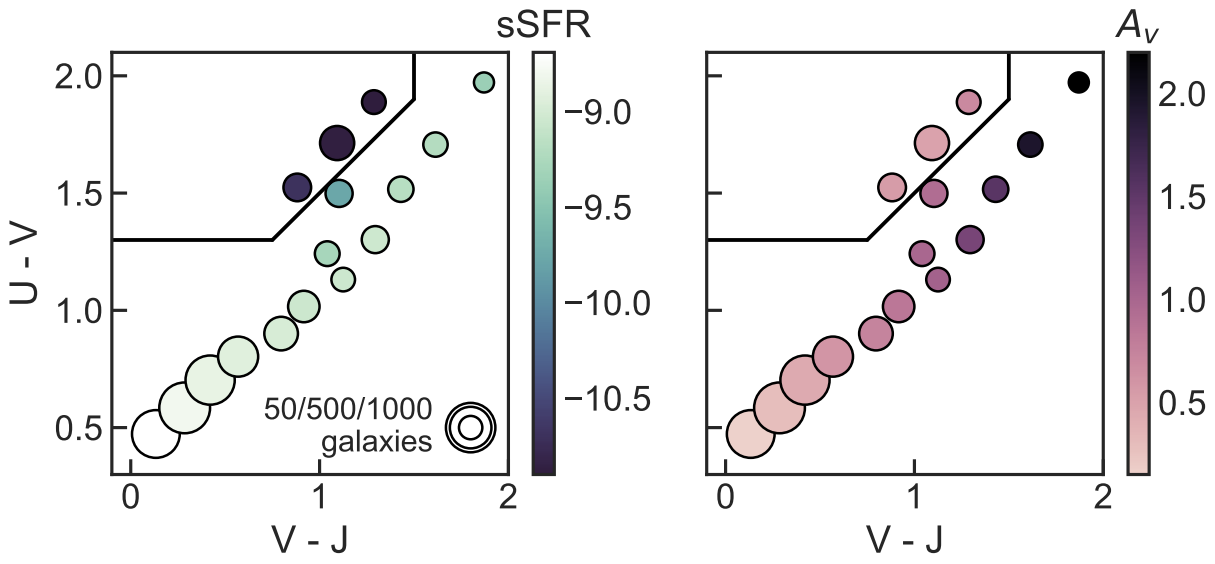

Figure 5.3: UVJ location of all groups, colored by sSFR (left) or A_v (right). The area of the symbol is proportional to the number of galaxies in the group. sSFR decreases slightly moving up the UVJ star-forming sequence, and decreases dramatically moving from the star-forming to quiescent region of UVJ space. A_v, however, shows most variation moving up the UVJ star-forming sequence, with galaxies in the upper-right corner being significantly dustier than those in the lower-left corner.

et al. (2012) and Tomczak et al. (2014): we scale the K_s-band magnitude and mass of each galaxy in the group that has a signal-to-noise value close to our cutoff ($20 \leq$ S/N ≤ 50) down to the flux completeness of the survey (Straatman et al., 2016). We take the 90th percentile of these masses as the mass completeness of the group. We calculate this mass completeness in three redshift bins: $1.0 \leq z < 1.5$, $1.5 \leq z < 2.0$, and $2.0 \leq z \leq 2.5$. The results that follow will also be broken into these same redshift intervals.

Figure 5.4 shows example images of galaxies in each group as a function of mass and redshift. These postage stamps demonstrate that galaxy structure and morphology clearly depends on both SED shape, mass, and redshift.

5.3 Results

Over the past decade, many studies have explored the distribution of galaxies both in the size-mass plane (e.g., Shen et al., 2003; van der Wel et al., 2014; Omand et al., 2014; Whitaker et al., 2017b; Mowla et al., 2019b; Suess et al., 2019a) and the Σ_1-mass plane (e.g., Fang et al., 2013; Barro et al., 2017b; Whitaker et al., 2017b; Lee et al., 2018; Woo & Ellison,

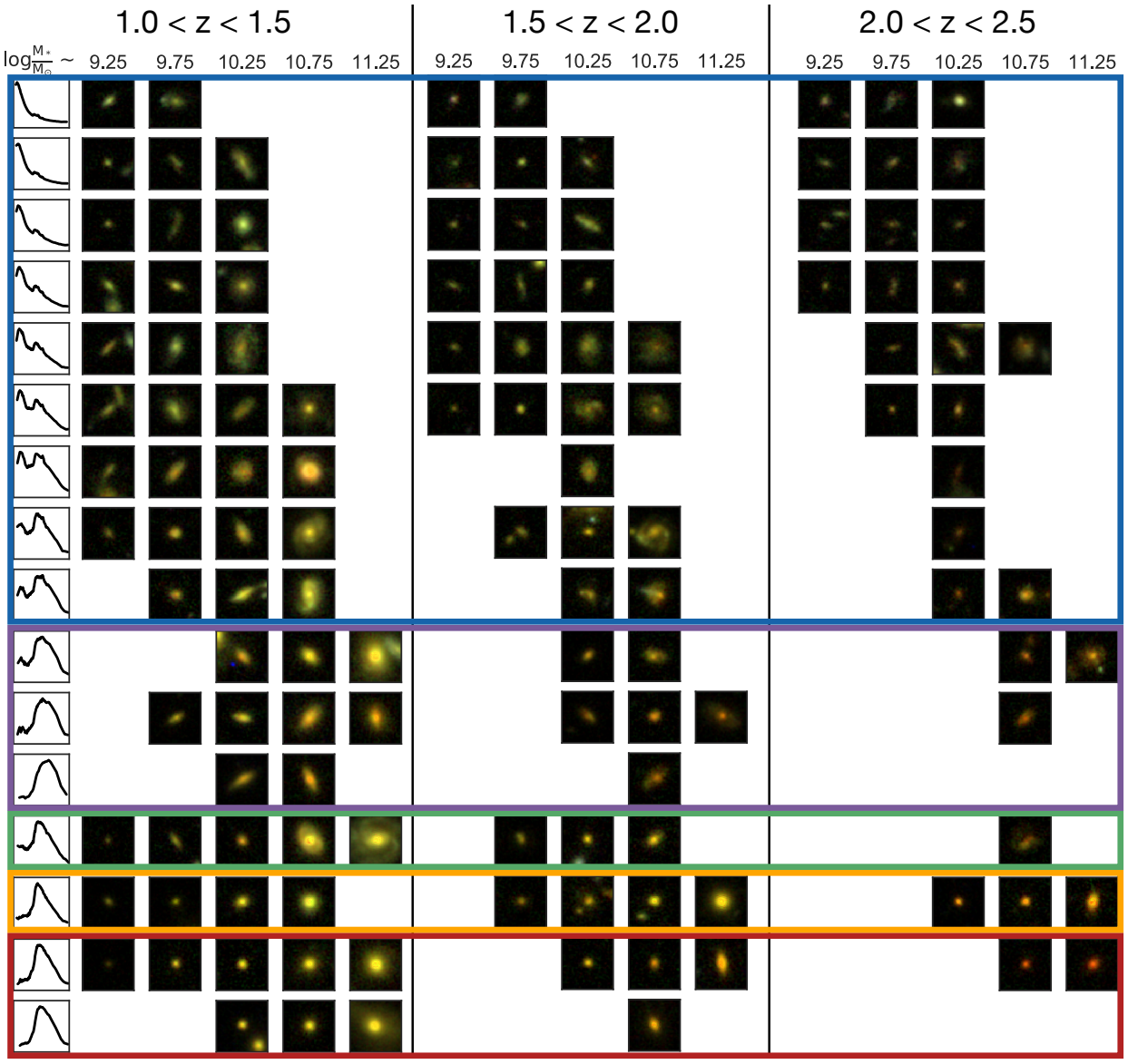

Figure 5.4: Example color images of galaxies in each group across mass and redshift (from F160W, F125W, and F814W CANDELS imaging). Cutouts are 3" per side; this corresponds to $\sim$ 25 kpc across our full redshift range. No image is shown if a group does not contain any galaxies in a given mass and redshift bin. Unobscured star-forming galaxies are highlighted in blue, dusty star-forming galaxies in purple, green valley galaxies in green, post-starburst galaxies in yellow, and quiescent galaxies in red. Galaxy structure clearly depends on both SED shape, redshift, and mass, as explored in detail in the remainder of this chapter.

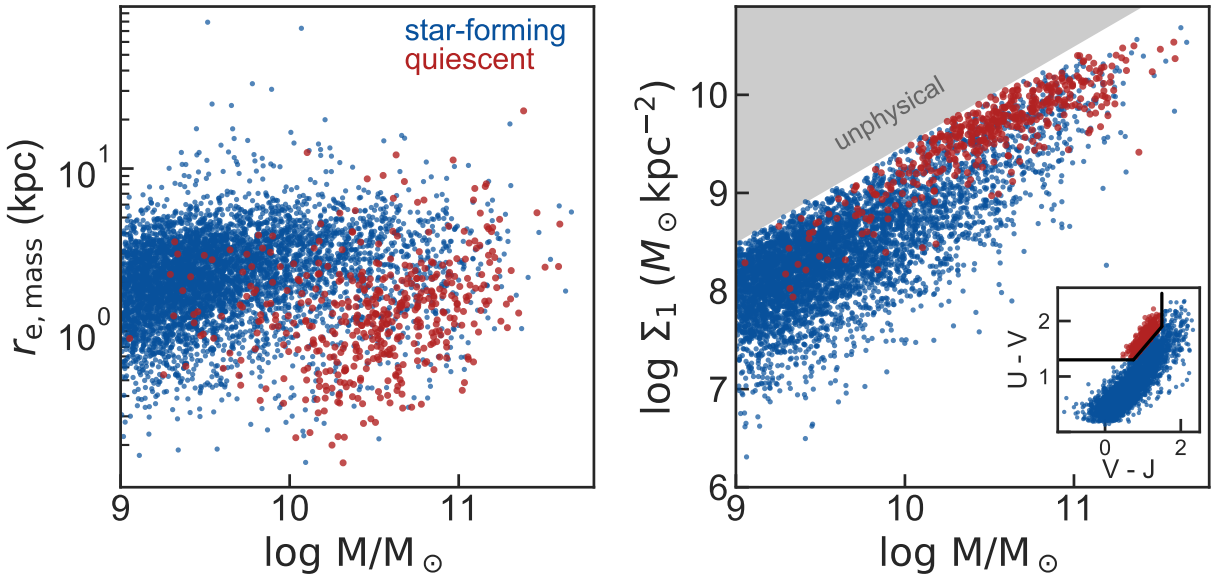

Figure 5.5: Our full sample in size-mass (left) and Σ_1-mass (right) space. The inset shows the full sample in UVJ space. Star-forming galaxies are shown in blue, and quiescent galaxies in red. Because the median half-mass radii of galaxies do not evolve rapidly over the $1.0 \leq z \leq 2.5$ interval we study here (Suess et al., 2019a,b), for brevity we show all redshifts in the same figure. The grey shaded region in Σ_1-mass space shows the unphysical regime, where $> 100\%$ of the galaxy's mass lies within the central kiloparsec. While star-forming and quiescent galaxies follow relatively tight relations with similar slopes in Σ_1-mass space, they have more scatter and clearly different slopes in size-mass space. The slope of the star-forming size-mass relation is nearly flat, consistent with the minimal size evolution we observe over this redshift regime.

2019). In this chapter, we pursue two new avenues to advance this legacy of structural studies. First, our measurements are based on mass profiles; this removes potential biases due to radial color gradients (e.g., Szomoru et al., 2013; Chan et al., 2016; Suess et al., 2019a,b, 2020). Second, instead of studying the structures of UVJ-selected star-forming and quiescent galaxies, we study the structures of a large number of galaxy groups identified by their similar SED shapes (Section 5.2).

Before dissecting these structural relations, we consider how the traditional star-forming and quiescent size-mass and Σ_1-mass relations change when we use color gradient-corrected mass profiles. Figure 5.5 shows the the structural properties of our sample, with UVJ-selected star-forming galaxies in blue and UVJ-selected quiescent galaxies in red; the inset in the lower right shows the UVJ plane. The grey shaded region in the Σ_1-mass plane shows the unphysical regime where $M_{\mathrm{r<1kpc}} > M_{\mathrm{tot}}$. For brevity, we show the full $1.0 \leq z \leq 2.5$

redshift range in one panel; as shown in Suess et al. (2019a), galaxy half-mass radii of both star-forming and quiescent galaxies do not evolve significantly in this redshift regime. In agreement with the literature, both star-forming and quiescent galaxies lie on well-defined size-mass relations; quiescent galaxies are smaller at fixed mass, and have a steeper slope in size-mass space than star-forming galaxies (e.g., Shen et al., 2003; van der Wel et al., 2014; Mowla et al., 2019b). We also see that the quiescent size-mass relation clearly flattens below $\sim 10^{10} M_{\odot}$ (e.g., Cappellari et al., 2013; van der Wel et al., 2014; Whitaker et al., 2017b); we discuss this flattening further in Section 5.5.

Because we use half-mass radii, the overall structural relations we find for star-forming and quiescent galaxies differ from previous studies based on half-light radii. More massive galaxies have stronger color gradients, so the slope of the star-forming size-mass relation is flatter than found by previous studies using half-light radii (e.g., van der Wel et al., 2014; Mowla et al., 2019b; Suess et al., 2019a). For star-forming galaxies, this shallower slope can be explained by $A_{\rm v}$ gradients: massive star-forming galaxies are dustier (e.g. Whitaker et al., 2017a), and dust profiles in star-forming galaxies at these redshifts tend to be centrally-peaked (e.g., Nelson et al., 2016a; Tacchella et al., 2018). These $A_{\rm v}$ gradients cause more massive star-forming galaxies to have stronger negative color gradients, and thus smaller half-mass radii. As discussed in Suess et al. (2019b), this flatter slope is consistent with the minimal size growth that we observe at these redshifts. In turn, this slow growth agrees with IFU studies that show roughly flat dust-corrected sSFR profiles for star-forming galaxies in this redshift regime (e.g., Tacchella et al., 2015b,a; Nelson et al., 2016b).

Star-forming and quiescent galaxies also lie on well-defined relations in Σ_1-mass space. Unlike the size-mass relations, the Σ_1-mass relations of the two galaxy types have very similar slopes, and the scatter around the relations is smaller. Quiescent galaxies are offset to higher Σ_1 values at fixed mass, effectively tracing out the upper half of the star-forming Σ_1-mass relation. In agreement with previous studies, the quiescent Σ_1-mass relation is quite tight, with much less scatter than the quiescent size-mass relation (e.g., Fang et al., 2013; Barro et al., 2017b; Chen et al., 2020). Again, we find that the star-forming sequence is offset slightly from previous measurements (e.g., Barro et al., 2017b). This difference can also be ascribed to stronger color gradients in more massive star-forming galaxies, which increase our Σ_1 values for massive star-forming galaxies.

With this picture of the star-forming and quiescent size-mass and Σ_1-mass relations in place, we now begin to dissect these structural relations by examining the color gradients, sizes, and Σ_1 values for each group of galaxies shown in Figure 5.2.

Color gradient strength varies with SED shape

Color gradient strength depends on stellar mass (e.g., Tortora et al., 2010; Suess et al., 2019a), redshift (Suess et al., 2019a,b) and age along the quiescent sequence (Suess et al., 2020); here, we test whether these systematic color gradient differences extend to the sixteen star-forming, transitional, and quiescent SED types shown in Figure 5.2. As in Suess et al. (2019a,b, 2020), we use the ratio of the galaxy's half-mass and half-light radius to probe color

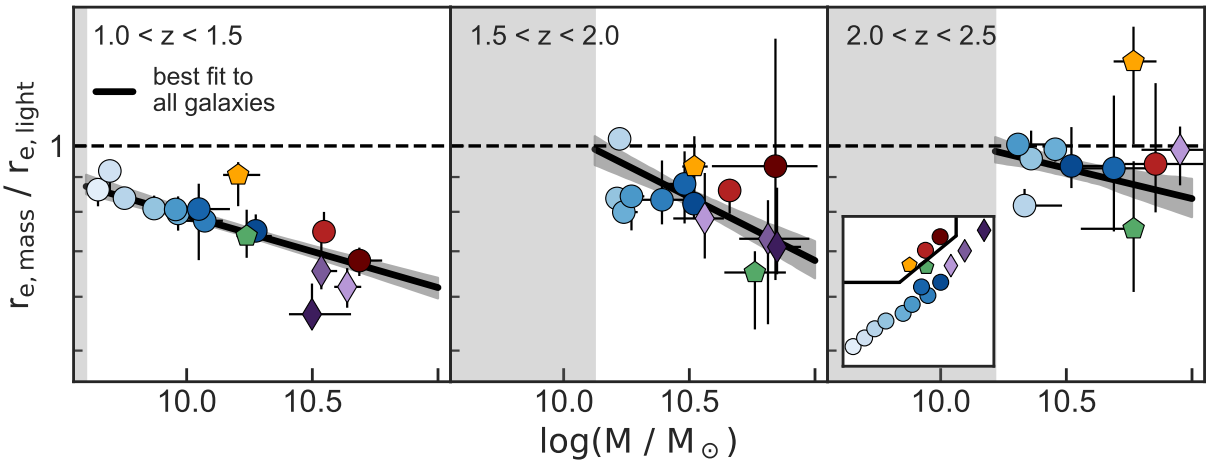

Figure 5.6: Median color gradient strength as a function of median stellar mass for each galaxy group. Each point represents one SED group; the color and symbol used for each group corresponds to its location in UVJ space, as shown in the inset. Error bars on individual points represent the 1σ spread in bootstrap resamples of the median $r_{\rm e,mass}/r_{\rm e,light}$. The black line and grey shaded region show the Suess et al. (2019a) fit to all galaxies and its 1σ error. The grey shaded region on the left shows the mass completeness in each redshift interval. Groups have systematically different color gradient strengths, but typically have the expected value for their mass; notable exceptions are the post-starburst galaxies (yellow pentagon), which have weak to flat color gradients, and dusty star-forming galaxies (purple diamonds), which have strongly negative color gradients at low redshift.

gradient strength. High values of $r_{\rm e,mass}/r_{\rm e,light}$ indicate positive color gradients, where the center of the galaxy is bluer than the outskirts; low values of $r_{\rm e,mass}/r_{\rm e,light}$ indicate negative color gradients, where the center of the galaxy is redder than the outskirts; $r_{\rm e,mass}/r_{\rm e,light} = 1$ indicates no radial color gradient.

Each point in Figure 5.6 shows the median $r_{\rm e,mass}/r_{\rm e,light}$ value of all galaxies in a group as a function of the group's median stellar mass. Median points exclude galaxies below the mass completeness limit at each redshift (shaded vertical grey region). The symbols and colors of the points correspond to the group's location in UVJ space, as shown in the inset. The solid black line (and grey region) indicate a best-fit line (and 16-84% confidence interval) to the trend in color gradient strength as a function of stellar mass for all galaxies in the sample (Suess et al., 2019a).

Figure 5.6 shows that different groups of galaxies have systematically different color gradients. In general, groups with higher masses and lower specific star formation rates tend to have more strongly negative color gradients. These variations in color gradient strength with SED shape are generally consistent with the Suess et al. (2019a) relation between color

gradient strength and stellar mass for all galaxies. The most notable outliers from this trend are the post-starburst galaxies, shown in yellow. These young quiescent galaxies have systematically *weaker* color gradients than expected given their stellar mass. As discussed in Suess et al. (2020) and Section 5.5, these flat color gradients are consistent with post-starburst galaxies being the result of a "fast" quenching process that requires structural change. The other possible outliers are dusty star-forming galaxies, which at $1.0 \leq z \leq 2.5$ appear to have stronger color gradients than expected from their stellar mass. We discuss the color gradients of dusty star-forming galaxies in detail in Section 5.5.

These variations in color gradient strength with SED shape systematically alter the half-light radii of different types of galaxies. It is therefore *essential* that we account for these varying color gradients when dissecting the size-mass and Σ_1-mass relations. In this study, we account for these varying color gradients by examining the half-*mass* radii of galaxies.

Galaxies lie in distinct parts of size-mass & Σ_1-mass space

We now turn towards understanding where the galaxies in each group lie in size-mass and Σ_1-mass space, corrected for color gradients. Figure 5.7 shows half-mass radius as a function of stellar mass for the galaxies in each group. The leftmost column shows the composite SED of the group, as well as the group's location in UVJ space. The right columns show three different redshift slices of the size-mass diagram. The black points indicate the masses and half-mass radii of the galaxies with that particular SED type. The blue and red contours show the full galaxy population, divided into star-forming and quiescent groups using the UVJ classification of Whitaker et al. (2012b). The blue and red dashed lines represent the $r_{\rm mass} - M_*$ relations from Suess et al. (2019a), calculated from the same galaxy sample and size measurements used in this study. The size-mass contours and best-fit relations are the same in each column, and are shown to indicate how each group compares to the traditional 'blue vs. red' view of the galaxy size-mass diagram. For brevity, several groups which have very similar composite SEDs and locations in size-mass space are shown in the same row of Figure 5.7. For these combined groups, we show only one composite SED (which includes all galaxies from both groups), but show both UVJ points.

In general, stellar mass increases and sSFR decreases as we move down the rows of Figure 5.7 and march up the UVJ diagram. The mass completeness limits also increase with decreasing sSFR, but star-forming galaxies are less massive than quiescent galaxies even when we consider a very conservative mass cut. This increase in mass with decreasing sSFR is expected: it is a natural consequence of the shallow slope of the star-forming main sequence (e.g., Brinchmann et al., 2004; Noeske et al., 2007; Daddi et al., 2007; González et al., 2010; Whitaker et al., 2012b).

Figure 5.7 shows that each group of galaxies occupies a distinct and fairly localized region of size-mass space. Breaking the size-mass plane into just two relations, star-forming and quiescent, is an oversimplification of the complexity we see in Figure 5.7: both the star-forming and quiescent regions of size-mass space are comprised of multiple different galaxy

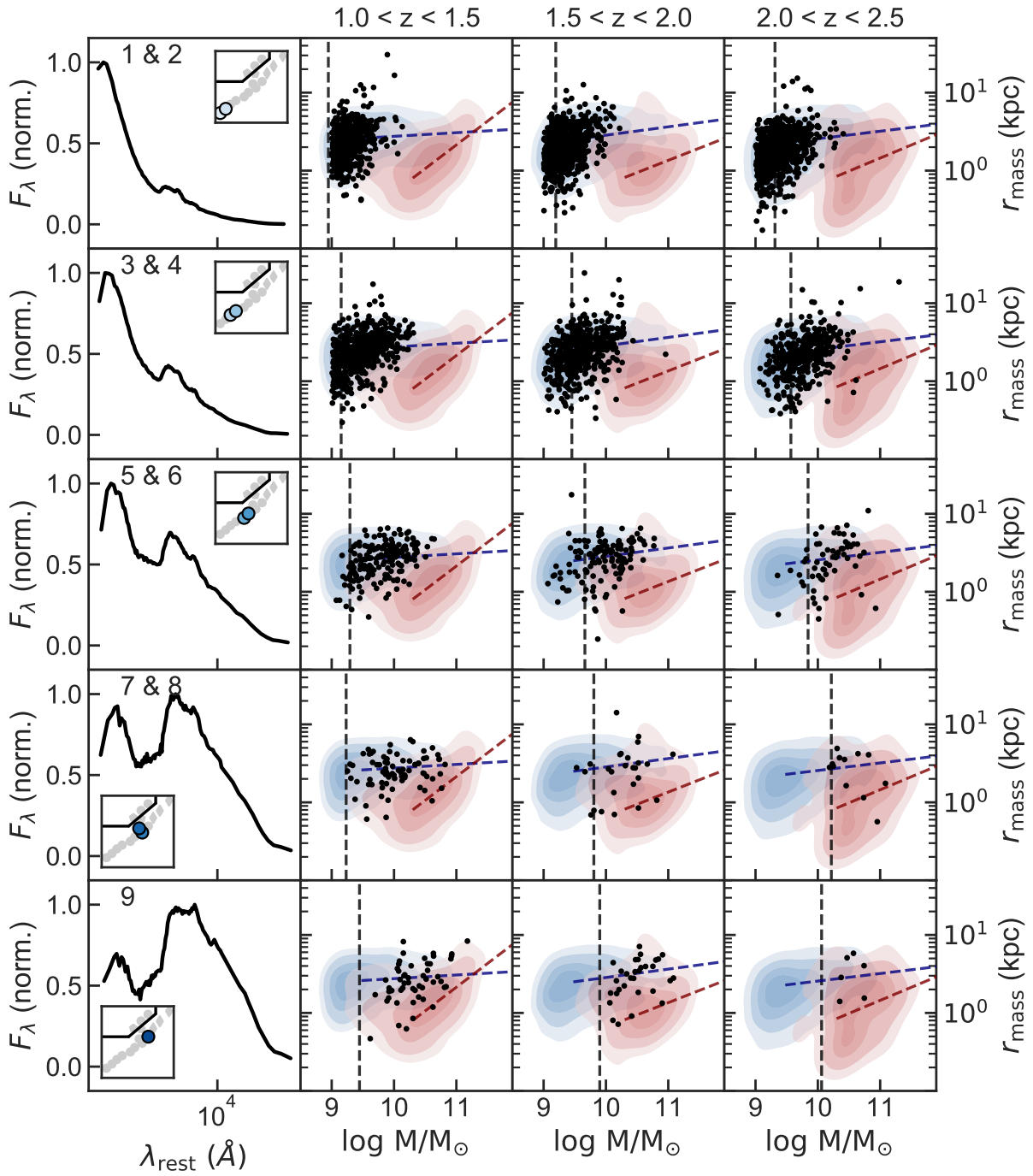

Figure 5.7: Half-mass radius versus mass for each group of galaxies, ordered by decreasing sSFR. Left: composite SED of the group, normalized to a peak flux of 1.0. The inset shows the group's location in UVJ space. The next three panels show $r_{e,mass}$ as a function of stellar mass for three different redshift ranges. Black points show the galaxies in that group; for comparison, the total sample of star-forming (quiescent) galaxies is shown as blue (red) contours. The contours enclose 25, 50, 75 and 98% of the full sample at each redshift. The vertical grey dashed line shows the mass completeness for each group. The blue and red dashed lines show the $r_{e,mass} - M_*$ relations from Suess et al. (2019a).

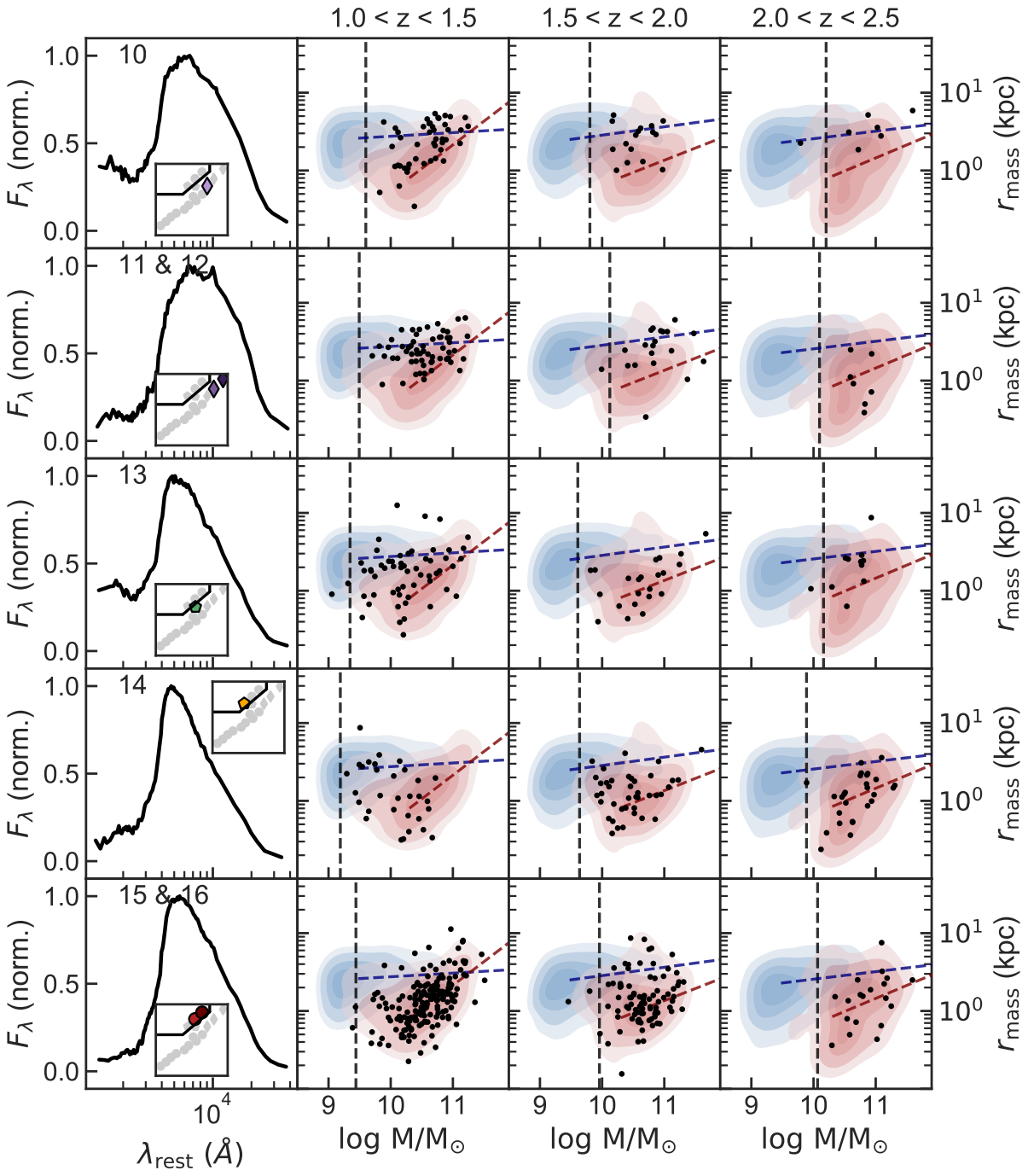

Figure 5.7: Continuation of previous figure.

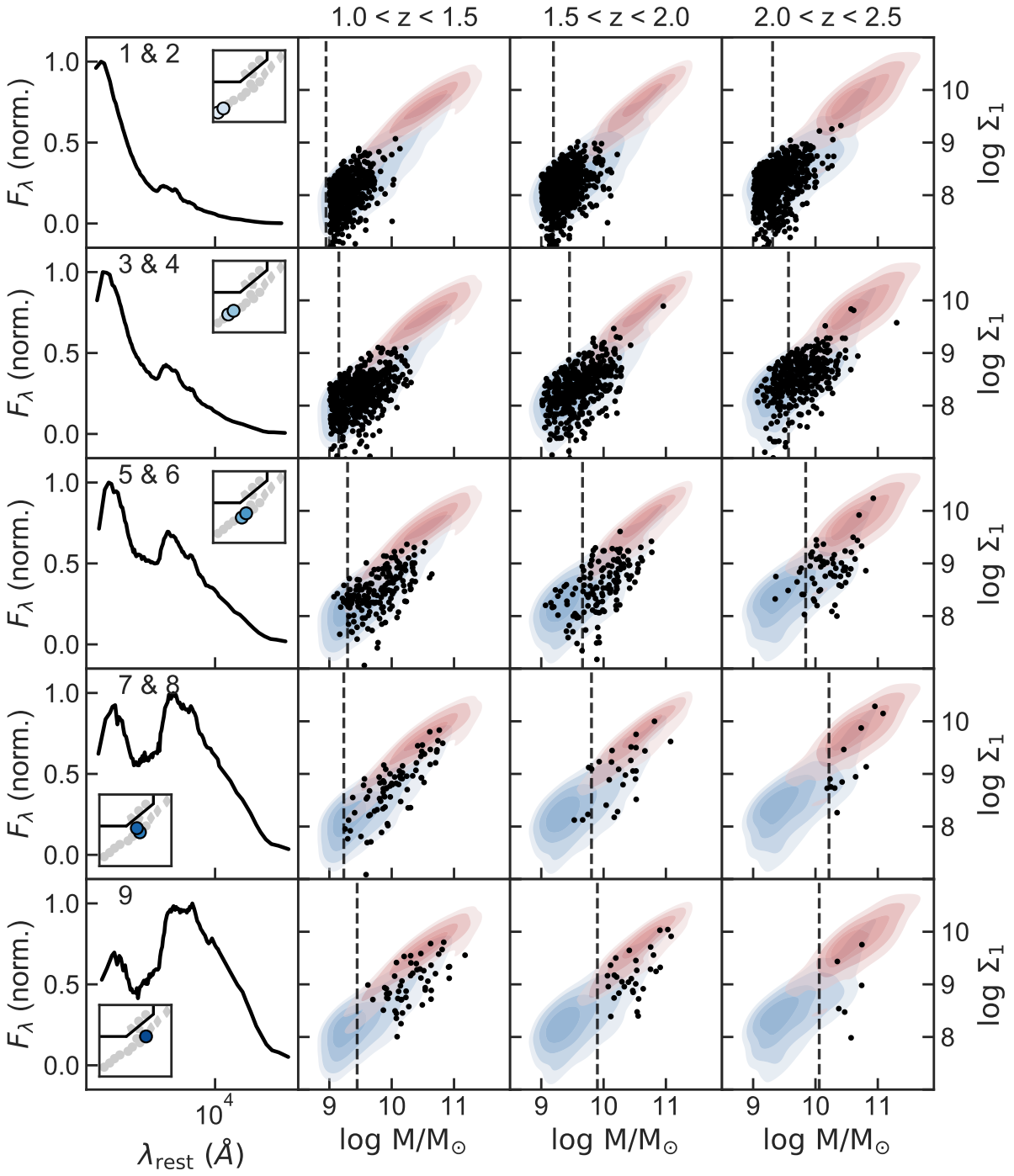

Figure 5.8: Same as Figure 5.7, but showing Σ_1 versus mass for each group.

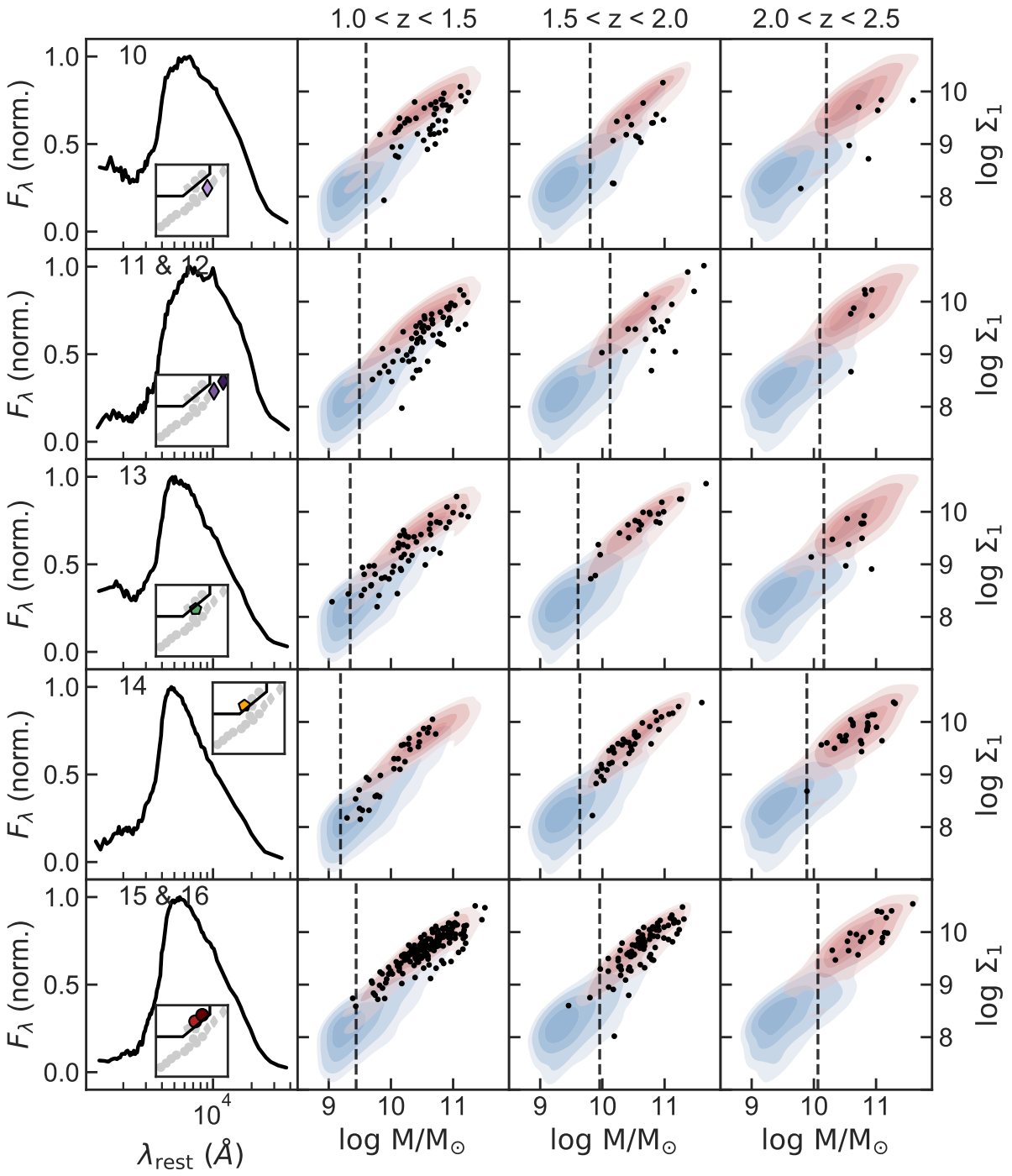

Figure 5.8: Continuation of previous figure.

groups with distinct SED shapes and different sSFRs. The star-forming region in particular is populated by many different groups, discussed in detail in Section 5.4.

Additionally, we find that there are transitional phases where the galaxies lie between the star-forming and quiescent size-mass relations. These transitional phases include post-starburst galaxies (yellow pentagon), green valley galaxies (green pentagon), and high-mass dusty star-forming galaxies (purple diamonds). Interestingly, the sizes of these transitional galaxies clearly depend on redshift. In Section 5.5 we investigate these groups further and discuss how they may represent different pathways to galaxy quenching.

Figure 5.8 replicates Figure 5.7, but showing where each group lies in Σ_1-mass space instead of size-mass space. Contours again show the full sample divided into quiescent (red) and star-forming (blue) using a UVJ cut. Individual groups of star-forming galaxies trace out the overall Σ_1-mass relation up to higher and higher masses as sSFR decreases. Dusty star-forming galaxies appear to be slightly offset to lower Σ_1 values, tracing out the high-mass regime below the bulk of the quiescent population; we discuss the implications of these results in detail in Section 5.5. Post-starburst galaxies have high Σ_1 values consistent with the quiescent population, in agreement with our previous results (Suess et al., 2020). Green valley galaxies also have relatively high Σ_1 values, especially at $z > 1.5$.

Figures 5.7 & 5.8 demonstrate the need to move beyond classifying galaxies into just two groups, star-forming *or* quiescent. By creating such broad categories, we are averaging over a huge amount of interesting behavior. Additionally, it is only by looking at smaller groups of galaxies that we can start to build up an understanding of how galaxies evolve *through* these spaces– an understanding that may translate to a greater knowledge of the physical mechanisms responsible for both the mass assembly histories of galaxies and the quenching process.

The remainder of this chapter will be devoted to summarizing, discussing, and contextualizing the data shown in Figures 5.7 & 5.8.

Median sizes and Σ_1 values as a function of sSFR

We begin distilling the size-mass data shown in Figure 5.7 by considering the median size of the galaxies in each group. We compute these median sizes in two mass bins, $10.25 < \log \mathrm{M}_*/\mathrm{M}_\odot < 10.75$ and $10.75 < \log \mathrm{M}_*/\mathrm{M}_\odot < 11.25$. Both mass bins are above the mass completeness limit for all groups at all redshifts. Choosing narrow mass bins also allows us to compute median half-mass radii without taking into account the slope of the size-mass relation. Figure 5.9 shows median size as a function sSFR for both mass bins. Because the half-mass radii of both star-forming and quiescent galaxies do not show significant redshift evolution between $z = 1$ and $z = 2.5$ (Suess et al., 2019a), we do not split Figure 5.9 by redshift. We have verified that the interpretation of this figure remains unchanged if we do split the sample into multiple redshift ranges.

In agreement with previous studies, we find that quiescent galaxies are smaller on average than star-forming galaxies in both mass bins (e.g., Shen et al., 2003; van der Wel et al., 2014; Mowla et al., 2019b). However, there is not a sudden jump in galaxy size at some sSFR:

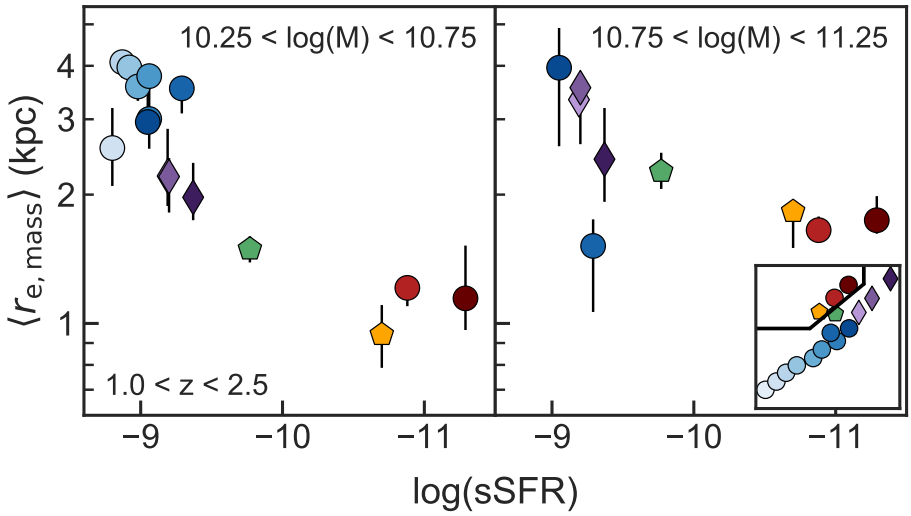

Figure 5.9: Median half-mass radius as a function of sSFR for each group. Each panel represents a different mass range, $10.25 < \log \mathrm{M} < 10.75$ on the left and $10.75 < \log \mathrm{M} < 11.25$ on the right. These mass ranges are chosen to be above the maximum mass completeness limit for all galaxy types at all redshifts. Error bars on the median mass show the 16-84% range of 1000 bootstrap resamples of the median half-mass radius. A median point is only shown for each group if there are more than 5 galaxies in a given group and mass range. The median sizes of galaxies decrease gradually as sSFR decreases. Transitioning galaxies, especially green valley galaxies, have intermediate sizes.

instead, the median size of each galaxy group decreases *smoothly* with decreasing sSFR. We find that the sizes of star-forming galaxies decrease by ~ 0.2 dex as sSFR decreases. This is a slightly stronger trend between size and sSFR than found by Whitaker et al. (2017b), likely due to the fact that we correct for A_v gradients (expected to be stronger in higher-mass and lower-sSFR star-forming galaxies due to their increased dust content, e.g. Magnelli et al., 2009; Murphy et al., 2011; Bourne et al., 2017; Whitaker et al., 2017a). Our results also quantitatively agree with predictions from simulations, where the sizes of star-forming galaxies tend to decrease with decreasing sSFR (e.g., Furlong et al., 2017; Genel et al., 2018). Furthermore, we find that transitional galaxy groups— especially green valley galaxies— have median sizes between those of star-forming and quiescent galaxies (in agreement with previous studies, e.g. Mendez et al., 2011; Yano et al., 2016; Wu et al., 2018). As in Suess et al. (2020), we find that the median sizes of post-starburst galaxies are not significantly smaller than those of older quiescent galaxies at fixed mass.

In Figure 5.10, we consolidate the Σ_1-mass trends seen in Figure 5.8 by showing the sSFR of each group as a function of the median Σ_1 value of galaxies in that group. Each panel shows a different redshift range, and has a corresponding mass completeness cut as indicated at

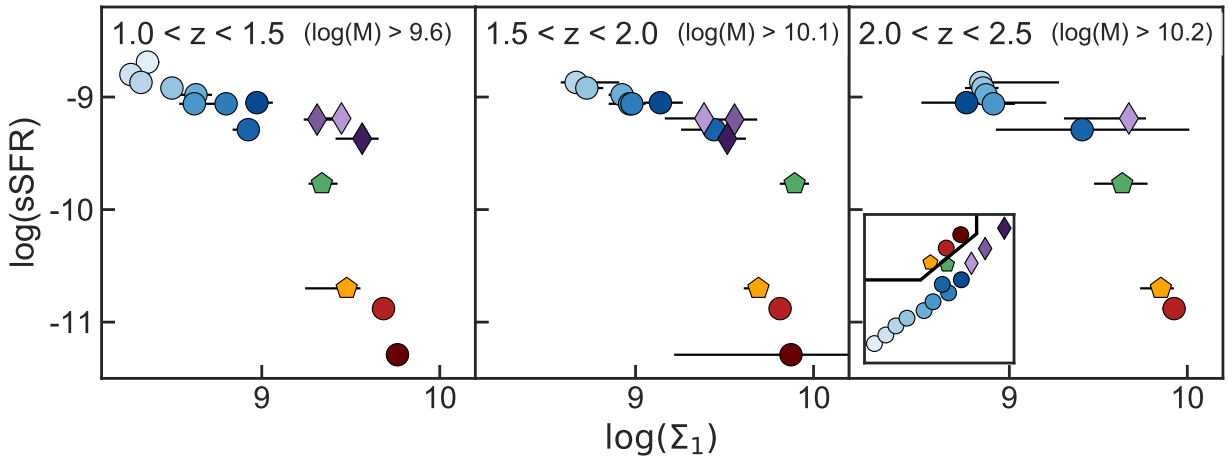

Figure 5.10: Median Σ_1 as a function of sSFR for all galaxy groups. Each panel shows a different redshift interval (and has a corresponding mass completeness level). We see broad agreement with the Barro et al. (2017b) "L-shaped track": star-forming galaxies increase Σ_1 as sSFR gradually decreases, and transitioning and quiescent galaxies have uniformly high Σ_1.

the upper right of each panel. This mass completeness cut corresponds to the most stringent mass completeness cut of any individual group at that redshift. We see broad agreement with the "L-shaped track" from Barro et al. (2017b): sSFR decreases only slightly as star-forming galaxies increase their central densities, then over a relatively narrow range in Σ_1 the sSFRs of galaxies plummets towards quiescence. The bend in this diagram, where a small change in Σ_1 corresponds to a large change in sSFR, consists of massive dusty star-forming galaxies, green valley galaxies, and post-starburst galaxies. These transitional galaxy populations have similar Σ_1 values but dramatically different sSFRs: dusty star-forming galaxies have sSFRs consistent with the star-forming population, green valley galaxies have slightly but not fully suppressed sSFRs, and post-starburst galaxies have low sSFRs close to those of fully quiescent galaxies. We discuss the structures of these transitioning galaxies further in Section 5.5.

The Σ_1 value at which galaxies transition from star-forming to quiescent appears to be a strong function of redshift in Figure 5.10. We caution that this is in large part due to the fact that we take a different mass cut in each redshift interval to retain a mass-complete sample. Because Σ_1 is correlated with mass (e.g., Fang et al., 2013; Barro et al., 2017b; Suess et al., 2020) and our sample does not include lower-mass galaxies at high redshift, our median Σ_1 values for all galaxy types are slightly higher at higher redshift. At fixed mass, the Σ_1 quenching threshold is a much slower function of redshift than it appears in Figure 5.10: in Suess et al. (2020), we show that Σ_1 decreases by just ~ 0.13 dex over this

redshift range (see also, e.g., Barro et al., 2017b; Chen et al., 2020; Estrada-Carpenter et al., 2020).

5.4 Implications for the star-forming sequence

In this section, we discuss the interpretation and implications of our measurements for the star-forming structural relations. We only consider groups 1 - 9, which lie in the star-forming region of the UVJ diagram and have $A_v < 1.5$. Groups 10 - 12— the most massive and dusty star-forming galaxies— and group 13, the green valley galaxies, are discussed in Section 5.5.

Individual star-forming groups follow steep size-mass relations

Figure 5.8 shows that each group of star-forming galaxies traces out a different mass range of the star-forming Σ_1-mass relation. As sSFR decreases, total mass and Σ_1 increase; this indicates that, on average, star-forming galaxies gradually increase both their total mass and the mass in their central kiloparsec as they grow. The slope and scatter of each group of galaxies is similar to the slope and scatter of the overall star-forming Σ_1-mass relation.

In contrast, Figure 5.7 shows that each individual star-forming group appears to have a relatively steep slope in size-mass space, more similar to the quiescent best-fit relation than the star-forming relation. Directly fitting a size-mass relation to each individual galaxy group is challenging due to the clear truncation of our sample at low masses (for details, see e.g. Mantz, 2019). Instead, we test whether each group of star-forming galaxies is better fit by the overall star-forming size-mass relation, or by a relation with the steeper quiescent size-mass slope. We first re-normalize the quiescent size-mass relation, sliding it over in mass to match the observed mass range of each group of star-forming galaxies. We then compute the sum of the root mean square deviations between our observed data and each potential fit. We compare these two values and find that all star-forming groups at all redshifts— other than groups 7 & 8 at high redshift, which have too few galaxies to reliably fit— are better fit by a shifted quiescent relation than by the star-forming size-mass relation. While the data does not demand that each star-forming group lies on a relation with a steep slope similar to the quiescent relation, it does support that conclusion.

It is unlikely that this result is driven purely by sample selection effects. The slope of each star-forming group is steep due to a lack of massive, compact galaxies. However, these massive, compact galaxies have high surface brightness and are thus relatively easy to detect: if they exist, they should be included in our sample. Furthermore, we do not observe any systematic change in observed axis ratio along each star-forming size-mass relation; this indicates that the trends we see are not due to orientation effects. We additionally verify that these trends are not caused purely by orientation effects by examining the sizes and masses of mock observations of simulated star-forming galaxies viewed from different orientations (Price et al., 2017). We find that orientation effects do not preferentially scatter galaxies in the direction of the steep size-mass relations we observe for each star-forming galaxy group.

In light of these observations, we propose a new way to look at the star-forming size-mass relation. Instead of viewing it as a single monolithic relation that holds for all star-forming galaxies, we instead suggest that *the global star-forming size-mass relation is composed of many parallel relations, each of which has a relatively steep slope.* As star-forming galaxies evolve, their SED shapes change, their sSFRs decrease, their masses increase, and their sizes increase mildly in order to move the group up to the next parallel relation. This view of the star-forming size-mass relation is effectively an example of "Simpson's paradox," where trends in aggregated data (e.g., the entire UVJ star-forming population) differ substantially from trends in non-aggregated data (e.g., groups of star-forming galaxies with similar SED shapes).

This parallel relations picture also explains the correlation between galaxy size and sSFR at fixed mass (e.g., Figure 5.9; Whitaker et al., 2017b). Because each group has a relatively broad mass distribution that overlaps with neighboring groups, at fixed mass we are selecting galaxies from multiple different star-forming groups. However, because each group follows a steep size-mass relation, a fixed mass cut preferentially selects large galaxies from the higher-sSFR group (toward the "upper end" of their parallel relation) and small galaxies from the lower-sSFR group (toward the "lower end" of their parallel relation). This can be seen in right panel of Figure 5.11: a vertical mass cut selects the large galaxies in the ligher-blue, higher-sSFR groups, and small galaxies from the darker-blue, lower-sSFR groups.

Explaining the size-mass relation as a reflection of the Σ_1-mass relation and its scatter

We now turn to the connection between the size-mass and Σ_1-mass planes to understand the origin of the steep slopes we observe for each group of star-forming galaxies. Σ_1 and half-mass radius for a given galaxy are connected by the shape and normalization of the galaxy's full mass profile. If we assume that star-forming galaxies follow $n = 1$ Sérsic profiles (e.g., exponential disks), there exists an exact mapping from one structural plane to the other. Because the Σ_1-mass relation has significantly less scatter than the size-mass relation (e.g., Fang et al., 2013), in what follows we use the best-fit Σ_1-mass relation and its scatter to predict how galaxies populate the size-mass plane.

Equations 5 & 6 of Barro et al. (2017b) rewrite the Sérsic profile as a relationship between total stellar mass and Σ_1. Rearranging these equations:

$$\begin{aligned} \log \Sigma_1 &= \log \mathrm{M}_* - \log \pi + \log \gamma(2n, b_n r_e^{-1/n}) \\ &\approx \log \mathrm{M}_* - \log \pi + c_0 + c_1 \log r_e + c_2 (\log r_e)^2 \end{aligned} \tag{5.3}$$

where the c_i values are coefficients describing a second-order power-law fit to the incomplete gamma function. For an $n = 1$ disk profile, Barro et al. (2017b) find $c_0 = 0.31$, $c_1 = 0.96$, and $c_2 = 0.75$.

Equation 5.3 relates Σ_1 to the stellar mass and effective radius. By assuming a best-fit Σ_1-mass relation of the form $\log \Sigma_1 = s \times \log \mathrm{M}_* + k$, we can substitute for Σ_1 and re-write Equation 5.3 as relationship between galaxy sizes and masses:

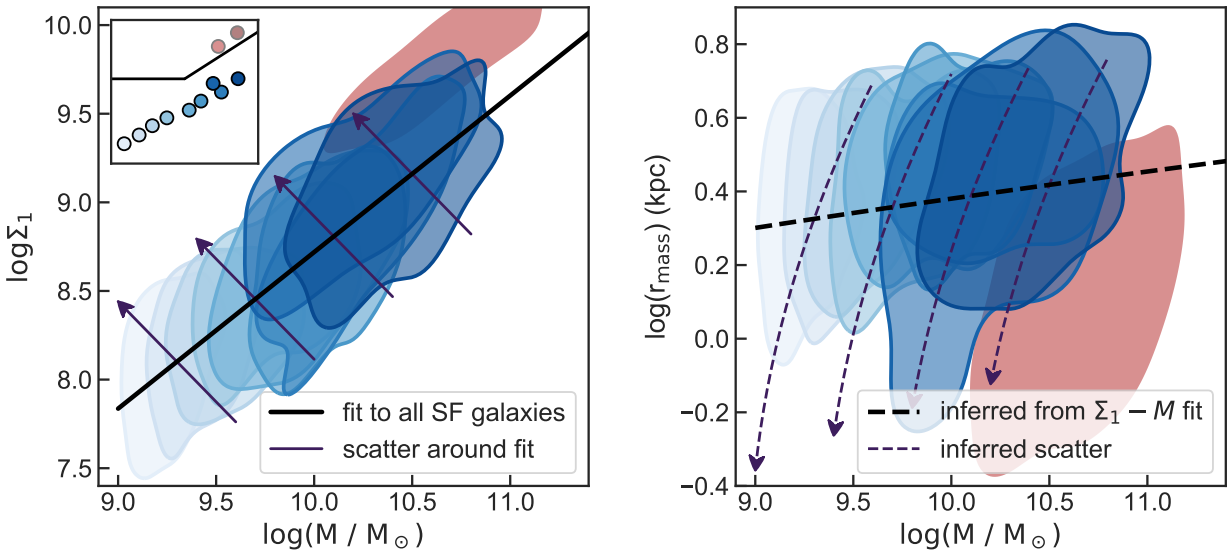

Figure 5.11: The distribution of star-forming galaxies in both the Σ_1-mass (left) and size-mass (right) planes. Blue shaded contours enclose the central 68% of galaxies in each star-forming group (see inset UVJ); the red shaded contour shows the central 68% of the two quiescent groups. Only $z < 2$ galaxies with masses above the $z = 2$ mass completeness limit are shown. While each star-forming group traces out scatter around the Σ_1-mass relation, individual star-forming groups have steep size-mass slopes similar to the quiescent size-mass relation. This reveals that the star-forming size-mass relation is not a single monolithic relation: it is composed of *a series of many steep, overlapping parallel relations* for galaxies with different sSFRs. Furthermore, the distribution of star-forming galaxies in size-mass space can be fully described as a reflection of the Σ_1-mass relation and its scatter. The thick solid line in the left panel shows a linear fit to the star-forming Σ_1-mass relation; the thin perpendicular lines show representative scatter around this relation. Dashed lines in the right panel show *this same fit & scatter*, transformed to the size-mass plane by assuming that star-forming galaxies follow $n \sim 1$ Sérsic profiles. In both panels, arrows point towards more compact galaxies. This transformed Σ_1-mass fit & scatter does an excellent job describing the data in the size-mass plane.

$$\log r_e = \frac{-c_1 + \sqrt{c_1^2 - 4c_2(c_0 + k + \log \pi + (s-1)\log \mathrm{M}_*)}}{2c_2} \tag{5.4}$$

Where we have disregarded the negative root of the quadratic because it produces unphysically small sizes ($\lesssim$ 0.01 kpc). We fit all star-forming galaxies in our sample (e.g., the blue points in Figure 5.5) to find the coefficients k and s that describe the best-fit Σ_1-mass relation for all star-forming galaxies. We find:

$$\log \Sigma_1 = (0.88 \pm 0.01) \times \log \mathrm{M}_* + (-0.11 \pm 0.10) \tag{5.5}$$

These best-fit values are consistent with the Barro et al. (2017b) star-forming Σ_1-mass relation within 1σ, despite differences in the methods used to calculate mass profiles and Σ_1 values from multi-band imaging.

Next, we consider how *scatter* in the Σ_1-mass plane will transform to the size-mass plane. We note that this scatter is not dominated by measurement errors, but reflects true variations in the Σ_1 values of galaxies at fixed mass. We assume that, at some given stellar mass $\mathrm{M}_* = \mathrm{M}_0$, the scatter around the Σ_1-mass relation can be described by a line perpendicular to the best-fit Σ_1-mass relation. Such a perpendicular line can be described by the equation:

$$\begin{aligned} \log \Sigma_1 &= -\frac{1}{s} \times \log \mathrm{M}_* + \left(\frac{\mathrm{M}_0}{s} + \mathrm{M}_0 s + k \right) \\ &= s' \times \log \mathrm{M}_* + k' \end{aligned} \tag{5.6}$$

By plugging these values of s' and k' into Equation 5.4, we can investigate how the scatter in Σ_1-mass space transforms to size-mass space.

We show this transformation from Σ_1-mass to size-mass space in Figure 5.11. The thick line in the left panel shows our best-fit Σ_1-mass relation; the thick dashed line in the right panel shows how this relation transforms to the size-mass plane using Equation 5.4. The thin lines in the left panel show representative scatter around the Σ_1-mass relation. These lines are spaced at equal $\log \mathrm{M}_*$ intervals and each span 0.3 dex in stellar mass; the arrows point towards more compact/smaller galaxies. The dashed lines in the right panel show how this representative scatter transforms to the size-mass plane using Equations 5.4 & 5.6; again, arrows point towards smaller/more compact galaxies. Intriguingly, scatter in the Σ_1-mass plane does *not* translate to lines that are perpendicular to the overall size-mass relation. Instead, scatter in the Σ_1-mass plane corresponds to steep slopes in the size-mass plane.

We then compare the predicted size-mass relation and scatter to our observations. Each shaded blue contour in Figure 5.11 shows the central 68% of galaxies in a single star-forming group; the red contour shows the central 68% of the two quiescent groups to guide the eye. Figure 5.11 includes only $1.0 < z < 2.0$ galaxies with masses above our mass completeness limit at $1.5 < z < 2.0$; this allows us to include high-sSFR galaxies, which typically have stellar masses below our $2.0 < z < 2.5$ completeness limit. We find that the size-mass relation predicted from the best-fit Σ_1-mass relation matches both the normalization and the shallow

slope of the full star-forming sequence. While perhaps unsurprising— we calculate both our Σ_1 and half-mass radius data points from the same mass profiles— this mapping between the size-mass and Σ_1-mass relations has not previously been demonstrated. More surprisingly, we find that the transformed scatter around the Σ_1-mass relation provides a good match to the steep size-mass slopes we observe for each group of star-forming galaxies. This allows us to provide a physical explanation for the "parallel relations" view of the star-forming size-mass relation that we propose in Section 5.4: star-forming galaxies with similar SED shapes populate steep tracks in size-mass space because those steep tracks trace out intrinsic scatter around the Σ_1-mass relation. This mapping also explains why the Σ_1-mass relation is tighter than the size-mass relation: as seen in Figure 5.11 and Equation 5.3, the same $\delta \log \mathrm{M}_*$ produces a relatively small range in Σ_1 but a large range in $\log r_e$ (see also Equation 13 of Barro et al., 2017b).

In Figure 5.12, we show that our transformation from the Σ_1-mass plane to the size-mass plane does not strongly depend on our choice of Sérsic index n as long as it is within typical values for star-forming galaxies. While the slopes and normalizations differ slightly for $n = 0.5$ and $n = 2$ than for $n = 1$, the predictions remain qualitatively similar and remain consistent with our data.

The growth of star-forming galaxies

Several previous studies have suggested that the tight scatter and mild redshift evolution of the star-forming Σ_1-mass relation implies that galaxies evolve *along* the Σ_1-mass relation (e.g., Tacchella et al., 2015a; Barro et al., 2017b; Woo & Ellison, 2019; Chen et al., 2020). At the same time, other studies have concluded that star-forming galaxies evolve along the size-mass relation (e.g., van Dokkum et al., 2015; Lilly & Carollo, 2016; Nelson et al., 2019; Wilman et al., 2020; see also van der Wel et al., 2009). Figure 5.11 allows us to unify these two pictures of the evolution of star-forming galaxies: galaxies grow along the size-mass relation because that growth directly corresponds to evolution along the Σ_1-mass relation. Changes in both the Σ_1-mass and size-mass relations are reflections of the same underlying changes in galaxy mass profiles.

We note that this size growth is relatively slow over the $1.0 < z < 2.5$ range we study here: the change in star-forming half-mass radii at fixed mass is much smaller than expected from half-light radii (Suess et al., 2019b). This nearly self-similar growth is consistent with the roughly flat sSFR profiles that Tacchella et al. (2015b) and Nelson et al. (2016b) observe in $\log M_*/M_\odot \lesssim 10.5$ galaxies at these redshifts. Furthermore, this minimal size growth is consistent with our picture of star-forming galaxies evolving along the structural relations: the slope of the star-forming size-mass relation is only ~ 0.1, implying that sizes increase only sightly as galaxies increase their stellar mass. Similarly, the slope of the Σ_1-mass relation is only slightly less than unity, implying that the mass in galaxy cores grows almost, but not quite, as quickly as total mass (see also Woo & Ellison, 2019).

While star-forming sizes do not evolve rapidly over this redshift range, the strength of color gradients does (Suess et al., 2019a,b). Part of this color gradient evolution could be

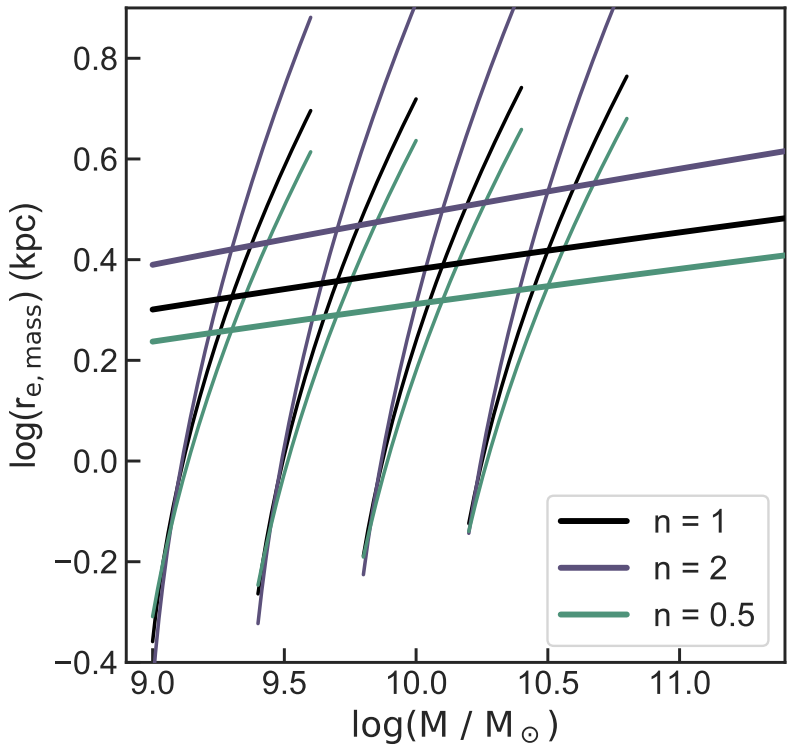

Figure 5.12: How the best-fit Σ_1-mass relation (Equation 5.5) transforms to the size-mass plane assuming different choices of Sérsic index n. While the normalization of the best-fit relation changes slightly, the qualitative picture remains the same despite choice of n.

caused by A_v gradients becoming stronger as galaxies become more massive (e.g., Whitaker et al., 2017a). Mild negative age gradients may also develop as galaxy sizes increase slightly. Probing the relative contribution of metallicity and age gradients could shed further light on how star-forming galaxies assemble their stellar mass. However, our current methods are unable to disentangle age, dust, and metallicity; spatially-resolved spectroscopy or rest-frame mid-IR imaging is required to break these degeneracies. *JWST* will enable the first such studies for a large sample of $z > 1$ galaxies.

Finally, this view of star-forming structural evolution could explain the origin of the steep slope of the quiescent size-mass relation. If some massive star-forming galaxies quench their star formation without significantly altering their structures (e.g., Section 5.5; Wu et al., 2018), then the steep size-mass slope of individual star-forming groups could be preserved as galaxies quench. Galaxies could thus join the red sequence with a steep size-mass slope *already in place*. Minor merger growth after quenching produces steep tracks in the size-mass plane (e.g., Bezanson et al., 2009; Naab et al., 2009; van Dokkum et al., 2010; Patel et al., 2013), further preserving and reinforcing the steep slope of the quiescent size-mass relation.

Like for star-forming galaxies, this steep slope in size-mass space reflects scatter around the Σ_1-mass relation.

5.5 Structures of transitional galaxies

Next, we consider the structural properties of transitioning and quiescent galaxies. Our sample includes three distinct classes of possible quiescent progenitors: post-starburst galaxies, green valley galaxies, and dusty star-forming galaxies. All three of these transitional types lie in the region of Figure 5.10 where a small change in Σ_1 corresponds to a large change in sSFR.

Figure 5.13 shows the color gradient strengths (as measured by $r_{\rm e,mass}/r_{\rm e,light}$), Σ_1 values, and half-mass radii of quiescent and transitional galaxies as a function of stellar mass. Quiescent galaxies (groups 15 and 16) are shown in red; post-starburst galaxies (group 14) are shown in yellow; green valley galaxies (group 13) are shown in green, and dusty star-forming galaxies (groups 10, 11, and 12) are shown in purple. We smooth the data points for each type of galaxies using locally weighted scatterplot smoothing (LOWESS), and use bootstrap resampling to calculate the 16-84% confidence interval. We only show results for groups that contain > 10 galaxies at a given redshift; this cut excludes green valley galaxies at $2.0 < z < 2.5$.

Figure 5.13 shows that the structural properties of transitioning galaxies present a complex picture: different groups have distinct structural properties, and there is obvious dependence on both stellar mass and redshift. This is in contrast to UVJ-selected star-forming and quiescent galaxies, whose structures do not evolve significantly over the redshift range studied here (Suess et al., 2019a,b). The following subsections discuss the structures of each type of transitional galaxies in detail.

Post-Starburst Galaxies

Post-starburst galaxies have low sSFRs and strong Balmer breaks; their spectra indicate that they recently shut off a major burst of star formation (e.g., Dressler & Gunn, 1983; Couch & Sharples, 1987; Zabludoff et al., 1996; Le Borgne et al., 2006). Figure 5.13 shows that $\log M_*/M_\odot \gtrsim 10$ post-starburst galaxies have sizes and Σ_1 values consistent with quiescent galaxies. However, post-starburst galaxies have flat or even slightly positive color gradients, unlike the negative color gradients we observe in both star-forming and quiescent galaxies at this mass and redshift (Suess et al., 2019a). These measurements agree with our previous results in Suess et al. (2020), which used a slightly different UVJ color-based selection method to identify post-starburst galaxies (see also Maltby et al., 2018). In Suess et al. (2020), we argue that these structural properties are consistent with post-starburst galaxies quenching via a rapid "compaction"-like process, where elevated central star formation rates flatten existing negative color gradients, raise Σ_1, and decrease half-mass and half-light radii (see, e.g., Dekel & Burkert, 2014; Zolotov et al., 2015; Tacchella et al., 2016).

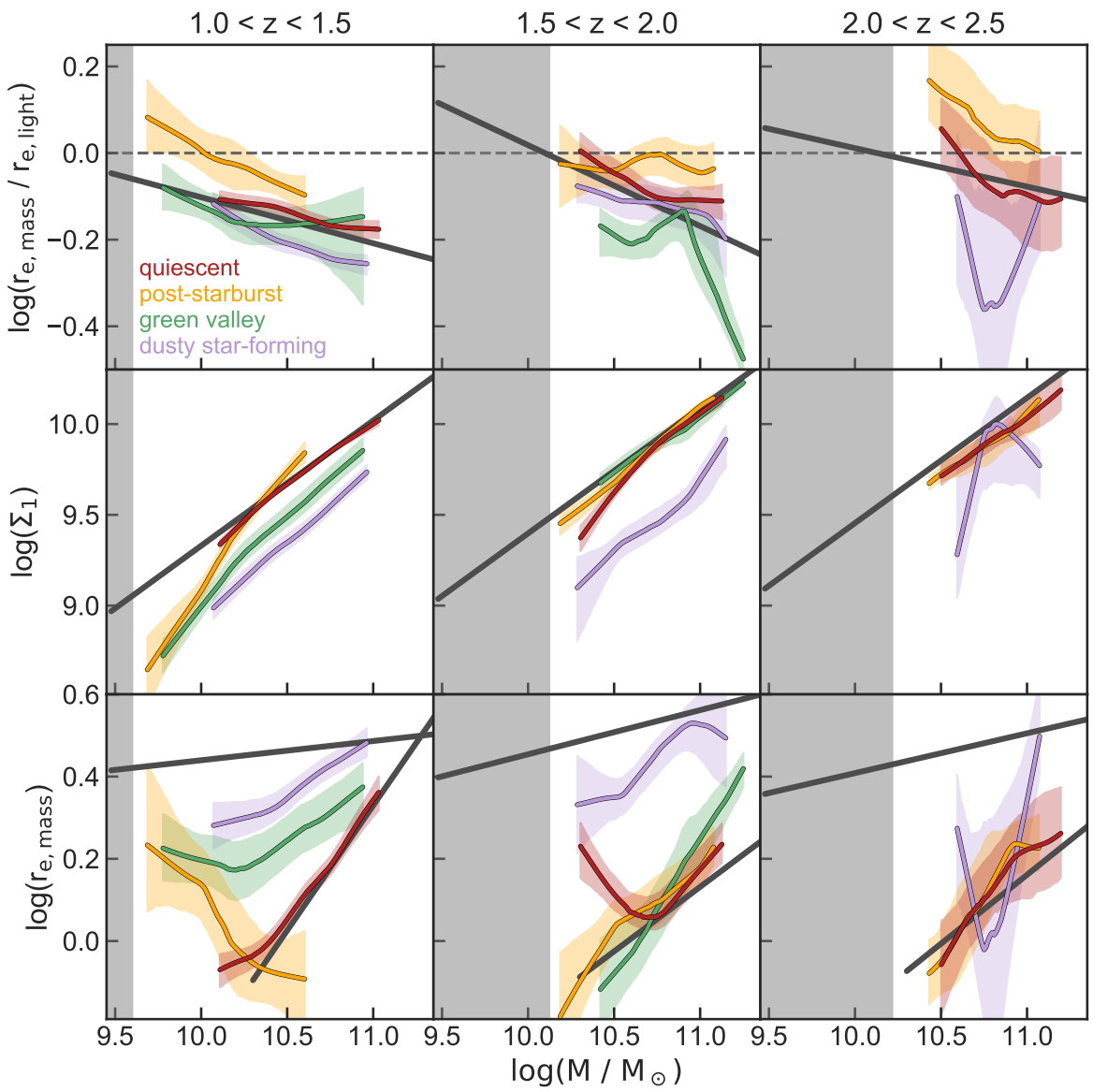

Figure 5.13: Color gradient strength (top row), central density (middle row) and half-mass radius (bottom row), for post-starburst galaxies (yellow), green valley galaxies (green), fully quiescent galaxies (red), and dusty star-forming galaxies (purple). Scatter points for each group of galaxies have been smoothed using LOWESS regression; the shaded regions represent the 1σ confidence interval from 500 bootstrap realizations of the LOWESS smoothing. A given group is only shown if it contains > 10 galaxies at that redshift; this excludes green valley galaxies at $2.0 < z < 2.5$. Grey lines show the best-fit color gradient-mass relations (Figure 5.6), the quiescent Σ_1-mass relation (Suess et al., 2020), and the star-forming and quiescent size-mass relations (Suess et al., 2019a).

In contrast to $z > 1.5$, there are no high-mass ($\log M_*/M_\odot \gtrsim 10.5$) post-starburst galaxies in our sample at $z < 1.5$. This result is consistent with previous studies which find that the number density of massive post-starburst galaxies drops by a factor of $\sim 2-5$ between $z \sim 2$ and $z \sim 1$ (e.g., Whitaker et al., 2012a; Wild et al., 2016; Belli et al., 2019). High-mass transitional galaxies do exist in our sample at low redshift; however, they are classified as either green valley or dusty star-forming galaxies, not post-starburst galaxies.

At $1.0 < z < 1.5$, we see a significant population of low-mass ($\log M_*/M_\odot \lesssim 10$) post-starburst galaxies (in agreement with number density measurements from Wild et al., 2016). These low-mass post-starburst galaxies have distinct structures from their more massive counterparts: while massive post-starburst galaxies have small sizes and high Σ_1 values, low-mass post-starburst galaxies have relatively larger sizes and lower Σ_1 values. These results agree with Maltby et al. (2018), who used light profiles to conclude that low-redshift post-starburst galaxies tend to have low masses and large sizes. Our results additionally show that low-redshift, low-mass post-starburst galaxies have more positive color gradients (e.g., relatively bluer centers) than their higher-mass counterparts. The distinct structural properties of these low-mass post-starburst galaxies may imply they are quenching via a different process than high-mass post-starburst galaxies. In particular, environmental effects are typically more important for $M_* \lesssim 10^{10} M_\odot$ galaxies, and may be playing an additional role in transforming both the sSFRs and structures of these galaxies (e.g., Peng et al., 2010; Schawinski et al., 2014; Ji et al., 2018). Both Socolovsky et al. (2018) and Moutard et al. (2018) show that low-mass, low-redshift post-starburst galaxies are more likely to reside in dense environments than in isolation, confirming that environmental effects are important for these galaxies.

Green Valley Galaxies

Green valley galaxies have intermediate star formation rates and lie along the diagonal edge of the UVJ quiescent box; previous studies have suggested they are on their way towards quiescence (see, e.g., Patel et al., 2011; Fang et al., 2018; Gu et al., 2018). We note that the term "green valley" was originally used to refer to transitional galaxies selected from color-magnitude or color-mass space (e.g., Bell et al., 2004; Martin et al., 2007; Wyder et al., 2007; Faber et al., 2007; Mendez et al., 2011; Gonçalves et al., 2012). However, these single-color selections can include both dusty star-forming galaxies (e.g., Brammer et al., 2009) and multiple different types of transitional galaxies (e.g., Schawinski et al., 2014). Later studies therefore introduced a second color, selecting green valley galaxies from color-color space (e.g., Patel et al., 2011; Arnouts et al., 2013; Fang et al., 2018; Gu et al., 2018). The green valley sample we discuss in this section is selected by rest-frame SED shape (Section 5.2), and is more similar to a color-color selected sample than a color-magnitude selected sample.

Our composite SED fits show that the green valley galaxies in our sample have longer star formation timescales and larger A_v values than our post-starburst group. Like post-starburst galaxies, we see significant changes in the green valley population across redshift. Unlike post-starburst galaxies, however, we find that green valley galaxies are more abundant

towards lower redshift. There are just nine green valley galaxies in our sample at $z > 2$, too few to show in Figure 5.13.

At $1.5 < z < 2.0$, green valley galaxies have high Σ_1 values and relatively small sizes that are similar to both post-starburst and quiescent galaxies. However, green valley galaxies have stronger negative color gradients than either post-starburst or quiescent galaxies. As discussed further in Section 5.6, these differences in color gradient strength indicate that green valley and post-starburst galaxies have different formation mechanisms. Furthermore, the fact that both green valley galaxies and star-forming galaxies have negative color gradients indicates that green valley galaxies do not have to significantly alter the radial distribution of their stellar populations in order to quench. We discuss the implications of these measurements for quenching in Section 5.6.

Massive ($\log M_*/M_\odot \gtrsim 10.5$) green valley galaxies at $1.0 < z < 1.5$ have slightly larger sizes and lower Σ_1 values than their higher-redshift counterparts. The sizes and Σ_1 values of these green valley galaxies are no longer consistent with the bulk of the quiescent population. These differences are accentuated at low masses, where green valley galaxies are further offset towards large sizes and low Σ_1. At these low masses and redshifts, the sizes and Σ_1 values of green valley galaxies are consistent with those of post-starburst galaxies. But again, green valley and post-starburst galaxies have different color gradient strengths suggesting differences in the radial distributions of their stellar populations. Similar to low-mass post-starburst galaxies, environmental effects are likely important for quenching low-mass green valley galaxies (e.g., Peng et al., 2010)

We note that the large sizes of low-mass green valley and post-starburst galaxies appear to be responsible for the previously-observed flattening of the quiescent size-mass relation at $\log M_*/M_\odot \lesssim 10$ (e.g., Cappellari et al., 2013; van der Wel et al., 2014; Norris et al., 2014; Whitaker et al., 2017b). If we used UVJ colors to bin our sample into just two groups, star-forming or quiescent, most post-starburst galaxies and some green valley galaxies would be classified as quiescent. The large sizes of these transitional galaxies at low masses would drag the median inferred size of quiescent galaxies up.

Dusty Star-Forming Galaxies

The dusty star-forming galaxies in our sample have $A_\mathrm{v} > 1.5$ mag, high stellar masses, and relatively high Σ_1 values (Figure 5.10). We note that on average, the dusty star-forming galaxies in our sample are less extreme than submillimeter-selected dusty star-forming samples, with SFR $\sim 200 M_\odot \mathrm{yr}^{-1}$ and modest submillimeter fluxes (e.g., Spitler et al., 2014). Figure 5.13 shows that the structures of dusty star-forming galaxies depend on redshift. At $z \lesssim 2$, dusty star-forming galaxies tend to have mild negative color gradients, relatively large sizes, and Σ_1 values below the quiescent population. At $z > 2$, however, we find that most dusty star-forming galaxies have small sizes, high Σ_1 values, and strong negative color gradients.

These compact $z > 2$ dusty star-forming galaxies have similar properties to "blue nugget" or "compact star-forming galaxy" samples that are selected by their small sizes or high Σ_1

values (e.g., Barro et al., 2014; van Dokkum et al., 2015). The compact structures, high stellar masses, and rapid number density evolution of these galaxies has led previous studies to conclude that compact star-forming galaxies are likely progenitors of compact quiescent galaxies (e.g., Barro et al., 2014; Nelson et al., 2014; van Dokkum et al., 2015; Barro et al., 2017a,b). Interestingly, we have recovered a structurally similar sample despite not explicitly selecting for compactness. This implies that compact structures are actually the norm for massive dusty star-forming galaxies at $z > 2$. Moreover, we show that the mass profiles of these compact galaxies are even more concentrated than their light profiles.

The strong negative color gradients we observe in $z > 2$ dusty star-forming galaxies are consistent with the idea that these galaxies are experiencing a strong dust-obscured central starburst before reaching quiescence (e.g., Barro et al., 2017a). IFU and ALMA studies of a small sample of dusty star-forming galaxies indicate that they have extremely dust-obscured centers and strong radial A_v gradients (e.g., Nelson et al., 2016a; Barro et al., 2017a; Tacchella et al., 2018; Tadaki et al., 2020). While a central starburst also creates positive age gradients, these strong A_v gradients likely dominate to create our observed negative color gradients.

At $1.0 < z < 2.0$, the dusty star-forming galaxies in our sample have mild negative color gradients, relatively large sizes, and lower Σ_1 values. These galaxies are consistent with an extension of the star-forming sequence discussed in Section 5.4: dusty star-forming galaxies have slightly higher masses, lower sSFRs, smaller median sizes, and higher Σ_1 values than their lower-A_v counterparts. But unlike high-redshift dusty star-forming galaxies, low-redshift dusty star-forming galaxies do not have dramatically different structures than galaxies with slightly higher sSFRs.

The lack of compact dusty star-forming galaxies in our sample at $z < 2$ is broadly consistent with Barro et al. (2013) and van Dokkum et al. (2015), who found that the number density of compact star-forming galaxies decreases rapidly below $z \sim 2$. We do, conversely, see some extended dusty star-forming galaxies at $z > 2$. Like their lower-redshift counterparts, these galaxies have relatively lower Σ_1 and more mild negative color gradients. From Figures 5.7 & 5.8, we see that these extended galaxies are typically found in group 10, which has less dust and a lower sSFR than groups 11 & 12. In Section 5.6, we discuss the implications of both extended and compact dusty star-forming galaxies for quenching and the buildup of the red sequence.

Finally, we note that our size measurements for these dusty star-forming galaxies do not appear to be driven by observational biases. First, inclination bias does not seem to play an important role: the observed axis ratios of the compact and extended $z > 2$ dusty star-forming galaxies do not differ significantly (though see Mowla et al., 2019a). Second, our methods appear able to accurately recover the half-mass radii of dusty star-forming galaxies despite their highly dust-obscured centers. We test this by cross-matching our catalog to the rest-frame far-IR sizes of massive star-forming galaxies as measured by Tadaki et al. (2020); these ALMA measurements are able to peer through dust and provide an independent and potentially less-biased view of the mass profiles of these galaxies. We find a median offset of just 0.15 dex between our half-mass radii and the Tadaki et al. (2020) rest-frame far-IR sizes, indicating that our methodology is not drastically overestimating galaxy sizes due to

underestimated A_v gradients. We note that the half-light radii of galaxies in our sample are offset from the Tadaki et al. (2020) measurements by 0.4 dex.

5.6 Implications for galaxy growth and quenching

A growing number of recent studies have suggested the existence of two distinct pathways to quench galaxies, a "fast" pathway in which galaxies stop their star formation abruptly, and a "slow" path in which quenching happens more gradually (e.g., Barro et al., 2013, 2014; Schawinski et al., 2014; Wild et al., 2016; Carnall et al., 2018; Forrest et al., 2018; Wu et al., 2018; Rowlands et al., 2018; Woo & Ellison, 2019; Belli et al., 2019). Fast-quenching galaxies tend to have post-starburst SEDs, while slow-quenching galaxies typically fall into the "green valley" region between the quiescent and star-forming regions of the UVJ diagram. In addition to differences in timescales, these studies have found that slow-quenching green valley galaxies are on average larger and diskier than fast-quenching post-starburst galaxies.

The above studies have ascribed these differences in structures and quenching timescales to two distinct physical quenching mechanisms operating in green valley and post-starburst galaxies. However, other studies suggest that we may see rapidly-quenching galaxies at high redshift because there is some intrinsic spread in galaxy star formation timescales, and at high redshift the universe is simply too young to observe any slow-quenching galaxies (e.g., Lilly & Carollo, 2016; Abramson et al., 2016). In this case, the larger sizes of green valley galaxies can be explained through progenitor bias: star-forming galaxies are smaller at high redshift, so galaxies which quench rapidly at high redshift are smaller than galaxies which quench slowly at low redshift.

In this section, we explore what our structural measurements imply for galaxy growth and quenching, and evaluate whether our observations support two distinct physical mechanisms for quenching. Our study adds multiple new pieces of information to this discussion. First, our sizes and Σ_1 values are calculated from mass profiles, mitigating biases introduced by variations in color gradient strength between different galaxy types (Figure 5.6). Second, we are able to use the strengths of color gradients themselves as an additional tool to understand how galaxies grow and evolve. Third, our sample includes galaxies of all types across both the star-forming and quiescent sequences, instead of pre-selecting just a few types of transitional galaxies. In particular, this allows us to understand how massive dusty star-forming galaxies fit into the story of how galaxies quench.

Table 5.2 summarizes our structural measurements, discussed in detail in Sections 5.4 & 5.5. Further details on the structures of post-starburst and quiescent galaxies can also be found in Suess et al. (2020).

Two distinct quenching pathways

Here we assess whether our observations support multiple distinct physical mechanisms for quenching. If the physics responsible for quenching green valley and post-starburst galaxies

Table 5.2: Summary of our structural measurements, discussed in detail in Sections 5.4 & 5.5. For brevity we have only included our highest- and lowest-redshift intervals. At intermediate redshifts, both post-starburst and green valley galaxies have similar sizes as quiescent galaxies.

	high z ($2 \lesssim z \lesssim 2.5$)			low z ($1 \lesssim z \lesssim 1.5$)		
	Σ_1	size	color gradient	Σ_1	size	color gradient
star-forming	low	large	negative	low	large	negative
dusty star-forming	high	small	strong negative	intermediate	large	negative
green valley	rare			intermediate	intermediate	negative
post-starburst (massive)	high	small	flat	rare		
post-starburst (low-mass)	below completeness limit			intermediate	intermediate	flat
quiescent	high	small	negative	high	small	negative

is the same— post-starburst galaxies just have rapid star formation timescales, whereas green valley galaxies have slower star formation timescales— then any difference in their structures would be due to progenitor bias effects. In this scenario, green valley and post-starburst galaxies should have comparable structures at fixed mass and redshift, because they are quenching from the same population of star-forming galaxies. At $1.5 < z < 2.0$ our sample includes both post-starburst and green valley galaxies with $\log M_*/M_\odot \gtrsim 10$, where environmental effects are likely not dominant. This overlapping sample allows us to test this prediction.

Figure 5.13 shows that the sizes and Σ_1 values of post-starburst and green valley galaxies at $1.5 < z < 2.0$ are indeed consistent. However, the two classes of galaxies have *systematically different color gradients*. Because these color gradients describe radial variations in stellar population properties, these systematic color gradient differences indicate that post-starburst and green valley galaxies likely assembled their stellar mass via different physical processes. The differences between these slow- and fast-quenching galaxies cannot simply be ascribed to differences in their star formation timescales or overall dust content: they must have different formation mechanisms (see also, e.g., Barro et al., 2013; Woo & Ellison, 2019;

Belli et al., 2019; Wu et al., 2020). Our novel color gradient measurements thus support the idea that green valley and post-starburst galaxies represent two truly different pathways to quenching.

Figure 5.14 provides an illustration of how these fast and slow quenching pathways map onto the Σ_1-mass, size-mass, color gradient-mass, and UVJ diagrams we discuss in this chapter. Again, we emphasize that these two pathways show proposed *average* growth and quenching mechanisms: the tracks that individual galaxies follow in these structural planes are likely more complex and stochastic. This figure also illustrates $z \gtrsim 1.5$, where green valley and post-starburst galaxies have similarly compact sizes; the relatively larger sizes of low-redshift green valley galaxies are discussed further in Section 5.6.

We create two toy models to illustrate these fast and slow quenching pathways in UVJ space. These toy models assume a delayed-τ star formation history and use FSPS (Conroy et al., 2009; Conroy & Gunn, 2010) to generate model UVJ colors. Following Barro et al. (2014) and Belli et al. (2019), we assume that dust evolves following the star formation rate, A_v peaks at 2.5 mag, and quiescent galaxies have $A_v = 0.4$ mag. The black track shows a slow pathway, with $\tau = 500$ Myr; the grey track shows a fast pathway, with $\tau = 100$ Myr. The fast pathway goes through the post-starburst region of UVJ space after just ~ 600 Myr. The slow pathway joins the quiescent sequence through the green valley after ~ 2 Gyr without crossing through the post-starburst region. Both of the fast and slow tracks cross through the dusty star-forming region; however, the fast track does so just 150 Myr into its evolution, whereas the slow track does so after nearly a full gigayear.

We note that altering our assumptions about dust evolution will change the exact locations of these tracks in UVJ space. A lower maximum A_v will cause the tracks to quench without going through the dusty star-forming region. Alternately, additional dust can cause the fast track to go close to the diagonal UVJ quiescent line, near the green valley region. This implies that selecting green valley galaxies by their location in UVJ space alone may include some dusty fast-quenching galaxies at high redshift (see, e.g., Zick et al., 2018). We emphasize again that our selection in this study is based on SED shape, not UVJ colors alone.

Slow growth & quenching

In Section 5.4, we discuss a slow average growth mode where star-forming galaxies gradually increase their masses, sizes, and Σ_1 values as they form stars. The bottom panels of Figure 5.14 show how this growth maps onto the Σ_1-mass and size-mass planes, and the top right panel shows the corresponding color gradient-mass evolution. We suggest that galaxies are born at low stellar masses and low Σ_1 values with some intrinsic scatter around the Σ_1-mass relation. This scatter around the Σ_1-mass relation maps onto the size-mass plane as relatively steep slopes similar to that of the traditional quiescent size-mass relation (Section 5.4). This scatter may be caused by variations in the concentration of dark matter halos (e.g., Jiang et al., 2019; Chen et al., 2020).

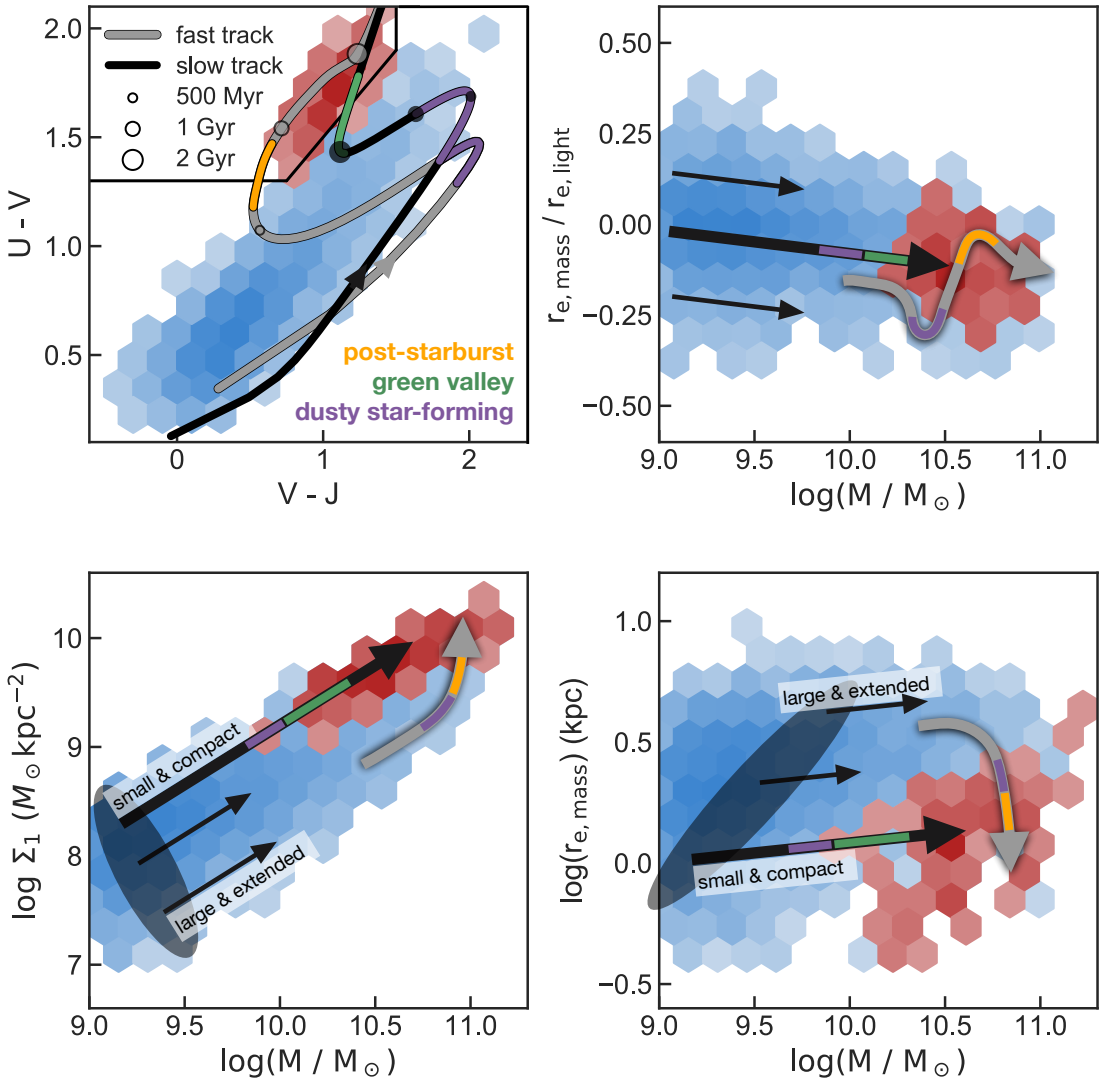

Figure 5.14: Schematic of our proposed growth and quenching pathways for the evolution of galaxies in the UVJ, Σ_1-mass, and size-mass planes at $z \sim 1.5$. Red and blue shaded hexagons show the galaxies in our sample, binned into quiescent and star-forming groups using the Whitaker et al. (2012b) UVJ classification. Toy model UVJ tracks show the evolution of a fast-quenching/post-starburst galaxy with $\tau = 100$ Myr (grey) and a slow-quenching/green valley galaxy with $\tau = 500$ Myr (black). Shaded circles along the UVJ tracks indicate 500 Myr, 1 Gyr, and 2 Gyr into the track's evolution. The right two panels show how our structural measurements map onto these growth and quenching pathways. We propose that, on average, galaxies are born with some intrinsic scatter around the Σ_1-mass relation (corresponding to steep tracks in the size-mass plane), then grow parallel to the best-fit Σ_1-mass and size-mass relations. Green valley galaxies quench after this growth eventually pushes them across the high Σ_1 quenching threshold; post-starburst galaxies quench after a compaction event causes their Σ_1 values to increase and half-mass radii to decrease. The complex color gradient evolution we propose for post-starburst galaxies reflects a highly dust-obscured central starburst: once the burst stops and the strong A_v gradients fade, the products of this rapid quenching process should show flat or positive age gradients. The two pathways are shown operating at different masses purely for readability; both slow and fast quenching can produce quiescent galaxies across a wide stellar mass range. Again, we stress that these growth and quenching pathways represent the average evolution of galaxies in these structural planes— the evolution of individual galaxies is likely much more complex and stochastic.

Figure 5.11 shows that as we go up in mass and down in sSFR, star-forming galaxies with similar SED shapes march up the Σ_1-mass and size-mass structural relations, roughly preserving the scatter around the Σ_1-mass relation and its reflection in size-mass space. Physically, this means that larger galaxies will stay larger and smaller galaxies will stay smaller as they form stars (as shown by small black arrows in Figure 5.14). This small size increase with increasing mass implies that star-forming galaxies at these masses grow their outskirts slightly faster than their cores, creating shallow negative age gradients observable as negative color gradients.

If this slow growth continues, galaxies will eventually evolve far enough along the Σ_1-mass, size-mass, and color gradient-mass relations to reach the high Σ_1 values required for quiescence. Before becoming fully quiescent, these slow-quenching galaxies will pass through a transitional phase where they have intermediate sSFRs and Σ_1 values. The structural measurements we present in Section 5.5 indicate that green valley galaxies represent this slow-quenching transitional phase. Furthermore, at $z \lesssim 2$ we find that dusty star-forming galaxies have relatively large sizes and low Σ_1 values in between those of green valley galaxies and the rest of the star-forming sequence. These results suggest that some slow-quenching galaxies go through a dusty star-forming phase before passing through the green valley to the quiescent sequence. This agrees with the slow-quenching toy model shown in Figure 5.14, which passes through the dusty star-forming region before reaching the green valley.

Fast quenching

The fast quenching pathway is associated with "compaction"-type events (e.g., Dekel & Burkert, 2014; Zolotov et al., 2015; Tacchella et al., 2016). In this picture, strong gas inflows or gas-rich major mergers funnel gas to the center of the galaxy, causing a central starburst. This centrally-concentrated starburst will increase Σ_1 and decrease size, effectively lifting galaxies up to the quiescent Σ_1-mass relation (e.g., Woo et al., 2015; Woo & Ellison, 2019). During a compaction event, we expect galaxies to show high Σ_1, small sizes, and negative color gradients due to their highly dust-obscured central starbursts. These structural properties are consistent with our observations of high-redshift compact dusty star forming galaxies (Section 5.5). After star formation stops and A_v gradients fade, this scenario predicts small sizes and high Σ_1 values. The color gradients of these galaxies should also be less extreme: young stars created in the central starburst are no longer highly dust-obscured, resulting in a positive age gradient. These predicted sizes, Σ_1 values, and color gradients are consistent with our observations of post-starburst galaxies in Figure 5.13 (though whether age gradients in post-starburst galaxies are flat or positive is observationally unclear, see e.g., Setton et al., 2020; D'Eugenio et al., 2020). Thus, our measurements lead us to speculate that fast-quenching galaxies may go through a compact dusty star-forming phase then a post-starburst phase before ultimately joining the quiescent population. This matches the fast-quenching toy model shown in Figure 5.14, which goes through the dusty star-forming region of UVJ space before the post-starburst phase. Further studies directly comparing the number density and star formation histories of dusty star-forming galaxies and post-

starburst galaxies could directly test this theory, but are beyond the scope of our current study.

Finally, we note that in Figure 5.14 we show this compaction process taking place at $\log M_*/M_\odot \sim 10.75$. This is mostly for illustrative purposes: in principal, fast quenching could create quiescent galaxies over a wide mass range. However, this compaction process *is* expected to operate primarily at higher redshift, towards the peak of the cosmic star formation rate (e.g., Dekel et al., 2009; Kereš et al., 2009; Zolotov et al., 2015).

Implications for the buildup of the red sequence

We have described two distinct routes for galaxies to join the red sequence: fast quenching through the post-starburst phase, and slow quenching through the green valley. Here, we describe how these two pathways work in tandem to build up the massive ($\log \mathrm{M_*/M_\odot} \gtrsim 10$) range of the red sequence.

At $z > 2$, we find that transitional galaxies tend to belong to the post-starburst group, while green valley galaxies are much less abundant. This indicates that massive quiescent galaxies are produced primarily through the rapid quenching pathway (in agreement with, e.g., Wild et al., 2016; Belli et al., 2019). Because post-starburst galaxies have small sizes and high Σ_1, most galaxies that join the quiescent sequence at $z > 2$ will be compact. The dominance of the rapid pathway at high redshift is unsurprising given that the universe is still young: most slow-quenching galaxies have not yet had sufficient time to reach high Σ_1. However, we do begin to see some relatively large, low Σ_1 dusty star-forming galaxies at this redshift. These galaxies, which in Section 5.6 we argue are part of the slow quenching pathway, point towards the emergence of a larger population of slow-quenching green valley galaxies towards lower redshift.

Indeed, at $1.5 < z < 2.0$ we find that both green valley and post-starburst galaxies contribute to the growth of the quiescent population. Both transitional types have small sizes and high Σ_1 values at this redshift; again, this means that relatively compact galaxies are being added to the red sequence. Because the sizes and Σ_1 values of newly-quenched galaxies do not evolve significantly from $z \sim 2.5$ to $z \sim 1.5$, progenitor bias does not contribute significantly to evolution of the quiescent sequence at these redshifts (see also Suess et al., 2019b, 2020). At these intermediate redshifts, compact dusty star-forming galaxies have essentially disappeared from our sample (in agreement with, e.g., Barro et al., 2014, 2016; van Dokkum et al., 2015). Because these compact dusty star-forming galaxies galaxies are likely linked to the fast quenching pathway, their disappearance signals a lack of massive post-starburst galaxies in our sample at $z < 1.5$.

At $1.0 < z < 1.5$, we find that massive quiescent galaxies are primarily produced via the slow pathway: green valley galaxies are common, whereas we do not find any massive post-starburst galaxies (in agreement with, e.g., Whitaker et al., 2012a; Wild et al., 2016; Rowlands et al., 2018; Belli et al., 2019). The lack of fast-quenching galaxies at low redshift makes sense given that the compaction events thought to trigger rapid quenching rely on rapid gas inflow to create a central starburst (e.g., Dekel & Burkert, 2014; Zolotov et al.,

2015; Tacchella et al., 2016). However, because the gas content of galaxies declines rapidly towards lower redshift (e.g., Tacconi et al., 2020, and references therein), compaction events and rapidly-quenched galaxies should become relatively rare at lower redshift.

Interestingly, we find that green valley galaxies have larger sizes and lower Σ_1 values at $1.0 < z < 1.5$ than at $z > 1.5$, indicating that more extended galaxies are being added to the quiescent population. The larger sizes of these green valley galaxies are not primarily caused by an increase in the sizes of their star-forming progenitors: the half-mass radii of star-forming galaxies do not grow significantly between $z \sim 2.5$ and $z \sim 1$ (Suess et al., 2019a,b). Instead, as illustrated in Figure 5.14, we expect that galaxies which are born above the median Σ_1-mass relation are the first to quench through the green valley— these small, compact galaxies have a head start on reaching the high Σ_1 values required for quiescence. As we move to lower redshift, there is more time for galaxies born below the median Σ_1-mass relation to grow to high Σ_1 values. Adding these larger, lower Σ_1 green valley galaxies to the quiescent population at $z < 1.5$ will drive the median size of quiescent galaxies to increase, and the median Σ_1 of quiescent galaxies to decrease (e.g., progenitor bias, van Dokkum & Franx, 2001; Carollo et al., 2013; Lilly & Carollo, 2016). Indeed, Barro et al. (2017b) shows that the zeropoint of the quiescent Σ_1-mass relation decreases by ~ 0.2 dex between $z \sim 1.25$ and $z \sim 0.25$. Because this progenitor bias effect is primarily caused by slow-quenching green valley galaxies, it is most important at low redshift. This explains the apparent discrepancy between Suess et al. (2020)— who find that Σ_1 does not depend on age for quiescent galaxies at $z \sim 1.5$— and Tacchella et al. (2017), who find that Σ_1 *does* depend on age at $z \sim 0$.

Finally, we note that the prevalence of slow quenching at $z \lesssim 1$ naturally explains the occurrence of large quiescent disk galaxies at $z \lesssim 0.5$ (e.g., van den Bergh, 1976; Couch et al., 1998; Dressler et al., 1999; Masters et al., 2010; Bundy et al., 2010). Slow-quenching green valley galaxies appear to shut down their star formation without significantly altering their structures (e.g., Section 5.6; Wu et al., 2018), allowing them to retain the disky structures of their star-forming progenitors as they quench. The cutouts in Figure 5.4 show that many low-redshift green valley galaxies are indeed large and disky, resulting in large disky quiescent galaxies.

In summary, we suggest that the $\log M_*/M_\odot \gtrsim 10$ quiescent sequence is built up primarily by rapidly-quenching post-starburst galaxies at $z \gtrsim 1.5$, then by slow-quenching green valley galaxies at $z \lesssim 1.5$. Progenitor bias effects become more important at lower redshift as larger green valley galaxies begin joining the quiescent population. Compact dusty star-forming galaxies at high redshift are primarily associated with fast quenching, whereas extended dusty star-forming galaxies at low redshift seem to be more consistent with green valley progenitors. Finally, we note that our sample includes low mass ($\log M_*/M_\odot \lesssim 10$) galaxies only at $1.0 < z < 1.5$. We find that low-mass transitional galaxies can be found in either the post-starburst or green valley groups, but tend to have large sizes and low Σ_1 values. These galaxies may be produced via environmental quenching processes (e.g., Peng et al., 2010; Schawinski et al., 2014; Ji et al., 2018).

5.7 Summary

In this chapter, we move beyond a bimodal view of the galaxy size-mass and Σ_1-mass relations to study the masses, half-mass radii, Σ_1 values, and color gradient strengths of a wide range of galaxy types. We use a clustering algorithm to separate a sample of $\sim 7,000$ galaxies at $1.0 < z < 2.5$ into sixteen groups with similar rest-frame SED shapes. Different groups of galaxies have distinct stellar masses, sSFRs, ages, and dust content. These groups represent different phases of galaxy evolution, ranging from young unobscured star-forming galaxies to old quiescent galaxies. We then use these groups to investigate how different types of galaxies populate the size-mass and Σ_1-mass structural planes.

We find that the strength of radial color gradients differs for each group of galaxies. In Suess et al. (2019a), we established that more massive galaxies have more strongly negative color gradients; the color gradients of most galaxy groups are fairly well-predicted by this color gradient - mass relation. However, we find two outliers: post-starburst galaxies have flatter color gradients than expected from their mass and redshift, while extremely dusty star-forming galaxies tend to have stronger negative radial color gradients than expected. The fact that the strength of color gradients varies between different groups of galaxies underscores the importance of using mass profiles and half-mass radii: using light profiles and half-light radii would result in biased structural measurements.

We show that each group of galaxies populates a distinct and fairly localized region of size-mass space. Moving beyond a simple "star-forming vs quiescent" bimodal sample selection reveals that, on average, galaxy sizes and Σ_1 values vary smoothly with SED type. In particular, we find that the size of galaxies at fixed mass is a gradual function of sSFR: there is not a sudden jump from large star-forming galaxies to small quiescent galaxies, but instead a gradual decrease in average size towards lower sSFRs.

We find that each group of star-forming galaxies appears to lie on a steep size-mass relation, more consistent with the quiescent size-mass slope than the shallow overall star-forming slope. These steep relations can be explained by considering the size-mass plane as a reflection of the Σ_1-mass plane. We show that, if we assume star-forming galaxies follow simple $n = 1$ Sérsic profiles, the best-fit Σ_1-mass relation predicts both the normalization and the shallow slope of the star-forming size-mass sequence. Scatter around the best-fit Σ_1-mass relation produces steep tracks in the size-mass plane that agree with our data for each star-forming group. These results allow us to introduce a novel way to view the star-forming size-mass relation. Instead of a single monolithic relation which holds for all star-forming galaxies, we propose that the canonical star-forming size-mass relation is comprised of a series of steep, overlapping parallel relations. Each one of these parallel relations reflects intrinsic scatter around the star-forming Σ_1-mass relation; this scatter may be caused by variations in dark matter halo properties. These results support a growth mode where, on average, star-forming galaxies evolve *along* the Σ_1-mass and size-mass relations: as star-forming galaxies increase their masses and decrease their sSFRs, they also increase their Σ_1 values and slightly increase their sizes (see also van Dokkum et al., 2015; Tacchella et al., 2015b; Barro et al., 2017b; Woo & Ellison, 2019; Nelson et al., 2019; Chen et al., 2020;

Wilman et al., 2020).

Using our mass profiles and novel galaxy classification method, we also confirm previous results suggesting that the mass density within 1 kpc, Σ_1, is a powerful predictor of quiescence. Our groups of galaxies follow a "L-shaped track" in Σ_1-mass space (Barro et al., 2017b): Σ_1 increases gradually along the star-forming sequence, then sSFR drops once galaxies reach a critical quenching threshold in Σ_1. The bend in this diagram, where small changes in Σ_1 correspond to large changes in sSFR, is populated by transitional galaxies, including the most massive dusty star-forming galaxies, green valley galaxies, and post-starburst galaxies.

Our measurements support the view that there are (at least) two distinct ways for galaxies to reach the high Σ_1 values required for quiescence. In the "slow" pathway, galaxies continue to gradually grow along the star-forming structural relations until they naturally reach high Σ_1 values. The intermediate sizes, Σ_1 values, color gradients, and sSFRs of green valley galaxies indicate that they are undergoing this slow quenching process. This slow quenching picture predicts that the most compact galaxies quench first: this explains both the larger sizes of low-redshift green valley galaxies and the increasing importance of progenitor bias effects towards $z \sim 0$. We also find that $z \lesssim 2$ dusty star-forming galaxies have extended structures and mild negative color gradients, indicating that they may be linked to this slow quenching pathway. The long timescales required for this slow growth— $\gtrsim 2$ Gyr from simple toy models— explains why it is most prevalent at lower redshifts.

In contrast, we find that post-starburst galaxies tend to have small sizes, dense cores, and flat color gradients. These flat color gradients are inconsistent with the negative color gradients found in green valley galaxies, indicating that the two populations have different radial distributions of their stellar populations and represent different pathways to quenching. These flat color gradients also indicate that post-starburst galaxies likely experienced some event that created young stars at their centers before they shut down star formation. As discussed in detail in Suess et al. (2020), the structures of these galaxies are consistent with a "fast" quenching process triggered by a compaction-type event. The compact structures and strong radial color gradients of high-redshift dusty star-forming galaxies indicate that these galaxies are also part of this fast quenching pathway, and may represent the "burst" before galaxies are observed as post-starburst. Future work directly comparing the number densities and star formation histories of post-starburst and compact dusty star-forming galaxies can directly test this theory. Both massive post-starburst galaxies and compact dusty star-forming galaxies are absent from our sample at $z \lesssim 1.5$, indicating that this rapid quenching pathway is primarily operational at high redshift.

This study demonstrates the power of moving beyond simple "star forming vs. quiescent" sample selections, measuring structural properties from mass profiles, and introducing radial color gradients as an additional probe of galaxy structural evolution. Using these novel approaches, we have gained significant insights into galaxy growth and quenching. The next step forward in understanding the structural evolution of galaxies is decomposing our observed color gradients into age, metallicity, and A_v gradients which can be more straightforwardly interpreted and compared to numerical predictions. Direct measurements of these stellar population gradients will soon be possible with the advent of rest-frame

mid-IR photometric surveys with *JWST*.

Chapter 6

Massive quenched galaxies at $z \sim 0.7$ retain large molecular gas reservoirs

The content of this chapter is drawn from Suess et al. (2017), with permission from the co-authors.

In this chapter, we focus on the rapid route to quenching discussed in detail in Chapters 4 & 5. We identify a sample of bright intermediate-redshift post-starburst galaxies that are the ideal candidates for follow-up observations. We then use ALMA to investigate their molecular gas contents.

6.1 Sample selection

To identify a sample of massive post-starburst galaxies bright enough for follow-up study, we select galaxies from the SDSS DR12 (Alam et al., 2015) spectroscopic catalog with $i < 19$, $z \geq 0.5$, and median spectral signal-to-noise ratio > 3.7. We identify galaxies dominated by A-type stars following the method introduced in Kriek et al. (2010), which selects post-starburst galaxies by their strong Balmer breaks and their blue slopes redward of the break. The final selection was checked by eye to remove stars and brown dwarfs, and consists of 50 post-starburst galaxies at $0.5 \leq z \leq 0.8$ with a median redshift of $z = 0.6$.

To derive the stellar masses of the post-starburst galaxy sample, we fit the SDSS spectra with the stellar population synthesis fitting code FAST (Kriek et al., 2009) using the Bruzual & Charlot (2003) stellar population library, a Chabrier (2003) initial mass function (IMF), a delayed exponential star formation history, and the Kriek & Conroy (2013) dust attenuation law. The mass was aperture corrected using the difference between the photometric magnitude in the SDSS g, r, and i filters and the same magnitudes as measured from the optical spectra; this correction increased the adopted stellar mass by a mean factor of 1.5.

We measured SFRs using the aperture-corrected line flux of the [O II] λ3727 doublet and the SFR conversion in Kennicutt (1998b), adjusted to a Chabrier IMF. To measure the [O II] flux, we modeled the region around the doublet as a single Gaussian centered at the

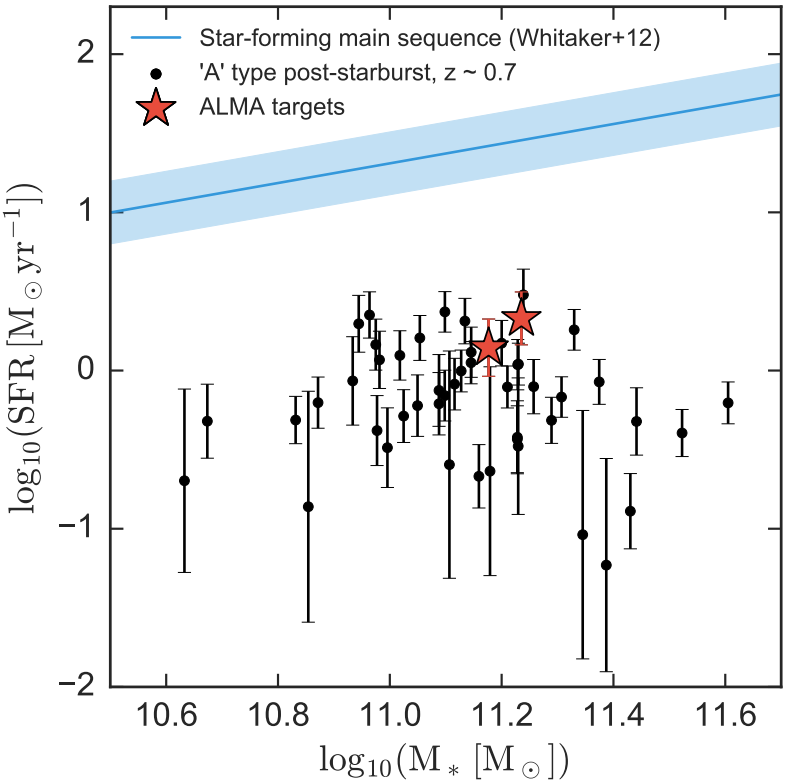

Figure 6.1: SFR, estimated using the dust-corrected [O II] λ3727 luminosity, as a function of stellar mass for 'A-type' post-starburst galaxies selected from the SDSS. Red stars indicate the galaxies observed with ALMA. The blue shaded line indicates the star-forming main sequence at z=0.6 from Whitaker et al. (2012b); all post-starburst galaxies in the sample lie significantly below the main sequence.

mean wavelength of [O II] plus a straight-line continuum with a free slope and intercept. The width of the Gaussian line was held equal to the stellar velocity dispersion, given in the MPA-JHU catalogs (Aihara et al., 2011). In all cases, the velocity dispersion resulted in a single Gaussian wider than the separation between the two lines in the [O II] doublet. Uncertainties in the SFR were bootstrapped from 1,000 realizations of the [O II] line flux fit. We corrected the SFR for dust attenuation using the best-fit dust attenuation value from the stellar population fit (median A_v=0.8 mag).

Figure 6.1 shows the SFR as a function of stellar mass for the full post-starburst galaxy sample. All galaxies lie significantly below the star-forming main sequence at this redshift (Whitaker et al., 2012b).

Table 6.1: Post-starburst targets. Errors in M_* are dominated by systematics, which we estimated by varying the model library, star formation history, and dust law in the stellar population fits.

ID	z	M_* $[M_\odot]$	SFR $[M_\odot/\mathrm{yr}]$	Ap. Corr.	L_{CO} $[\mathrm{K\,km\,s^{-1}\,pc^2}]$	$M_{\mathrm{gas}}[M_\odot]$
J0912+1523	0.747	$(1.7 \pm 0.3)\times10^{11}$	2.1 ± 0.8	1.13±0.01	8.5 ± 0.4	$(34.0\pm1.6)\times10^9$
J2202-0033	0.657	$(1.5 \pm 0.2)\times10^{11}$	1.4 ± 0.6	1.11±0.01	1.6 ± 0.2	$(6.4\pm0.8)\times10^9$

6.2 ALMA observations

We selected two of the highest-redshift, brightest galaxies– SDSS J0912+1523 and SDSS J2202-0033– from the full sample for follow-up observations with ALMA. The SDSS discovery spectra of these two galaxies are shown in Figure 6.2, and basic parameters are listed in Table 6.1. The ALMA observations were carried out in program 2016.1.01126.S (PI: R. Bezanson) in January and March 2017 using the ALMA Band 4 receivers (Asayama et al., 2014). Observations were made in 80 min blocks, with two blocks dedicated to each target. The total on-source integration time for each target was ∼100 min. The data were reduced using the standard ALMA pipeline, which produced good results for both SDSS J0912+1523 observing blocks and one SDSS J2202-0033 block. In the second observation of SDSS J2202-0033, many antennas were shadowed by other antennas during observations of the bandpass calibrator due to the compact array configuration. This caused the automatic pipeline to flag the shadowed antennas for the remainder of the observing block. We instead derived the frequency-dependent response of the affected antennas using the repeated observations of the complex gain calibrator carried out during the remainder of the track. While the gain calibrator is not as bright as the bandpass calibrator, we verified that the bandpass solutions derived in this way are consistent with those using the bandpass calibrator for the antennas which were not shadowed.

The observations reach a spatial resolution of $2.2\times3.0''$ (16×22 kpc) and $1.7\times2.4''$ (12×17 kpc) for SDSS J2202-0033 and SDSS J0912+1523, respectively, in images inverted using natural weighting, which maximizes sensitivity at the expense of slightly lower spatial resolution. No 2 mm continuum emission was detected in either source, with a 3σ upper limit $< 75\,\mu$Jy.

CO(2–1) is significantly detected in both target galaxies. Inspection of the image cubes and a comparison of the maximum pixel values with the integrated flux density indicate that SDSS J0912+1523 is marginally spatially resolved, with a deconvolved source FWHM of $1.9 \pm 0.3''$ (14 ± 2 kpc). SDSS J2202-0033 is not spatially resolved at the depth and resolution of our data. To extract spectra, we fit a point source (SDSS J2202-0033) or a circular Gaussian (SDSS J0912+1523) to the visibility data using the *uvmultifit* package (Martí-Vidal et al., 2014), averaging 24 (SDSS J2202-0033) or 6 (SDSS J0912+1523) channels, yielding a velocity resolution of ≈ 200 and $50\,\mathrm{km\,s^{-1}}$, respectively. These spectra, as well as images integrated over the full linewidths of each target, are shown in Figure 6.3.

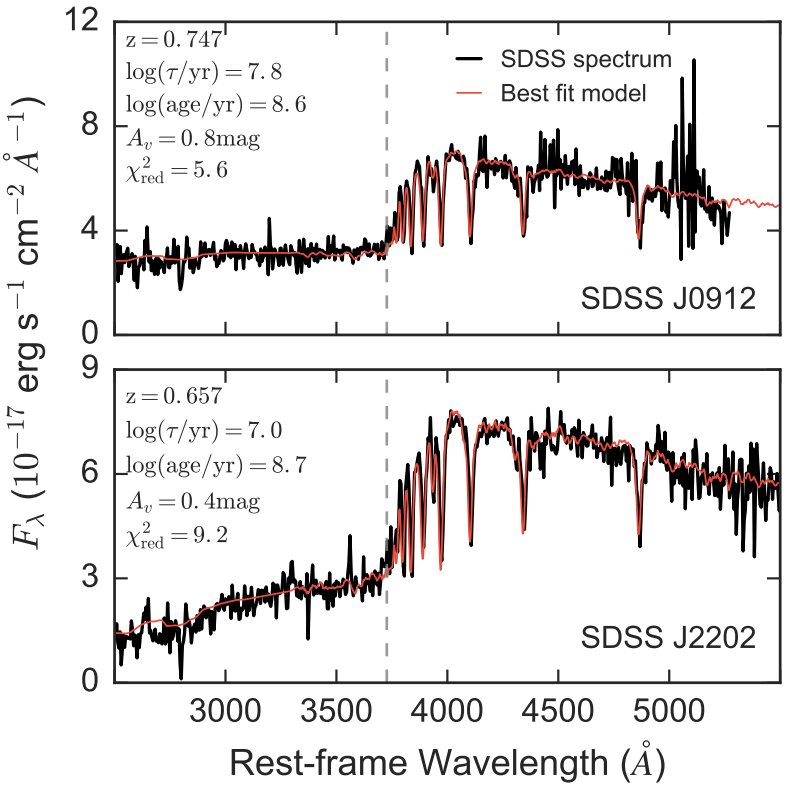

Figure 6.2: SDSS discovery spectra of SDSS J0912+1523 and SDSS J2202-0033. Best-fit stellar population synthesis models are overplotted in red. The grey dashed line indicates the location of the [O II] λ3727 doublet used to measure the SFR.

6.3 Molecular gas masses

Both sources are significantly detected in CO(2–1) emission (see Figure 6.3). We fit simple Gaussian profiles to these spectra, which yield integrated line fluxes of 1.07 ± 0.05 and 0.27 ± 0.03 Jy km s^{-1} for SDSS J0912+1523 and SDSS J2202-0033, respectively. At the redshifts of each source, these fluxes correspond to line luminosities $L'_{CO} = 8.5 \pm 0.4$ and $1.6 \pm 0.2 \times 10^9$ K km s^{-1} pc^2, respectively.

The CO line luminosity can be converted to a molecular gas mass using the conversion factor α_{CO}. In high metallicity objects, α_{CO} typically varies from $\approx 0.8\,M_\odot/(K\,km\,s^{-1}\ pc^2)$ in highly star-forming objects (typically gas-rich merging systems) to $\approx 4\,M_\odot/(K\,km\,s^{-1}\ pc^2)$ in the Milky Way and other normal star-forming galaxies, principally due to the escape probability in the optically-thick CO line (see Bolatto et al. 2013 for a recent review; hereafter we suppress the units of α_{CO}).

We estimate the value of α_{CO} using the numerical models of Narayanan et al. (2012).

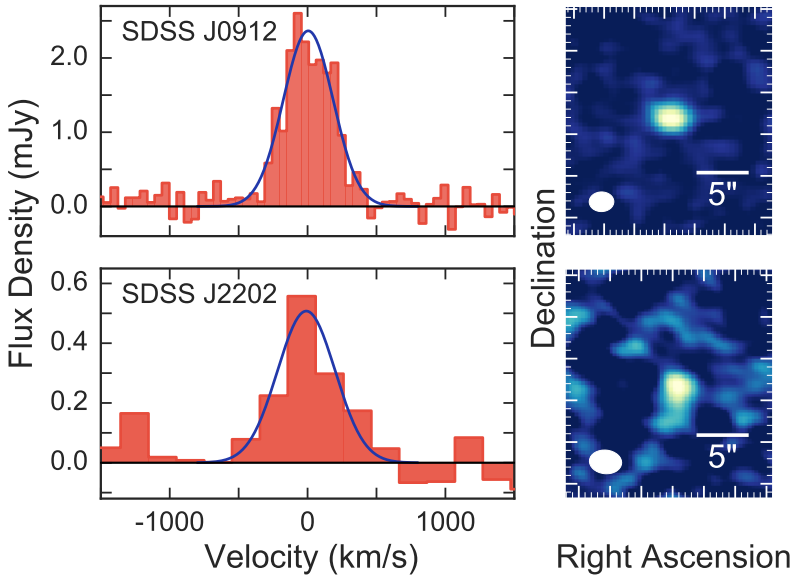

Figure 6.3: Left: ALMA CO(2–1) spectra for each target. The blue line shows the best-fit Gaussian used to extract the total line flux. Right: integrated line images for each target. The white oval shows the ALMA beam.

These authors combined hydrodynamical modeling of a variety of isolated and merging galaxies with molecular line radiative transfer to develop a fitting formula for $\alpha_{\rm CO}$ as a function of the CO surface brightness. SDSS J2202-0033 is not spatially resolved at the depth and resolution of our data, which yields a lower limit on the CO surface brightness and an upper limit on the conversion factor of $\alpha_{\rm CO} \lesssim 7.0$. Our data spatially resolve SDSS J0912+1523; combined with its CO luminosity, this implies $\alpha_{\rm CO} \sim 3.5$. For ease of comparison with the literature, we therefore adopt $\alpha_{\rm CO} = 4.0$ for both of our targets.

Additionally, $\alpha_{\rm CO}$ is valid and applies only to the CO(1–0) transition, so observations of higher CO lines require a correction factor to the ground state. Based on observations of a wide variety of galaxies at many redshifts, the CO(2–1)/CO(1–0) line ratio likely falls in the range 0.7–1.0 in temperature units, where 1.0 indicates thermalized emission (e.g., Combes et al., 2007; Dannerbauer et al., 2009; Young et al., 2011). We assume thermalized emission in our analysis. This is a conservative assumption, yielding a minimum CO(1–0) line luminosity; the true values may be higher by $\approx 30\%$.

Given these assumptions, we find molecular gas masses of $M_{\rm gas} = (34.0 \pm 1.6) \times 10^9\,{\rm M}_\odot$ for SDSS J0912+1523 and $M_{\rm gas} = (6.4 \pm 0.8) \times 10^9\,{\rm M}_\odot$ for SDSS J2202-0033. These uncertainties reflect only the statistical uncertainties on the measured CO luminosities; we stress that there are also factor of two systematic uncertainties associated with the CO excitation and conversion factor.

In Figure 6.4, we show SFR versus molecular gas mass for SDSS J0912+1523 and SDSS J2202-

0033. It is clear that our observations, especially SDSS J0912+1523, are significantly offset from measurements of star-forming galaxies at both low and high redshifts. Adopting the CO size, the gas mass surface density of SDSS J0912+1523 is a factor of 11 higher than expected from its SFR surface density (Kennicutt, 1998b). SDSS J0912+1523 has a gas mass a factor of two larger than expectations from the empirical scaling relation in Genzel et al. (2015); SDSS J2202-0033 has a gas mass three times lower than expected from the same scaling.

In Figure 6.4 we show for comparison the low-redshift 'K+A' post-starburst galaxies in French et al. (2015), an 'active' post-starburst galaxy in the Sell et al. (2014) sample observed in CO by Geach et al. (2013), and star-forming and quiescent galaxies at $z \sim 0$ (COLD GASS, Saintonge et al. 2011; ATLAS-3D, Young et al. 2011; Cappellari et al. 2011, 2013; Davis et al. 2013, 2014; and MASSIVE, Davis et al. 2016) as well as $z \sim 1.2$ (PHIBSS, Tacconi et al. 2013). Molecular gas fractions ($f_{\rm gas} \equiv M_{\rm gas}/M_*$) vary significantly both amongst the three post-starburst samples and within in each sample: the K+A post-starbursts have $f_{\rm gas} \sim 1 - 40\%$, the active post-starburst has $f_{\rm gas} \sim 19\%$, and SDSS J0912+1523 and SDSS J2202-0033 have respective $f_{\rm gas} \sim 20\%$ and 4%.

6.4 Implications for galaxy quenching

Our results imply that star formation can be suppressed in galaxies that still have significant reservoirs of molecular gas. Models that require the complete depletion or ejection of molecular gas to quench star formation are inconsistent with the large gas masses in SDSS J0912+1523 and SDSS J2202-0033. Models that explain star formation suppression without removing the gas– such as morphological quenching (Martig et al., 2009), which suggests that a buildup of stars into a bulge can stabilize some cold molecular gas against collapse– are more consistent with our observations. However, it is not clear that current quenching models can fully explain the observed elevated molecular gas masses, especially for SDSS J0912+1523.

Alternatively, the star formation in SDSS J0912+1523 and SDSS J2202-0033 may only be temporarily suppressed. Simulations of massive z$\sim$2 galaxies predict a large amount of variability in ISM properties and star formation activity on short ($\sim$tens of Myr) timescales (Feldmann et al., 2017). These simulations contain a small number of galaxies with molecular gas fractions and SFR/M_* similar to SDSS J2202-0033. However, they are not able to reproduce a counterpart of the more extreme case of SDSS J0912+1523.

The factor of five difference in gas mass between SDSS J0912+1523 and SDSS J2202-0033 indicates that, unsurprisingly, quenching may proceed differently from galaxy to galaxy. A larger galaxy sample is required to investigate intrinsic variations in the gas properties of post-starburst galaxies and determine whether SDSS J0912+1523 is an intriguing outlier or representative of recently quenched galaxies.

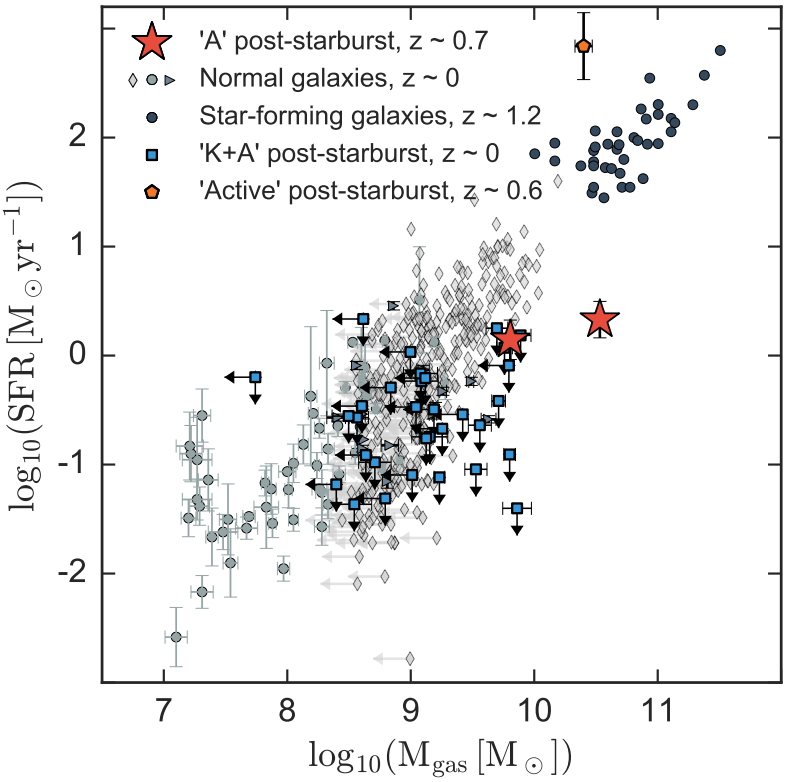

Figure 6.4: SFR as a function of molecular gas mass for SDSS J2202-0033 and SDSS J0912+1523 (red stars) as well as comparison samples. Blue squares indicate the French et al. (2015) low-redshift 'K+A' post-starburst galaxies; all SFRs are upper limits due to possible LINER emission. Dark grey points are star-forming galaxies from PHIBSS at $z \sim 1.2$. Grey diamonds are normal galaxies from COLDGASS, grey circles are from ATLAS-3D, and grey triangles are from MASSIVE. The orange pentagon is an 'active' post-starburst galaxy identified in Sell et al. (2014), with a gas mass measured by Geach et al. (2013). All have been normalized to $\alpha_{\rm CO} = 4$. SDSS J0912+1523 and SDSS J2202-0033 are clearly offset from star-forming galaxies at both $z \sim 0$ and $z \sim 1.2$.

6.5 Comparison to other studies

Our results are similar to French et al. (2015), who found high molecular gas masses given the SFR of 'K+A' post-starburst galaxies at $0.01 < z < 0.12$. These authors interpret their observations as evidence for suppressed star-formation efficiency, a low $\alpha_{\rm CO}$, or a bottom-heavy IMF in these galaxies.

There are, however, significant differences between the French et al. (2015, hereafter 'K+A sample') post-starburst galaxies, the post-starburst galaxies in this study, and the post-starburst galaxies in other studies such as Sell et al. (2014, hereafter 'active sample'). The K+A sample includes $z < 0.12$, $M_* \sim 10^{10.6}\,M_\odot$ galaxies with strong Balmer lines and low ongoing star formation. The active sample includes $z \sim 0.6$, $M_* = 10^{10.5}$ - $10^{11.5}\,M_\odot$ galaxies with strong Balmer absorption and weak nebular emission. In this study, we select $z \sim 0.6$, $M_* \sim 10^{11.1}\,M_\odot$ galaxies with strong Balmer breaks and blue slopes redward of the break. Despite all selections emphasizing 'post-burst' criteria, the median stacked optical spectra of the three samples (top panel of Figure 6.5) are clearly distinct. The active sample shows prominent UV continuum as well as [O II] and [O III] emission lines; inferred SFRs are $\sim 300\ M_\odot\ {\rm yr}^{-1}$. The K+A sample does not show UV continuum or emission lines, but has excess emission at rest-frame $\lambda \gtrsim 4500$ Å indicating a larger fractional contribution from old stars than the 'A-type' post-starburst selection in this study.

To further illustrate the differences between the post-starburst samples, we show the Hδ_A index as a function of D_n4000 for all three samples as well as SDSS DR12 galaxies with $0.05 \leq\ z \leq 0.07$ and $M_\odot \geq 10^{10} M_\odot$ (bottom panel of Figure 6.5). The Hδ_A index traces recent star formation, and D_n4000 is sensitive to the age of the stellar population. For all three post-starburst samples we measured Hδ_A using EZ_Ages (Graves & Schiavon, 2008), adopting the Princeton 1D VDISP measurement for the velocity dispersion correction; we measured D_n4000 from the SDSS spectra (Balogh et al., 1999). Purple lines of increasing shade indicate the time evolution of Bruzual & Charlot (2003) single/double-burst models with an increasing contribution from old stars. The first model is a simple stellar population; the second is a model where 90% of the stars were formed in a starburst 4 Gyr before the current star formation epoch; the third is a model where 95% of the stars were formed in a previous starburst.

The active sample lies at low D_n4000 and has a range of Hδ_A values likely corresponding to emission partially filling in the $H\delta$ absorption feature. Given their high inferred SFR, these galaxies are still 'active' and have not yet fully quenched their star formation; it is possible that after they quench, these galaxies will resemble A-type post-starburst galaxies. The K+A post-starbursts are consistent with models where only 5-10% of the galaxy's mass was formed in the most recent burst. This indicates that these galaxies formed the majority of their stars at higher redshift, and have just quenched a small amount of late-time star formation. Their spectra show the signatures of recently formed A-type stars as well as older K-type stars from previous star formation episodes. The A-type post-starbursts selected in this study are consistent with a simple stellar population model; i.e., they likely just finished their primary epoch of star formation and thus look like A-type stars.

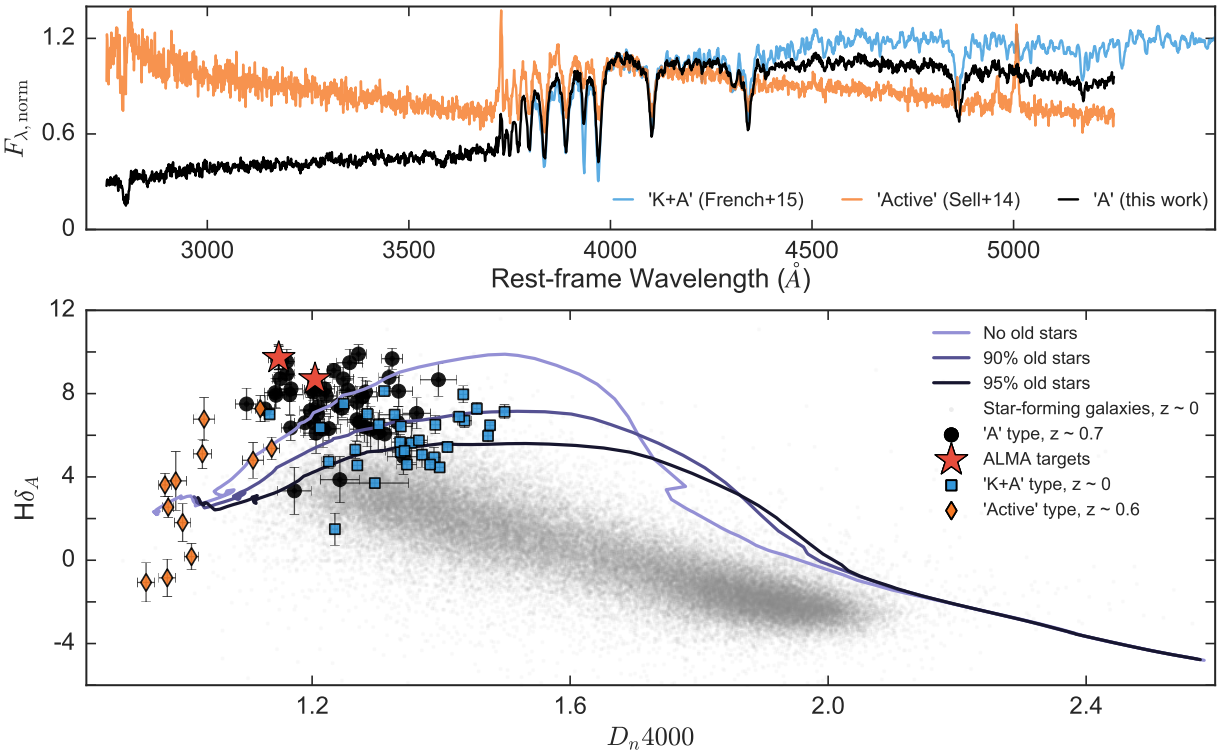

Figure 6.5: Top: median stacked spectra of 'K+A' (French et al., 2015, blue), 'active' (Sell et al., 2014, orange), and 'A' type (black) post-starburst galaxies. Bottom: $H\delta_A$ vs D_n4000 for the same three post-starburst samples. ALMA targets are shown with red stars; SDSS galaxies are shown in grey. Purple lines indicate Bruzual & Charlot (2003) models where 0, 90, and 95% of stars were formed in a previous burst. As time increases, the model tracks evolve left to right.

Given these differences, it is not clear that the same physical mechanisms should quench both the late-time star formation in the $z \sim 0$ K+A galaxies and the primary epoch of star formation in the $z \sim 0.7$ A-type post-starburst galaxies. It is surprising that both the low-redshift K+A post-starbursts and intermediate-redshift A-type post-starbursts show high gas molecular gas masses for their SFR, indicating quenching in both redshift regimes can occur without exhausing or depleting molecular gas reservoirs.

6.6 Discussion

In this chapter, we present ALMA CO(2-1) observations of two recently-quenched post-starburst galaxies at $z \sim 0.7$. These galaxies were selected from a unique sample of 50 A-type post-starburst galaxies at $z \sim 0.6$. Unlike low-redshift K+A post-starburst galaxies,

these massive galaxies have just concluded their major star-forming episode. Additionally, this sample lies at low enough redshift that follow-up observations of low-J CO transitions are feasible. The observed molecular gas masses in these galaxies are significantly higher than expected given their low ongoing SFR. This indicates that galaxies may quench their primary epoch of star formation without completely depleting or exhausting their molecular gas.

However, there are several alternative explanations for the high gas masses in SDSS J0912+1523 and SDSS J2202-0033. Short-term SFR variations, seen in some higher-redshift galaxy simulations, could account for the elevated gas mass of SDSS J2202-0033. As in French et al. (2015), a lower $\alpha_{\rm CO}$ value could decrease the inferred gas mass and a bottom-heavy IMF could increase the inferred SFR, alleviating tension between the gas supply and low ongoing SFR. It is also possible that there is significant obscured star formation in SDSS J0912+1523 or SDSS J2202-0033.

We place a constraint on the dust-obscured star formation of each target using the non-detection of the 2mm ALMA continuum. We assume that the dust emission follows a standard modified blackbody function with $T_{\rm dust} = 30\,{\rm K}$ (typical of star-forming galaxies; e.g., Magdis et al., 2012). The resulting upper limits on the FIR luminosity imply 3σ upper limits on the obscured SFR $\lesssim 50\,{\rm M}_{\odot}/{\rm yr}$. We additionally constrain the obscured star formation with WISE 12μm data (Mainzer et al., 2011), using the log average of Dale & Helou (2002) templates with $1 \leq \alpha \leq 2.5$ to convert the observed 12μm luminosity to a total IR luminosity, following Whitaker et al. (2012b); this gives an upper limit of $\sim 60\,{\rm M}_{\odot}/yr$. Just $\sim 6\ M_{\odot}$/yr of obscured star formation– well below the current constraints from either WISE or 2mm continuum– would place SDSS J2202-0033 in line with the expected relation. In contrast, $\sim 60\ M_{\odot}$/yr of obscured star formation is required to account for the significant gas reservoir in SDSS J0912+1523. Both the radio and IR SFR upper limits are highly uncertain, and deeper rest-frame infrared measurements are required to place stronger constraints on any obscured star formation.

Finally, we note that the sample size of this study is very small; measurements of the molecular gas in a larger sample of post-starburst galaxies are necessary to determine if these galaxies are simply outliers. Thus, moving forward we need to obtain a larger sample of galaxies with gas measurements and tight constraints on the dust-obscured SFR. By studying the intrinsic variation in molecular gas properties of 'A-type' post-starburst galaxies, we may be able to constrain the primary mechanisms behind galaxy quenching.

Chapter 7

SQuIGG$\vec{L}$E: Studying Quenching in Intermediate-z Galaxies— Gas, Angu$\vec{L}$ar Momentum, and Evolution

The content of this chapter is drawn from Suess et al. (2021b), submitted, with permission from the co-authors.

Here, we expand on the intermediate-redshift post-starburst galaxy sample presented in Chapter 6. We aim to find a large sample of galaxies that have high burst mass fractions and are therefore in the process of shutting down their major epoch of star formation. At the same time, we want these galaxies to be bright enough to conduct full multi-wavelength follow-up studies with reasonable telescope investments. We will select a large sample of these bright, young, intermediate-redshift post-starburst galaxies from the SDSS DR14 (Abolfathi et al., 2018). With this sample, we will be Studying Quenching in Intermediate-z Galaxies–Gas, angu$\vec{L}$ar momentum, and Evolution (SQuIGG$\vec{L}$E). The SQuIGG$\vec{L}$E sample will serve as the ideal testbed to study the quenching process in massive galaxies in detail.

This chapter is organized as follows. In Section 7.1, we describe our post-starburst sample selection. We also generate mock galaxy spectra with known properties, and use those mocks to investigate what types of galaxies are included in our sample selection. In Section 7.2, we use the `Prospector` Bayesian stellar population synthesis code to fit the stellar masses, dust properties, and star formation histories of the galaxies in our sample. In particular, we use these derived star formation histories to investigate how long SQuIGG$\vec{L}$E post-starburst galaxies have been quiescent, the fraction of their mass that was formed in a recent starburst, and their ongoing star formation rates (SFRs). In Section 7.3, we calculate SFRs from spectral lines present in the SDSS spectra of our galaxies, and compare these results to the `Prospector` SFRs. In Section 7.4, we place the SQuIGG$\vec{L}$E sample in context by comparing it to other post-starburst samples. Finally, in Section 7.5 we briefly describe the science objectives of the remainder of the SQuIGG$\vec{L}$E survey.

7.1 Sample selection

In this section, we describe how we select post-starburst galaxies from the SDSS. Our selection is designed to select the brightest, most massive, most burst-dominated post-starburst galaxies at $z \sim 0.7$, with the goal of identifying galaxies that are ideal targets for multi-wavelength follow-up studies of the quenching process. We explore the differences between our sample selection algorithm and those used in previous studies in Section 7.4.

For the SQuIGG$\vec{L}$E sample, we follow the Kriek et al. (2010) method and select post-starburst galaxies from the SDSS based on their unique spectral shapes. Synthetic medium-band rest-frame U_m, V_m, and B_m filters are designed to target both the Balmer break and the slope of the spectrum redward of the break; as shown in Figure 7.1, these two rest-frame colors alone are effective at selecting post-starburst galaxies. Model spectra (generated with FSPS, Conroy et al., 2009; Conroy & Gunn, 2010) of a post-starburst galaxy (black), a fully quiescent galaxy (red), an unobsured star-forming galaxy (blue) and a dusty star-forming galaxy (purple) are shown over the same wavelength range. The inset in Figure 7.1 shows the location of these four spectra in UBV space, as well as the density of all SDSS spectra with $z > 0.5$. Our post-starburst color selection cuts, described in detail below, are shown with black lines. The color cuts include the post-starburst galaxy while excluding both star-forming and older quiescent galaxies; just $\sim 5\%$ of all $z > 0.5$ galaxies in the SDSS satisfy these color cuts. Figure 7.1 shows that unobscured star-forming galaxies have similar $B_m - V_m$ colors to post-starburst galaxies, but weaker Balmer breaks that do not satisfy our $U_m - B_m$ cut. In contrast, both dusty star-forming galaxies and older quiescent galaxies have similar $U_m - B_m$ colors as post-starburst galaxies, but redder $B_m - V_m$ colors. Spectrally, older quiescent galaxies and post-starburst galaxies can be distinguished by the differences in the strength of the Balmer break, the slope of the spectrum redward of the break, and the depth of both the Balmer absorption lines and the Calcium H & K lines. Dusty star-forming galaxies differ from post-starburst galaxies mainly in the slope of the spectrum redward of the Balmer break and the strength of the nebular emission lines.

Our parent sample consists of all 1,921,000 galaxies in the SDSS DR14 spectroscopic catalog (Abolfathi et al., 2018) with $z > 0.5$. We then make a quality cut which removes non-physical spectra: we calculate the $r - i$ and $i - z$ colors from the SDSS spectrum, and remove any galaxies for which these spectral colors differ from the SDSS photometric colors by more than 0.25 dex. We note that at these redshifts, the fiber encompasses $\gtrsim 75\%$ of the total light from these compact post-starburst galaxies; typically the spectral and photometric colors are within 0.05 dex. We ensure that the wavelength range of the SDSS spectrum covers our rest-frame U_m, B_m, and V_m filters, then calculate the flux in each synthetic rest-frame filter. To ensure high quality spectra, we require a signal-to-noise ratio (S/N) ≥ 6 in both our B_m and V_m filters; this S/N cutoff was chosen by examining representative spectra by eye. We do not require a minimum S/N in the U_m filter, because post-starburst galaxies typically have minimal UV flux and thus low S/N blueward of the Balmer break (see, e.g., Figure 7.1). 32,168 galaxies remain in the parent sample after these initial quality cuts. Finally, we select all objects in this sample with $U - B > 0.975$ and $-0.25 < B - V < 0.45$

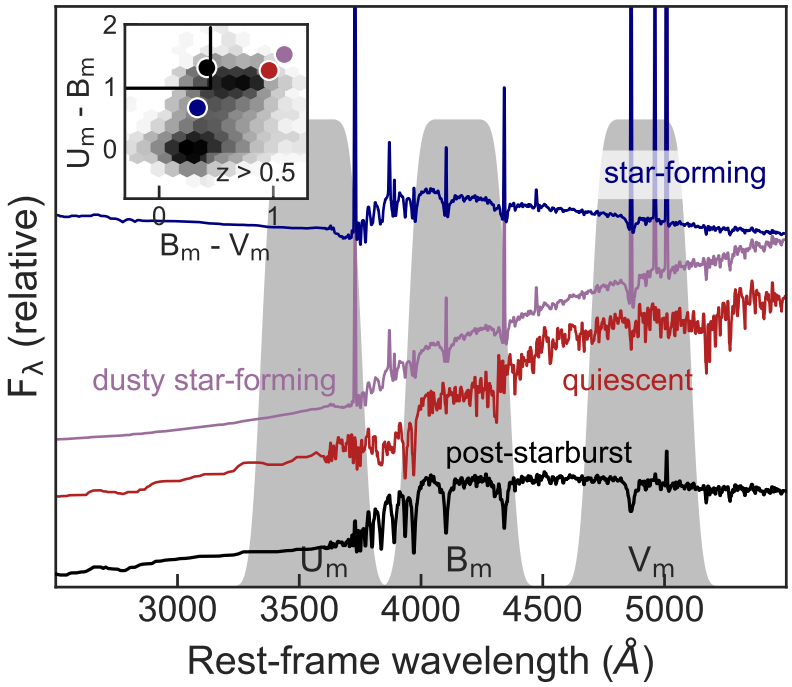

Figure 7.1: Demonstration of color-based selection technique. Grey shaded regions show the synthetic rest-frame U_m, B_m, and V_m filters. Blue, purple, red, and black curves show example synthetic spectra of an unobscured star-forming galaxy, a dusty star-forming galaxy, a quiescent galaxy, and a post-starburst galaxy; spectra have an arbitrary factor added to F_λ for visibility. The inset shows $U_m - B_m$ as a function of $B_m - V_m$; the shaded background represents the relative density of all $z > 0.5$ galaxies in the SDSS, while the black, blue, purple, and red points show the colors of the spectra shown in the main plot. The black lines in the inset show our color criteria for a galaxy to be selected as post-starburst. Post-starburst galaxies can be easily distinguished from other galaxy types in this color-color space: the $U_m - B_m$ color separates post-starburst galaxies from unobscured star-forming galaxies, while the $B_m - V_m$ color separates post-starburst galaxies from dusty star-forming galaxies and older quiescent galaxies.

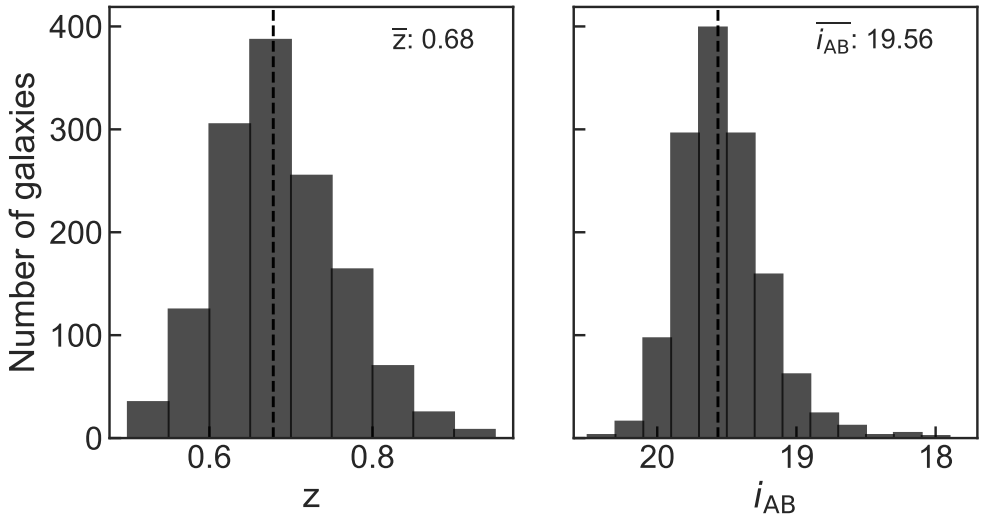

Figure 7.2: Histograms of the redshift and i-band magnitude of all SQuIGG$\vec{L}$E galaxies.

as post-starburst galaxies. Our final sample includes 1,318 unique post-starburst galaxies. These galaxies form the full SQuIGG$\vec{L}$E sample.

Figure 7.2 shows histograms of the redshift and i-band magnitude distribution of the full SQuIGG$\vec{L}$E sample. By construction, all galaxies have $z \geq 0.5$. The median sample redshift is $z = 0.68$, with a tail of galaxies up to $z = 0.94$. This redshift distribution is effectively a competition between apparent magnitude (there are fewer high-S/N SDSS spectra at higher redshift) and the number density evolution of post-starburst galaxies (there are many more post-starburst galaxies at higher redshift, e.g., Wild et al., 2016; Belli et al., 2019). The i-band magnitudes of SQuIGG$\vec{L}$E galaxies range from 17.9 to 20.5, with the faint end cutoff primarily driven by our S/N cut.

Figure 7.3 shows a stacked spectrum of all 1,318 post-starburst galaxies in SQuIGG$\vec{L}$E, normalized using the flux between 4150 and 4250 Å. The grey shaded region shows the 16-84th percentile of all spectra. This stacked spectrum clearly shows the representative characteristics of a post-starburst galaxy: a strong Balmer break, deep Balmer absorption lines, and weak [O II] emission.

We also measure the Hδ equivalent width and the D_n4000 index for all galaxies in our sample. Hδ traces recent star formation, while D_n4000 probes the age of the stellar population; together, these indices provide a fairly reliable indication of the galaxy's evolutionary stage. We use the `pyphot` python package to calculate Hδ_A, and obtain error bars via bootstrap resampling. We measure D_n4000 from the SDSS spectra using the bandpass definitions from Balogh et al. (1999). In Figure 7.4, we show Hδ_A as a function of D_n4000 for all galaxies in our sample (black points). To guide the eye, we also show the distribution of all galaxies in the SDSS DR7 (purple hexagons; values taken from the MPA-JHU catalogs at

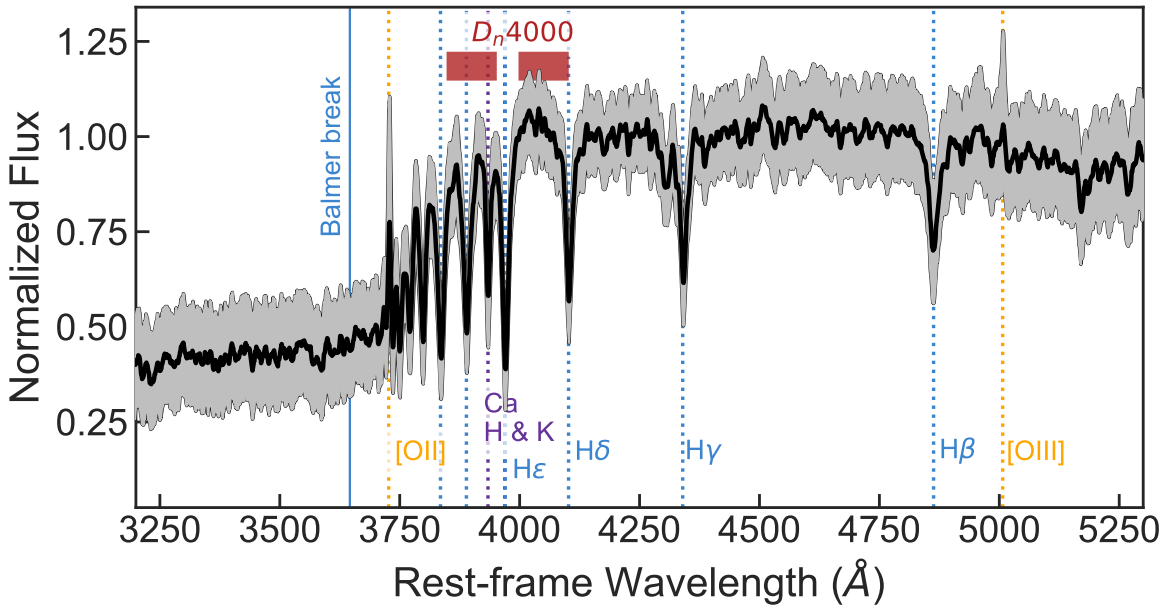

Figure 7.3: Stack of all post-starburst galaxies in the SQuIGG$\vec{L}$E sample. The black line shows the median stacked spectrum; the grey shaded region indicates the 16-84th percentile range of all spectra. SQuIGG$\vec{L}$E galaxies have strong Balmer breaks, blue slopes redward of the break, deep Balmer absorption lines, and typically weak or absent [O II] and [O III] emission lines.

$0.05 \leq z \leq 0.07$). Despite the fact that we do not explicitly select post-starburst galaxies using either index (unlike some post-starburst galaxy selection techniques, which use an Hδ_A cut), we see that the SQuIGG$\vec{L}$E galaxies are clustered at high Hδ_A and low D_n4000. This result confirms that the galaxies in the SQuIGG$\vec{L}$E sample are indeed fairly young. Again, we see that SQuIGG$\vec{L}$E galaxies lie a relatively extreme region of parameter space compared to the majority of low-redshift SDSS galaxies.

Table 7.1 lists the basic properties of the post-starburst galaxies identified by SQuIGG$\vec{L}$E.

Why were these galaxies targeted by SDSS?

Here, we examine the target flags of the selected SQuIGG$\vec{L}$E galaxies to understand why they were included in the SDSS spectroscopic sample. The vast majority of SQuIGG$\vec{L}$E galaxies—1,132 out of 1,318, $\sim 82\%$— are part of the main "CMASS" BOSS sample (Dawson et al., 2013). The CMASS selection used color-magnitude cuts designed to target massive galaxies at $0.4 < z < 0.7$. An additional 11 galaxies are part of the sparse CMASS sample, which includes fainter and bluer galaxies than the main CMASS sample. 64 galaxies are part of the "commissioning" CMASS sample, which used slightly different color cuts than the final

Table 7.1: Basic properties of SQuIGG$\vec{L}$E post-starburst galaxies

SDSS ID	RA (deg)	Dec (deg)	$z_{\rm spec}$	Hδ_A (Å)	D_n4000	σ_* (km/s)[a]	aperture correction
spec-6137-56270-0195	353.79039	16.10073	0.7473	7.86±0.51	1.12±0.02	186±52	1.50
spec-0978-52431-0077	260.01290	30.28743	0.6840	9.45±0.33	1.16±0.01	223±42	1.07
spec-5192-56066-0419	238.72249	38.33752	0.7237	7.49±0.62	1.31±0.03	222±123	1.21
spec-5288-55865-0858	132.07321	13.07628	0.5233	8.53±0.47	1.19±0.02	211±53	0.95
spec-4575-55590-0605	144.35677	36.50522	0.6206	8.11±0.43	1.30±0.02	167±20	1.39
spec-3817-55277-0279	135.90519	3.81953	0.7570	4.54±0.50	1.34±0.02	261±46	1.47
spec-5140-55836-0177	21.74532	14.35716	0.6946	7.87±0.53	1.27±0.02	164±43	1.35
spec-1630-54476-0502	53.22548	-6.20368	0.5715	5.02±0.39	1.30±0.02	239±33	1.29
spec-3754-55488-0041	120.22957	32.94343	0.7037	5.26±0.65	1.40±0.03	265±62	1.64
spec-6649-56364-0311	166.58688	45.04543	0.6391	6.53±0.59	1.32±0.03	191±35	1.72
spec-5048-56218-0165	337.14303	10.75239	0.6671	7.82±0.71	1.30±0.03	129±65	1.57
spec-6054-56089-0547	225.25613	42.77234	0.6094	5.58±0.39	1.30±0.02	234±28	1.45
spec-4403-55536-0765	27.85715	6.27124	0.6698	5.28±0.64	1.21±0.02	232±50	1.72
spec-6032-56067-0159	236.68717	45.81196	0.6819	8.75±0.63	1.24±0.03	205±64	1.26
spec-6639-56385-0597	177.92877	43.34649	0.7691	7.64±0.73	1.26±0.02	229±47	1.58
spec-4013-55629-0073	228.42489	2.08515	0.7409	5.92±0.52	1.29±0.02	146±40	1.48
spec-5993-56070-0251	199.47152	22.03277	0.7208	7.73±0.44	1.21±0.02	218±57	1.68
spec-5014-55717-0745	257.42214	27.66418	0.6926	8.97±0.69	1.36±0.03	175±52	1.35
spec-5291-55947-0601	132.52735	11.19210	0.6111	6.98±0.57	1.16±0.02	288±21	1.35
spec-5475-56011-0379	222.19133	10.16960	0.6462	7.28±0.34	1.23±0.01	209±30	1.71
...	...	...	...	...	...	...	

[a] From the pPXF fits described in Greene et al. (2020).
(This table is available in its entirety in a machine-readable form in the online journal. A portion is shown here for guidance regarding its form and content.)

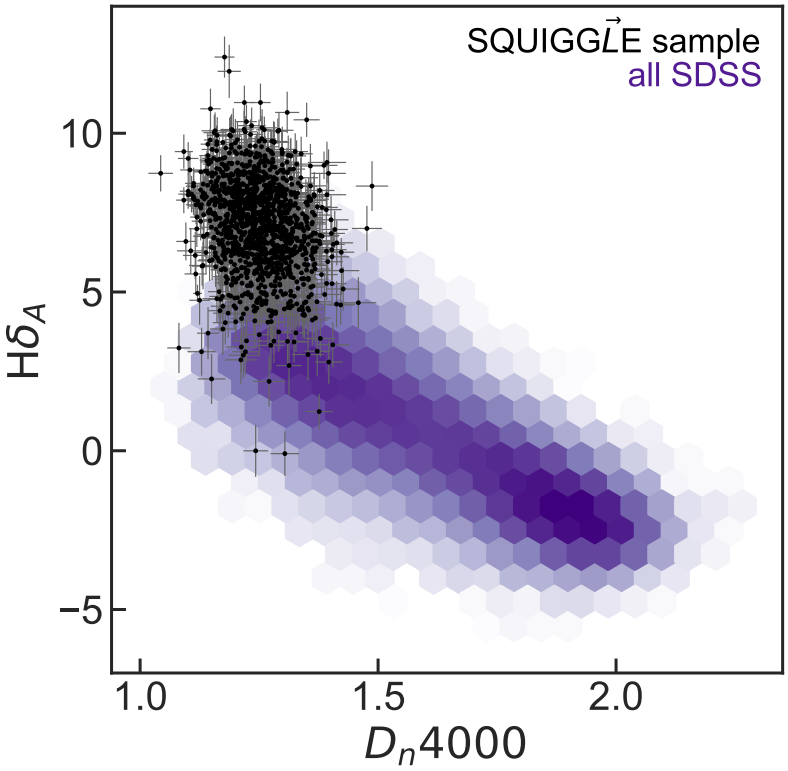

Figure 7.4: $H\delta_A$ as a function of D_n4000 for all SQuIGG$\vec{L}$E galaxies (black points). Age increases towards the lower right of the diagram. The distribution of the full SDSS (from the MPH-JHU catalogs at $0.05 \leq z \leq 0.07$) is shown by the shaded purple background. Our selection has clearly resulted in a sample of galaxies with high $H\delta$ equivalent widths and low D_n4000 indices, despite not explicitly selecting on these parameters.

CMASS survey. The remaining 111 PSBs were targeted as part of 24 different programs within SDSS. The majority of these 111 galaxies were selected as BOSS ancillary targets because their *ugriz* or WISE colors resembled those of high-redshift quasars or LRGs. Several others were selected because they had matches in the Chandra Source Catalog (Evans et al., 2010) or the FIRST radio survey (Becker et al. 1995, see also Greene et al. 2020). Galaxies with non-CMASS target flags tend to be slightly brighter and lie at lower redshifts than the median of the full SQuIGG$\vec{L}$E sample.

Understanding our sample selection: how do physical parameters map onto $U_m - B_m$ and $B_m - V_m$ colors?

In order to understand the types of galaxies that fall into our color-based selection method, we generate a set of mock SDSS-like spectra then map their physical properties onto UBV color space. We generate these mock galaxy spectra using FSPS (Conroy et al., 2009; Conroy & Gunn, 2010) assuming a Chabrier (2003) IMF, the Calzetti et al. (2000) dust law, a total stellar mass of $10^{11.25} M_{\odot}$, and a velocity dispersion of 200 km/s. We vary the dust attenuation ($0 \leq A_v/\mathrm{mag} \leq 2.5$), the metallicity ($0 \leq \log Z/Z_{\odot} \leq 0.5$), and the spectral S/N (10-90% noise levels of our observed SQuIGG$\vec{L}$E spectra). We model the SFHs of the mock galaxies as a delayed τ component plus a recent top-hat burst; we vary the mass fraction in the recent burst ($10\% \leq f_{\mathrm{burst}} \leq 99\%$), the duration of the recent burst ($100 \leq t_{\mathrm{burst}}/\mathrm{Myr} \leq 600$), the time since quenching ($0.05 \leq t_q/\mathrm{Gyr} \leq 1.0$), and the star formation rate after quenching (e.g., the amount of "frosting", $10^{-5} \leq \mathrm{SFR_q}/M_{\odot}\mathrm{yr}^{-1} \leq 30$). We explain the generation of these mock spectra in more detail in a forthcoming paper, Suess et al. in prep., which examines the best methods to recover accurate SFHs for post-starburst galaxies.

We generate 5,000 mock galaxy spectra, then run our color-based selection algorithm (Section 7.1) on the set of mock spectra. 1,821 of the 5,000 of the mock galaxies are classified as post-starburst by our sample selection criteria. Figure 7.5 shows $U_m - B_m$ versus $B_m - V_m$ for all 5,000 mock spectra. Each panel is colored by a different physical parameter, and our post-starburst color cuts are shown by the solid black lines. While f_{burst}, t_q, A_v, and SFR_q show clear gradients across UBV space, neither metallicity nor the length of the recent burst exhibit coherent trends. This indicates that our sample selection does not prefer galaxies of a specific t_{burst} or metallicity. However, the galaxies that we select as post-starburst tend to have high f_{burst}, low t_q, and relatively low A_v and SFR_q. This indicates that our sample selection algorithm is sensitive to relatively dust-free galaxies that recently quenched after a large starburst— exactly the types of galaxies we were attempting to target.

We also briefly explore correlations between these parameters. Figure 7.6 shows time since quenching as a function of burst mass fraction for the mock galaxies which are classified as post-starburst by our selection algorithm. The blue contours show relatively dust-free mock post-starburst galaxies, and the red contours show the dusty mock post-starburst galaxies. Relatively dust-free post-starburst galaxies can be found at a range of t_q and f_{burst} values. However, dusty galaxies are only classified as post-starburst if they quenched very recently, within the past $\sim$ 200 Myr. We can therefore expect that, while the majority of galaxies in the SQuIGG$\vec{L}$E sample are likely not highly dust-obscured, some especially young dusty galaxies may be included in the sample. We do not find a significant difference in the t_q and f_{burst} values of low- and high-SFR mock post-starburst galaxies.

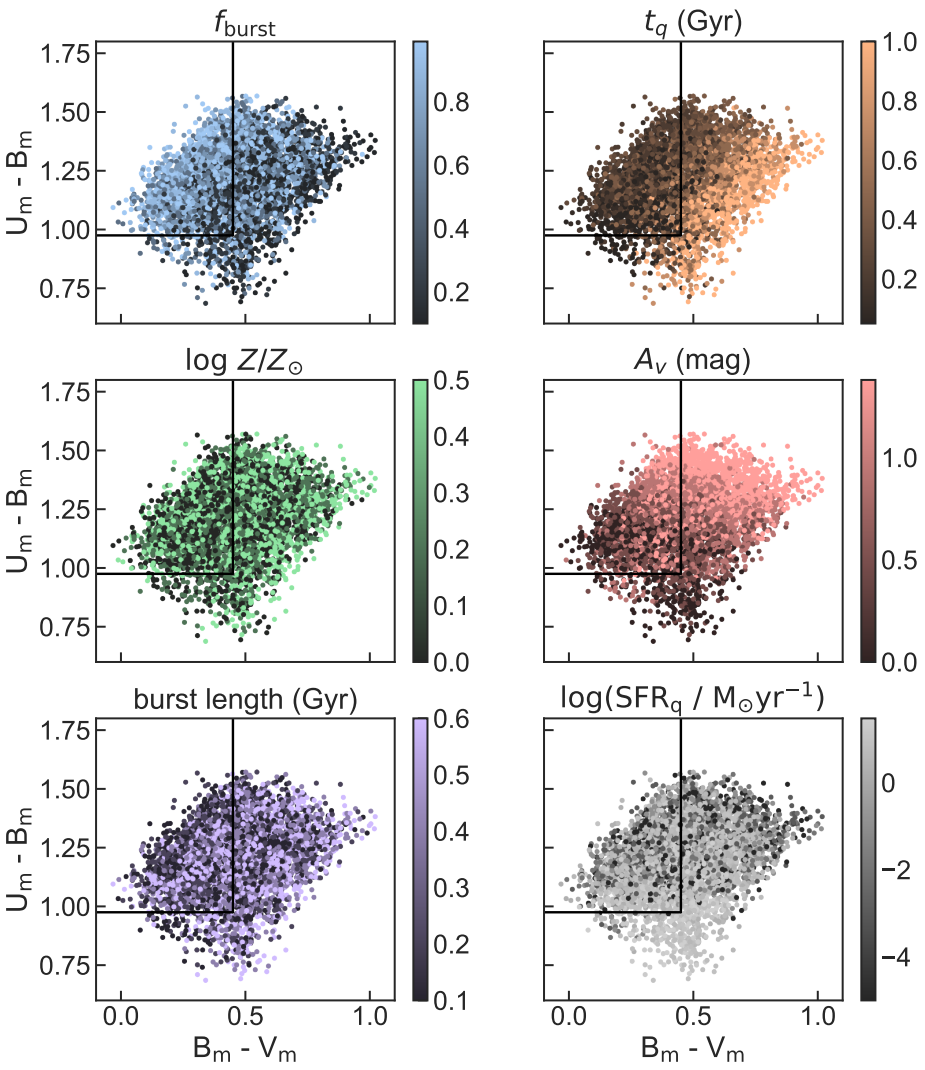

Figure 7.5: $U_m - B_m$ vs $B_m - V_m$ colors for 5,000 synthetic spectra generated with FSPS. The black lines show our color-based post-starburst galaxy sample selection. Each panel is colored by one of the parameters we vary to create the grid of synthetic spectra. $U_m - B_m$ and $B_m - V_m$ are sensitive to changes in burst mass fraction, time since quenching, dust extinction, and current SFR; however, the colors are not sensitive to metallicity or the timescale of the older burst of star formation. Galaxies that fall into our post-starburst galaxy selection tend to have high $f_{\rm burst}$, low t_q, low A_v, and relatively low SFR.

7.2 Extracting star formation histories via spectral energy distribution fitting

In this section, we use the `Prospector` stellar population synthesis fitting code (Johnson & Leja, 2017; Leja et al., 2017; Johnson et al., 2020) to investigate the stellar masses,

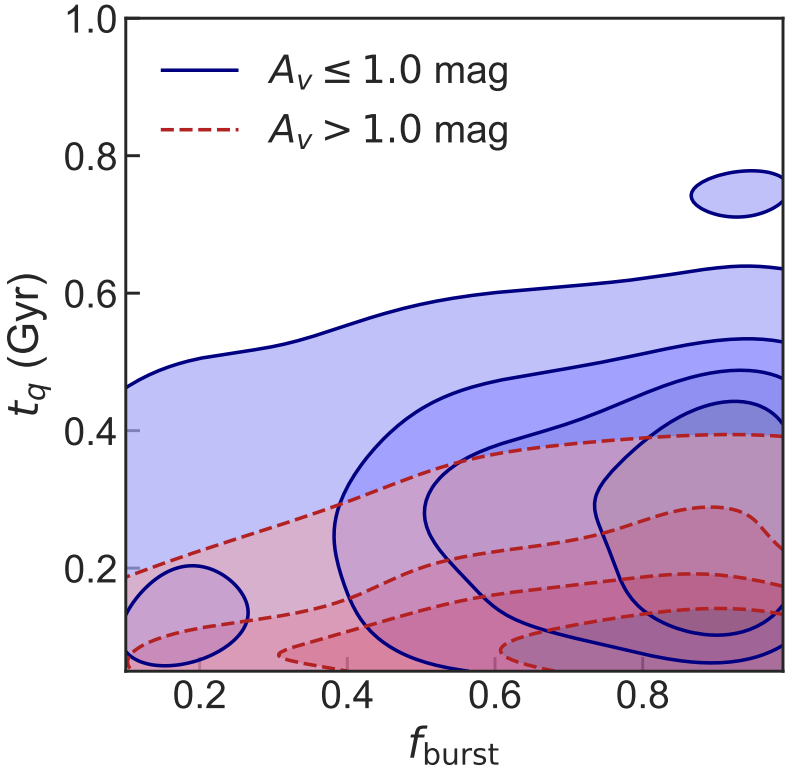

Figure 7.6: Time since quenching as a function of burst mass fraction for mock post-starburst galaxies that fall within our selection, split into more dusty (red, $A_v > 1.0$ mag) and less obscured (blue, $A_v \lesssim 1.0$ mag) galaxies. Our sample tends to select post-starburst galaxies with relatively high $f_{\rm burst}$ and low t_q. Dusty galaxies only fall in our sample if they quenched very recently.

dust properties, metallicities, SFRs, and star formation histories (SFHs) of galaxies in the SQuIGG$\vec{L}$E sample.

Robust SFHs provide a wealth of information, allowing us to investigate how long these galaxies have been quenched (t_q), the fraction of their mass that was formed in the recent burst ($f_{\rm burst}$), and the timescale of both the recent burst and the quenching process. However, traditional "parametric" SFH models that depend on just a few parameters impose strong priors on sSFRs and mass-weighted ages, and results from these parametric fits may not accurately reflect the true mass assembly histories of galaxies (e.g., Carnall et al., 2019). Previous studies have worked to mitigate these biases by modeling post-starburst SFHs as the sum of two parametric components, one for the recent burst and one for the older stellar population (e.g., Kaviraj et al., 2007; French et al., 2018; Wild et al., 2020). While this approach improves on traditional parametric approaches by allowing the mass fraction

in the recent burst to vary, it still explicitly imposes a specific shape for the recent burst and may thus bias results. Here, we use a "non-parametric" form for the SFH, which allows for arbitrary SFR in adjacent timebins. This approach introduces a larger number of free parameters into the fit in exchange for allowing more flexibility and freedom in the derived SFH. These non-parametric SFHs have been shown to more accurately recover galaxy properties such as stellar mass (e.g., Lower et al., 2020). Here, we develop and use an non-parametric model specifically tuned to recover the SFHs of post-starburst galaxies. With these fits, we allow for full flexibility in the burst shape, burst duration, burst mass fraction, and quenching timescale of SQuIGG$\vec{L}$E post-starburst galaxies.

SED fitting setup

We fit the SEDs of all SQuIGG$\vec{L}$E galaxies using the `Prospector` stellar population synthesis fitting software (Johnson & Leja, 2017; Leja et al., 2017; Johnson et al., 2020). We use the `dynesty` dynamic nested sampling package (Speagle, 2020), the FSPS stellar population synthesis models (Conroy et al., 2009; Conroy & Gunn, 2010), the MILES spectral library (Sánchez-Blázquez et al., 2006; Falcón-Barroso et al., 2011), and the MIST isochrones (Choi et al. 2016; Dotter 2016; based on MESA, Paxton et al. 2011, 2013, 2015). We assume the Chabrier (2003) initial mass function, fix the model redshift to the SDSS spectroscopic redshift, and add nebular emission to the spectra using the default fixed parameters in `Prospector` (see Byler et al., 2017). We fit for stellar mass and metallicity using the mass-metallicity prior described in Leja et al. (2019b). We also fit for the velocity dispersion of the SDSS spectra, using a gaussian prior with the mean and sigma of the output pPXF (Cappellari, 2017) velocity dispersion fits (see Greene et al., 2020). We assume the Kriek & Conroy (2013) dust law, with a free A_v and dust index; in this dust law, the bump strength is tied to the slope. Following e.g. Wild et al. (2020), we assume that the attenuation is doubled around young ($< 10^7$ yr) stars. We fix the shape of the IR SED following the Draine & Li (2007) dust emission templates, with $U_{\rm min} = 1.0$, $\gamma_e = 0.01$, and $q_{\rm PAH} = 2.0$. We also include both a spectroscopic jitter term and the `Prospector` pixel outlier model, which are designed to prevent mis-estimated spectroscopic uncertainties or bad spectral pixels from skewing the output.

Our adopted SFH is a modified version of the flexible continuity prior from Leja et al. (2019a), and is illustrated in Figure 7.7. The SFH includes three fixed-edge time bins at the beginning of the universe, five flexible-edge time bins covering the 2 Gyr before observation, and a final bin where we fit for both the bin length and the SFR. All five of the flexible-edge bins form an equal stellar mass, and the edges of the flexible bins are adjusted at each likelihood call based on the log(SFR) ratio between adjacent bins; this parameterization is described in detail in Leja et al. (2019b). The SFH thus has nine free parameters: eight log(SFR) ratios, plus the width of the final timebin. Following Leja et al. (2019b), we place Student-t priors on the log(SFR) ratio between adjacent timebins. We center the priors such that they follow the predicted SFH for a massive quiescent galaxy at similar redshift from UniverseMachine (Behroozi et al., 2019). This prior is more physically-motivated than a

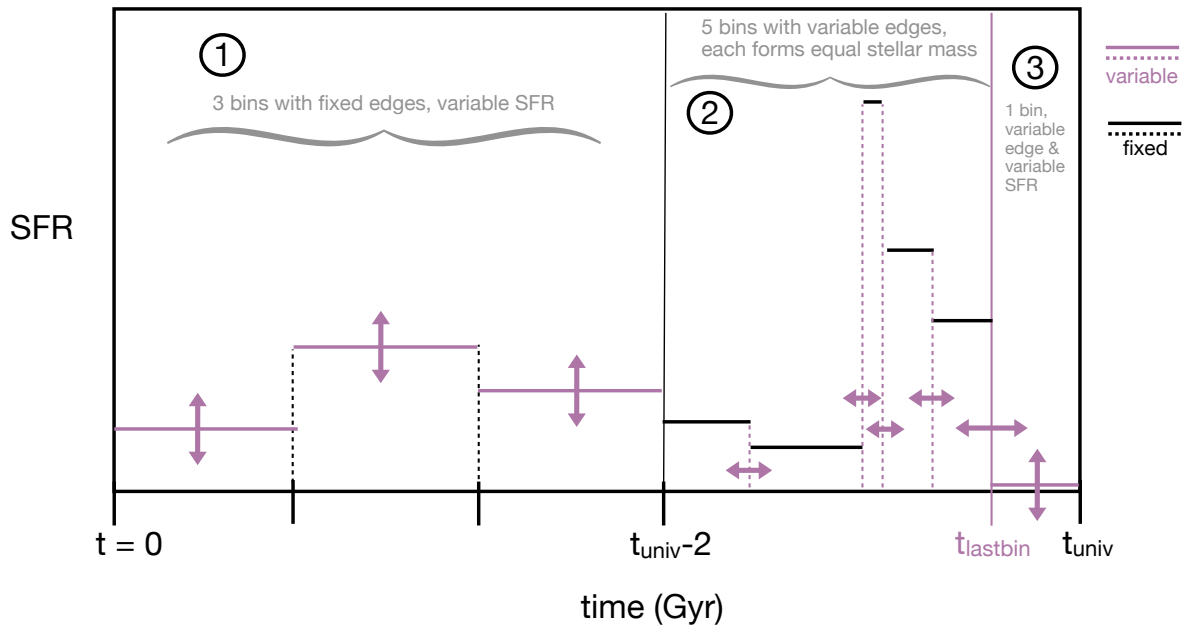

Figure 7.7: Graphical representation of the SFH model used in this work. The model consists of three parts: the oldest section contains three bins with variable SFR but fixed edges, the middle section contains 5 bins with variable edges, and the most recent portion is modeled as a single bin with free width and SFR. Purple lines with arrows are used to indicate quantities that are allowed to vary; black lines indicate fixed quantities.

prior centered at zero, which would imply that galaxies form stars at a constant rate across time. A forthcoming paper, Suess et al. in prep., describes this SFH model in more detail and presents mock recovery tests and comparisons with multiple other SFH parameterizations. The SFH we use here was designed to use a relatively small number of parameters to capture both a recent burst of arbitrary mass fraction and length, a variable quenching timescale, and a variable amount of residual star formation after the burst ends. Suess et al. in prep. shows that for SQuIGG$\vec{L}$E-like galaxies this fitting methodology recovers t_q with just 0.06 dex of scatter and $f_{\rm burst}$ with 0.12 dex of scatter.

We define a "burst" for each galaxy based on the output SFH. We interpolate the SFH to a uniform 1 Myr time scale, then define the burst start and end as the time when the time derivative of the SFH rises above and drops below a threshold value. This threshhold is the same for all galaxies in the sample, and was tuned by visual examination of representative SFHs. In addition to basic quantities such as stellar mass and A_v, we also report several quantities derived from this burst. We define t_q as the time when the recent starburst ended based on our SFH derivative threshold; this quantity tells us how long the galaxy has been quenched. We also define $m_{\rm burst}$ to be the stellar mass formed in the burst, and $f_{\rm burst}$ to be

the *fraction* of the total stellar mass formed during the burst. Suess et al. in prep. describes these definitions in more detail, and explores several alternate definitions of t_q including the sSFR-based definitions used by Tacchella et al. (2021). While the exact numerical value of t_q depends on the definition used, in general different definitions produce quantitatively similar results.

Data included in the SED fits

We fit the `Prospector` model described above jointly to both photometry and spectroscopy. We include the SDSS *ugriz* photometry and the WISE 3.4μm and 4.6μm photometric points. However, we do not include the WISE 12μm and 24μm photometry in our fit. Alatalo et al. (2017) shows that post-starburst galaxies in the local universe have complex and unusual mid-infrared properties: the WISE photometry of these galaxies cannot be reproduced by starlight alone, but appear to be significantly influenced by emission from AGN, PAH features, and/or AGB dust. Due to the complex and still poorly understood nature of this part of the spectrum, in particular for post-starburst galaxies, the mid-IR data points will not help constrain the properties we aim to address in this study. We ensured that excluding these points did not bias our recovered SFRs: for a randomly-selected subsample of ~ 100 galaxies, there was no significant difference in the median SFR in fits where we included or excluded the WISE 12μm and 24μm photometry. Further analysis of the mid-IR data points are beyond the scope of this study and will be subject to a future investigation. We discuss the WISE properties of our sample further in Section 7.2.

In addition to seven-band photometry, we fit the SDSS spectrum of each galaxy. We aperture-correct the spectrum using the observed SDSS photometry in the *gri* bands. We note that at $z \sim 0.7$, the diameter of the SDSS/BOSS fiber is larger than the effective radius of these compact post-starburst galaxies and thus the SDSS spectrum includes the majority of the light from each galaxy; our median aperture correction is a factor of 1.3. Both Maltby et al. (2018) and Suess et al. (2020) find that post-starburst galaxies have flat color gradients, indicating that the aperture-corrected SDSS spectra are likely accurate reflections of the total integrated stellar light from these galaxies. In our fits, we mask all spectral pixels within 50Åof the 3727Å[O II] line, or within 100Åof the 5007Å[O III] line. Previous studies have found that [O II] emission in post-starburst galaxies is primarily caused by LINER or AGN activity (e.g., Lemaux et al., 2010; Yan et al., 2006). Greene et al. (2020) shows that some SQuIGG$\vec{L}$E galaxies have extreme [O III] equivalent widths, again due to the presence of AGN. Because it is currently not possible to model the AGN contribution to these forbidden lines in `Prospector`, we mask them in our fits.

SED fitting results

Here, we show the results of our SED fitting to the full SQuIGG$\vec{L}$E sample. Figure 7.8 shows example `Prospector` fits to three galaxies in SQuIGG$\vec{L}$E. The upper left panel shows the observed and best-fit SDSS and WISE photometry; the upper right panel shows the

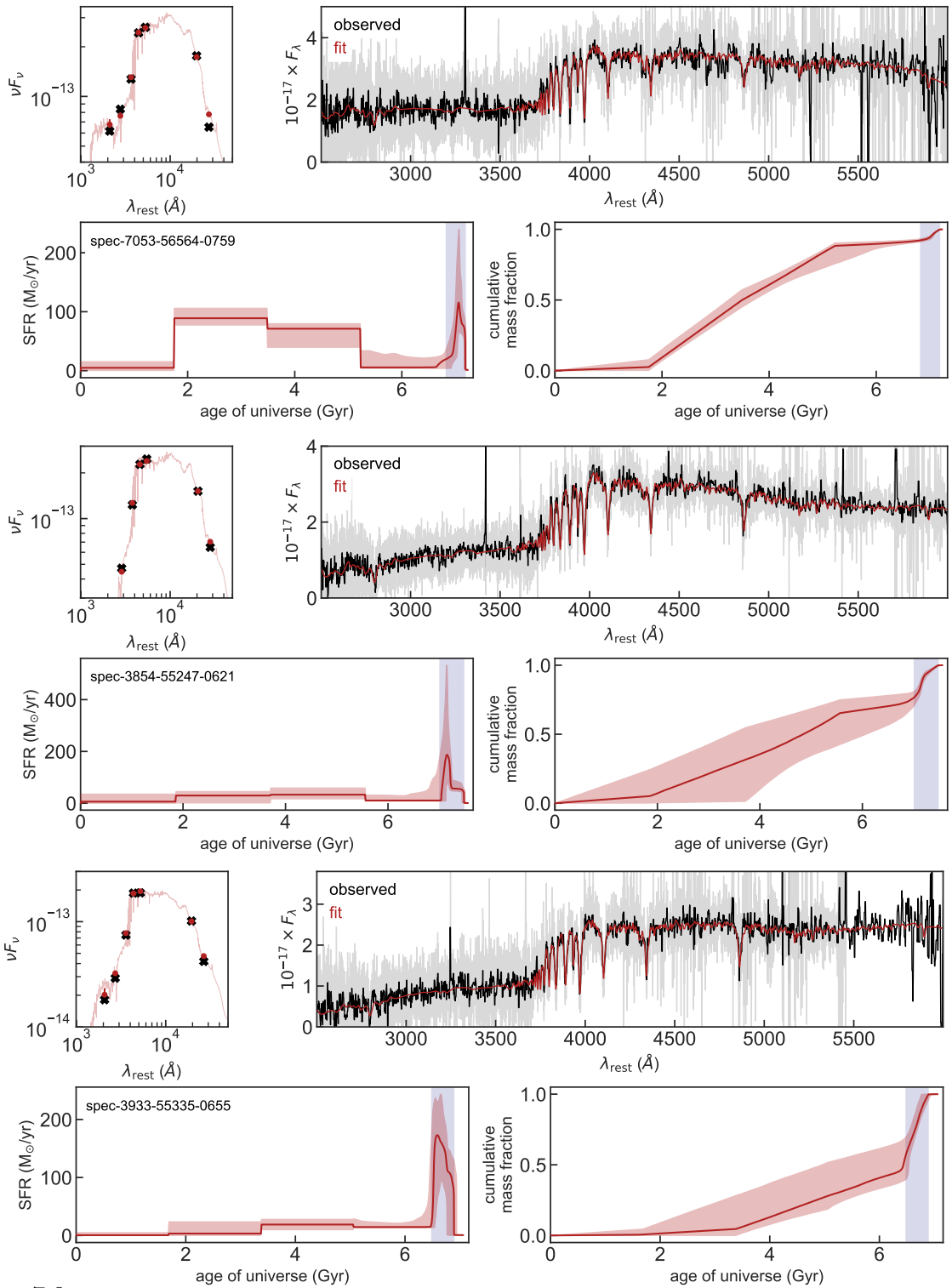

Figure 7.8: Three example fits using our `Prospector` model, chosen to roughly span the observed range in t_q and $f_{\rm burst}$. The fits are ordered by increasing t_q. The upper left panel shows the observed (black cross) and best-fit (red point) SDSS and WISE photometry. The upper right panel shows the observed spectrum (grey), a 7-pixel median boxcar smoothed version of the observed spectrum (black), and the best-fit spectrum (red). The lower left panel shows the derived SFH and its 16-84th percentile confidence interval; the blue shaded region represents the "burst" defined using a derivative-based threshhold described in the text. The lower right panel shows the cumulative fraction of the mass formed over time.

Table 7.2: `Prospector` SED fitting results for SQuIGG$\vec{L}$E post-starburst galaxies

SDSS ID	$\log \mathrm{M}_*/\mathrm{M}_\odot$	$\log Z/Z_\odot$	A_v (mag)[a]	dust index[a]	t_q (Myr)	f_{burst}
spec-6137-56270-0195	$11.40^{+0.07}_{-0.11}$	$0.55^{+0.09}_{-0.10}$	$0.86^{+0.15}_{-0.09}$	$0.20^{+0.07}_{-0.10}$	106^{+17}_{-26}	$0.36^{+0.24}_{-0.10}$
spec-0978-52431-0077	$11.31^{+0.06}_{-0.03}$	$0.20^{+0.32}_{-0.07}$	$0.44^{+0.07}_{-0.05}$	$-0.00^{+0.19}_{-0.14}$	165^{+9}_{-52}	$0.42^{+0.07}_{-0.13}$
spec-5192-56066-0419	$11.44^{+0.06}_{-0.06}$	$-0.02^{+0.10}_{-0.11}$	$0.34^{+0.07}_{-0.06}$	$-0.69^{+0.23}_{-0.18}$	495^{+123}_{-126}	$0.51^{+0.28}_{-0.16}$
spec-5288-55865-0858	$11.05^{+0.07}_{-0.08}$	$0.28^{+0.10}_{-0.07}$	$0.58^{+0.10}_{-0.10}$	$-0.21^{+0.17}_{-0.15}$	183^{+21}_{-24}	$0.38^{+0.12}_{-0.13}$
spec-4575-55590-0605	$11.30^{+0.04}_{-0.05}$	$0.06^{+0.06}_{-0.06}$	$0.37^{+0.07}_{-0.07}$	$-0.03^{+0.18}_{-0.17}$	480^{+88}_{-115}	$0.41^{+0.15}_{-0.08}$
spec-3817-55277-0279	$11.59^{+0.03}_{-0.03}$	$-0.28^{+0.09}_{-0.08}$	$0.17^{+0.03}_{-0.03}$	$-0.71^{+0.23}_{-0.18}$	715^{+521}_{-217}	$0.98^{+0.02}_{-0.23}$
spec-5140-55836-0177	$11.23^{+0.04}_{-0.03}$	$0.24^{+0.18}_{-0.11}$	$0.23^{+0.05}_{-0.06}$	$-0.45^{+0.30}_{-0.27}$	217^{+102}_{-81}	$0.70^{+0.13}_{-0.19}$
spec-1630-54476-0502	$11.56^{+0.04}_{-0.08}$	$0.12^{+0.09}_{-0.07}$	$0.35^{+0.06}_{-0.07}$	$0.22^{+0.12}_{-0.19}$	55^{+14}_{-13}	$0.15^{+0.23}_{-0.03}$
spec-3754-55488-0041	$11.54^{+0.03}_{-0.05}$	$0.21^{+0.10}_{-0.11}$	$0.15^{+0.07}_{-0.06}$	$-0.48^{+0.42}_{-0.36}$	358^{+105}_{-90}	$0.16^{+0.13}_{-0.04}$
spec-6649-56364-0311	$11.47^{+0.04}_{-0.09}$	$-0.01^{+0.18}_{-0.17}$	$0.17^{+0.05}_{-0.07}$	$-0.44^{+0.31}_{-0.29}$	352^{+115}_{-115}	$0.23^{+0.34}_{-0.09}$
spec-5048-56218-0165	$11.53^{+0.04}_{-0.05}$	$0.03^{+0.08}_{-0.09}$	$0.52^{+0.09}_{-0.07}$	$-0.44^{+0.24}_{-0.23}$	271^{+139}_{-94}	$0.32^{+0.17}_{-0.10}$
spec-6054-56089-0547	$11.65^{+0.02}_{-0.03}$	$0.71^{+0.09}_{-0.10}$	$0.14^{+0.04}_{-0.04}$	$-0.18^{+0.25}_{-0.21}$	94^{+34}_{-22}	$0.19^{+0.03}_{-0.03}$
spec-4403-55536-0765	$11.50^{+0.05}_{-0.04}$	$0.15^{+0.13}_{-0.08}$	$1.24^{+0.07}_{-0.08}$	$0.11^{+0.09}_{-0.09}$	38^{+20}_{-14}	$0.56^{+0.13}_{-0.11}$
spec-6032-56067-0159	$11.16^{+0.04}_{-0.05}$	$0.37^{+0.19}_{-0.21}$	$0.28^{+0.08}_{-0.08}$	$-0.33^{+0.22}_{-0.34}$	147^{+52}_{-51}	$0.32^{+0.11}_{-0.08}$
spec-6639-56385-0597	$11.54^{+0.02}_{-0.03}$	$0.00^{+0.12}_{-0.08}$	$0.14^{+0.05}_{-0.04}$	$-0.75^{+0.45}_{-0.18}$	159^{+44}_{-32}	$0.47^{+0.20}_{-0.08}$
spec-4013-55629-0073	$11.48^{+0.05}_{-0.06}$	$0.15^{+0.16}_{-0.11}$	$0.08^{+0.06}_{-0.04}$	$-0.21^{+0.32}_{-0.41}$	150^{+77}_{-48}	$0.32^{+0.39}_{-0.09}$
spec-5993-56070-0251	$11.46^{+0.06}_{-0.08}$	$0.24^{+0.15}_{-0.10}$	$0.30^{+0.13}_{-0.10}$	$-0.40^{+0.32}_{-0.29}$	130^{+58}_{-37}	$0.33^{+0.29}_{-0.11}$
spec-5014-55717-0745	$11.32^{+0.07}_{-0.07}$	$0.04^{+0.14}_{-0.13}$	$0.54^{+0.12}_{-0.12}$	$0.13^{+0.19}_{-0.30}$	195^{+179}_{-73}	$0.43^{+0.35}_{-0.21}$
spec-5291-55947-0601	$11.30^{+0.10}_{-0.06}$	$0.13^{+0.08}_{-0.07}$	$0.26^{+0.07}_{-0.09}$	$-0.38^{+0.24}_{-0.31}$	47^{+34}_{-15}	$0.44^{+0.49}_{-0.34}$
spec-5475-56011-0379	$11.60^{+0.04}_{-0.07}$	$0.05^{+0.05}_{-0.05}$	$0.37^{+0.08}_{-0.06}$	$-0.34^{+0.16}_{-0.15}$	76^{+36}_{-26}	$0.33^{+0.61}_{-0.14}$
...	...	...	...	...	...	...

[a] Assuming the Kriek et al. (2010) dust law.
(This table is available in its entirety in a machine-readable form in the online journal. A portion is shown here for guidance regarding its form and content.)

observed SDSS spectrum and the best-fit stellar population model; the lower left panel shows the derived SFH; as an alternate way of viewing the SFH, the lower right panel shows the cumulative mass fraction formed as a function of time. The shaded vertical blue region in the third and fourth columns marks the recent starburst (using the derivative-based method described in detail in Suess et al. in prep.). This figure illustrates that our data and modeling framework are able to place strong constraints on the SFH for each galaxy.

Figure 7.9 shows histograms of derived properties for the full SQuIGG$\vec{L}$E sample. These fits confirm that SQuIGG$\vec{L}$E galaxies are massive; nearly all galaxies in the sample have $\mathrm{M}_* \gtrsim 10^{11}\mathrm{M}_\odot$. This is not unexpected: these $z > 0.5$ galaxies had to be bright enough to be targeted spectroscopically by SDSS and meet our S/N$\geq$ 6 criterion. We also see that— as expected— the majority of SQuIGG$\vec{L}$E galaxies are relatively dust-free, with a median $\mathrm{A}_v \sim 0.3$ mag. Very dusty post-starburst galaxies are generally too red to fall into our color-based sample selection (Section 7.1; Figure 7.6). The best-fit metallicities tend to be slightly supersolar, as expected for massive galaxies according to the Gallazzi et al. (2005) mass-metallicity prior we used in the fits. We see a wide range of dust indices, roughly spanning the prior range allowed in our fits. This is likely because our data have relatively little leverage on this parameter due to our short wavelength range and lack of UV and IR

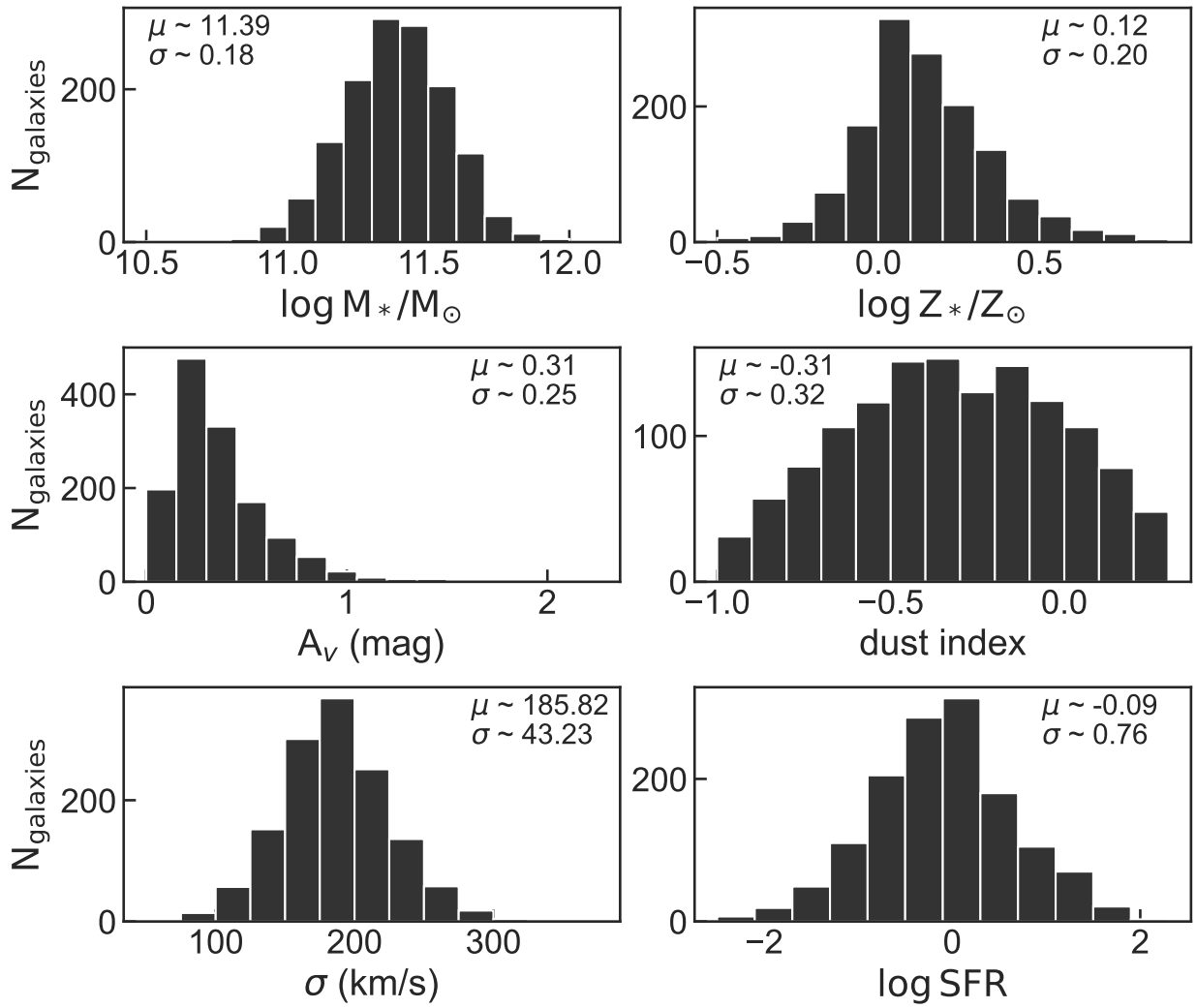

Figure 7.9: Histograms of recovered properties from SED fitting. The median and standard deviation of each parameter is shown in the upper left or right corner of the plot. SQuIGG$\vec{L}$E galaxies tend to have very high stellar masses and relatively low dust attenuation.

data. These massive galaxies have relatively high velocity dispersions, $\sigma \sim 200$ km/s, as expected from the pPXF results we used as a prior (Greene et al., 2020).

SED SFRs

Next, we use the `Prospector` fitting results to investigate where the SQuIGG$\vec{L}$E sample lies in relation to the star-forming main sequence: is star formation truly suppressed in these post-starburst galaxies? SED-based SFRs are notoriously tricky to calculate, and depend

sensitively on the assumed SFH (e.g., Lee et al., 2009, 2010; Maraston et al., 2010; Wuyts et al., 2011). It is therefore *essential* that we test our SFH model and fitting framework before relying on SED SFRs. A forthcoming paper, Suess et al. in prep., fits the mock galaxies described in Section 7.1 and investigates how well the output SFHs capture the ongoing SFRs of the mock post-starburst galaxies. We find that SFRs above $1M_\odot$/yr are slightly underestimated ($\lesssim 0.1$ dex median offset) but generally recovered well, with ~ 0.15 dex of scatter. However, below $1M_\odot$/yr the data do not have significant constraining power on the SFR. Given the high stellar masses of our galaxies, this limit corresponds to very low sSFRs of $\lesssim 10^{-11}$ yr^{-1}. Higher-quality spectra and/or additional wavelength coverage would likely be required to recover lower levels of ongoing star formation.

Figure 7.10 shows the derived SFRs as a function of stellar mass for all galaxies in the SQuIGG$\vec{L}$E sample. The shaded blue bar indicates the star-forming main sequence from Whitaker et al. (2012b). The dashed black line shows the reliability limit of our SFR measurements. The median SFR of the SQuIGG$\vec{L}$E galaxies is *below* our detectability threshold: the majority of SQuIGG$\vec{L}$E galaxies have $1M_\odot$/yr or less of ongoing star formation. This is more than an order of magnitude offset from the star-forming main sequence, which lies at $\sim 40M_\odot$/yr at this mass and redshift. While several galaxies in our sample do have higher ongoing SFRs, these galaxies are rare: just $\sim 2\%$ of SQuIGG$\vec{L}$E galaxies have SFRs on or above the star-forming main sequence.

We note that these SFRs are based on photometry with $\lambda_{\rm rest} \lesssim 12\mu$m, and thus we cannot exclude the possibility these objects host some amount of additional star formation that is fully obscured by dust. Observations at longer wavelengths, such as those described in Section 7.5, are required to fully rule out higher obscured SFRs.

Properties of the recent burst

The flexibility of our SFH model allows us to characterize the recent starburst. As described in detail in Section 7.2, we define the burst start and end based on the time derivative of the output SFH. Our modeling framework is able to accurately infer the end time of the recent burst (t_q) with a scatter of just 0.06 dex, as demonstrated in Suess et al. in prep. We are also able to place conservative limits on the mass fraction formed in the recent burst: while our recovered mass fractions tend to saturate at $\sim 60\%$, we are able to recover lower burst mass fractions with high fidelity (scatter ~ 0.1 dex). This saturation is likely due to the fact that our prior assumes that the SFH follows the average UniverseMachine SFH of a massive quiescent galaxy (Behroozi et al., 2019); this effectively asserts that these quenched galaxies likely formed a significant amount of their mass at early times. This choice allows our model to effectively "hide" a large number of old, red stars under a large recent burst, disfavoring extremely high burst mass fractions.

Figure 7.11 shows the time since quenching (t_q) as a function of the burst mass fraction ($f_{\rm burst}$). These SED fitting results allow us to confirm that SQuIGG$\vec{L}$E galaxies recently quenched a major epoch of star formation. The quenching timescale distribution peaks at ~ 175 Myr, with a tail towards longer quenching times. Galaxies which quenched > 400 Myr

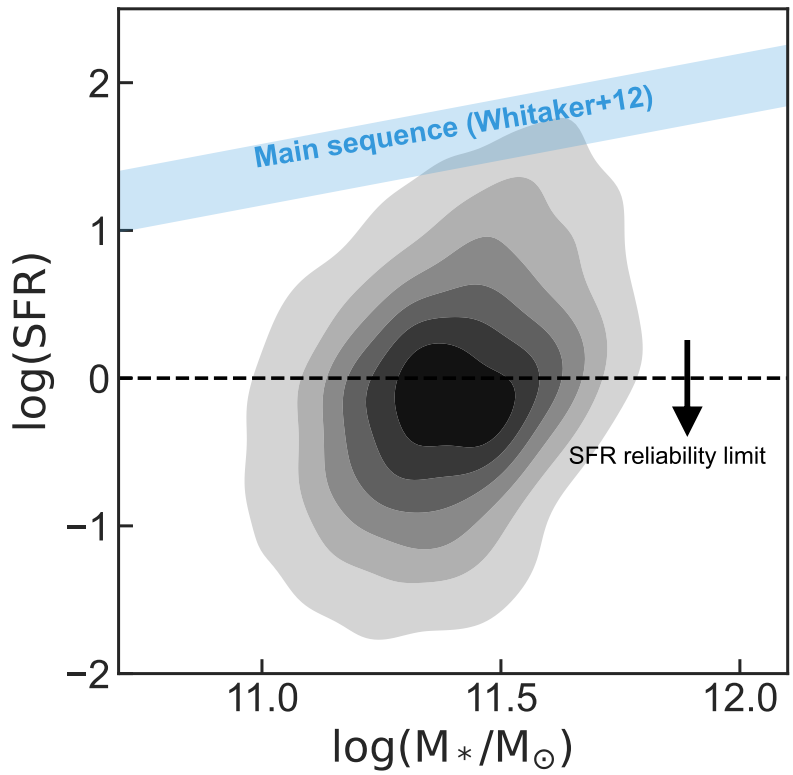

Figure 7.10: Star formation rate as a function of stellar mass for SQuIGG$\vec{L}$E galaxies (contours), compared to the $z = 0.7$ star-forming main sequence from Whitaker et al. (2012b) (blue shaded region). The contours are evenly spaced between 10% and 85% of the full distribution of best-fit SFRs. All recovered SFRs below $1M_{\odot}/yr$ should be treated as upper limits at $1M_{\odot}/yr$; our spectra and fitting methods cannot distinguish between lower levels of ongoing star formation. Galaxies in SQuIGG$\vec{L}$E are quenched, with the majority of galaxies lying more than an order of magnitude below the main sequence. Just 2% of post-starburst galaxies in our color-selected sample have SFRs on or above the main sequence.

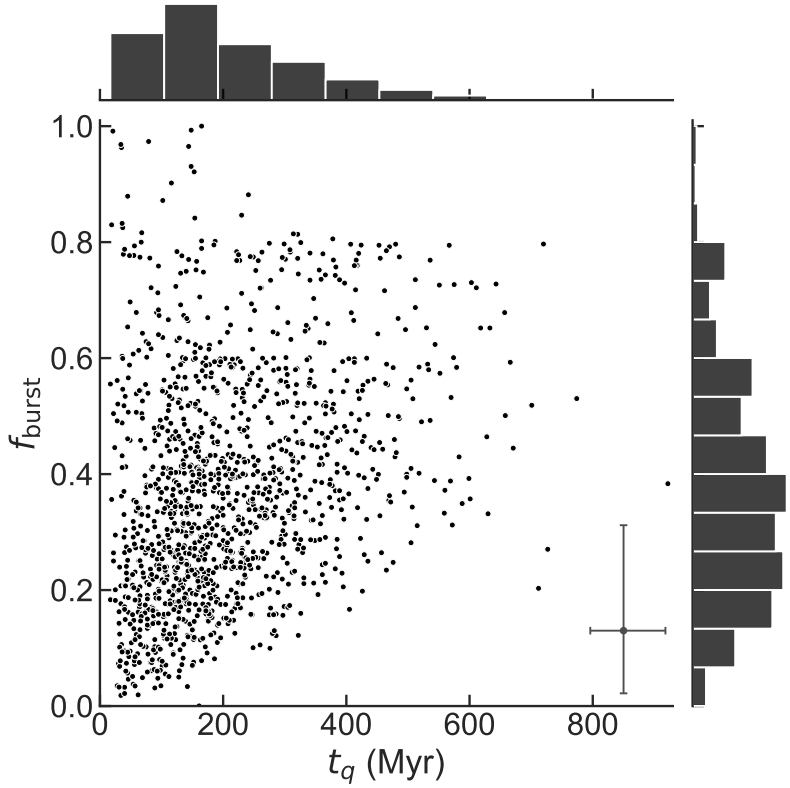

Figure 7.11: Burst mass fraction versus time since quenching for all SQuIGG$\vec{L}$E galaxies; histograms show the marginal distribution of each parameter. The point in the lower right shows a typical error bar; we note that the error on $f_{\rm burst}$ is typically asymmetric, with a higher tail towards high burst mass fractions. SQuIGG$\vec{L}$E galaxies have a wide range of burst mass fractions and quenching timescales. However, galaxies which quenched longer ago are only included in our sample if they also have high burst mass fractions; galaxies with high t_q and low $f_{\rm burst}$ are likely too red to satisfy our color-based selection criteria.

ago make up just 9% of the SQuIGG$\vec{L}$E sample. As expected based on their spectral shapes (Figure 7.3), our post-starburst sample does not include any galaxies which quenched more than a gigayear before observation. We find that galaxies with large t_q values are included in our sample only if they also have relatively high $f_{\rm burst}$ values (as expected from Figure 7.6). The 16-84th percentile range on our inferred t_q values is $\sim 80-350$ Myr, which corresponds to the main sequence lifetimes of $\sim 4-7 M_\odot$ stars. Thus, $\sim 7 M_\odot$ stars are generally the most massive stars we expect to be alive in SQuIGG$\vec{L}$E galaxies. This stellar mass corresponds roughly to the B4V classification, which is the boundary where stellar spectra begin to show very deep Balmer lines and strong Balmer breaks— exactly the spectral shapes we selected for. Our shortest recovered t_q values are thus consistent with the main sequence lifetimes of the highest-mass stars we would expect to find in these galaxies.

Figure 7.11 also illustrates that, while SQuIGG$\vec{L}$E galaxies have a large range in burst mass fractions, in general these galaxies recently concluded a major burst. More than 75% of SQuIGG$\vec{L}$E galaxies formed at least a quarter of their total stellar mass during the recent burst, and 20% of SQuIGG$\vec{L}$E galaxies formed *more than half* of their total stellar mass in the recent burst. Despite our relatively conservative priors on burst mass fraction, we find that SQuIGG$\vec{L}$E galaxies appear to be much more burst-dominated than local post-starburst galaxies; French et al. (2018) found that $z \sim 0$ post-starburst galaxies often formed just $\sim 10-15\%$ of their mass during the recent starburst. By going to intermediate redshift, we were able to identify the tail end of the peak quenching era at cosmic noon.

SQuIGG$\vec{L}$E galaxies have anomalous mid-infrared properties

In the local universe, several studies have found that post-starburst galaxies have unusual mid-infrared properties. Alatalo et al. (2017) showed that $z < 0.3$ post-starburst galaxies have strong infrared emission, shallow [3.4] - [4.6] colors, and flat or rising slopes at [12] - [22]. These properties are unlikely to be produced through star formation alone, and indicate the presence of AGN, strong PAH features, and/or significant contributions from dust-enshrouded AGB stars. Smercina et al. (2018) showed that $z \sim 0$ post-starburst galaxies exhibit high PAH abundances and very strong PAH features as well as large reservoirs of warm dust indicating atypical radiation fields. These features are unusual for either star-forming or quiescent galaxies, and indicate that a "standard" SED fitting setup is unlikely to accurately reproduce the mid-infrared properties of post-starburst galaxies.

These results lead us to question whether the post-starburst galaxies in SQuIGG$\vec{L}$E may have unusually high WISE fluxes or anomalous WISE colors. Because the exact nature of the processes contributing to this mid-IR flux is uncertain, we did *not* include the WISE 12μm (W3) or 22μm (W4) photometry in our SED fitting. Here, we test whether the predicted WISE photometry from our `Prospector` modeling matches the observed data points.

We first carefully flag which SQuIGG$\vec{L}$E galaxies are detected in the W3 and W4 bands. We consider all W3 and W4 measurements $\geq 3\sigma$ to be detections. Because W1 and W2 are both significantly more sensitive than W3/W4 and have much better characterized PSFs, we then use the positions of W1 and W2 sources to confirm lower-S/N W3 and W4 sources.

We consider W3 and W4 measurements at $> 1.7\sigma$ ($> 90\%$ confidence) to be detections if they correspond to a W1/W2 source detected at $> 2.5\sigma$. While individually these lower-S/N sources would not be formal detections, the combination of multiple bands of WISE imaging results in a robust $> 3\sigma$ identification of a source, albeit with large uncertainties on the individual WISE fluxes. For all sources that do not meet these criteria, we set robust 3σ upper limits on the W3 and W4 flux based on the measured background in the WISE bands. In total, we find that 511 SQuIGG$\vec{L}$E galaxies are detected in W3 and 176 are detected in W4.

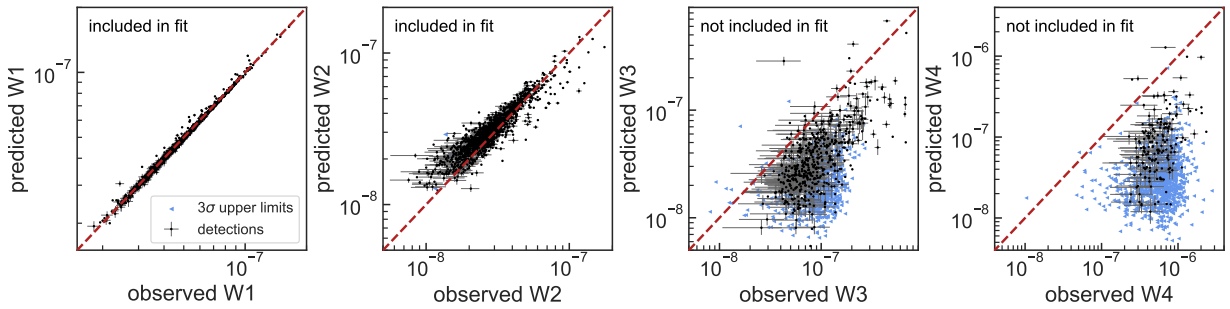

Figure 7.12: Predicted vs. observed WISE fluxes. Non-detections are indicated with blue triangles. While both W1 (3.4μm) and W2 (4.6μm) are well-predicted by our `Prospector` modeling, we find that SQuIGG$\vec{L}$E galaxies detected in the W3 (12μm) and W4 (22μm) bands tend to have much higher fluxes than predicted.

Figure 7.12 shows the WISE fluxes predicted from our `Prospector` modeling as a function of the observed WISE fluxes. The left two panels show W1 (3.4μm) and W2 (4.6μm), both of which are included in our `Prospector` fits; the right two panels show W3 (12μm) and W4 (22μm), which are *not* included in our fitting. The dashed red line in each panel shows the one-to-one relation. We find that the observed W1 and W2 values are well-matched by our fits, with a < 0.005 dex offset in W1 and a 0.03 dex offset in W2. However, the fluxes of SQuIGG$\vec{L}$E galaxies that are detected in W3 and W4 tend to be significantly underpredicted by our modeling. In W3, detected galaxies have fluxes ~ 0.4 dex higher than our predictions; for W4 detections, the observations are ~ 0.8 dex higher than the predictions. We note that including the W3 and W4 data points in our modeling does not resolve these offsets, indicating that the mid-infrared properties of these galaxies cannot be captured by our modeling framework. Understanding the nature of this excess mid-infrared flux is beyond the scope of this work, and will be studied in future SQuIGG$\vec{L}$E papers.

7.3 SFRs from lines

In this section, we compare the SFRs obtained by our SED fitting (Figure 7.10) with several alternate techniques for estimating SFRs based on optical lines; our goal here is to compare our `Prospector` SFRs with other SFR indicators commonly used in the literatures. Two spectral features in the SDSS wavelength regime— Hβ and [O II] λ3727— are often used as SFR indicators. Both of these lines are imperfect SFR indicators for post-starburst galaxies. First, due to the strong A-star signatures of our post-starburst galaxies (Figure 7.3), we typically see Hβ in absorption, not emission. While jointly modeling the continuum absorption along with the line emission can provide estimates of how much Hβ emission is filling in the absorption line, these line flux measurements are extremely difficult for massive galaxies with broad lines. Second, LINER emission can contribute to both [O II] and Hβ line flux; previous studies have found that this LINER emission is common in post-starburst galaxies (e.g., Lemaux et al., 2010; Kocevski et al., 2011; French et al., 2015). In this case, [O II] and Hβ SFRs should be treated as *upper* limits, as in French et al. (2015): star formation is not the only contributor to the measured line flux. However, both Hβ and [O II] are affected by dust. The SDSS spectra do not cover the Hα regime, and thus our best estimate of the dust attenuation in these galaxies comes from our SED fitting. If these dust values are underestimated, the SFR values should be considered *lower* limits. The competing effects of dust and LINER emission thus make it unclear whether Hβ and [O II] SFRs should be treated as upper or lower limits for post-starburst galaxies: the answer likely depends on the individual galaxy. For this reason— like Belli et al. (2021)— we conclude that the SED SFRs are more reliable than line-based SFRs for post-starburst galaxies. Nonetheless, here we compute both Hβ and [O II] SFRs to serve as a comparison point for the `Prospector` SFRs calculated in Section 7.2.

We adopt Hβ line flux measurements from Greene et al. (2020), who used the public penalized pixel-fitting code pPXF (Cappellari & Emsellem, 2004) to fit the stellar continuum as well as Hβ and [O III] emission lines. We assume an intrinsic line ratio of Hα/Hβ = 2.86 to estimate the Hα flux. We correct these fluxes for dust using the `Prospector` dust index and A_v values. Again, our fitting assumes that lines (including Hα and Hβ) are twice as attenuated as the stellar continuum. We then use the Kennicutt (1998b) conversion, adjusted to a Chabrier (2003) IMF, to estimate the SFR. We note that our `Prospector` fits include the Hβ line, and thus this line is a also a major contributor to the SFRs shown in Figure 7.10. However, the Kennicutt (1998b) conversion assumes solar metallicity and a constant SFH, whereas the `Prospector` SFRs takes into account the metallicity and SFH.

To calculate [O II] SFRs, we measure the aperture-corrected flux from the [O II] doublet by modeling the region of the spectrum around the line with a single Gaussian centered at the mean wavelength of the [O II] doublet plus a straight-line fit to the continuum. Our spectra do not resolve the [O II] doublet. We hold the width of the Gaussian line profile fixed to the velocity as measured by pPXF (Greene et al., 2020). Again, we correct the measured line flux for dust extinction using the `Prospector` fitting results. Finally, we used the conversion in Kennicutt (1998b) (adjusted to a Chabrier 2003 IMF) to convert our measured line flux

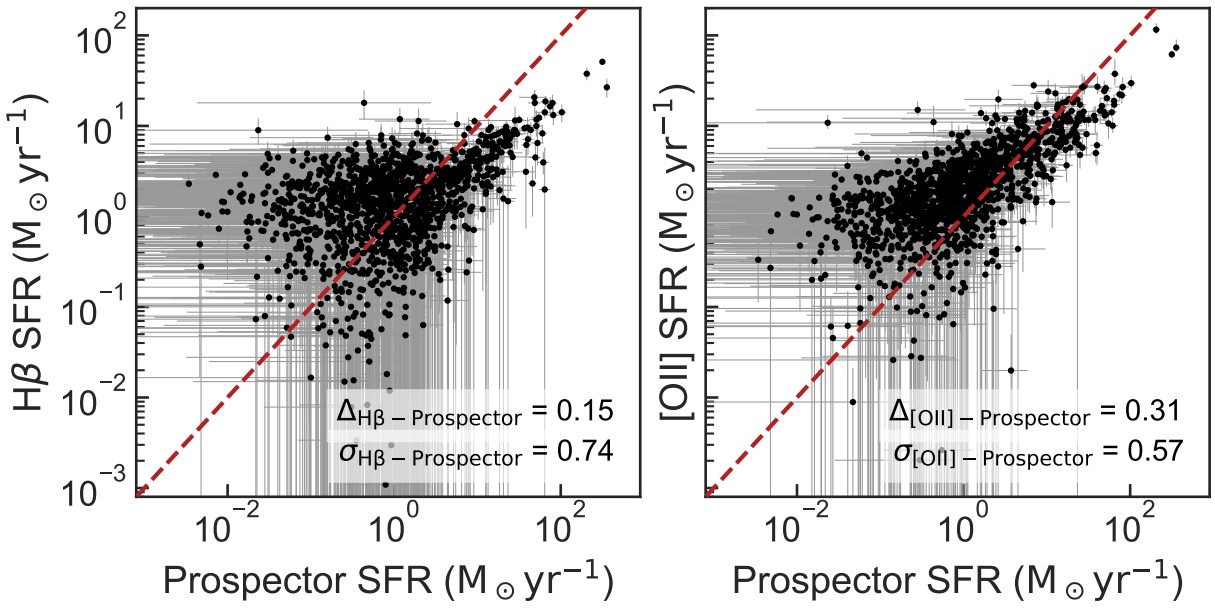

Figure 7.13: Comparison of SFR measured directly from both the Hβ and [O II] lines with the `Prospector` SFRs described in Section 7.2. There is significant scatter in both line measurements at the low-SFR end. Towards high SFRs, the [O II] SFRs are offset slightly higher than the `Prospector` SFRs, likely due to LINER contributions; the Hβ SFRs are offset lower than the `Prospector` SFRs.

to a SFR. Error bars on the SFR were obtained using 1,000 bootstrap realizations of the measured line flux.

Figure 7.13 shows the SFR estimated from both Hβ (left) and [O II] (right) as a function of the `Prospector` SFR (Section 7.2). Again, our mock recovery tests indicate that `Prospector` SFRs do not have significant constraining power below $1 M_{\odot} yr^{-1}$. We see that, while the line-based SFRs generally correlate with the `Prospector` SFRs, there is a large amount of scatter, particularly at the low-SFR end. Hβ SFRs are typically higher than `Prospector` SFRs at low SFRs, likely because the Hβ fluxes in this regime are dominated by spectral noise. At high SFR, Hβ SFRs are offset lower than the `Prospector` SFRs; this could be due to the fact that the `Prospector` SFRs do not assume a constant SFH and solar metallicity, as the Kennicutt (1998b) conversion does. Median [O II] SFRs are offset slightly from `Prospector` SFRs at all SFRs. This difference is largest at the lowest SFRs, likely due to an increasing fraction of [O II] flux originating from LINER emission. For all three SFR indicators, there are a small fraction ($\sim 2\%$) of SQuIGG$\vec{L}$E galaxies that have high SFRs consistent with the star-forming main sequence. Because of the effects of both LINER emission and dust, we take the `Prospector` SFRs as the most reliable SFR indicator available for the full SQuIGG$\vec{L}$E sample (see also, e.g., Belli et al., 2021). However, we note that no matter

which SFR indicator is used— `Prospector`, Hβ, or [O II]— the median SFRs of all galaxies in the SQuIGG$\vec{L}$E sample is an order of magnitude or more below the main sequence.

7.4 Comparison to other samples of post-starburst galaxies

Here, we place the SQuIGG$\vec{L}$E sample in the context of existing large samples of post-starburst galaxies. As discussed in Section 7.1, a myriad of studies have selected recently-quenched galaxies across redshift by their spectral line strengths, spectral shapes, or colors. The largest spectroscopic samples of post-starburst galaxies come from the low-redshift universe, $z \lesssim 0.1$, where large spectroscopic surveys such as the SDSS allow for the identification of rare recently-quenched galaxies (e.g., Zabludoff et al., 1996; Quintero et al., 2004; French et al., 2015; Alatalo et al., 2016). While post-starburst galaxies are common at $z \gtrsim 1$ (e.g., Whitaker et al., 2012a; Wild et al., 2016; Belli et al., 2019), spectroscopic samples tend to be smaller due to the difficulty of high-redshift spectroscopy. The only other large intermediate-redshift spectroscopic sample of post-starburst galaxies comes from Pattarakijwanich et al. (2016), who also select from the SDSS & BOSS surveys. In Section 7.4, we compare SQuIGG$\vec{L}$E to lower- and higher-redshift samples; in Section 7.4, we compare SQuIGG$\vec{L}$E to the Pattarakijwanich et al. (2016) sample at the same redshift.

Comparison to post-starburst samples across redshift

Figure 7.14 shows the SQuIGG$\vec{L}$E sample in context of one low-redshift (French et al., 2015) and one high-redshift (Wild et al., 2020) sample of post-starburst galaxies. The French et al. (2015) sample was selected by their high Hδ and low Hα equivalent widths, while the Wild et al. (2020) sample was selected using a PCA technique. Figure 7.14 shows that SQuIGG$\vec{L}$E galaxies lie at intermediate redshift, and tend to have higher stellar masses than many of the French et al. (2015) or Wild et al. (2020) galaxies. The lack of low-mass galaxies in SQuIGG$\vec{L}$E is likely a selection effect: our sample *must* have had high mass in order to fall into the SDSS spectroscopic sample and exceed our S/N cut. While the three populations of post-starburst galaxies overlap significantly in Hδ - D_n4000 space, the bulk of the SQuIGG$\vec{L}$E galaxies lie at smaller D_n4000 values and slightly higher Hδ_A values than the French et al. (2015) or Wild et al. (2020) samples. Because stellar age typically increases towards the lower right of this diagram, this indicates that SQuIGG$\vec{L}$E galaxies are slightly *younger* on average than either of these samples. This is confirmed by SFH modeling: both Wild et al. (2020) and French et al. (2018) found older post-burst ages for their samples than we find in Section 7.2. However, it is difficult to directly compare the inferred t_q values because each study uses a slightly different SFH parameterization and definition of t_q.

The bottom panel of Figure 7.14 shows a stack of the spectra in all three samples. Both the SQuIGG$\vec{L}$E and French et al. (2015) stacks are created using public SDSS data. As in

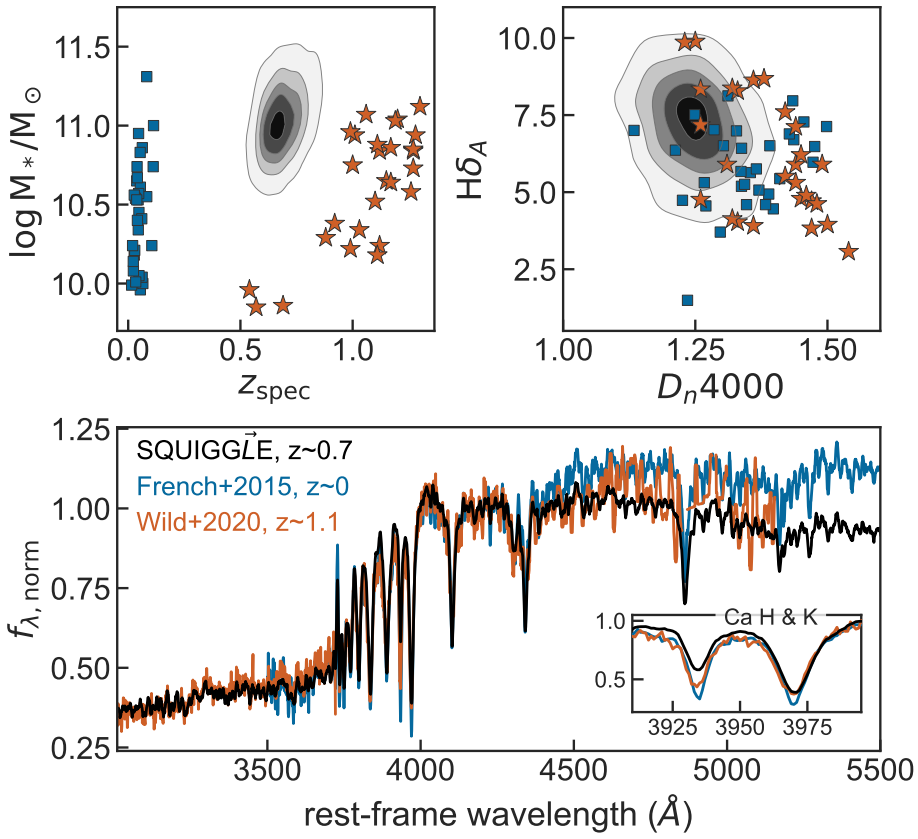

Figure 7.14: Comparison between the SQuIGG$\vec{L}$E sample (black) and other samples of post-starburst galaxies, including the French et al. (2015) sample of $z \sim 0$ galaxies (blue) and the higher-redshift sample from Wild et al. (2020) (orange). The SQuIGG$\vec{L}$E sample lies at high stellar mass and intermediate redshift. The bulk of SQuIGG$\vec{L}$E galaxies have lower D_n4000 values and slightly higher Hδ values than either the Wild et al. (2020) or French et al. (2015) samples, indicating younger stellar ages. The French et al. (2015) and Wild et al. (2020) stacks show slightly more flux at $\lambda_{\rm rest} > 4500$Åand more symmetric Ca H & K features than the SQuIGG$\vec{L}$E stack; these differences likely reflect a higher fraction of older stars.

Figure 7.3, all individual spectra are normalized using the flux between 4150 and 4250 Å. Spectra from the Wild et al. (2020) sample come from both the UDSz ESO Large Programme (PI: Almaini) and Maltby et al. (2016); Maltby et al. in prep. provides further details about the spectroscopic data reduction. In addition to normalizing the Wild et al. (2020) spectra (again, between 4150 and 4250 Å), we smooth the stack using a nine-pixel median filter past $\sim$ 4300Å, where fewer than 15 spectra have wavelength coverage. We do not show the Wild et al. (2020) stacked spectrum past $\sim$ 5150Å, where fewer than five individual spectra have wavelength coverage.

We see two notable differences in the stacked spectra shown in Figure 7.14: the depth of the absorption lines, and the spectral shape redward of $\sim$ 4400Å. The calcium H & K lines are deep and nearly symmetric for the French et al. (2015) stack, while they are shallower and much more asymmetric in the SQuIGG$\vec{L}$E stack (because the CaH line is more significantly contaminated by Hϵ). These spectral differences indicate that SQuIGG$\vec{L}$E galaxies are younger than the French et al. (2015) galaxies. We also find that the French et al. (2015) spectra have nearly a flat slope redward of $\sim$ 4400Å, while (by construction) the SQuIGG$\vec{L}$E stack shows a relatively blue slope. The Wild et al. (2020) stack has a slope intermediate between the French et al. (2015) and SQuIGG$\vec{L}$E samples. This difference in slope indicates that both the French et al. (2015) and Wild et al. (2020) samples contain galaxies with larger contributions from old stars. For the French et al. (2015) sample, this aligns with expectations from the SFH fitting in French et al. (2018): these galaxies have best-fit burst mass fractions that are often $\lesssim$ 20%, lower than the SQuIGG$\vec{L}$E burst mass fractions shown in Figure 7.11. However, Wild et al. (2020) finds burst mass fractions that are often $\sim 60-80\%$, above the median burst mass fractions for the SQuIGG$\vec{L}$E sample. This difference is likely primarily caused by differences in the fitting methodology and definition of "burst mass fraction" used in Wild et al. (2020) and this study. Furthermore, the Wild et al. (2020) stack shown in Figure 7.14 is dominated by low-redshift, lower $f_{\rm burst}$ galaxies at these longer wavelengths.

Comparison to the Pattarakijwanich et al. (2016) sample

In Figure 7.15, we compare the SQuIGG$\vec{L}$E sample to the Pattarakijwanich et al. (2016) sample. This study also selected post-starburst galaxies from SDSS spectroscopy. Unlike SQuIGG$\vec{L}$E, Pattarakijwanich et al. (2016) used a template-fitting approach to find post-starburst galaxies: galaxies were fit with a sum of both an old ('K') component and a young ('A') component, then identified as post-starburst if the light-weighted A/(A+K) ratio exceeded 0.25. Pattarakijwanich et al. (2016) selected spectra from both the SDSS and BOSS surveys, including galaxies with redshifts as low as $z = 0.05$. In Figure 7.15, to facilitate a direct comparison with SQuIGG$\vec{L}$E we show only galaxies with $z \geq 0.5$. The median stacked spectrum of the $z > 0.5$ Pattarakijwanich et al. (2016) sample has significantly more flux at longer wavelengths; again, this indicates older stellar ages. However, the 16-84% confidence interval of the Pattarakijwanich et al. (2016) encompasses a large range of

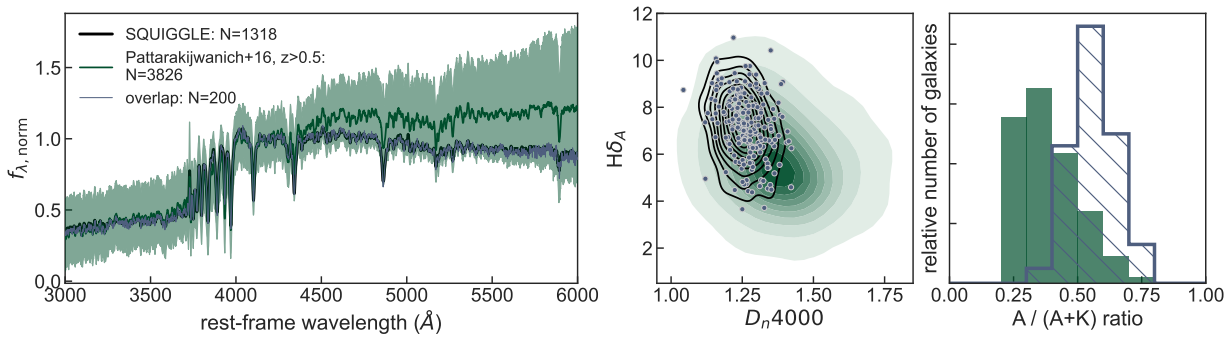

Figure 7.15: Comparison between the SQuIGG$\vec{L}$E sample (black) and the Pattarakijwanich et al. (2016) sample, which is also selected from the SDSS. The left panel shows a stacked spectrum of all SQuIGG$\vec{L}$E galaxies (black), all Pattarakijwanich et al. (2016) galaxies with $z \geq 0.5$ (green; 16-84% range shaded), as well as galaxies identified as post-starburst in *both* samples (blue; overlaps with black spectrum). The central panel shows the same three sets of post-starburst galaxies in Hδ and D_n4000, with the overlapping sample shown as blue dots. While on average the Pattarakijwanich et al. (2016) sample includes older galaxies with lower burst mass fractions, the distribution of this sample is very broad and the 1σ range just encompasses young post-starburst galaxies like those found by SQuIGG$\vec{L}$E. The right panel shows histograms of the A/(A+K) ratio (e.g., the light-weighted fractional contribution of A-type stars) for the full Pattarakijwanich et al. (2016) as well as the overlap between the Pattarakijwanich et al. (2016) and SQuIGG$\vec{L}$E samples. The galaxies selected by SQuIGG$\vec{L}$E tend to have higher A/(A+K) ratios than the full Pattarakijwanich et al. (2016) sample.

spectral slopes. The lower 16% interval encompasses the SQuIGG$\vec{L}$E stack, indicating that the Pattarakijwanich et al. (2016) sample includes some post-starburst galaxies as young as those in SQuIGG$\vec{L}$E. This larger median age and wider age spread is also reflected in the $H\delta$ – D_n4000 values: the median value of the Pattarakijwanich et al. (2016) sample is offset from the SQuIGG$\vec{L}$E median, but the distribution is broad and overlaps significantly with SQuIGG$\vec{L}$E.

We find that 210 post-starburst galaxies are selected both by SQuIGG$\vec{L}$E and Pattarakijwanich et al. (2016). These galaxies reflect the full distribution of SQuIGG$\vec{L}$E galaxies: they trace the SQuIGG$\vec{L}$E contours in $H\delta$ – D_n4000 space, and their stacked spectrum is indistinguishable from the full SQuIGG$\vec{L}$E sample. This relatively small number of overlapping galaxies is primarily due to the fact that Pattarakijwanich et al. (2016) selected galaxies from SDSS DR9, whereas the SQuIGG$\vec{L}$E selection is performed on SDSS DR14. Nearly half of SQuIGG$\vec{L}$E-identified post-starburst galaxies were observed *after* DR9, and thus could not have been included in Pattarakijwanich et al. (2016).

The right panel of Figure 7.15 shows the A/(A+K) ratio as calculated by Pattarakijwanich et al. (2016), both for the full Pattarakijwanich et al. (2016) sample and the galaxies

selected by both Pattarakijwanich et al. (2016) and SQuIGG$\vec{L}$E. SQuIGG$\vec{L}$E galaxies have a higher median A/(A+K) ratio than the full Pattarakijwanich et al. (2016) sample, indicating that we are generally selecting more burst-dominated galaxies.

In summary, the SQuIGG$\vec{L}$E sample is smaller and more targeted than the Pattarakijwanich et al. (2016) sample: SQuIGG$\vec{L}$E consists of uniformly young post-starburst galaxies with a narrow spread in Hδ-D_n4000 space. The Pattarakijwanich et al. (2016) sample includes a wider range of stellar ages, but does not include the majority of young SQuIGG$\vec{L}$E galaxies which were observed after DR9.

7.5 SQuIGG$\vec{L}$E science objectives

The large sample of bright, intermediate-redshift, recently-quenched galaxies in SQuIGG$\vec{L}$E enables a wide range of studies into the rapid quenching process. Most of these science cases rely on the stellar population synthesis modeling presented in this study in combination with other multi-wavelength datasets. SQuIGG$\vec{L}$E is not intended to be a complete sample of post-starburst galaxies at these redshifts: the selection function is complex, and not conducive to number density studies. Instead, SQuIGG$\vec{L}$E was designed to select the brightest, most massive, most burst-dominated post-starburst galaxies at intermediate redshifts. These galaxies serve as *laboratories* to conduct detailed multi-wavelength dives into the processes responsible for shutting down star formation. Here, we briefly summarize the primary science objectives of SQuIGG$\vec{L}$E.

Molecular gas reservoirs

Theoretical quenching mechanisms generally rely on processes which remove the available fuel for star formation by depleting, heating, or ejecting cold molecular gas reservoirs. One of the primary science objectives of SQuIGG$\vec{L}$E is to directly test this assumption. An initial ALMA study of the CO(2–1) emission of two SQuIGG$\vec{L}$E post-starburst galaxies revealed abundant gas reservoirs despite low ongoing star formation rates (Suess et al., 2017). This result indicates that— contrary to expectations— quenching does not require the total removal of molecular gas. We are currently conducting an ALMA survey of the molecular gas contents of eleven additional SQuIGG$\vec{L}$E post-starburst galaxies (R. Bezanson et al., in prep.). This study will allow us to test whether these abundant gas reservoirs are common after quenching, and whether the gas fraction depends on other galaxy properties such as time since quenching (Section 7.2).

These molecular gas measurements, in combination with SFRs, will allow us to place these galaxies on the Kennicutt-Schmidt relation and investigate how efficiently they are forming stars (e.g., Kennicutt, 1998a). As part of this work, we are in the process of obtaining other robust estimators of the SFR in these galaxies. In particular, we are using the VLA to investigate possible highly-obscured SFR, and using Keck/NIRES to calculate Balmer decrement-corrected Hα SFRs.

Morphologies & sizes

Some studies predict that quenching can be triggered by a gas-rich major merger: in this scenario, the merger funnels gas to the galaxy's center where it is consumed in an intense starburst (e.g., Hopkins et al., 2006; Wellons et al., 2015). Deep, high-resolution imaging of SQuIGG$\vec{L}$E galaxies will allow us to quantify the fraction of recently-quenched galaxies that show signs of recent mergers (including tidal features and asymmetric morphologies). Sazonova et al. (2021) suggests that these disturbed morphologies are common for post-starburst galaxies at $z \sim 0$. Our team has obtained *Hubble Space Telescope* WFC3/F125W imaging for three SQuIGG$\vec{L}$E galaxies targeted as part of our ALMA survey (Figure 7.16). These galaxies are clearly disturbed: J2202-0033 has a large tidal feature to the west, and both J0027+0129 and J0912+1523 have nearby companions which may be physically associated. The image of J0912+1523 also reveals that it has a spheroidal component embedded within a disk.

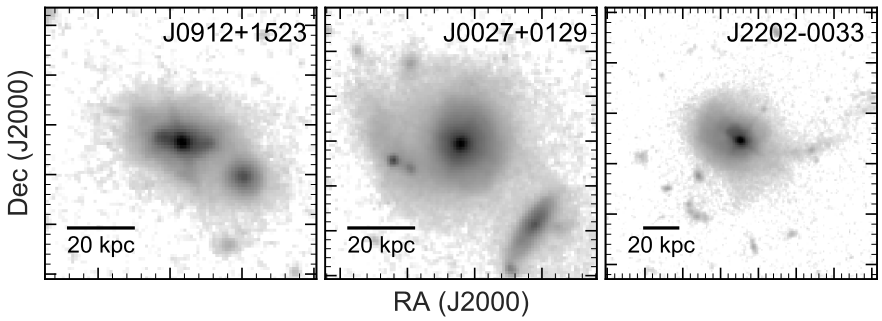

Figure 7.16: *HST*/WFC3 F110W images of three galaxies in our sample. We show a 80 kpc square cutout for J0912+1523 and J0027+0129. J2202-0033 is shown in a 150 kpc square cutout to capture the full extent of the tidal tail that stretches to the west. All three galaxies exhibit complex morphologies and merger signatures.

Some previous studies have found that post-starburst galaxies have extremely compact sizes, and may be smaller than their older quiescent counterparts (e.g., Whitaker et al., 2012a; Yano et al., 2016; Almaini et al., 2017). Suess et al. (2020) suggests that these size differences may be primarily caused by the effects of radial color gradients (see also Maltby et al., 2018; Setton et al., 2020). In either case, differences in the sizes and/or color gradients of post-starburst galaxies and older quiescent galaxies could provide clues both to the formation mechanisms for post-starburst galaxies and the processes contributing to evolution along the quiescent sequence. Deep, high-resolution images such as those shown in Figure 7.16 will allow us to calculate the sizes of SQuIGG$\vec{L}$E post-starburst galaxies and compare them to a mass-matched sample of older quiescent galaxies.

While the images presented in Figure 7.16 shed light on the morphologies and sizes of a few individual SQuIGG$\vec{L}$E galaxies, obtaining *HST* imaging for a statistical sample of

post-starburst galaxies is prohibitively expensive. A much larger set of deep, high-resolution images comes from the overlap of the SQuIGG$\vec{L}$E sample and the public Hyper SuprimeCam survey (Aihara et al., 2018). One of our major science objectives is to use the > 150 high-quality HSC images of SQuIGG$\vec{L}$E galaxies to investigate the sizes, morphologies, and merger fractions of these recently-quenched galaxies (D. Setton et al., in prep.).

Kinematics

In general, star-forming galaxies tend to be rotationally-supported disks, while quiescent galaxies are more likely to be kinematically hot and supported by random motions (e.g., Emsellem et al., 2011). However, it is still not understood why a cessation of star formation correlates with a change in kinematics. Furthermore, it is unclear whether this kinematic transition occurs before, after, or at the same time as star formation shuts down. The bright, recently-quenched SQuIGG$\vec{L}$E galaxies provide an ideal testbed for IFU studies to directly probe the kinematics of galaxies just after quenching. An early result for one SQuIGG$\vec{L}$E target (J0912+1523, also shown in Figure 7.16) revealed that the galaxy is a rotating disk (Hunt et al., 2018). A larger followup study of five additional SQuIGG$\vec{L}$E galaxies showed that only $\sim$half of post-starburst galaxies show clear velocity gradients, while the other half are dominated by random motions (Setton et al., 2020).

Resolved stellar populations

Studying the spatially-resolved properties of post-starburst galaxies could provide additional clues to the quenching process. Radial age or sSFR gradients can be used to help determine whether quenching proceeded inside-out or outside-in (e.g., Tacchella et al., 2018; Woo & Ellison, 2019); radial metallicity gradients can help distinguish between in- and ex-situ components, important when mergers are suggested as a trigger for quenching (e.g., Greene et al., 2015; Chan et al., 2016; Woo & Ellison, 2019). Our preliminary study of six SQuIGG$\vec{L}$E galaxies shows that they have flat age gradients as probed by Hδ (Setton et al., 2020). In the absence of strong radial dust or metallicity gradients, these flat age gradients are consistent with the flat color gradients that Maltby et al. (2018) and Suess et al. (2020) find for post-starburst galaxies. Setton et al. (2020) find that these six post-starburst galaxies have young light-weighted ages at all radii, implying that star formation shut off uniformly throughout the galaxy. In the future, we plan to expand the sample size of SQuIGG$\vec{L}$E post-starburst galaxies with spatially-resolved stellar population measurements; facilities like *JWST* would be useful to perform these studies further in the infrared, where it is easier to break the age-dust-metallicity degeneracy.

AGN incidence

One popular theoretical mechanism for quenching galaxies invokes strong feedback from AGN (e.g., Di Matteo et al., 2005; Hopkins et al., 2006). This feedback, possibly induced

by a major merger (Springel & Hernquist, 2005; Hopkins et al., 2006; Wellons et al., 2015), could heat the interstellar medium and/or drive molecular gas from the galaxy, removing the fuel for star formation (Alatalo et al., 2015). Establishing a direct causal connection between AGN activity and star formation suppression has unfortunately proven difficult, in part because AGN vary dramatically on much shorter timescales than star formation. A large number of AGN surveys have shown that AGN activity depends on star formation rate and mass (e.g., Hickox et al., 2014). The SQuIGG$\vec{L}$E sample allows us to ask how many recently-quenched galaxies show AGN activity, and test whether certain types of post-starburst galaxies are more likely to host AGN. Greene et al. (2020) used SQuIGG$\vec{L}$E to show that the incidence of AGN depends strongly on D_n4000: recently-quenched galaxies from SQuIGG$\vec{L}$E are ten times more likely to host an optical AGN than a mass-matched sample of older quiescent galaxies. This hints that AGN activity is indeed correlated with the quenching process in these massive galaxies.

IR properties

As shown in Figure 7.12, SQuIGG$\vec{L}$E galaxies have puzzlingly high W4 fluxes. Previous studies at $z \lesssim 0.3$ have found that the mid-infrared spectra of post-starburst galaxies are influenced by emission from AGN, TP-AGB stars, and strong PAH features (e.g., Alatalo et al., 2017; Smercina et al., 2018). In future studies, we will perform stacking analyses of the WISE imaging for SQuIGG$\vec{L}$E galaxies to understand the nature of this excess W4 emission. Additionally, the mid-infrared capabilities of *JWST* may allow us to understand the origin of this emission. These infrared studies can be paired with studies of the molecular gas reservoirs in order to obtain a more complete picture of the interstellar medium (ISM) conditions as galaxies cease forming stars.

7.6 Discussion & summary

In this chapter, we present the sample selection, stellar population properties, star formation histories, and objectives of the SQuIGG$\vec{L}$E survey of post-starburst galaxies. We select bright, intermediate-redshift, recently-quenched galaxies from the SDSS spectroscopic sample using a simple color-based selection criterion. Using just two rest-frame color cuts, we are able to isolate 1,318 post-starburst galaxies at $0.5 < z \lesssim 0.9$. These galaxies all have high Hδ equivalent widths, low D_n4000 values, and BV/A-star dominated spectra indicating young stellar ages. These recently-quenched galaxies serve as laboratories to study the processes responsible for shutting down star formation in galaxies: the signatures of the quenching process should still be imprinted on their morphologies, kinematics, and gas properties.

We use the `Prospector` spectral energy distribution fitting code to recover the stellar population parameters and star formation histories of all SQuIGG$\vec{L}$E galaxies. We find that these galaxies are very massive— nearly all SQuIGG$\vec{L}$E galaxies have $M_* > 10^{11} M_\odot$— and have relatively low dust attenuation values. Our fitting also shows that these galaxies

are indeed quenched: the median SFRs recovered from our SED fitting are more than an order of magnitude below the star-forming main sequence (Whitaker et al., 2012b). The quenched nature of this sample is consistent with SFR estimates based on both the Hβ and [O II] spectral lines: while these SFRs are likely less reliable than the SED SFRs due to the competing effects of LINER emission and dust (see also, e.g., Belli et al., 2021), the median Hβ and [O II] SFRs also lie well below the main sequence. Longer-wavelength data would be required to fully rule out the possibility of highly dust-obscured star formation.

Our SED fitting also allow us to quantify the properties of the recent burst. By using non-parametric SFHs, our SED fitting methodology accurately recovers both how long these galaxies have been quenched (t_q) and the fraction of the total stellar mass formed in the recent burst ($f_{\rm burst}$). We find that SQuIGG$\vec{L}$E galaxies quenched their star formation extremely recently, with a median t_q value of just 175 Myr. Galaxies which quenched longer ago, up to $\sim$ 800 Myr before the time of observation, are also included in SQuIGG$\vec{L}$E; however, these older post-starburst galaxies are only selected if they also have relatively high burst mass fractions. The $f_{\rm burst}$ distribution of SQuIGG$\vec{L}$E galaxies peaks at around $\sim 30\%$ of the total stellar mass being formed in the recent burst. We note that due to our conservative choice of priors, we likely underestimate $f_{\rm burst}$ for the most extreme and burst-dominated objects. Despite this choice, we find that 20% of the galaxies in SQuIGG$\vec{L}$E formed a *majority* of their total stellar mass during the recent burst.

We find that these extreme objects are younger and more burst-dominated than samples of "K+A" or "E+A" post-starburst galaxies at $z \sim 0$: SQuIGG$\vec{L}$E galaxies have higher median Hδ equivalent width, lower D_n4000 values, and bluer spectral slopes than the French et al. (2015) sample of local post-starburst galaxies. This difference is also confirmed by the SFH fitting in French et al. (2018): many local post-starburst galaxies have burst mass fractions $\lesssim 20\%$, in contrast to the higher burst mass fractions we find for SQuIGG$\vec{L}$E galaxies. While SQuIGG$\vec{L}$E galaxies may have slightly lower average burst mass fractions than $z \sim 1$ post-starburst galaxies from Wild et al. (2020), SQuIGG$\vec{L}$E galaxies are on average younger than the Wild et al. (2020) post-starburst galaxies. Together, these results indicate that our selection was able to identify the rare intermediate-redshift tail of the peak epoch of quenching at $z > 1$: SQuIGG$\vec{L}$E galaxies recently and rapidly shut down a major burst of star formation. By targeting these bright, intermediate-redshift galaxies, SQuIGG$\vec{L}$E is able to strike a balance between low enough redshift that follow-up observations are feasible, and high enough redshifts that we can use these galaxies to understand how galaxies shut down their major star-forming epoch.

This large sample of recently-quenched galaxies opens a wide range of future studies. Different theoretical quenching mechanisms predict qualitatively different morphologies, age gradients, kinematics, AGN incidence, and ISM conditions. We have already begun to use this sample of galaxies to constrain the mechanisms responsible for quenching. We have found that, in contrast to theoretical predictions, quenching does *not* require the total removal of molecular gas (Suess et al., 2017). Furthermore, we have found that these recently-quenched galaxies can have a range of different kinematic structures, but tend to have flat age

gradients indicating that the recent starburst was not purely centrally-concentrated (Hunt et al., 2018; Setton et al., 2020). We have also shown that AGN likely play an important role in quenching: SQuIGG$\vec{L}$E galaxies are more than ten times more likely to host an optical AGN than a mass-matched sample of older quiescent galaxies, and the AGN fraction is even higher in the youngest SQuIGG$\vec{L}$E galaxies (Greene et al., 2020). These studies represent just the beginning of the insights that the SQuIGG$\vec{L}$E sample will provide into the mechanisms responsible for transforming galaxies from disky blue star-formers to quiescent red ellipticals.

Chapter 8

Conclusions & future directions

In this thesis, we have investigated the growth and transformation of galaxies across cosmic time. The first section of this thesis concentrated on radial color gradients in galaxies. We used these color gradient measurements to quantify the size evolution of galaxies and inform our understanding of how galaxy structures evolve. The second section of this thesis explored post-starburst galaxies as laboratories to study the rapid quenching process in massive galaxies.

We have found that color gradients in galaxies serve as both a bias and a tool. Color gradients are a *bias* in the sense that that they impact our understanding of the size evolution of galaxies. In Chapters 2 & 3, we find that color gradients in both star-forming and quiescent galaxies evolve with redshift: color gradients are nearly flat at high redshift, and become increasingly more negative towards lower redshift. Previous studies of the galaxy size-mass relation used half-light radii, which include the effects of both true size evolution and these evolving color gradients. After correcting for color gradients, we find that both star-forming and quiescent galaxies evolve much slower than previously thought. In particular, in Chapter 3 we found that the evolution of quiescent galaxies is consistent with a minor merger growth model alone. This indicates that progenitor bias does not contribute significantly to the growth of quiescent galaxies at $z \lesssim 2$. In Chapter 4, we saw that color gradients can also bias studies of the sizes of different types of galaxies. We performed the first study of how galaxy color gradients, sizes, and central densities evolve along the quiescent sequence. In contrast to previous studies, we found the youngest quiescent galaxies are *not* significantly smaller than their older quiescent counterparts. Instead, these young quiescent galaxies have flatter color gradients.

Because color gradients are caused by radial variations in stellar population properties, they also serve as a *tool* to study the processes driving galaxy evolution. In Chapter 4, we found that color gradients become more strongly negative as quiescent galaxies age. In combination with the lack of dependence of Σ_1 on age, these results support a picture where quiescent galaxies grow inside-out via minor mergers. In Chapter 5, we used color gradients and half-mass radii to study how galaxy structures evolve as galaxies move from star-forming to quiescent. We suggest a new interpretation for the star-forming size-mass

relation as a series of overlapping parallel relations that are driven by scatter in the Σ_1-mass plane. We also found that even at fixed redshift, mass, and size, green valley galaxies and post-starburst galaxies have distinct color gradients. These color gradient differences reflect different formation scenarios. We suggest a picture where galaxies grow slowly up the Σ_1-mass and size-mass relations until (a) they naturally pass through the green valley and gradually reach quiescence, or (b) they experience a rapid compaction-type event that lifts them to high Σ_1 and quiescence.

In Chapters 6 & 7, we concentrated on the products of the rapid quenching process, post-starburst galaxies. By studying the properties of these galaxies in detail, we aim to understand the mechanisms responsible for shutting down their star formation. In Chapter 6, we found that two of these post-starburst galaxies retained large molecular gas reservoirs despite low ongoing star formation rates. These large gas reservoirs indicate that star formation can shut down while galaxies still have an abundance of fuel, and challenge our views of the quenching process. In Chapter 7, we present the SQuIGG$\vec{L}$E survey of intermediate-redshift post-starburst galaxies. This sample builds on the sample presented in Chapter 6, including a larger number of galaxies and detailing their properties in more detail. In particular, we perform non-parametric star formation history fitting to find that these galaxies recently and rapidly quenched a major epoch of star formation.

8.1 Future directions

While the work presented in this thesis has answered several important outstanding questions in galaxy growth and transformation, it has also unveiled new puzzles.

The physical origin of color gradients

This thesis has established that the strength of color gradients evolves from $0 \lesssim z \leq 2.5$. However, we do not understand the *origins* of these color gradients. Color gradients can be caused by radial gradients in age, metallicity, or dust extinction. The next frontier in using multi-wavelength imaging to probe galaxy structural evolution is to disentangle these different possible origins for color gradients. This is particularly important for quiescent and transitioning galaxies, because different quenching mechanisms predict unique stellar population gradients. *Gas-rich mergers* predict negative age and metallicity gradients (young, metal-poor centers, e.g., Hopkins et al., 2009; Woo et al., 2017). *Compaction* caused by migration of gas clumps predicts positive age gradients and weak metallicity gradients (e.g., Ceverino et al., 2015). *Dissipative collapse* in an early universe predicts metallicity gradients, but no age gradients (e.g., Wellons et al., 2015). These signatures are observable as color gradients. But because dust gradients also cause color gradients, it is imperative to measure dust, age, and metallicity gradients *simultaneously* to distinguish between these proposed quenching mechanisms.

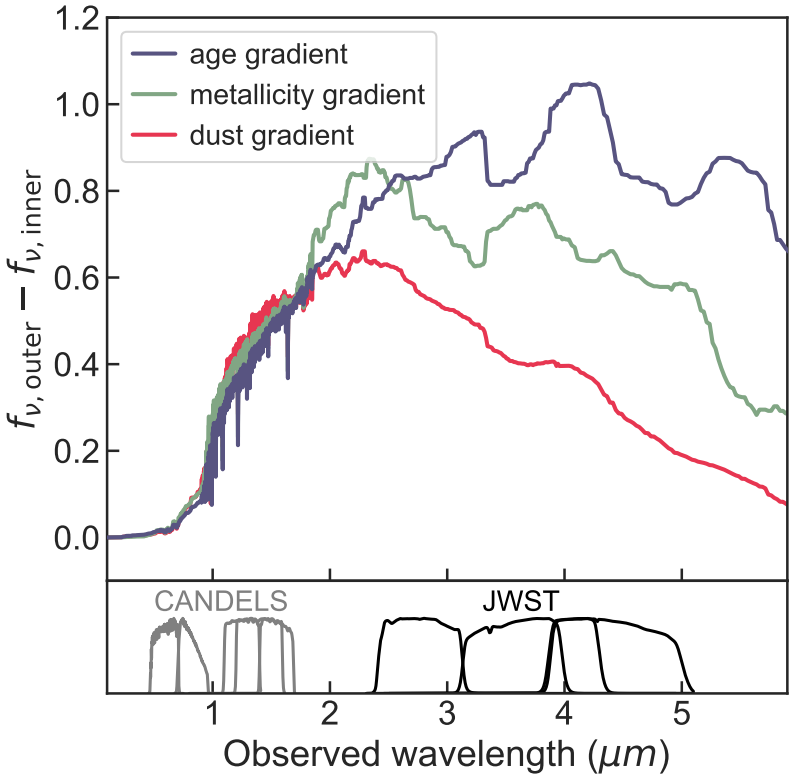

Figure 8.1: Difference in flux between outer and inner annuli of a quiescent galaxy at $z = 1.5$ assuming different stellar population gradients. Existing *HST* CANDELS data cannot distinguish the three scenarios; however, they produce *clearly different effects* in the long-wavelength *JWST* NIRCam filters.

Disentangling age, metallicity, and dust is difficult, and requires rest-frame near-IR imaging and/or spatially-resolved spectroscopy. Local quiescent galaxies have modest metallicity gradients and ∼flat age gradients (e.g., La Barbera et al., 2005; Tortora et al., 2010; Greene et al., 2015; Bluck et al., 2020). However, because age gradients fade very rapidly, these galaxies did not necessarily have flat age gradients when they quenched at z∼2 (e.g., Chan et al., 2016). Observations at cosmic noon are required to provide true constraints on the stellar population gradients caused by quenching. Unfortunately, it has not yet been possible to directly measure stellar population gradients at $z \gtrsim 1$ due to small samples and a lack of rest-frame near-IR data (e.g., Guo et al., 2011; Gargiulo et al., 2012; Chan et al., 2016).

These measurements will soon be possible for a large sample of galaxies due to the advent of *JWST*. Figure 8.1 shows the predicted difference in flux between the inner and outer regions of a quiescent galaxy, assuming a radial gradient in age (blue), metallicity (green), or dust (red). While the effects of these three different stellar population gradients

are indistinguishable with the existing *HST* data used in this thesis, the addition of rest-frame infrared filters with *JWST* would allow us to shed light on the physical origins of observed color gradients. *JWST* data for large numbers of galaxies in the CANDELS fields will be publicly available thanks to the JADES and CEERS surveys.

Mapping molecular gas reservoirs in post-starburst galaxies

In Chapter 6, we showed that two post-starburst galaxies retained large molecular gas reservoirs. The existence of these gas reservoirs challenges most theoretical predictions for the quenching process. The next step forward from the observational perspective is to understand the incidence of these gas reservoirs: are certain types of post-starburst galaxies more likely to host large gas reservoirs? If so, what does this tell us about the processes responsible for quenching?

One possible avenue for this future work is to study whether the amount of molecular gas left in post-starburst galaxies depends on the amount of time they have been quenched, t_q, or the mass fraction in their recent burst, $f_{\rm burst}$. In Chapter 7, we demonstrated that these properties can be robustly determined from SDSS spectroscopy.

A second possible avenue is to investigate how active galactic nuclei (AGN) play a role in the quenching of galaxies. Greene et al. (2020) demonstrated that the SQuIGG$\vec{L}$E sample of post-starburst galaxies has a higher AGN incidence than a control sample of older quiescent galaxies. In the future, additional ALMA observations of post-starburst AGN hosts could help determine whether the presence of an AGN is correlated with molecular gas.

Bibliography

Abolfathi, B., Aguado, D. S., Aguilar, G., et al. 2018, ApJS, 235, 42
Abramson, L. E., Gladders, M. D., Dressler, A., et al. 2016, The Astrophysical Journal, 832, 7
Aihara, H., Allende Prieto, C., An, D., et al. 2011, ApJS, 193, 29
Aihara, H., Arimoto, N., Armstrong, R., et al. 2018, PASJ, 70, S4
Akins, H. B., Narayanan, D., Whitaker, K. E., et al. 2021, arXiv e-prints, arXiv:2105.12748
Alam, S., Albareti, F. D., Allende Prieto, C., et al. 2015, ApJS, 219, 12
Alatalo, K., Lacy, M., Lanz, L., et al. 2015, ApJ, 798, 31
Alatalo, K., Cales, S. L., Rich, J. A., et al. 2016, ApJS, 224, 38
Alatalo, K., Bitsakis, T., Lanz, L., et al. 2017, ApJ, 843, 9
Almaini, O., Wild, V., Maltby, D. T., et al. 2017, MNRAS, 472, 1401
Arnouts, S., Le Floc'h, E., Chevallard, J., et al. 2013, A&A, 558, A67
Asayama, S., Takahashi, T., Kubo, K., et al. 2014, PASJ, 66, 57
Balogh, M. L., Morris, S. L., Yee, H. K. C., Carlberg, R. G., & Ellingson, E. 1999, ApJ, 527, 54
Barro, G., Faber, S. M., Pérez-González, P. G., et al. 2013, ApJ, 765, 104
—. 2014, ApJ, 791, 52
Barro, G., Kriek, M., Pérez-González, P. G., et al. 2016, ApJ, 827, L32
—. 2017a, ApJ, 851, L40
Barro, G., Faber, S. M., Koo, D. C., et al. 2017b, ApJ, 840, 47
Becker, R. H., White, R. L., & Helfand, D. J. 1995, ApJ, 450, 559
Bédorf, J., & Portegies Zwart, S. 2013, MNRAS, 431, 767
Behroozi, P., Wechsler, R. H., Hearin, A. P., & Conroy, C. 2019, MNRAS, 488, 3143
Bell, E. F. 2008, ApJ, 682, 355
Bell, E. F., & de Jong, R. S. 2001, ApJ, 550, 212
Bell, E. F., Wolf, C., Meisenheimer, K., et al. 2004, ApJ, 608, 752
Belli, S., Newman, A. B., & Ellis, R. S. 2015, ApJ, 799, 206
—. 2019, ApJ, 874, 17
Belli, S., Contursi, A., Genzel, R., et al. 2021, ApJ, 909, L11
Bezanson, R., van Dokkum, P., van de Sande, J., Franx, M., & Kriek, M. 2013, ApJ, 764, L8
Bezanson, R., van Dokkum, P. G., Tal, T., et al. 2009, ApJ, 697, 1290

Blanton, M. R., Hogg, D. W., Bahcall, N. A., et al. 2003, ApJ, 594, 186
Bluck, A. F. L., Mendel, J. T., Ellison, S. L., et al. 2014, MNRAS, 441, 599
Bluck, A. F. L., Maiolino, R., Piotrowska, J. M., et al. 2020, MNRAS, 499, 230
Bolatto, A. D., Wolfire, M., & Leroy, A. K. 2013, ARA&A, 51, 207
Bourne, N., Dunlop, J. S., Merlin, E., et al. 2017, MNRAS, 467, 1360
Brammer, G. B., van Dokkum, P. G., & Coppi, P. 2008, ApJ, 686, 1503
Brammer, G. B., Whitaker, K. E., van Dokkum, P. G., et al. 2009, ApJ, 706, L173
Brammer, G. B., van Dokkum, P. G., Franx, M., et al. 2012, ApJS, 200, 13
Bremer, M. N., Phillipps, S., Kelvin, L. S., et al. 2018, MNRAS, 476, 12
Brinchmann, J., Charlot, S., White, S. D. M., et al. 2004, MNRAS, 351, 1151
Brown, M. J. I., Moustakas, J., Caldwell, N., et al. 2009, ApJ, 703, 150
Bruzual, G., & Charlot, S. 2003, MNRAS, 344, 1000
Bundy, K., Scarlata, C., Carollo, C. M., et al. 2010, ApJ, 719, 1969
Byler, N., Dalcanton, J. J., Conroy, C., & Johnson, B. D. 2017, ApJ, 840, 44
Calzetti, D., Armus, L., Bohlin, R. C., et al. 2000, ApJ, 533, 682
Cappellari, M. 2017, MNRAS, 466, 798
Cappellari, M., & Emsellem, E. 2004, PASP, 116, 138
Cappellari, M., Emsellem, E., Krajnović, D., et al. 2011, MNRAS, 413, 813
Cappellari, M., McDermid, R. M., Alatalo, K., et al. 2013, MNRAS, 432, 1862
Carnall, A. C., Leja, J., Johnson, B. D., et al. 2019, ApJ, 873, 44
Carnall, A. C., McLure, R. J., Dunlop, J. S., & Davé, R. 2018, MNRAS, 480, 4379
Carollo, C. M., Bschorr, T. J., Renzini, A., et al. 2013, ApJ, 773, 112
Ceverino, D., Dekel, A., Tweed, D., & Primack, J. 2015, MNRAS, 447, 3291
Chabrier, G. 2003, PASP, 115, 763
Chan, J. C. C., Beifiori, A., Mendel, J. T., et al. 2016, MNRAS, 458, 3181
Chen, Z., Faber, S. M., Koo, D. C., et al. 2020, ApJ, 897, 102
Cheung, E., Faber, S. M., Koo, D. C., et al. 2012, ApJ, 760, 131
Choi, E., Somerville, R. S., Ostriker, J. P., Naab, T., & Hirschmann, M. 2018, ApJ, 866, 91
Choi, J., Dotter, A., Conroy, C., et al. 2016, ApJ, 823, 102
Combes, F., Young, L. M., & Bureau, M. 2007, MNRAS, 377, 1795
Conroy, C., & Gunn, J. E. 2010, ApJ, 712, 833
Conroy, C., Gunn, J. E., & White, M. 2009, ApJ, 699, 486
Couch, W. J., Barger, A. J., Smail, I., Ellis, R. S., & Sharples, R. M. 1998, ApJ, 497, 188
Couch, W. J., & Sharples, R. M. 1987, MNRAS, 229, 423
Cowie, L. L., Songaila, A., Hu, E. M., & Cohen, J. G. 1996, AJ, 112, 839
Daddi, E., Renzini, A., Pirzkal, N., et al. 2005, ApJ, 626, 680
Daddi, E., Dickinson, M., Morrison, G., et al. 2007, ApJ, 670, 156
Dale, D. A., & Helou, G. 2002, ApJ, 576, 159
Damjanov, I., Zahid, H. J., Geller, M. J., et al. 2019, ApJ, 872, 91
Damjanov, I., McCarthy, P. J., Abraham, R. G., et al. 2009, ApJ, 695, 101
Damjanov, I., Abraham, R. G., Glazebrook, K., et al. 2011, ApJ, 739, L44
Dannerbauer, H., Daddi, E., Riechers, D. A., et al. 2009, ApJ, 698, L178

Davis, T. A., Greene, J., Ma, C.-P., et al. 2016, MNRAS, 455, 214
Davis, T. A., Alatalo, K., Bureau, M., et al. 2013, MNRAS, 429, 534
Davis, T. A., Young, L. M., Crocker, A. F., et al. 2014, MNRAS, 444, 3427
Dawson, K. S., Schlegel, D. J., Ahn, C. P., et al. 2013, AJ, 145, 10
Dekel, A., & Burkert, A. 2014, MNRAS, 438, 1870
Dekel, A., Sari, R., & Ceverino, D. 2009, ApJ, 703, 785
D'Eugenio, F., van der Wel, A., Wu , P.-F., et al. 2020, MNRAS, 497, 389
Di Matteo, T., Springel, V., & Hernquist, L. 2005, Nature, 433, 604
Dotter, A. 2016, ApJS, 222, 8
Draine, B. T., & Li, A. 2007, ApJ, 657, 810
Dressler, A., & Gunn, J. E. 1983, ApJ, 270, 7
Dressler, A., Smail, I., Poggianti, B. M., et al. 1999, ApJS, 122, 51
Dutton, A. A., & van den Bosch, F. C. 2009, MNRAS, 396, 141
Dutton, A. A., van den Bosch, F. C., Faber, S. M., et al. 2011, MNRAS, 410, 1660
Emsellem, E., Cappellari, M., Krajnović, D., et al. 2011, MNRAS, 414, 888
Estrada-Carpenter, V., Papovich, C., Momcheva, I., et al. 2020, arXiv e-prints, arXiv:2005.12289
Evans, I. N., Primini, F. A., Glotfelty, K. J., et al. 2010, ApJS, 189, 37
Faber, S. M., Willmer, C. N. A., Wolf, C., et al. 2007, ApJ, 665, 265
Falcón-Barroso, J., Sánchez-Blázquez, P., Vazdekis, A., et al. 2011, A&A, 532, A95
Fang, J. J., Faber, S. M., Koo, D. C., & Dekel, A. 2013, ApJ, 776, 63
Fang, J. J., Faber, S. M., Koo, D. C., et al. 2018, ApJ, 858, 100
Feldmann, R. 2019, Astronomy and Computing, 29, 100331
Feldmann, R., Carollo, C. M., & Mayer, L. 2011, ApJ, 736, 88
Feldmann, R., Quataert, E., Hopkins, P. F., Faucher-Giguère, C.-A., & Kereš, D. 2017, MNRAS, 470, 1050
Forrest, B., Tran, K.-V. H., Broussard, A., et al. 2018, ApJ, 863, 131
Franx, M., van Dokkum, P. G., Förster Schreiber, N. M., et al. 2008, ApJ, 688, 770
French, K. D., Yang, Y., Zabludoff, A., et al. 2015, ApJ, 801, 1
French, K. D., Yang, Y., Zabludoff, A. I., & Tremonti, C. A. 2018, ApJ, 862, 2
Furlong, M., Bower, R. G., Crain, R. A., et al. 2017, MNRAS, 465, 722
Gallazzi, A., Charlot, S., Brinchmann, J., White, S. D. M., & Tremonti, C. A. 2005, MNRAS, 362, 41
García-Benito, R., González Delgado, R. M., Pérez, E., et al. 2019, A&A, 621, A120
Gargiulo, A., Saracco, P., Longhetti, M., La Barbera, F., & Tamburri, S. 2012, MNRAS, 425, 2698
Geach, J. E., Hickox, R. C., Diamond-Stanic, A. M., et al. 2013, ApJ, 767, L17
Genel, S., Nelson, D., Pillepich, A., et al. 2018, MNRAS, 474, 3976
Genzel, R., Tacconi, L. J., Lutz, D., et al. 2015, ApJ, 800, 20
Giovanelli, R., Haynes, M. P., Kent, B. R., et al. 2005, AJ, 130, 2598
Gonçalves, T. S., Martin, D. C., Menéndez-Delmestre, K., Wyder, T. K., & Koekemoer, A. 2012, ApJ, 759, 67

González, V., Labbé, I., Bouwens, R. J., et al. 2010, ApJ, 713, 115
Goto, T. 2005, MNRAS, 357, 937
Graves, G. J., & Schiavon, R. P. 2008, ApJS, 177, 446
Greene, J. E., Janish, R., Ma, C.-P., et al. 2015, ApJ, 807, 11
Greene, J. E., Murphy, J. D., Comerford, J. M., Gebhardt, K., & Adams, J. J. 2012, ApJ, 750, 32
Greene, J. E., Setton, D., Bezanson, R., et al. 2020, ApJ, 899, L9
Grogin, N. A., Kocevski, D. D., Faber, S. M., et al. 2011, ApJS, 197, 35
Gu, Y., Fang, G., Yuan, Q., Cai, Z., & Wang, T. 2018, ApJ, 855, 10
Guo, Y., Giavalisco, M., Cassata, P., et al. 2011, ApJ, 735, 18
Hickox, R. C., Mullaney, J. R., Alexander, D. M., et al. 2014, ApJ, 782, 9
Hill, A. R., Muzzin, A., Franx, M., et al. 2017, ApJ, 837, 147
Hopkins, P. F., Bundy, K., Murray, N., et al. 2009, MNRAS, 398, 898
Hopkins, P. F., Somerville, R. S., Hernquist, L., et al. 2006, ApJ, 652, 864
Huang, K.-H., Fall, S. M., Ferguson, H. C., et al. 2017, ApJ, 838, 6
Hubble, E. P. 1926, ApJ, 64, 321
Hunt, Q., Bezanson, R., Greene, J. E., et al. 2018, ApJ, 860, L18
Iyer, K., & Gawiser, E. 2017, ApJ, 838, 127
Iyer, K. G., Gawiser, E., Faber, S. M., et al. 2019, ApJ, 879, 116
Ji, Z., Giavalisco, M., Williams, C. C., et al. 2018, ApJ, 862, 135
Jiang, F., Dekel, A., Kneller, O., et al. 2019, MNRAS, 488, 4801
Johnson, B., & Leja, J. 2017, Bd-J/Prospector: Initial Release, doi:10.5281/zenodo.1116491
Johnson, B. D., Leja, J., Conroy, C., & Speagle, J. S. 2020, arXiv e-prints, arXiv:2012.01426
Kauffmann, G., Heckman, T. M., White, S. D. M., et al. 2003, MNRAS, 341, 54
Kaviraj, S., Kirkby, L. A., Silk, J., & Sarzi, M. 2007, MNRAS, 382, 960
Kennicutt, Robert C., J. 1998a, ApJ, 498, 541
Kennicutt, Jr., R. C. 1998b, ARA&A, 36, 189
Kereš, D., Katz, N., Davé, R., Fardal, M., & Weinberg, D. H. 2009, MNRAS, 396, 2332
Kocevski, D. D., Lemaux, B. C., Lubin, L. M., et al. 2011, ApJ, 737, L38
Koekemoer, A. M., Faber, S. M., Ferguson, H. C., et al. 2011, ApJS, 197, 36
Kravtsov, A. V. 2013, ApJ, 764, L31
Kriek, M., & Conroy, C. 2013, ApJ, 775, L16
Kriek, M., van Dokkum, P. G., Labbé, I., et al. 2009, ApJ, 700, 221
Kriek, M., van Dokkum, P. G., Whitaker, K. E., et al. 2011, ApJ, 743, 168
Kriek, M., Labbé, I., Conroy, C., et al. 2010, ApJ, 722, L64
Kriek, M., Conroy, C., van Dokkum, P. G., et al. 2016, Nature, 540, 248
Kriek, M., Price, S. H., Conroy, C., et al. 2019, ApJ, 880, L31
La Barbera, F., de Carvalho, R. R., Gal, R. R., et al. 2005, ApJ, 626, L19
Lang, P., Wuyts, S., Somerville, R. S., et al. 2014, ApJ, 788, 11
Le Borgne, D., Abraham, R., Daniel, K., et al. 2006, ApJ, 642, 48
Lee, B., Giavalisco, M., Whitaker, K., et al. 2018, ApJ, 853, 131
Lee, S.-K., Ferguson, H. C., Somerville, R. S., Wiklind, T., & Giavalisco, M. 2010, ApJ, 725,

1644
Lee, S.-K., Idzi, R., Ferguson, H. C., et al. 2009, ApJS, 184, 100
Leja, J., Carnall, A. C., Johnson, B. D., Conroy, C., & Speagle, J. S. 2019a, ApJ, 876, 3
Leja, J., Johnson, B. D., Conroy, C., van Dokkum, P. G., & Byler, N. 2017, ApJ, 837, 170
Leja, J., Johnson, B. D., Conroy, C., et al. 2019b, ApJ, 877, 140
Lemaux, B. C., Lubin, L. M., Shapley, A., et al. 2010, ApJ, 716, 970
Lilly, S. J., & Carollo, C. M. 2016, ApJ, 833, 1
Liu, F. S., Jiang, D., Faber, S. M., et al. 2017, ApJ, 844, L2
Lower, S., Narayanan, D., Leja, J., et al. 2020, ApJ, 904, 33
Magdis, G. E., Daddi, E., Béthermin, M., et al. 2012, ApJ, 760, 6
Magnelli, B., Elbaz, D., Chary, R. R., et al. 2009, A&A, 496, 57
Maier, C., Lilly, S. J., Zamorani, G., et al. 2009, ApJ, 694, 1099
Mainzer, A., Bauer, J., Grav, T., et al. 2011, ApJ, 731, 53
Maltby, D. T., Almaini, O., Wild, V., et al. 2018, MNRAS, 480, 381
—. 2016, MNRAS, 459, L114
Mantz, A. B. 2019, MNRAS, 485, 4863
Maraston, C., Pforr, J., Renzini, A., et al. 2010, MNRAS, 407, 830
Marchesini, D., van Dokkum, P. G., Förster Schreiber, N. M., et al. 2009, ApJ, 701, 1765
Martí-Vidal, I., Vlemmings, W. H. T., Muller, S., & Casey, S. 2014, A&A, 563, A136
Martig, M., Bournaud, F., Teyssier, R., & Dekel, A. 2009, ApJ, 707, 250
Martin, D. C., Wyder, T. K., Schiminovich, D., et al. 2007, ApJS, 173, 342
Masters, K. L., Mosleh, M., Romer, A. K., et al. 2010, MNRAS, 405, 783
Mendez, A. J., Coil, A. L., Lotz, J., et al. 2011, ApJ, 736, 110
Mo, H. J., Mao, S., & White, S. D. M. 1998, MNRAS, 295, 319
Momcheva, I. G., Brammer, G. B., van Dokkum, P. G., et al. 2016, ApJS, 225, 27
Mosleh, M., Hosseinnejad, S., Zahra Hosseini-ShahiSavandi, S., & Tacchella, S. 2020, arXiv e-prints, arXiv:2011.04656
Mosleh, M., Tacchella, S., Renzini, A., et al. 2017, ApJ, 837, 2
Moutard, T., Sawicki, M., Arnouts, S., et al. 2018, MNRAS, 479, 2147
Mowla, L., van der Wel, A., van Dokkum, P., & Miller, T. B. 2019a, ApJ, 872, L13
Mowla, L. A., van Dokkum, P., Brammer, G. B., et al. 2019b, ApJ, 880, 57
Murphy, E. J., Chary, R. R., Dickinson, M., et al. 2011, ApJ, 732, 126
Muzzin, A., Marchesini, D., Stefanon, M., et al. 2013, ApJ, 777, 18
Naab, T., Johansson, P. H., & Ostriker, J. P. 2009, ApJ, 699, L178
Narayanan, D., Krumholz, M. R., Ostriker, E. C., & Hernquist, L. 2012, MNRAS, 421, 3127
Nelson, E., van Dokkum, P., Franx, M., et al. 2014, Nature, 513, 394
Nelson, E. J., van Dokkum, P. G., Momcheva, I. G., et al. 2016a, ApJ, 817, L9
Nelson, E. J., van Dokkum, P. G., Förster Schreiber, N. M., et al. 2016b, ApJ, 828, 27
Nelson, E. J., Tadaki, K.-i., Tacconi, L. J., et al. 2019, ApJ, 870, 130
Newman, A. B., Ellis, R. S., Bundy, K., & Treu, T. 2012, ApJ, 746, 162
Nipoti, C., Treu, T., Auger, M. W., & Bolton, A. S. 2009, ApJ, 706, L86
Noeske, K. G., Weiner, B. J., Faber, S. M., et al. 2007, ApJ, 660, L43

Norris, M. A., Kannappan, S. J., Forbes, D. A., et al. 2014, MNRAS, 443, 1151
Omand, C. M. B., Balogh, M. L., & Poggianti, B. M. 2014, MNRAS, 440, 843
Oser, L., Ostriker, J. P., Naab, T., Johansson, P. H., & Burkert, A. 2010, ApJ, 725, 2312
Patel, S. G., Kelson, D. D., Holden, B. P., Franx, M., & Illingworth, G. D. 2011, ApJ, 735, 53
Patel, S. G., van Dokkum, P. G., Franx, M., et al. 2013, ApJ, 766, 15
Pattarakijwanich, P., Strauss, M. A., Ho, S., & Ross, N. P. 2016, ApJ, 833, 19
Paxton, B., Bildsten, L., Dotter, A., et al. 2011, ApJS, 192, 3
Paxton, B., Cantiello, M., Arras, P., et al. 2013, ApJS, 208, 4
Paxton, B., Marchant, P., Schwab, J., et al. 2015, ApJS, 220, 15
Peng, C. Y., Ho, L. C., Impey, C. D., & Rix, H.-W. 2002, AJ, 124, 266
Peng, Y.-j., Lilly, S. J., Kovač, K., et al. 2010, ApJ, 721, 193
Poggianti, B. M., Moretti, A., Calvi, R., et al. 2013, ApJ, 777, 125
Price, S. H., Kriek, M., Feldmann, R., et al. 2017, ApJ, 844, L6
Quadri, R. F., Williams, R. J., Franx, M., & Hildebrandt, H. 2012, ApJ, 744, 88
Quintero, A. D., Hogg, D. W., Blanton, M. R., et al. 2004, ApJ, 602, 190
Rowlands, K., Wild, V., Bourne, N., et al. 2018, MNRAS, 473, 1168
Saglia, R. P., Maraston, C., Greggio, L., Bender, R., & Ziegler, B. 2000, A&A, 360, 911
Saintonge, A., Kauffmann, G., Kramer, C., et al. 2011, MNRAS, 415, 32
Salim, S., Lee, J. C., Davé, R., & Dickinson, M. 2015, ApJ, 808, 25
Sánchez-Blázquez, P., Peletier, R. F., Jiménez-Vicente, J., et al. 2006, MNRAS, 371, 703
Sanders, R. L., Shapley, A. E., Kriek, M., et al. 2018, ApJ, 858, 99
Saracco, P., Gargiulo, A., Ciocca, F., & Marchesini, D. 2017, A&A, 597, A122
Sazonova, E., Alatalo, K., Rowlands, K., et al. 2021, arXiv e-prints, arXiv:2105.09956
Schawinski, K., Urry, C. M., Simmons, B. D., et al. 2014, MNRAS, 440, 889
Sell, P. H., Tremonti, C. A., Hickox, R. C., et al. 2014, MNRAS, 441, 3417
Setton, D. J., Bezanson, R., Suess, K. A., et al. 2020, arXiv e-prints, arXiv:2010.04734
Shen, S., Mo, H. J., White, S. D. M., et al. 2003, MNRAS, 343, 978
Skelton, R. E., Whitaker, K. E., Momcheva, I. G., et al. 2014, ApJS, 214, 24
Smercina, A., Smith, J. D. T., Dale, D. A., et al. 2018, ApJ, 855, 51
Socolovsky, M., Almaini, O., Hatch, N. A., et al. 2018, MNRAS, 476, 1242
Somerville, R. S., Barden, M., Rix, H.-W., et al. 2008, ApJ, 672, 776
Somerville, R. S., Behroozi, P., Pandya, V., et al. 2018, MNRAS, 473, 2714
Speagle, J. S. 2020, MNRAS, 493, 3132
Spitler, L. R., Straatman, C. M. S., Labbé, I., et al. 2014, ApJ, 787, L36
Springel, V., & Hernquist, L. 2005, ApJ, 622, L9
Straatman, C. M. S., Spitler, L. R., Quadri, R. F., et al. 2016, ApJ, 830, 51
Suess, K. A., Bezanson, R., Spilker, J. S., et al. 2017, ApJ, 846, L14
Suess, K. A., Kriek, M., Price, S. H., & Barro, G. 2019a, ApJ, 877, 103
—. 2019b, ApJ, 885, L22
—. 2020, ApJ, 899, L26
—. 2021, ApJ, 915, 87

Szomoru, D., Franx, M., & van Dokkum, P. G. 2012, ApJ, 749, 121
Szomoru, D., Franx, M., van Dokkum, P. G., et al. 2013, ApJ, 763, 73
—. 2010, ApJ, 714, L244
Tacchella, S., Carollo, C. M., Faber, S. M., et al. 2017, ApJ, 844, L1
Tacchella, S., Dekel, A., Carollo, C. M., et al. 2016, MNRAS, 458, 242
Tacchella, S., Carollo, C. M., Renzini, A., et al. 2015a, Science, 348, 314
Tacchella, S., Lang, P., Carollo, C. M., et al. 2015b, ApJ, 802, 101
Tacchella, S., Carollo, C. M., Förster Schreiber, N. M., et al. 2018, ApJ, 859, 56
Tacchella, S., Conroy, C., Faber, S. M., et al. 2021, arXiv e-prints, arXiv:2102.12494
Tacconi, L. J., Genzel, R., & Sternberg, A. 2020, ARA&A, 58, 157
Tacconi, L. J., Neri, R., Genzel, R., et al. 2013, ApJ, 768, 74
Tadaki, K.-i., Belli, S., Burkert, A., et al. 2020, ApJ, 901, 74
Tomczak, A. R., Quadri, R. F., Tran, K.-V. H., et al. 2014, ApJ, 783, 85
Tortora, C., Napolitano, N. R., Cardone, V. F., et al. 2010, MNRAS, 407, 144
van de Sande, J., Kriek, M., Franx, M., et al. 2013, ApJ, 771, 85
van den Bergh, S. 1976, ApJ, 206, 883
van der Wel, A., Bell, E. F., van den Bosch, F. C., Gallazzi, A., & Rix, H.-W. 2009, ApJ, 698, 1232
van der Wel, A., Bell, E. F., Häussler, B., et al. 2012, ApJS, 203, 24
van der Wel, A., Franx, M., van Dokkum, P. G., et al. 2014, ApJ, 788, 28
van Dokkum, P. G., & Franx, M. 2001, ApJ, 553, 90
van Dokkum, P. G., Franx, M., Kriek, M., et al. 2008, ApJ, 677, L5
van Dokkum, P. G., Whitaker, K. E., Brammer, G., et al. 2010, ApJ, 709, 1018
van Dokkum, P. G., Brammer, G., Fumagalli, M., et al. 2011, ApJ, 743, L15
van Dokkum, P. G., Leja, J., Nelson, E. J., et al. 2013, ApJ, 771, L35
van Dokkum, P. G., Bezanson, R., van der Wel, A., et al. 2014, ApJ, 791, 45
van Dokkum, P. G., Nelson, E. J., Franx, M., et al. 2015, ApJ, 813, 23
Wellons, S., Torrey, P., Ma, C.-P., et al. 2015, MNRAS, 449, 361
Whitaker, K. E., Kriek, M., van Dokkum, P. G., et al. 2012a, ApJ, 745, 179
Whitaker, K. E., Pope, A., Cybulski, R., et al. 2017a, ApJ, 850, 208
Whitaker, K. E., van Dokkum, P. G., Brammer, G., & Franx, M. 2012b, ApJ, 754, L29
Whitaker, K. E., Bezanson, R., van Dokkum, P. G., et al. 2017b, ApJ, 838, 19
Wild, V., Almaini, O., Dunlop, J., et al. 2016, MNRAS, 463, 832
Wild, V., Almaini, O., Cirasuolo, M., et al. 2014, MNRAS, 440, 1880
Wild, V., Taj Aldeen, L., Carnall, A., et al. 2020, MNRAS, 494, 529
Williams, C. C., Giavalisco, M., Bezanson, R., et al. 2017, ApJ, 838, 94
Williams, R. J., Quadri, R. F., Franx, M., van Dokkum, P., & Labbé, I. 2009, ApJ, 691, 1879
Wilman, D. J., Fossati, M., Mendel, J. T., et al. 2020, ApJ, 892, 1
Woo, J., Carollo, C. M., Faber, S. M., Dekel, A., & Tacchella, S. 2017, MNRAS, 464, 1077
Woo, J., Dekel, A., Faber, S. M., & Koo, D. C. 2015, MNRAS, 448, 237
Woo, J., & Ellison, S. L. 2019, MNRAS, 487, 1927

Wu, P.-F., van der Wel, A., Bezanson, R., et al. 2018, ApJ, 868, 37
—. 2020, ApJ, 888, 77
Wuyts, S., Cox, T. J., Hayward, C. C., et al. 2010, ApJ, 722, 1666
Wuyts, S., Franx, M., Cox, T. J., et al. 2009, ApJ, 696, 348
Wuyts, S., Labbé, I., Franx, M., et al. 2007, ApJ, 655, 51
Wuyts, S., Förster Schreiber, N. M., van der Wel, A., et al. 2011, ApJ, 742, 96
Wuyts, S., Förster Schreiber, N. M., Genzel, R., et al. 2012, ApJ, 753, 114
Wyder, T. K., Martin, D. C., Schiminovich, D., et al. 2007, ApJS, 173, 293
Yan, R., Newman, J. A., Faber, S. M., et al. 2006, ApJ, 648, 281
Yano, M., Kriek, M., van der Wel, A., & Whitaker, K. E. 2016, ApJ, 817, L21
Young, L. M., Bureau, M., Davis, T. A., et al. 2011, MNRAS, 414, 940
Zabludoff, A. I., Zaritsky, D., Lin, H., et al. 1996, ApJ, 466, 104
Zibetti, S., Charlot, S., & Rix, H.-W. 2009, MNRAS, 400, 1181
Zick, T. O., Kriek, M., Shapley, A. E., et al. 2018, ApJ, 867, L16
Zolotov, A., Dekel, A., Mandelker, N., et al. 2015, MNRAS, 450, 2327